



marine technology SOCIETY

Journal

The International, Interdisciplinary Society Devoted to Ocean and Marine Engineering, Science, and Policy

Volume 47 Number 3 May/June 2013



Focus on

**DeepStar® Global Deepwater
Technology Development**

OCEANS



2013

MTS/IEEE San Diego

EXHIBITORS

Good spaces are still left,
but going fast!

ATTENDEES

Registration opens May 20!

THE WORLD'S PREMIER OCEANS EVENT

September 23-26, 2013
AN OCEAN IN COMMON

OCEANS'13 CONFERENCE HIGHLIGHTS INCLUDE:

- Twelve Co-participating Societies
- Academic Host: Scripps Institution of Oceanography/UCSD
- Over 250 exhibits in two halls, plus Academic Row
- Opening Plenary with Ocean VIPs
- Extensive technical and scientific tracks and sessions
- Ultra-Deep Ocean Track with renowned presenters
- Tutorials with college credit
- Student Opportunities: Discounted Rates, Session Chairs, Poster Competition
- Golf Tournament
- Underwater Film Festival on two nights
- Gala on the Carrier U.S.S. Midway
- A celebration of the MTS 50th Anniversary
- STEM Educators Workshop



ACADEMIC
SPONSOR:



EXHIBIT SPACE

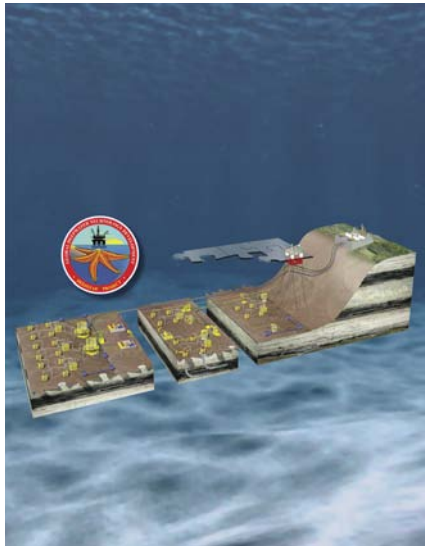
Space is filling up, but many good locations are still available. Visit the interactive Oceans 2013 Exhibit Hall Floor Plan at: oceans13mtsieeesandiego.org/exhibitor/floorplan and pick your spot. Or contact Sue Kingston, IEEE Exhibits Manager, for more information. e-mail: s.kingston@ieee.org • office: 1 (310) 937-1006 • cell 1 (310) 699-2609

VISIT US ONLINE

OCEANS13MTSIEEESANDIEGO.ORG

LIKE US ON FACEBOOK:

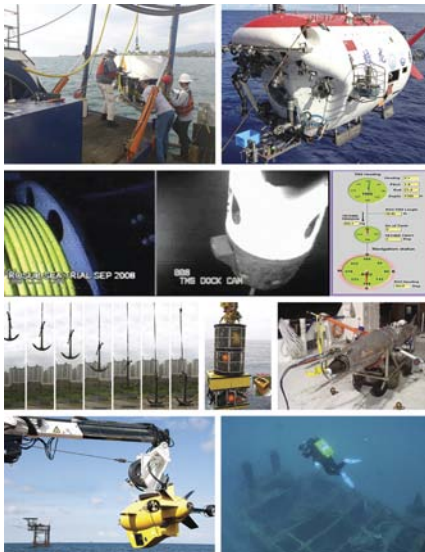
 /Oceans2013



Front Cover: DeepStar® cover graphic, artwork, and logo is a registered trademark of Chevron Intellectual Property LLC.

Back Cover: All images can be found within this issue.

Top row (l-r): Schmidt et al., Figure 6; Cui, Figure 4; 2nd row: Vedachalam et al., Figure 4; 3rd row (l-r): Yoon & Na, Figure 3; Vedachalam et al., Figure 15; Cooper et al., Figure 1; Bottom row (l-r): Jacobson, Figure 3; Peirano, Figure 2.



Text: SPI

Cover and Graphics:

Michele A. Danoff, Graphics By Design

The Marine Technology Society Journal

(ISSN 0025-3324) is published by the Marine Technology Society, Inc., 1100 H Street NW, Suite LL-100 Washington, DC 20005

Subscription Prices (all prices include shipping):

MTS members can purchase the printed *Journal* for \$32 domestic and \$110 international. Non-members and library subscriptions are \$435 **online only** (includes 13 years of archives); \$460 for **online with print** (includes 12 years of archives); \$135 **print only** within the U.S. and Canada, \$200 **print only** international. Single-issue (hardcopy) is \$20 plus \$7.50 S&H (domestic), \$24.50 S&H (international); Pay-per-view (worldwide): \$15/article. Postage for periodicals is paid at Washington, DC and additional mailing offices.

POSTMASTER:

Please send address changes to:

Marine Technology Society Journal

1100 H Street NW, Suite LL-100
Washington, DC 20005
Tel: (202) 717-8705; Fax: (202) 347-4305

Copyright © 2013 Marine Technology Society, Inc.

marine technology SOCIETY Journal

Volume 47, Number 3, May/June 2013

Focus on DeepStar® Global Deepwater Technology Development

In This Issue

Focus on DeepStar

5

DeepStar®: 22 Years of Success
DeepStar: A Global Deepwater Technology Development Program

Greg Kusinski, Art J. Schroeder, Jr., James E. Chitwood

13

DeepStar 11304: Laying the Groundwork for AUV Standards for Deepwater Fields

John Jacobson, Pierce Cohen, Amin Nasr, Art J. Schroeder, Jr., Greg Kusinski

19

DeepStar Metocean Studies: 15 years of Discovery

Cortis Cooper, Tom Mitchell, George Forristall, James Stear

27

Recent Development in IR Sensor Technology for Monitoring Subsea Methane Discharge

Mark Schmidt, Peter Linke, Daniel Esser

General Papers

37

Development of the *Jiaolong* Deep Manned Submersible

Weicheng Cui

55

Reliability-Centered Development of Deep Water ROV ROSUB 6000

Vedachalam Narayanaswamy, Ramesh Raju, Muthukumaran Durairaj, Aarthi Ananthapadmanabhan, Subramanian Annamalai, Gidugu Ananada Ramadass, Malayath Aravindakshan Atmanand

72

Anchor Drop Tests for a Submarine Power-Cable Protector

Han-Sam Yoon, Won-Bae Na

81

Elements of Underwater Glider Performance and Stability

Shuangshuang Fan, Craig Woolsey

99

Analysis of Underwater Acoustic Communication Channels

Sadia Ahmed, Huseyin Arslan

118

Wrecks on the Bottom: Useful, Ecological Sentinels?

Andrea Peirano

Marine Technology Society Officers

BOARD OF DIRECTORS

President

Drew Michael
ROV Technologies, Inc.

President-elect

Richard W. Spinrad
Oregon State University

Immediate Past President

Jerry Boatman
QinetiQ North America – Technology Solutions
Group

VP—Section Affairs

Lisa Medeiros
Geospace Offshore Cables

VP—Education and Research

Jill Zande
MATE Center

VP—Industry and Technology

Raymond Toll
Computer Sciences Corporation

VP—Publications

Donna Kocak
HARRIS Corporation

Treasurer and VP—Budget and Finance

Debra Kill
International Submarine Engineering

VP—Government and Public Affairs

Justin Manley
Teledyne Benthos

SECTIONS

Canadian Maritime

Vacant

Great Lakes

TBD

Gulf Coast

Laurie Jugan
Consultant

Hampton Roads

Raymond Toll
Computer Sciences Corporation

Hawaii

Stu Burley
Strategic Theories Unlimited

Houston

Aimee Marsh
EIC

Japan

Prof. Toshitsugu Sakou
Tokai University

Mid-Gulf Coast-Florida

Erica Moulton
MATE

Monterey

Jill Zande
MATE Center

New England

Chris Jakubiak
UMASS Dartmouth-SMAST

Norway

TBD

Newfoundland and Labrador

Gary Dinn
Memorial University

Oregon

Jeremy Childress
Oregon State University
College of Oceanic & Atmospheric Sciences

Puget Sound

Fritz Stahr
University of Washington

San Diego

David Velasco
SonTek/YSI

South Korea

Dr. Seok Won Hong
Maritime & Ocean Engineering Research Inst.
(MOERI/KORDI)

Washington, D.C.

Capt. Dennis “Mike” Egan, P.E.
EESS LLC

PROFESSIONAL COMMITTEES

Industry and Technology

Buoy Technology

Dr. Walter Paul
Woods Hole Oceanographic Institution
Cables and Connectors

Vacant

Deepwater Field Development Technology

Dr. Benton Baugh
Radoil, Inc.

Diving

Michael Lombardi
Ocean Opportunity
Michael Max
Hydrate Energy International LLC

Dynamic Positioning

Howard Shatto
Shatto Engineering
Manned Underwater Vehicles

William Kohnen
HYDROSPACE Group

Moorings

Jack Rowley
SAIC

Oceanographic Instrumentation

Dr. Carol Janzen
Sea-Bird Electronics, Inc.

Offshore Structures

Dr. Peter W. Marshall
MHP Systems Engineering

Remotely Operated Vehicles

Chuck Richards
C.A. Richards and Associates, Inc.

Ropes and Tension Members

Evan Zimmerman
Delmar Systems, Inc.

Seafloor Engineering

Craig Etka
Scorpio Ventures, LLC

Underwater Imaging

Dr. Fraser Dalgleish
Harbor Branch Oceanographic Institute

Unmanned Maritime Vehicles

Rafael Mandujano
Vehicle Control Technologies, Inc.

Education and Research

Marine Archaeology

Dan Warren
C & C Technologies

Marine Education

Erica Moulton
MATE Center

Marine Geodetic Information Systems

Dave Zilkoski
NOAA

Marine Materials

Capt. Dennis “Mike” Egan
EESS, LLC

Ocean Exploration

Shane Zigler
OceanGate, Inc.

Physical Oceanography/Meteorology

Dr. Richard L. Crout
National Data Buoy Center

Remote Sensing

Ryan Vandermeulen
University of Southern Mississippi

Government and Public Affairs

Marine Law and Policy

Vacant

Marine Mineral Resources

Dr. John C. Wiltshire
University of Hawaii

Marine Security

Dallas Meggitt
Sound & Sea Technology

Ocean Economic Potential

James Marsh

University of Hawaii
Ocean Observing Systems

Donna Kocak

HARRIS Corporation

Ocean Pollution

Ryan Morton
Anadarko Petroleum

Renewable Energy

Maggie L. Merrill
Marine Marketing Services and New England

MREC at UMass Dartmouth

Kenneth Baldwin
University of New Hampshire

STUDENT SECTIONS

Alpena Community College

Counselor: TBD

Brigham Young University

Counselor: TBD

College of William & Mary

Counselor: Heather MacDonald

Dalhousie University

Counselor: Tejana Ross, Ph.D.

Duke University

Counselor: Douglas Nowacek, Ph.D.

Florida Atlantic University

Counselor: Douglas A. Briggs, Ph.D.

Florida Institute of Technology

Counselor: Stephen Wood, Ph.D., P.E.

Long Beach City College

Counselor: Scott Fraser

Marine Institute (MI)

Counselor: TBD

Massachusetts Institute of Technology

Counselor: Alexandra Techet, Ph.D.

Memorial University (MUN)

Counselor: TBD

Monterey Peninsula College/Hartnell College

Counselor: Jeremy R. Hertzberg

Northeastern University

Counselor: Joseph Ayers, Ph.D.

Oregon State University

Counselor: R. Kipp Shearman

Texas A&M University—College Station

Counselor: Robert Randall, Ph.D.

Texas A&M—Corpus Christi

Counselor: Dugan Um, Ph.D.

Texas A&M University—Galveston

Counselor: David Talent, Ph.D.

United States Naval Academy

Counselor: Cmdr. David J. Robillard

University of Hawaii

Counselor: Dr. Reza Ghorbani

University of Houston

Counselors: Raresh Pascali, P.E.,
Chuck Richards

University of North Carolina—Charlotte

Counselor: James Conrad, Ph.D.

University of Southern Mississippi

Counselor: Stephen Howden, Ph.D.

University of Washington

Counselor: Rick Rupan

Webb Institute

Counselor: Matthew Werner

HONORARY MEMBERS

†Robert B. Abel

†Charles H. Bussmann

John C. Calhoun, Jr.

John P. Craven

†Paul M. Fye

David S. Potter

†Athelstan Spilhaus

†E. C. Stephan

†Allyn C. Vine

†James H. Wakelin, Jr.

†deceased

MTS Needs Your Assistance!



**This year the Marine Technology Society is celebrating
*50 years of excellence.***

And just one of the ways the Society is celebrating is publishing a coffee-table type book tracing the amazing advancements in marine technology over the past 50 years.

It is, of course, inevitable that MTS members will feature prominently. The broad diversity of the interests represented by our Professional Committees and our conference programs span all of the key disciplines that produced the advances that have helped the world do a better job of exploring, protecting and utilizing the precious ocean resources that cover 70 percent of the Earth's surface.

Your assistance is needed!

**We welcome your contributions of anecdotes,
personal remembrances, and pictures.**

And we look forward to seeing you at our big celebration at OCEANS'13 MTS/IEEE
San Diego in September!

Please send your materials to
Mary Beth Loutinsky at mbloutinsky@gmail.com.
Contributors will be listed in the book, and all photos and materials will be
acknowledged and returned.

Editorial Board

Ann E. Jochens, Ph.D.
Editor
Texas A&M University

Brian Bingham, Ph.D.
University of Hawaii at Manoa

Donna Kocak
HARRIS Corporation

Scott Kraus, Ph.D.
New England Aquarium

Dhugal Lindsay, Ph.D.
Japan Agency for Marine-Earth Science
& Technology

Justin Manley
Teledyne Benthos

Eugene Massion
Monterey Bay Aquarium Research Institute

Jill Zande
MATE Center

Editorial

Donna Kocak
VP of Publications

Ann E. Jochens, Ph.D.
Editor

Amy Morgante
Managing Editor

Administration

Drew Michel
President

Richard Lawson
Executive Director

Chris Barrett
Director of Professional Development
and Meetings

Jeanne Glover
Membership and Marketing Manager

Allan Gray
Financial Operations Manager

Jacob Sobin
Member Groups and Student
Outreach Manager

Suzanne Voelker
Subscription Manager

The Marine Technology Society is a not-for-profit, international professional society. Established in 1963, the Society's mission is to promote the exchange of information in ocean and marine engineering, technology, science, and policy.

Please send all correspondence to:
The Marine Technology Society
1100 H Street NW, Suite LL-100
Washington, DC 20005
(202) 717-8705 Tel.
(202) 347-4305 Fax

MTS Journal: morganteeditorial@verizon.net
Publications: publications@mtsociety.org
Membership: Jeanne.Glover@mtsociety.org
Programs: Jake.Sobin@mtsociety.org
Director: Rich.Lawson@mtsociety.org
Online: www.mtsociety.org

MEMBERSHIP INFORMATION

may be obtained by contacting the Marine Technology Society. Benefits include:

- Free subscription to the online *Marine Technology Society Journal*, with highly reduced rates for the paper version
- Free subscription to the bimonthly newsletter, *Currents*, covering events, business news, science and technology, and people in marine technology
- Member discounts on all MTS publications
- Reduced registration rates to all MTS and MTS-sponsored conferences and workshops
- Member-only access to an expansive Job Bank and Member Directory
- Reduced advertising rates in MTS publications
- National recognition through our Awards Program

Individual dues are \$75 per year. Life membership is available for a one-time fee of \$1,000. Patron, Student, Emeritus, Institutional, Business, and Corporate memberships are also available.

ADVERTISING

Advertising is accepted by the *Marine Technology Society Journal*. For more information on MTS advertising and policy, please contact Mary Beth Loutinsky, mbloutinsky@gmail.com

COPYRIGHT

Copyright © 2013 by the Marine Technology Society, Inc. Authorization to photocopy items for internal or personal use, or the internal or personal use of specific clients, is granted by the Marine Technology Society, provided that the base fee of \$1.00 per copy, plus .20 per page is paid directly to Copyright Clearance Center, 222 Rosewood Dr., Danvers, MA 01923.

For those organizations that have been granted a photocopy license by CCC, a separate system of payment has been arranged. The fee code for users of the Transactional Reporting Service is 0025-3324/89 \$1.00 + .20. Papers by U.S Government employees are declared works of the U.S. Government and are therefore in the public domain.

The Marine Technology Society cannot be held responsible for the opinions given and the statements made in any of the articles published.

ABSTRACTS

MTS Journal article abstracts, if available, can be accessed for free at <http://www.ingentaconnect.com/content/mts/mts.j>.

Print and electronic abstracts of *MTS Journal* articles are also available through *GeoRef* <<http://www.agiweb.org/georef/>>, *Aquatic Sciences and Fisheries Abstracts*, published by Cambridge Scientific Abstracts <<http://www.csa.com/factsheets/aquclust-set-c.php>>, and *Geobase's Oceanbase* published by Elsevier Science.

CONTRIBUTORS

Contributors can obtain an information and style sheet by contacting the managing editor. Submissions that are relevant to the concerns of the Society are welcome. All papers are subjected to a stringent review procedure directed by the editor and the editorial board. The *Journal* focuses on technical material that may not otherwise be available, and thus technical papers and notes that have not been published previously are given priority. General commentaries are also accepted and are subject to review and approval by the editorial board.

DeepStar[®]: 22 Years of Success

DeepStar: A Global Deepwater Technology Development Program

AUTHORS

Greg Kusinski
Chevron Energy Technology
Company and
DeepStar Director

Art J. Schroeder, Jr.
Energy Valley, Inc., and
DeepStar Consultant

James E. Chitwood
Chitwood Engineering and
DeepStar Consultant

Introduction

The oil and gas industry has long established a collaborative approach to reduce risks and optimize results, especially in the area of technology development for major exploration and production (E&P) projects. In 1991, a visionary group of industry operators laid the foundation for what is DeepStar[®] today, a highly successful initiative for technical collaboration to enhance deepwater exploration, drilling and production. The Chevron-managed, consensus-driven DeepStar consortium has evolved steadily during the past two decades to meet ever increasing technical challenges of deepwater development and production. However, it has never wavered from its core mission to provide our industry with an open platform to investigate complex technical challenges and collaboratively develop safe, viable solutions. This article outlines DeepStar's strategies and overviews

its organization, operation, and direction. Some additional detail is provided on historical major accomplishments as well as current research activities and a vision of the future for deepwater success.

DeepStar Overview

DeepStar is an operator-driven and funded research and development (R&D) collaboration between oil companies, vendors, regulators, and academic/research institutes started in 1991. Within the overlap of operator member-driven, collaborative space deepwater technology needs, DeepStar serves as a well-proven tool to leverage resources of a multitude of scarce sources. Leverage includes

- direct hard-dollar funding of third-party R&D suppliers;
- DeepStar member internal technical expertise, subject matter experts (SMEs) from both Participants (operators) and Contributors (manufacturers, service companies, universities, engineering firms, etc.);
- in-kind contributions including previous work in the field of interest;
- potential field test/demonstration opportunities;
- a well-honed, effective and efficient set of processes and procedures;
- a respected track record of success interfacing with regulatory agencies and standards-developing organizations.

Figure 1 outlines the role DeepStar occupies to meet operator members' collaborative technology needs.

With DeepStar membership including over 80 organizations employing well over 1 million people and operating in all of the world's deepwater and ultradeepwater basins, it is well positioned to ensure members are focused on the right technical challenges and leveraged to produce meaningful and value-added results. See Figure 2 for a listing of current members.

DeepStar has a proven and long-term record for delivery of value to its membership. Its mission is to facilitate a cooperative, globally aligned effort focused on identification and development of economically viable methods to drill, produce, and transport hydrocarbons from deepwater. DeepStar's current Phase XI program is focused on global deepwater development in water depths to 10,000+ feet. As the premier global forum to define deepwater technology needs, it provides value to its membership by leveraging financial and technical resources to

- define and rank important deepwater technology needs,
- deliver technologies via a well honed stage-gate process,
- build deepwater technical competency,
- adopt and deploy deepwater technologies.

DeepStar has established goals to

- **enhance existing deepwater technologies** by improving the safety, operability, flexibility, reliability, and profitability of existing deepwater production systems;

FIGURE 1

Collaborative space deepwater R&D needs.

Operator Members (Participants) have desire for collaborative funding where facilities & deepwater technologies will not provide a competitive advantage
 (This was the original driver that started DeepStar.)

- DeepStar is a proven well leveraged tool in a collaborative space
- DeepStar is an Operator-Driven Program (~30 Multi-Discipline Projects).
- DeepStar is a recognized Industry collaborative voice.
- There is an opportunity for members to benefit from DeepStar by participating in fewer – but larger and “better” JIPs

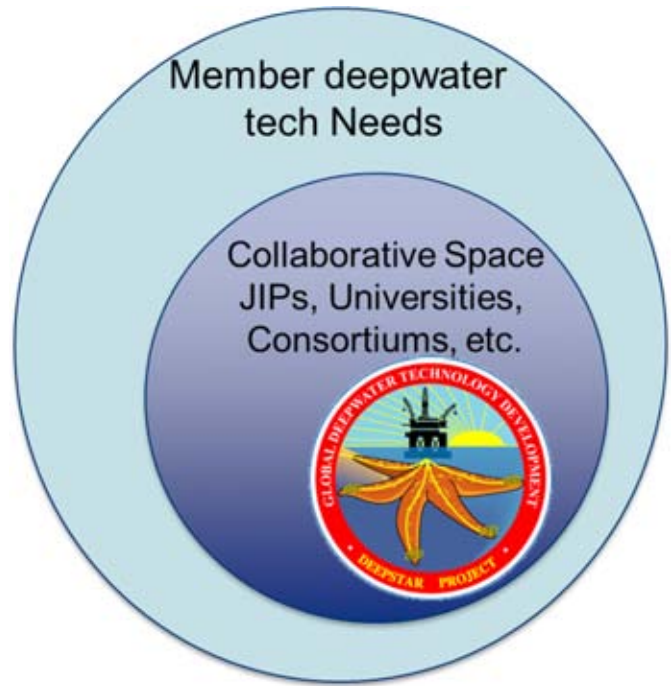


FIGURE 2

DeepStar is a consortium membership; Phase XI (as of 4/23/2013).

Phase XI Participants



Phase XI Contributors

ZH Offshore Inc.	Doris Engineering	Kvaerner Field Development	Saipem S.A
Aker Subsea Inc.	EDG, Inc	Lighthouse R&D Enterprises	SBM Atlantia, Inc.
Alan C. McClure Associates	Emas-AMC Inc.	Lockheed Martin, Corp	Schlumberger
Alcoa Inc.	Exmar Offshore Company	MagiQ Technologies	Scoperta, Inc.
Altair Engineering Inc	Floatec	Magma Global Limited	Seabox
American Bureau of Shipping	Fluor Enterprises, Inc.	Marintek USA, Inc	SeaTrepid International, LLC
Amog Consulting Inc.	FMC Technologies	MMI Engineering	Siemens Energy
Baker Petrolite Corporation	Frank's International, Inc.	Moog, Inc	Silixa
Battelle Memorial Institute	GE Oil & Gas (Vetco Gray Inc.)	Multiphase Solutions Kenny, Inc	Sonomatic, Inc.
Bechtel	Genesis	Nalco Energy Services	Southwest Research Institute
Blade Energy Partners	GL Noble Denton	National Oilwell Varco	Stress Engineering
BMT Reliability Consultants	Granherne, Inc	Nautilus International, LLC	Texas A&M University
Bornemann Pumps	GVA Consultants	Oceaneering International, Inc.	Universal Pegasus International
Cameron	Halliburton	Oil State Industries Inc	University of Houston
Champion Technologies, Inc.	Harris, Corp	Pipeline Research Council Int'l Inc.	Water Standard Management
CSI Technologies, LLC	Hytorc of Texas, Inc.	Pulse Structural Monitoring, Inc	Weatherford
Daewoo Shipbuilding	IntecSea	QinetiQ North America	Wood Group Kenny
& Marine Engineering Co., Ltd	InterMoor Inc.	READ ASA	
DNV	Knowledge Reservoir	SAAB North America, Inc	

- **develop new enabling deepwater technologies** by advancing novel technologies to allow production in areas that are currently technically unproven with the ultimate goal of developing technologies required for economic production in 12,000+ feet water depth;
- **gain acceptance of deepwater technologies by regulators and industry** by facilitating the development of industry standards and practices as appropriate and fostering communications with regulatory agencies;
- **provide a forum and process for discussion, guidance and feedback** with contractors, vendors, operators, regulators and academia, regarding deepwater technology, and promote standardization of component interfaces.

These goals are accomplished via the following DeepStar execution strategies:

- technology development aligned with business needs;
- transfer and apply technology to deepwater assets;
- gain acceptance of deepwater technologies by industry, standards organizations, and regulators;
- focus on the front end of the technology development cycle by advancing critical fundamental knowledge (science), providing proof of concepts and performing techno-economic engineering studies.

While the manufacturing and service sector members compete fiercely, most DeepStar work is considered a “non-competitive” area between the operators and thus a suitable space for collaboration. This also includes projects that support reliable and safe operations. From an operator perspective, there is high value in collaborating on these topics, as an incident with one operator can

cause a ripple affect across the entire industry. As such, DeepStar provides an outstanding opportunity for SMEs to collaborate and foster the exchange of ideas.

DeepStar Organization

DeepStar is managed by Chevron via a contractual arrangement with its participating organizations, utilizing Chevron back-office support services including legal, procurement, financing, accounting, and administrative. Chevron also provides a Director and a technical staff of two industry veterans to support the consortium. DeepStar, with 11 deepwater operating companies and approximately 80 contributing member companies, is the world’s longest running deepwater consortium. One thousand plus technical and management committee volunteers coupled with straightforward, well-honed and proven policies and procedures also make it one of the most successful. The SMEs are organized functionally into Technical Committees with operator chairs (and co-chairs) as shown in Figure 3.

The Technical Committees’ role is to identify technology needs and then generate “ideas”—captured on a cost, time, and resources (CTRs) form for Management Committee review. Once approved and bid out, their role is to review and recommend awards to the DeepStar Director. Once awarded, their role is to oversee and technically guide the execution of the work. The Technical Committees also table discussions/presentations of new technologies and/or challenges that could potentially be addressed within the DeepStar program. Time spent by the various Committee members on Technical Committee activities is contributed by their respective companies. The Technical Commit-

tees are currently charged as outlined below.

Geosciences Committee (×000) addresses challenges in prospect and reservoir delineation, characterization and surveillance, which are either specific to deepwater provinces or which relate to appraisal and development decisions leading to significant economic impact in such provinces.

Regulatory Committee (×100) provides liaison between DeepStar technical committees and governmental regulators such as the Bureau of Safety and Environmental Enforcement (BSEE) and the U.S. Coast Guard. The objective of the committee centers on the exchange of technical information between the working technical groups in DeepStar and regulatory representatives. The Regulatory Committee also works and communicates with leading industry organizations, such as the Offshore Operators Committee (OOC), American Petroleum Institute (API), and others. The objective of this interface between DeepStar and other parties is the expedient full review of relevant issues involved in deployment of new tools or processes under development.

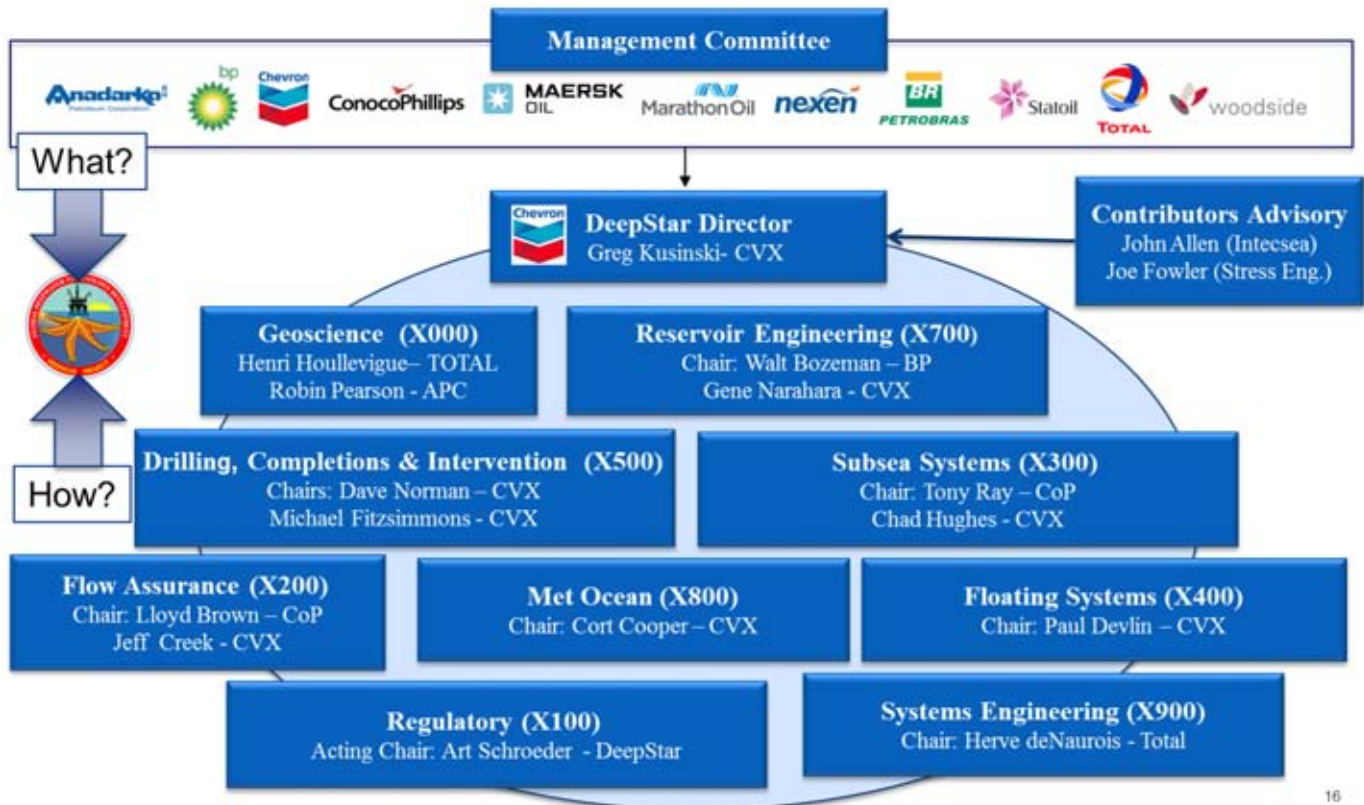
Flow Assurance Committee (×200) goal is to assure reliable and economic production in deepwater by appropriate design and operation through prediction of fluid behavior, flow management, and remediation of deposition and line plugs from the reservoir to the point of sale.

Subsea Systems Committee (×300) goal is to develop technology and qualify equipment to enable the deployment and IMR of “subsea facilities for 50+ mile tie-backs in 10,000 foot water depth.”

Floating Systems Committee (×400) role is to further technology

FIGURE 3

DeepStar organization.



and fill gaps related to deepwater floating systems and their associated moorings and risers.

Drilling, Completions, and Intervention Committee (x500) members share their experiences and data to identify technology improvements in deep water drilling, completion, and well intervention operations.

Administration and Technical Support (x600) — The Program Director heads this committee and oversees DeepStar’s leadership and administration responsibilities.

Reservoir Engineering Committee (x700) looks at trends that are of significant generic interest to the industry, while avoiding detailed reservoir issues where participants have competitive concerns. The committee has assembled the best available public domain information for use in learn-

ing global characteristics of deepwater reservoirs.

Met-Ocean Committee (x800) goal is to improve knowledge and modeling capabilities of ocean currents, waves and wind, which will provide more accurate facility design criteria and reduce downtime during deepwater drilling operations.

Systems Engineering Committee (x900) has the responsibility for analyzing existing and/or potential technology gaps, especially at the facility systems level and bringing them to the attention of the committee best suited to carry out further work in the specific technology area.

A huge benefit to members is the interconnectivity and continuity the staff bring by linking together the pieces of the deepwater technology puzzle as shown in Figure 4.

Operational Framework

The DeepStar R&D projects are funded by operator fees, and the de minimus cash fee from nonoperator members helps offset meeting costs. While all member classes may propose projects, the final funding decisions are taken by the operators, known within DeepStar as *Participants*. This makes sense not only by the fact they are the ones funding projects but they are also the “voice of the customer” for the manufacturing, engineering, and service company members, known as *Contributors*. The entire project selection process provides the Contributors with a very clear understanding of their customers’ needs and priorities in the collaborative space (Figure 5).

All DeepStar projects must have an operator *Champion*. Champions, along with DeepStar staff, are

FIGURE 4

DeepStar technical committees span the deepwater technology puzzle.

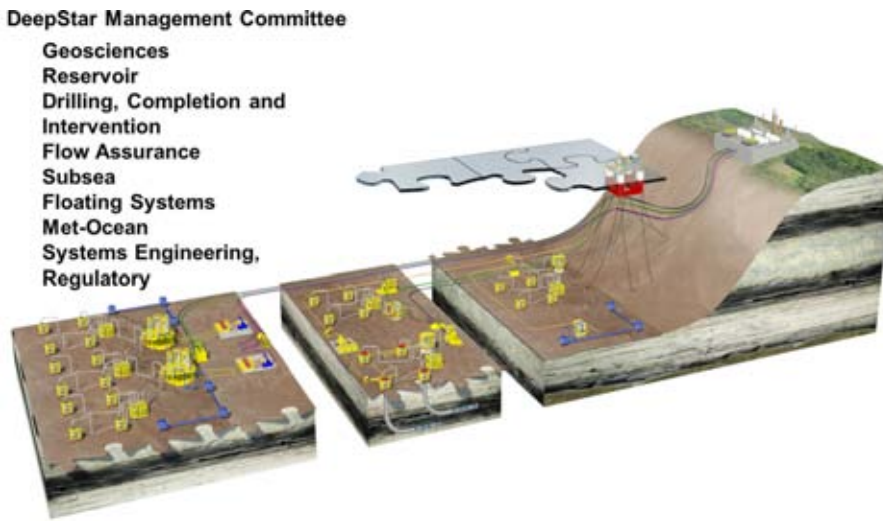
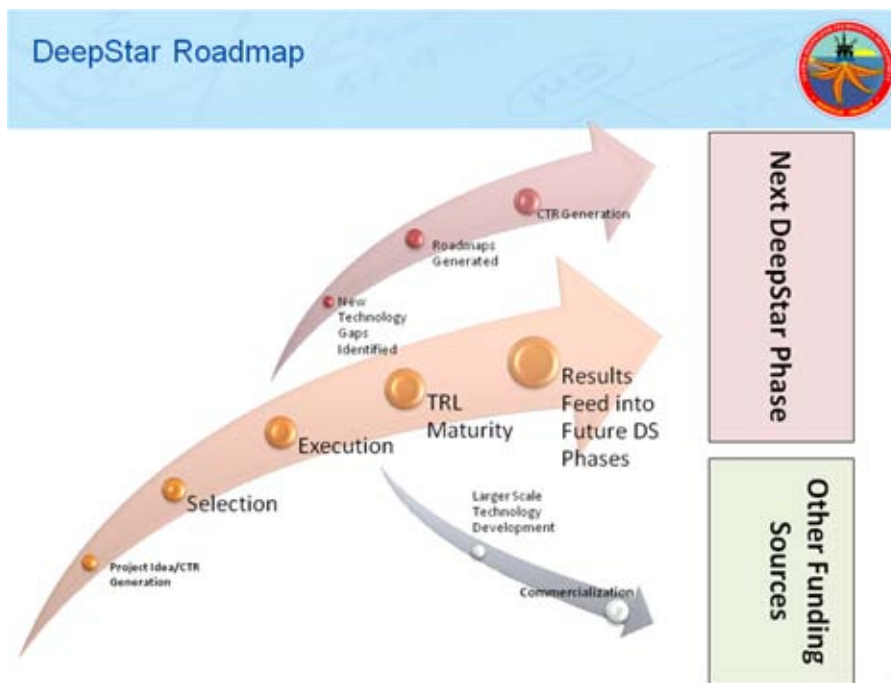


FIGURE 5

DeepStar project funding roadmap.



responsible for the execution of their projects and are held accountable for the deliverables (results, schedule, and cost). A subcommittee, or Working Committee, is usually formed to support the Champion in executing the

project and providing peer guidance. With DeepStar staff assistance, Champions and their Working Committees fulfill the following roles for each approved CTR:

- refine scope of work,

- define costs,
- implement CTR,
- select contractors (bid process),
- submit justification for management approval,
- insure contract implementation,
- arrange kickoff meeting,
- arrange for progress meetings,
- review monthly reports and provide periodic updates to the Technical Committee,
- maintain consensus,
- approve and confirm contractor invoices,
- approve Final Report.

While DeepStar projects can span the development spectrum, characteristics of a typical DeepStar project are as follows:

- operator championed,
- lower technology readiness level (i.e., TRLs 1–3 on a scale of 1–7),
- low cost (200 k–500 k USD),
- shorter duration (6–18 months), and
- multiphase stage-gated.

DeepStar Successes

DeepStar has successfully identified and executed hundreds of R&D projects over its 11 phases, which have subsequently enabled member companies to achieve their business objectives. Some of the successes have been in the following technical arenas:

- Poly rope: development, recommended practices, standards and regulatory approval;
- FPSOs: standards and regulatory approval;
- Vortex-Induced Vibration: understanding, prediction, mitigation and control;
- Met-Ocean: understanding, prediction and design practices and standards;
- Promulgator of standards and regulations;

- Flow assurance management, including modeling, operations, remediation.

As DeepStar members (not DeepStar itself) sell kit and services, the nonmember may have difficulty in immediately seeing the underlying DeepStar value-add. Outlined in Figure 6 are some of the standards and recommended practices emanating from DeepStar work in the equipment area.

Examples of areas where DeepStar work in the modeling and simulation arena has given rise to commercial solutions are presented in Figure 7.

Continually being at the forefront of deepwater developments, DeepStar, in its various studies, has set the groundwork on many of the safety standards we know today. In particular, DeepStar drove the development of the Technology Qualification Process (TQP), which much of industry leverages for their R&D efforts to accurately represent the maturity of new technology. Additionally, much of the DeepStar work that led to various standards and recommended practices has since been promulgated

FIGURE 7

DeepStar modeling and simulation tools.



- | | |
|---|--------------|
| ■ Life Cycle Well Cost Control Evaluation Tool | Commercial |
| ■ Well Control Software | Commercial |
| ■ Reservoir Characterization and Performance Database | Commercial |
| ■ GOM Current & MetOcean Forecast Models | Commercial |
| ■ Hydrate Plugging in Oil Model | Commercial |
| ■ Hydrate Disassociation Model | Benchmarking |
| ■ Asphaltene Deposition Model and Lab Test | Benchmarking |
| ■ Annulus Pressure Buildup for XHPHT Wells | Commercial |

to governmental agency rules and regulations, some of which are listed in Figure 8.

agement Committee. Current phase projects can be grouped as shown in Figures 9 and 10.

Current Phase XI Focus Areas

The DeepStar process utilizes an operator-driven CTR tool to help identify projects of interest. The CTRs are operator vetted and ranked at the Technical Committee level and then prioritized by the Senior Advisor Man-

DeepStar, the Future

While Neils Bohr is quoted as saying, “Prediction is very difficult, especially if it’s about the future,” it is clear that DeepStar’s future is bright as it will continue to evolve and remain relevant, following a strategy finely honed over the past 20 years. First, there is no shortage of “needs” for new technologies in the collaborative space. Post-Macondo, the industry is placing even more emphasis on building and maintaining sustainable Integrity Management programs with particular focus on inclusion addressing low probability, high consequence events. Additional efforts are also expected in the development of standards and protocols leading to greater reliability, better/more effective interfaces between individual components and equipment modules, and more effective maintenance procedures and practices, all adding up to a safer overall operating environment. These strategies should

FIGURE 6

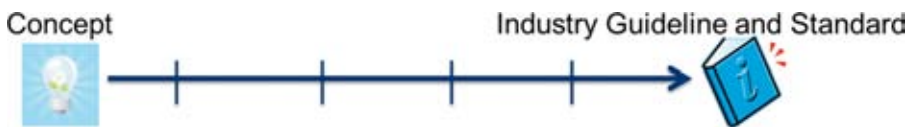
DeepStar equipment programs.



- | | |
|--|-----------------|
| ■ ROV Interfaces | InAPI 17H |
| ■ Subsea Equipment Qualification | API 17N |
| ■ HIPPs for the GOM | InAPI 17O |
| ■ Qualification of Large Bore HP Valves | Updated API 17D |
| ■ DW Pipeline Repair & Tie-Ins | DW RUPE |
| ■ Pipeline Limit State Design Codes | API RP 1111 |
| ■ Subsea Multiphase Flow Meters | API RP 85 |
| ■ Drilling Riser Recommended PracticeUpdated | API 16Q |

FIGURE 8

DeepStar safety programs.

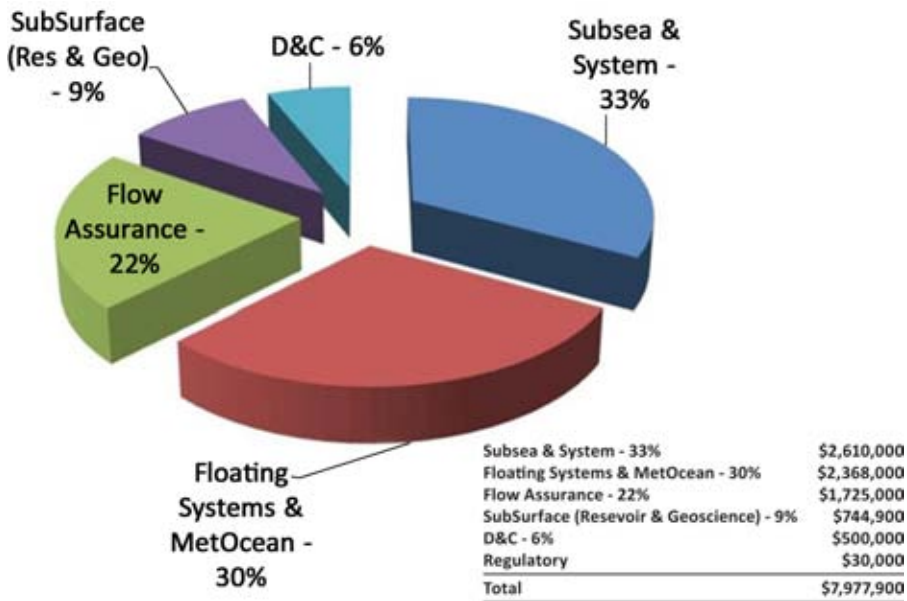


Safety is the guiding tenet during the design, deployment and operations phase of all DeepStar projects

- | | |
|---|--------------------|
| ■ DeepStar draft Deepwater Operating Plans | BSEE DWOP |
| ■ Safe Hydrate Remediation Guideline & Operations | DeepStar Guideline |
| ■ Real-Time SS Monitoring & Modeling for SS Control | Commercial |
| ■ Subsea Prod. System Reliability & Risk Mgmt | API 17 N |
| ■ Deepwater Pipeline Limit State Design in Codes | API RP 1111 |
| ■ Technology Qualification Process Standardization | API 17N |
| ■ Floating System Integrity Management Technologies | DeepStar Guideline |
| ■ Shallow Water Flow Management Best Practices | Standard Practice |

FIGURE 9

DeepStar Phase XI project types (only third-party direct spend included in budget numbers; in addition are the value of Participants and Contributors SME time and in-kind contributions).



also yield an overall lower total cost of ownership.

DeepStar's current Management and Technology Committee structure will continue as is and its time-honed processes have served its membership well, directing funds and resources to

those collaborative areas most highly ranked by the operators. Its "holistic" approach with eight Technical Committees provides a synergy that is greater than just the sum of the individual committees. Generally, DeepStar will continue with the successful

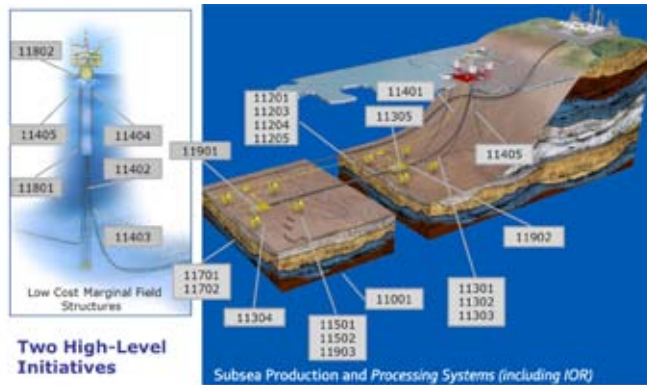
CTR "bottoms up" need-driven process with strategic overarching top-down direction. The needs will be both near term (to 5 years) and longer term (to 10 years). As such, DeepStar will continue to fund "individual projects" within all the Technical Committees that are operator driven and anticipates adopting a few overarching areas of focus with an emphasis on Standards where appropriate. Near term one could also expect projects supporting better appraisal tools, Increased Oil Recovery (IOR), particularly in the Lower Wilcox, Subsea processing and Drilling, Completion and Intervention projects focused on supporting safer operations with a lower overall cost.

The Management Committee will be encouraging "Bigger Impact" projects that are conducted in a more collaborative manner, particularly with larger Contributors. To better facilitate this outcome, there will be some sensible changes to the standard DeepStar Intellectual Property restrictions based on overall balance of value delivered to project. DeepStar traditionally provides the collective "Voice of the Customer" to member service and manufacturing companies, allowing them to provide better focused, more reliable services and products at a lower cost. Leveraging on this role, DeepStar is asking members to consider DeepStar as an alternative of choice versus spinning-up new or participating in other "one-off" Joint Industry Projects (JIPs).

DeepStar expects to continue interaction with regulators to ensure DeepStar-developed technologies can be readily accepted for deployment and use. The strategy will continue presenting a well-defined operational need and DeepStar's stage-gate technology development solution to regulators at an early enough point so as to be able to incorporate appropriate action

FIGURE 10

The current suite of projects and how they support DeepStar's current high-level field development scenarios.



plans to address any regulatory concern without incurring development delays.

Conclusions and Summary

The world's deepwater and ultra-deepwater basins hold tremendous resource promise to help meet global energy needs. DeepStar and its 80-plus member organizations have processes, procedures and most importantly a thousand-plus SMEs to help ensure that the most appropriate technologies are identified and then pursued and pulled through to commercialization.

DeepStar successes are numerous and have had long-term impact due in large part to the operator lead and operator "pull" on project selection. Additional contributing factors include the following:

- successful in defining and communicating gaps and needs, especially in the early TRL stages;
- R&D directly relate to operator's future Major Capital Projects (MCP) developments;
- long-term stability, proficiency, and consistency of staff
 - 20 years identifying and leading deepwater technology development and application,

- \$100 MM of projects and 325+ technical reports,
- 1,000+ Subject Matter Experts,
- 70+ member organizations provide ample opportunities for field test and demo;
- standardized, efficient and cost-effective processes and procedures
 - procurement and contracting,
 - portfolio vetting and selection,
 - project management,
 - technology transfer;
- freedom to fund when and how best to meet operators' strategic needs in a timely manner, no public disclosure, go at right speed, start-stop-change direction for optimum results. Refocused every 2 years.

Organizations, including operators, manufacturers, service companies, as well as universities interested in defining needs and developing new technologies to safely and profitably unlock the ultra-deepwater potential are invited to apply to join the DeepStar team. The reader of this paper is encouraged to connect with DeepStar staff about participation details. For more information, please visit www.DeepStar.com.

Acknowledgments

The authors gratefully acknowledge the contributions of the DeepStar member organizations for their input and support.

DeepStar 11304: Laying the Groundwork for AUV Standards for Deepwater Fields

AUTHORS

John Jacobson

Lockheed Martin Corporation

Pierce Cohen

Chevron Energy Technology Company and DeepStar Project Champion

Amin Nasr

Total SA and DeepStar Project Champion

Art J. Schroeder, Jr.

Energy Valley, Inc., and DeepStar Consultant

Greg Kusinski

Chevron Energy Technology Company and DeepStar Director

Introduction

Until recently, autonomous underwater vehicles (AUVs) in offshore oil and gas were limited primarily to bathymetric/geophysical survey, but emerging developments across the subsea industry now open the potential for safer, better, and cheaper pipeline inspection; structural survey; deepwater inspection, repair and maintenance (IRM); and field resident systems for remote/harsh environments. Industry developments range from low-logistics AUVs that simply “mow the lawn,” to semiautonomous “delivery trucks” with remotely operated payloads, to AUVs with highly integrated perception response autonomy that provides significant ability to interpret sensor data and respond accordingly. As these capabilities mature, AUVs will become an increasingly important tool for

ABSTRACT

Emerging autonomous underwater vehicles (AUVs) developments across the oil and gas industry now include pipeline inspection; structural survey; deepwater inspection, repair and maintenance (IRM); and field resident systems for remote/harsh environments. As these capabilities mature, AUVs will become an increasingly important tool for deepwater field operations. Early adoption of AUV standards will facilitate more rapid deployment of AUV technologies and enable the industry to reap a wide range of safety, environmental, operational, and economic benefits for its deepwater fields. The development of industry standards for AUV interfaces will facilitate more rapid implementation of AUV capabilities and lead to more cost-effective, compatible system designs by AUV vendors and field hardware manufacturers. The development of regulatory standards for the interpretation and acceptance of autonomous inspection results is also an essential step toward the achievement of more cost-effective operations and regulatory oversight of deepwater subsea fields. This paper describes a future vision for the use of AUVs in deepwater field operations, the benefits to be realized, and the future capabilities of AUVs that must be anticipated and facilitated within AUV standards to achieve that vision. Additionally, this paper describes the goals and objectives of DeepStar Project 11304, which is laying the groundwork to achieve accelerated standardization of AUV interfaces and the development of regulatory standards for AUV inspections.

Keywords: autonomous underwater vehicle (AUV), deepwater field, interface standards, regulatory standards, inspection

deepwater field operations. Early adoption of AUV standards will facilitate more rapid deployment of AUV technologies and enable the industry to reap a wide range of safety, environmental, operational and economic benefits for not only deepwater fields but potentially for all offshore developments.

Future Vision for AUVs in Deepwater Fields

The performance of IRM tasks in deepwater using current methods with remotely operated vehicles (ROVs) can be costly and inefficient. Deepwater ROVs require large dynamically

positioning (DP) II vessels and thousands of square feet of deck space for support equipment that can weigh up to 90 tons. Vessel operations are limited by weather, mobilization/demobilization timelines, and operational constraints, which can be due to umbilical deployment in deepwater. Extended vessel deployments at high day rates are required to complete ROV-based IRM operations due to these inefficiencies, driving the costs of field operations and maintenance in deepwater to millions of dollars per year. Under these circumstances, the development of smaller “marginal fields” or deepwater fields in remote

locations or hostile environments such as under arctic ice may drive a prospect to low or noncommercial viability.

The implementation of AUV-based IRM will provide significant improvements in safety, operating efficiency, and project economics for deepwater fields. No longer will large DP2 vessels with expensive and cumbersome ROV spreads be required for simple IRM. In the near term, AUVs can be deployed from smaller “utility class” vessels, be capable of operations in higher sea state and current conditions, and perform IRM tasks much more efficiently without the operational limitations and equipment hazards imposed by umbilical and tether management systems. Reduction in equipment complexity, vessel size, and crew size will also result in improved safety, reliability, and lower environmental impact. Eventually, AUVs will become “field resident,” residing in the subsea field for periods of months or years, resulting in the elimination of surface vessels, further improvements in environmental monitoring, equipment safety, and operating efficiencies, and substantial reductions in cost.

Future capabilities for deepwater AUVs will be substantially enhanced through the use of subsea docking stations and local Wi-Fi “hot spots.” The ability to upload high volumes of mission sensor data, download supervisory instructions, and recharge batteries will extend AUV mission life to days or weeks and eventually to months and/or years. The ability to have localized real-time high bandwidth wireless communications for critical IRM operations such as subsea production equipment monitoring, sampling, valve operations, and other intervention operations will eliminate the need to mobilize expensive surface vessels and large ROV spreads to accomplish

routine maintenance tasks. The value of these capabilities for remote deepwater and/or arctic locations cannot be overstated, since it provides immediate in-field access to complete tasks that would otherwise take days or weeks to accomplish, especially considering the mob-demob time associated with ROVs.

Current AUV Development Trends for Deepwater

There are a number of ongoing AUV developments for deepwater oil and gas that, when brought to full commercial capability, will have game-changing implications for deepwater field operations and maintenance. These include pipeline inspection, deepwater facilities inspection, and field resident AUV capabilities.

With its HUGIN AUV, Kongsberg Maritime has demonstrated autonomous multisensor pipeline inspection, including collection of detailed digital still imagery of an underwater pipeline by using interferometric synthetic aperture sonar (SAS), pipeline tracking software, a multibeam echo sounder, and a high-resolution still camera in a two-pass mission. In the first pass, side-scan data from the SAS are used to detect and track the pipelines in real time, extracting pipeline features in the sonar images. In the second pass, the AUV conducts a low-altitude inspection of the pipeline using its multibeam sonar and optical camera. Imagery is postprocessed into high-resolution sonar images and bathymetry maps of the pipeline (Borhaug & Hagen, 2011).

The autonomous inspection vehicle (AIV), currently under development by Subsea 7, is targeted for subsea facilities inspection. The AIV employs a compact, ROV-like shape to achieve

high maneuverability and full hovering capability, which will be used to conduct inspection of subsea infrastructure such as wellheads, manifolds, jumpers, spool pieces, flowlines, and risers. Sensors include still and HD video camera, lighting, 3D imaging sonar, and profiling sonar. The AIV is deployed by an “intelligent basket” that is lowered to the seabed and enables autonomous IRM operations without surface vessel support over a period of days until retrieved (Jamieson et al., 2012) (Figure 1).

The Sabertooth AUV, under development by Saab SeaEye, is targeted for autonomous, field resident, subsea facilities inspection. Designed for remote inspection and intervention tasks without the need for a support ship, the Sabertooth will be capable of long distance transits between work sites and of docking with a subsea docking station that is deployed within the subsea field. The docking station will provide interfaces for battery charging, high bandwidth data transfer, and mission planning and control. Targeted to remain submerged for up to 12 months, the system will also be capable of tethered operations using a microfiber tether. The system can deploy a range of sensors and tooling for inspection and intervention on subsea production systems (Furuholmen et al., 2010) (Figure 2).

FIGURE 1

SubSea 7's AIV.



FIGURE 2

Sabertooth AUV from Saab SeaEye.



The SWIMMER system, under development by Total and Cybernetix, employs a hybrid AUV-ROV approach to achieve vessel-independent, field resident IRM operations in remote and/or deepwater environments. The system features a large AUV that is launched from a support vessel, transits many kilometers to a docking station within a subsea field, and docks to one of many dedicated docking stations staged within the field. Once docked, a work-class ROV is deployed from the AUV to perform a wide range of IRM tasks using typical ROV tooling and sensors. The ROV can work within a 150-m watch circle from the docking station; work beyond that radius requires the AUV to transit to a new docking station to perform the work. The system is targeted for periods of up to 90 days submergence before being retrieved for maintenance (Tito & Rambaldi, 2009).

The Marlin[®] AUV, developed by Lockheed Martin, is designed to provide a wide range of structural integrity management capabilities, including structural survey, subsea facilities inspection, and pipeline inspection. Featuring a hydrodynamic hull form with hovering capability, an interchangeable, under-slung work package (pylon), the Marlin employs a 3D sonar to develop geo-registered 3D models of off-

FIGURE 3

Lockheed Martin's Marlin[®] AUV.



shore production platforms, downed structures, and debris fields in a matter of minutes or hours, with typical model resolution of ~5 cm. The capability to perform 3D laser inspections yielding 3D models with ~5 mm resolution is under development. Also under development is a 4,000-m depth-rated version of Marlin with full station keeping capability, which will be used to facilitate inspection of subsea infrastructure. This version of Marlin will be capable of being launched from a floating production system (FPS), conducting flowline and riser inspections during transits of 15–20 km, followed by inspection of in-field infrastructure such as wellheads, manifolds, jumpers, and spool pieces, and then returning to the FPS for recovery and mission data retrieval (McLeod et al., 2012) (Figure 3).

AUV Interface Standards for Deepwater Fields

Future capabilities for deepwater AUVs will be substantially enhanced through the use of permanently installed field infrastructure such as docking stations, communications nodes, and other interfaces. Docking stations will provide electrical and/or inductive interfaces for battery charging, optical or wireless interfaces for

high bandwidth communications and data transfer, and mechanical interfaces for docking, tool storage, and interchange. Docking stations may also facilitate the use of tether management systems for semiautonomous vehicle systems. Other permanently installed interfaces that would leverage the benefits of AUV capabilities include wireless subsea communication nodes (radio frequency (RF), acoustic, optical, and/or hybrid), data harvesting nodes, subsea production equipment monitoring and sampling points, and intervention tooling interfaces.

The development of industry standards for AUV interfaces, similar to the API/ISO standards for ROVs, will lead to compatible system designs by AUV vendors and field hardware manufacturers and will enable more cost effective development and more efficient operations of deepwater subsea fields. As sensor and AUV manufacturers design and operators deploy compatible kit, the expense (capex and opex) versus the value of subsea data collected will drop by orders of magnitude in a positive re-enforcing cycle. The offshore oil and gas industry has the benefit of many lessons learned from the development of ROV interfaces over a period of approximately 20 years of development from the early 1970s to the early 1990s. During the early days of ROVs, each field development project developed its own unique installation, operations, and maintenance procedures, which typically resulted in unique interfaces for intervention tooling. As a result, projects frequently paid a high price for “reinventing the wheel,” including the cost of nonrecurring engineering design, the cost to procure unique tooling (and the inability to reuse the tools on subsequent projects), and

the inability to invoke full competition for offshore services due to being tied to a single vendor's technology. As a result, the costs of operations, maintenance, and spares frequently grew over time due to the difficulty and complexity of maintaining unique tools and procedures for each subsea field. Further adding to cost and potentially compromising safety, the lack of standards drove the need for customized operator training for each installation and tended to complicate rotational and/or multiclient deployments. Through early standardization, the industry can leverage these lessons to reap the rewards with sensible, well-thought standardization for AUVs.

Regulatory Standards for AUV Inspections

In the future, AUVs will leverage a wide range of sensor technologies to meet both end user and regulatory requirements for integrity monitoring of offshore infrastructure. Offshore infrastructure that falls under regulatory oversight includes fixed platforms, floating structures, pipelines, risers, mooring lines and subsea production equipment. Sensor technologies that can be employed by AUVs to meet inspection requirements include video, photographic, sonar, laser, ultrasonic, magnetic, and others.

Today, most regulations and industry standards do not address the use of AUVs for inspection, primarily because the technology did not exist at the time the regulations were developed. While AUVs can be used to meet standards where only the sensor technology is specified (e.g., "sonar with frequency of at least 500 kHz"), the regulations are frequently either ambiguous or prohibitive regarding the use of AUVs. In other instances,

the regulation specifically recognizes the inspection method (diver or ROV inspection) where a human is "in the loop."

Additionally, as sensor and autonomy technologies advance, the deployment of autonomous inspection technologies will provide a range of new and as yet unrecognized formats for inspection results, which when assessed using state of the art engineering tools, have the potential to provide considerable improvements in inspection effectiveness as well as efficiency and cost. For example, the use of 3D modeling and autonomous change detection using 3D sonar, while not currently recognized by any regulatory standard, would dramatically improve the ability to quickly and effectively identify features that have changed since a previous structural survey. The capability to identify, map, and measure features such as free span, seabed scour, bent, missing or damaged structural members, and/or distorted or twisted beams would provide a significant advantage in posthurricane inspection operations. Similarly, performing autonomous structural inspection using a 3D laser would provide the capability to quickly and efficiently identify, map, and measure cracks and other structural defects or damage. Utilizing these advanced technologies and techniques will help minimize the need for divers, particularly in the initial incident triage phase where the risk of the unknown is highest.

The development of regulatory standards for the interpretation and acceptance of autonomous inspection results where no diver or ROV pilot is involved is therefore an essential step toward achievement of a safer, more cost-effective and efficient operations and maintenance of deepwater subsea fields.

DeepStar Project 11304: Laying the Groundwork for AUV Standards

DeepStar is a joint industry technology development project focused on advancing the technologies to meet its members' deepwater business needs to deliver increased production and reserves. It provides a forum to execute deepwater technology development projects and leverage the financial and technical resources of the offshore oil and gas industry. DeepStar's membership is composed of companies and organizations from across the industry and the globe, including oil companies, vendors, regulators, and academic and research institutions. DeepStar runs in 2-year funding phases, and participation is by phase. In Phase XI, membership includes 11 major oil companies and over 70 contributing companies from industry and academia.

DeepStar has funded Project 11304, AUV Standards for Deepwater Fields, and through this project is laying the groundwork to achieve accelerated standardization of AUV interfaces and the development of regulatory standards for AUV inspections. The project comprises two major tasks:

Task 1 – AUV Interface Standards for Deepwater Fields, and

Task 2 – Regulatory Standards for AUV Inspections.

The primary goals of this project are as follows:

(1) identify subsea interfaces that should be standardized for AUVs, develop recommendations for appropriate standards related to subsea interfaces for AUVs, and begin the process of approval/release through an appropriate standards organization; and

(2) identify current regulatory inspections that could be conducted

with AUVs, develop draft versions of appropriate standards for such AUV inspections of subsea infrastructure, and make available work products that could help facilitate regulatory agency review and potential adaptation.

In order to keep the scope of the project manageable, a single entity was selected for each Task as the primary stakeholder with whom to hold discussions and to whom to submit recommendations on AUV standards. For Task 1, the American Petroleum Institute (API) Subcommittee 17 (SC17) was identified as the most appropriate standards organization for the development of AUV interface standards. For Task 2, the U.S. Bureau of Safety and Environmental Enforcement (BSEE) was identified as the regulatory agency having most appropriate jurisdiction regarding AUV inspections.

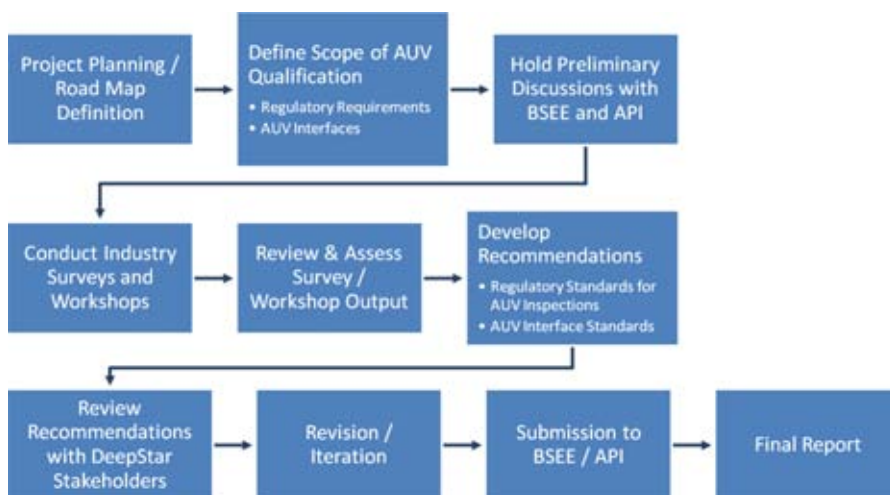
In order to achieve the project objectives, a road map has been developed to define top-level project activities and events leading to the development and submission of work-products to API and to BSEE. An overview of the project road map is provided in Figure 4.

The project is currently in progress with an anticipated completion date of March 2014. The scope of Task 1 and Task 2 efforts have been defined in detail, preliminary discussions with API and BSEE are in progress, and industry surveys and workshops are planned for spring 2013. Key industry stakeholders who will be engaged in the survey and workshop activities include Field Operators, EPC Contractors, Subsea Hardware Providers, ROV/AUV Service Contractors, AUV Developers, AUV Sensor Developers, and Interface Technology Developers.

The focus of Task 1 survey/workshop activities will be on (1) identifying and documenting the current

FIGURE 4

DeepStar 11304 Project Road Map.



and future AUV Interface implementations foreseen by the industry, (2) facilitating discussion and interaction amongst industry stakeholders regarding AUV interface standardization, and (3) developing consensus within the industry on what AUV interfaces should be standardized and what those recommended standards should include. The output of these activities will be shared with API SC17 in the form of a Task Report, which could result in formal initiation of the development of API standards for AUV Interfaces.

The focus of Task 2 survey/workshop activities will be on (1) identifying and documenting the current and future AUV inspection technologies foreseen by the industry, (2) facilitating discussion and interaction amongst industry stakeholders regarding current regulatory standards that could be met using AUV inspection technologies, and (3) developing work products that will be useful to BSEE, on which regulations could be most improved by allowing inclusion of AUV inspections.

After the survey and workshop activities are completed, project focus will shift to review and refine-

ment of recommendations within the DeepStar Project Team, presentation/discussion of recommendations with API SC17 and BSEE, and development of formal work-products reflecting the consensus opinion of the industry and the applicable standards agency.

Conclusion

The future vision for AUVs in deep-water field operations is compelling. AUV technologies are evolving at very rapid pace, bringing new and powerful capabilities that offer significant safety, environmental, operational and economic benefits. In order to fully realize these benefits, future capabilities of AUVs must be anticipated and facilitated within industry standards and regulatory allowances. DeepStar Project 11304 is laying the groundwork to achieve standardization of AUV interfaces and regulatory allowance for AUV inspections. By bringing industry stakeholders and standards agencies together, early adoption of standards can be achieved, thereby capturing the lessons learned with ROVs and accelerating implementation of these

game-changing AUV capabilities in deepwater fields.

ceedings, Offshore Technology Conference, May, 2009. Houston, TX: Offshore Technology Conference. <http://dx.doi.org/10.4043/19930-MS>.

Acknowledgments

The authors gratefully acknowledge the contributions of the DeepStar member organizations for their input and support.

Corresponding Author:

John Jacobson
Lockheed Martin Corporation
10375 Richmond Avenue,
Suite 400, Houston, TX 77042
Email: john.r.jacobson@lmco.com

References

Borhaug, E., & Hagen, P.E. 2011. AUVs Take On Pipeline Inspection. E&P Magazine Website. http://www.epmag.com/Production-Drilling/AUVs-On-Pipeline-Inspection_86704. (accessed March 6, 2013).

Furuholmen, M., Johansson, B., & Siesjö, J. 2010. Seaeye Sabertooth: A Hybrid AUV/ROV Offshore System. In: MTS/IEEE Oceans 2010 Proceedings, September, 2010. Seattle, WA: IEEE. <http://dx.doi.org/10.1109/OCEANS.2010.5663842>.

Jamieson, J., Wilson, L., Arredondo, M., Evans, J., Hamilton, K., & Sotzing, C. 2012. Autonomous Inspection Vehicle: A New Dimension in Life of Field Operations. Offshore Technology Conference Proceedings, April–May, 2012. Houston, TX: Offshore Technology Conference. <http://dx.doi.org/10.4043/23365-MS>.

McLeod, D., Jacobson, J., & Tangirala, S. 2012. Autonomous Inspection of Subsea Facilities-Gulf of Mexico Trials. In: Proceedings, Offshore Technology Conference, April–May, 2012. Houston, TX: Offshore Technology Conference. <http://dx.doi.org/10.4043/23512-MS>.

Tito, N., & Rambaldi, E. 2009. SWIMMER: Innovative IMR AUV. In: OTC 2009 Pro-

DeepStar Metocean Studies: 15 years of Discovery

AUTHORS

Cortis Cooper

Chevron Energy Technology Co.

Tom Mitchell

Consultant, Georgetown, Texas

George Forristall

Forristall Ocean Engineering, Inc.

James Stear

Chevron Energy Technology Co.

Introduction

Almost all aspects of offshore facilities are affected by winds, waves, and currents, including operations and capital costs. Indeed, in many deeper water locations, the choice of the basic facility is heavily influenced by the meteorological and oceanographic (metocean) conditions, second only to the reservoir characteristics and water depth.

Many mysteries remain concerning metocean variables, especially deep water currents and hurricane-driven winds and waves. Nowhere is this truer than in the Gulf of Mexico, where strong ocean currents can be generated by several different processes that can vary dramatically in magnitude over space scales of a few kilometers. Several of these processes were first discovered only recently, and their quantification has been led by Joint Industry Projects (JIP) like DeepStar, rather than the traditional university oceanographers. Hurricanes have also been an area of active industry research because they dominate the loads on most production facilities in deep water. Despite their importance, major uncertainty

ABSTRACT

In 1998, DeepStar began the first of many successful studies that have resolved important questions concerning meteorological and oceanographic (metocean) processes that can cause large loads or fatigue problems on deepwater facilities. In so doing, these studies have immeasurably enhanced the reliability and safety of deepwater structures and pushed the frontiers of ocean science that have traditionally been the realm of academic research. The efforts have focused on three major phenomena: the Loop Current, Topographic Rossby Waves (TRW), and storm winds. Much of the DeepStar effort has focused on improving numerical models of the respective phenomena because they can provide long historical databases at any site—data that serve as the basis for operating and extreme criteria with reasonable statistical uncertainty. Studies of the Loop include the first measurements of the Loop inflow and turbulence and evaluation of existing numerical models. Most of DeepStar's efforts on TRWs started in 2008, and in a 5-year period, it has developed a validated numerical model and used it to build a 50-year hindcast database. Efforts are underway to use those results to build a stochastic forecast model. Finally, DeepStar has analyzed a large set of wind measurements taken from the powerful recent hurricanes and found that recommended formulas for wind profiles and spectra have significant bias and will be corrected in future recommended practices.

Keywords: oceanography, meteorology, metocean, ocean currents, ocean waves, ocean winds

remains concerning winds and waves, in part because few measurements have been made in strong hurricanes.

As a result of these myriad uncertainties and the importance of metocean criteria on safety and reliability, DeepStar IV began significant funding of metocean studies in 1998 and has continued this investment since then. The following sections outline the major studies in more detail. Each section is focused on a particular phenomenon, e.g., Topographic Rossby Waves (TRWs), so it frequently will cover several studies. Each section describes the study goals, business drivers, and methods and summarizes the results.

Loop Current

The Loop Current is a strong permanent current that flows through the Yucatan Straits, loops northward, and then exits through the Florida Straits where it is renamed as the Gulf Stream. About once per year, the Loop moves northward of 27°N, becomes unstable, and forms a large eddy that breaks away and drifts to the west. The Loop (which will henceforth be taken to mean the Loop proper and its associated large anticyclonic eddies) can occasionally affect shelf waters but is typically found in water depths greater than 500 m. Radial speeds within the Loop can exceed 2 m/s and generate

the drag equivalent of a hurricane wave on mooring lines or generate vortex-induced vibrations that can lead to fatigue failure of risers. These effects influence the design of drilling and production risers, mooring tensions on production and drilling rigs, connection/disconnection of drilling risers, and installation of pipelines, mooring lines, tendons and hulls. Although no firm accounting has ever been done, we estimate that the Loop costs the industry on the order of \$10 million/year in rig delays.

The Loop was not discovered until the late 1960s, and the first current measurements did not occur until the early 1980s. Given the importance of the Loop and its relatively recent discovery, it is not surprising that there were many important unknowns that needed to be resolved as the industry moved into deeper water.

In 1998, DeepStar initiated its first oceanographic project by measuring the incoming source of the Loop Current—in other words, the water inflow through the Yucatan Strait. Oceanographers had long wanted to take these fundamental measurements but had been frustrated by the cost and the politics of deploying instruments in the eastern half of the Straits controlled by Cuba. Not to be deterred, DeepStar contracted CICESE, an oceanographic research institution in Mexico that had a cooperative research agreement with Cuban oceanographers. CICESE deployed eight moorings across the Yucatan Straits with 33 single-point current meters and eight acoustic Doppler current profilers (ADCPs). In addition, they conducted four ship surveys across the Strait during the 18 months that the moorings were in place. Results were documented in Abascal et al. (2003). The major benefit of the study was to provide the

first careful measurement of the inflow boundary condition for numerical models of the Loop. Such models are an important tool for developing design and operating conditions and, perhaps most importantly, for forecasting.

After the Yucatan Straits measurements, DeepStar quickly turned to answering another key question about the Loop Current: How turbulent is it? At the time, designers were worried about the ability of turbulence to excite higher modes in the tendons of Tension Leg Platforms (TLPs) and spars. Current speed fluctuations can affect these structures both by direct forcing and by reducing the effectiveness of VIV suppressing strakes. These effects have often been seen in model basins where the turbulence intensity is 10–20% of the mean velocity. Oceanic turbulence levels were thought to be much lower, but there was essentially no field data to prove that assumption. DeepStar filled the gap by funding measurements in a Loop Current eddy using a unique instrumentation system. The results are described by Mitchell et al. (2007).

Measurements were made within the eddy and across the strong frontal boundary that separates the eddy from the surrounding waters. A towed vehicle, the TOMI (Towed Ocean Microstructure Instrument), was equipped with a special 300-kHz ADCP that had its four beams directed fore, port, starboard, and down. The along-beam velocities resolved structures with wavelengths of 4–60 m. The vehicle also carried shear probes for measuring velocity fluctuations in the dissipation range (0.5–100 cycles per meter) and other environmental sensors for measuring temperature, salinity, depth, and vehicle orientation. The towed body is shown in Figure 1.

Tows were conducted at 25-, 50-, 100-, and 150-m depths around the

FIGURE 1

The TOMI instrument that was used to measure turbulence. The ADCP transducers are mounted on the bottom mast (forward looking), at the base of the (orange) upper mast (port and starboard looking), and behind the lower mast on the main body (downwards looking).



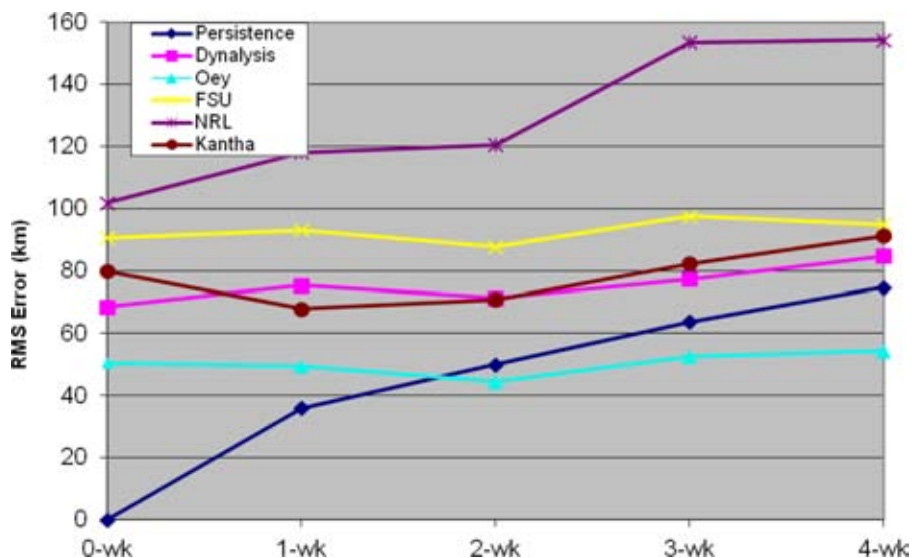
northern edge of the Loop Eddy in currents of up to 1.7 m/s. Turbulence was detected with the shear probes, but mostly in the 130–150 m depth range around the local salinity maxima. The level of turbulence was weak, and it was distributed intermittently in both space and time. The most energetic events of turbulence had eddy scales of at most 4 m and velocity scales of only 1 cm/s. The typical and average values were more than 10 times smaller.

After taking some basic physical measurements in the Loop Current, DeepStar's next effort was to understand the accuracy of available models. While many models were available at the time, none had been rigorously validated. To fill this gap, DeepStar initiated a study in 2004 to compare five existing forecast models. The modelers were asked to run a 1-year historical period for which DeepStar had a proprietary, detailed set of measurements never before seen by the modelers. Models were spun up by assimilating publicly available measurements such as satellite altimetry. On the first day of each month, the models were run for 4 weeks without any data assimilation. Model performance

was judged by comparing the forecasted to the observed distance of the nearest major Loop or eddy front to seven sites scattered over much of the deep Gulf east of 94°W. Model results were compared to persistence (the major fronts were assumed to remain stationary) for the entire month. Figure 2 compares the RMS (root mean square) error accumulated for the 12 runs at all seven sites. Only one of the models was found to beat persistence after about 12 days, but not by much. Perhaps most striking was the substantial error exhibited by all the models right from the start (0 week). This strongly suggests that the satellite imagery used to spin up the models was far from perfect, probably because it failed to resolve the meanders and frontal lobes commonly found on the Loop and its eddies. While these features may have relatively short length scales (order 50 km), they can significantly affect the error metrics. The fact that the models did poorly even in a nowcast mode suggested they may have had substantial errors even in a hindcast mode.

FIGURE 2

Comparison of forecast error from five Loop models with persistence.



The overall conclusion of the Phase 1 study was that the models were too inaccurate in forecast mode to be of much value to Industry operations, but that further work was justified given the substantial benefits that could be had from an accurate forecast.

Towards the end of the first model intercomparison study, a new model appeared on the scene that was quite different to the others tested in Phase 1. AEF's model was a so-called "feature" model, which utilized proprietary drifting buoys as well as satellite imagery to spin-up the model. Given the promise of this new approach, DeepStar decided to fund a Phase 2 study using the AEF model and the Oey model, winner of the Phase 1 study. Figure 3 compares the error from the two models with that of persistence. The AEF model consistently beat the Oey model and overtook persistence at about 1 week. Its forecast error stayed flat until the end of the second week and then slowly climbed until it was double the initial error after 4 weeks where it remained steady until nearly 7 weeks. Overall, the conclusion was

that the AEF model could provide forecasts with useful accuracy, but its success depended on having access to detailed *in situ* measurements from drifting buoys or other similar sources. Such measurements cost upwards of \$50,000/mo.

TRWs

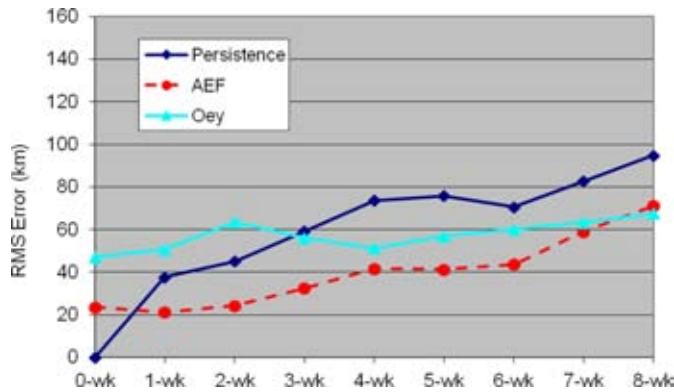
In the late 1990s, British Petroleum (BP) measured currents reaching about 1 m/s near the seafloor in about 2,000 m of water along an underwater feature known as the Sigsbee Escarpment. While the currents were most intense near the bottom, they remained substantial for hundreds of meters above the seafloor, finally reaching ambient conditions at about 1,000 m. The Bureau of Ocean Energy Management (BOEM; formally known as Minerals Management Service) deployed three current meters nearby for 18 months and observed similarly large currents. Figure 4 shows the time series of these currents. Subsequent analysis of the BOEM measurements by Hamilton and Lugo-Fernandez (2001) suggested that the currents were driven by Topographic Rossby waves (TRW), a 200-km-long wave with periods of 10–14 days.

TRWs can generate current speeds at the bottom near the Escarpment that far exceed those generated by any other phenomena. Such currents dominate the metocean extreme and fatigue loads on pipelines and risers, especially flexible risers (steel catenary risers or SCRs).

DeepStar began its study of TRWs in 2003 by taking measurements of the cross-Escarpment variation of the waves, a characteristic that had not been studied before. Eight current meters were placed near the seafloor across the Escarpment at 91°08'W,

FIGURE 3

Comparison of forecast error from two Loop models with persistence.

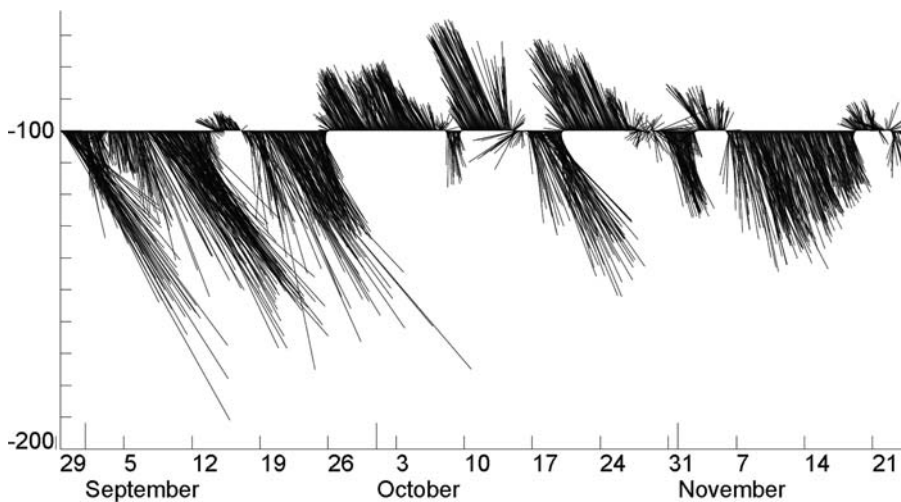


as depicted in Figure 5. BOEM had a through-column mooring, L4, deployed just to the south of the DeepStar array. Over the 1-year deployment, about a half-dozen TRWs were measured and showed the strongest currents occurred near the base of the Escarpment at S2 and S3. Only about 10 km north at S6 speeds dropped off rapidly to less than half those observed at S2. In contrast, the reduction on the down-dip side of the Escarpment was much smaller, e.g., L4 was about 30% less than S2.

In 2008, DeepStar restarted its efforts on TRWs because of increased exploration activity along the Escarpment and reports from drilling rigs that were adversely affected by strong bottom currents. That year, two projects were started. The first involved taking more current measurements, but this time with moorings spread along the Escarpment as well as across. Figure 6 shows the four DeepStar moorings as well as other moorings deployed by Chevron and Shell, which

FIGURE 4

Time series of near-bottom current vectors measured near the Sigsbee Escarpment. The vectors pointing up are flowing towards the northeast; those pointing down are flowing southwest.



overlap in time and were later obtained by DeepStar. The 1 year of measurements showed strong variation along the Escarpment and confirmed the strong cross-escarpment variation first observed in the 2003 DeepStar measurements.

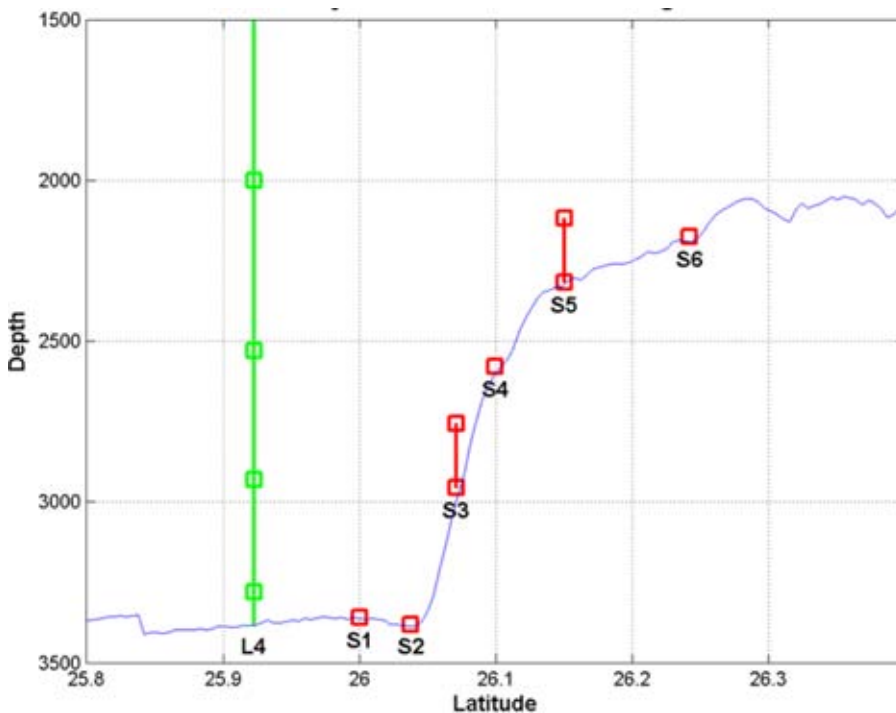
The second project, begun in 2008, focused on the development of a numerical model with the goal of eventually using it to develop operational and design criteria. Without a model, the industry would have had to develop criteria based on measurements of only a few TRWs at a few locations. The latter was especially troubling, because the measurements showed that TRW-generated currents varied significantly over length scales of a few kilometers.

Florida State University (FSU) was contracted to develop the model and soon discovered that the numerical discretization in standard ocean current models generated substantial numerical errors when dealing with the sharp bathymetric gradients of the Escarpment. A more advanced numerical technique was implemented, and the model was then used to hindcast the BOEM and DeepStar measurements (Dukhovskoy et al., 2009). Results were encouraging so a second modeling phase was kicked off, culminating in a well-validated model as suggested in the excellent comparison shown in Figure 7. In the process, FSU discovered that the TRWs were being generated by the collision of the Loop (or a recently detached eddy) on the outer slope of the Mississippi Fan, just south of the Delta (Morey et al., 2010).

With the successful validation of the model, DeepStar now had a tool that could be used to develop operational and extreme criteria. FSU developed the needed database by allowing the

FIGURE 5

Cross section of the current meters deployed across the Sigsbee Escarpment.

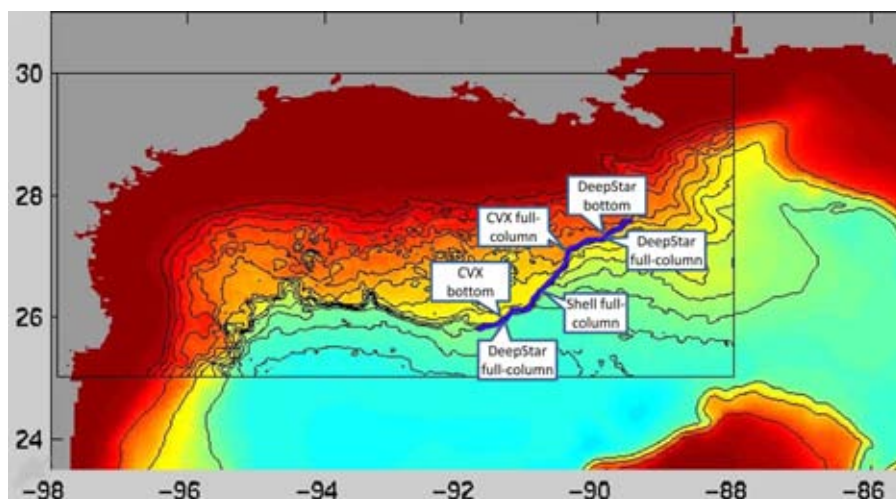


model to free run for a 50-year period. It was a daunting computation effort since it involved running a high-resolution (800 m grid size) nested model covering the Sigsbee Escarpment inside a 3.5 km model covering

the northern Caribbean and portions of the southeast Atlantic. Figure 8 shows the model domain. Results from the 50-year run were archived and are now being used by the Industry to develop design criteria.

FIGURE 6

Location of current measurements taken during 2008-2009. The dark blue curve shows the base of the Sigsbee Escarpment.



Finally, FSU recently started to apply their model results to develop a predictive capability that can eventually forewarn drillers and installers of major facilities, of an approaching TRW that might threaten their operations. Initial results have shown that the numerical model cannot predict the phase of TRWs very well since there are essentially no operational measurements in the lower deep water column available for model initialization or data assimilation. Instead of direct use of the model, FSU is using the 50-year database to develop a stochastic model based on independent variables like the position of the Loop. This approach will not suffer the phase issues and should also provide uncertainty estimates.

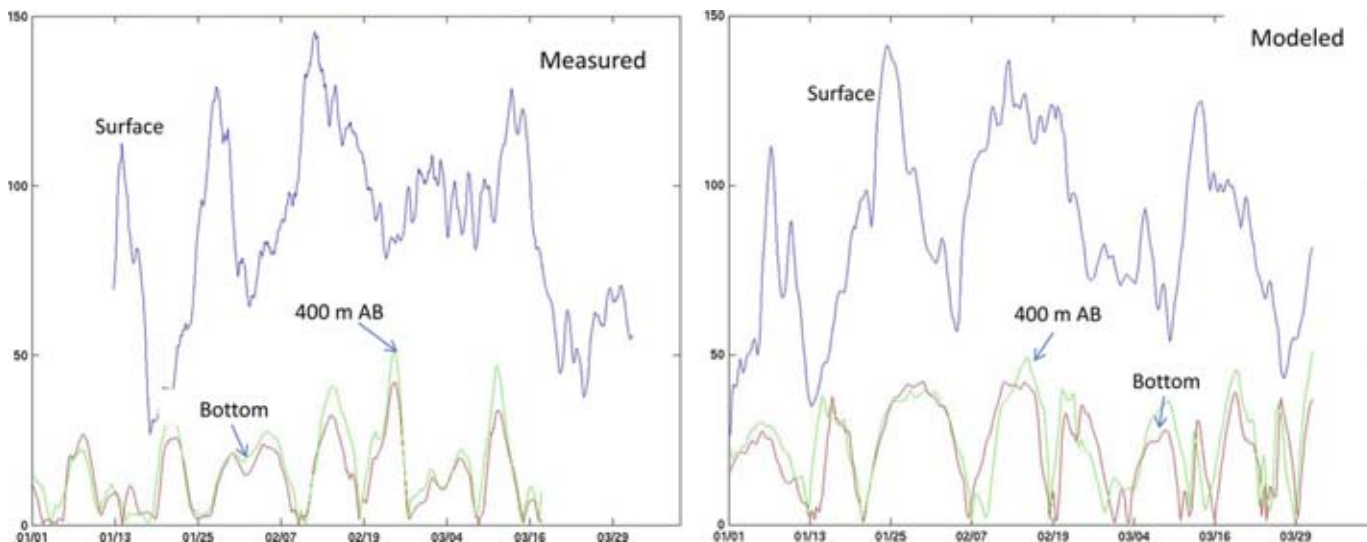
Hurricane Winds

In 2010, DeepStar funded a study to bring together all available hurricane wind data sets made in and around the Gulf since 1998, quality control them, and then analyze them in an effort to check the validity of the present American Petroleum Institute (API, 2012) recommended equations for hurricane winds. The data sets included dozens of offshore platform anemometer records, measurements from National Oceanic and Atmospheric Administration (NOAA) buoys, Coastal-Marine Automated Network (C-MAN), Automated Surface Observing System (ASOS), and National Ocean Service (NOS) stations, tower arrays of anemometers deployed along the coast, coastal weather radars, and dropsonde observations made by hurricane hunter aircraft.

The first phase of this study was completed in 2012 by Applied Research Associates, Inc., Texas Tech University, and the University of Florida

FIGURE 7

Comparison of model and observed current at three depths taken at one of the moorings shown in Figure 6.



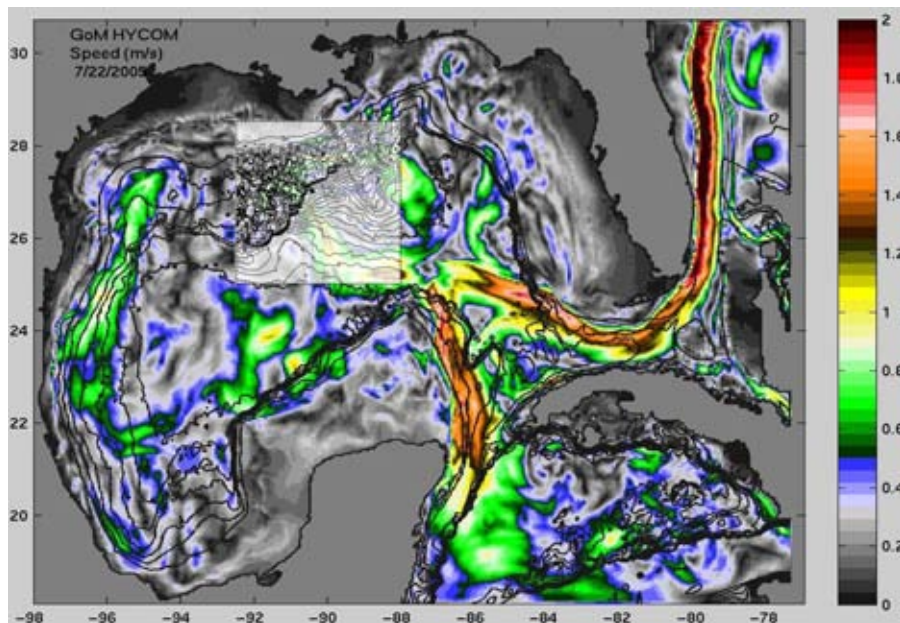
and identified deficiencies in the API (2012) equations for gust factors, profiles, and spectra when applied to hurricanes. Figure 9 compares measured speed profiles to the API (2012) and Engineering Sciences Data Unit

(ESDU, 1974, 1982, 1983) calculated profiles. While the API (2012) profile compares well within a few 10 s of meters of the sea surface, a 10% discrepancy appears at the higher elevations typical of platform deck heights

(30–60 m). Such a discrepancy translates to more than 20% in the static drag force. On the other hand, the API (2012) equation for gust factors was found to underestimate the observations as shown in Figure 10.

FIGURE 8

Contours showing the sea surface height over the large-scale (3.5 km) model. Insert shows the nested model around the Sigsbee Escarpment with a resolution of 800 m.



The second phase of the study is now underway, with the analysis extended to tropical storm wind records made off the northwest coast of Australia, the east coast of the United States, and a reexamination of the original Norway extratropical wind measurements used to develop the API relationships. The end goal of this phase is a revised set of wind design relations that may then be incorporated into the latest offshore standards, for both tropical and extratropical storms. The study is anticipated to be completed by late 2013.

Summary and Conclusions

In 1998, DeepStar began what was to become a highly insightful set of projects in the field of meteorology and oceanography (metocean). The first project focused on measuring the

FIGURE 9

Comparison of measured wind profiles with recommended profiles from API and ESDU for three different central pressure bins.

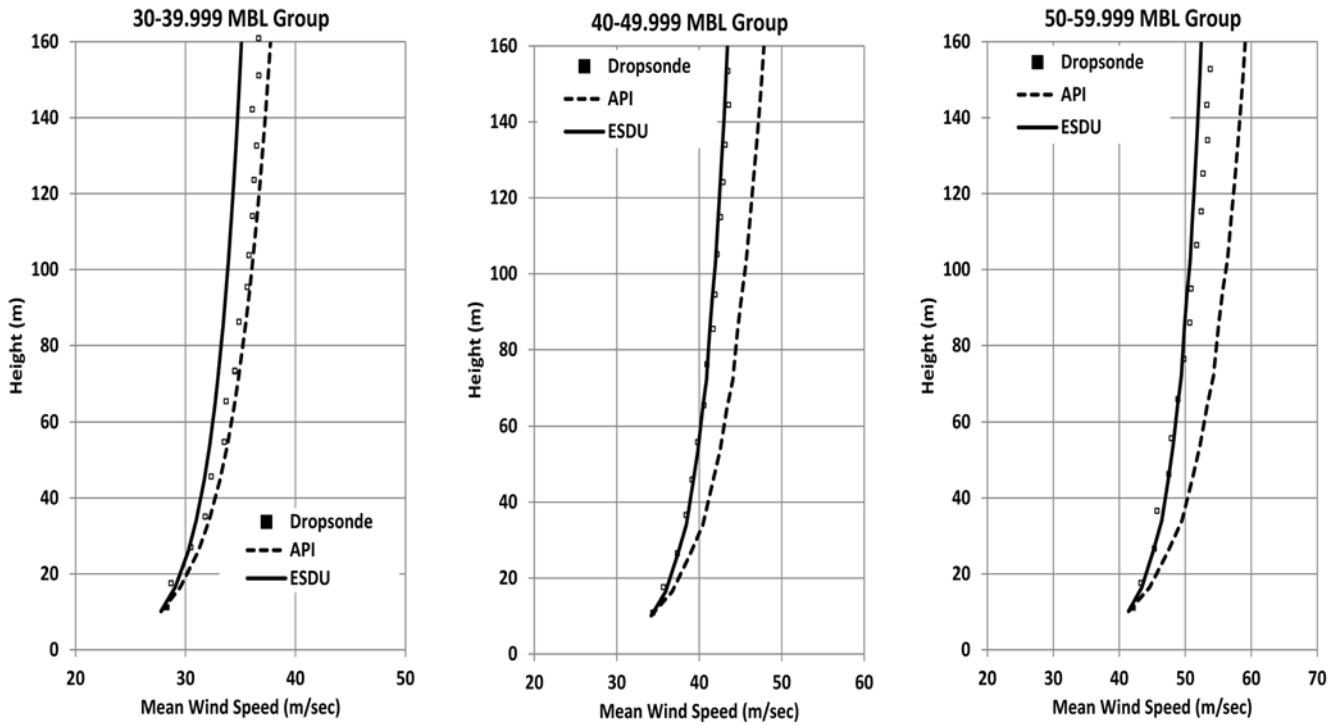
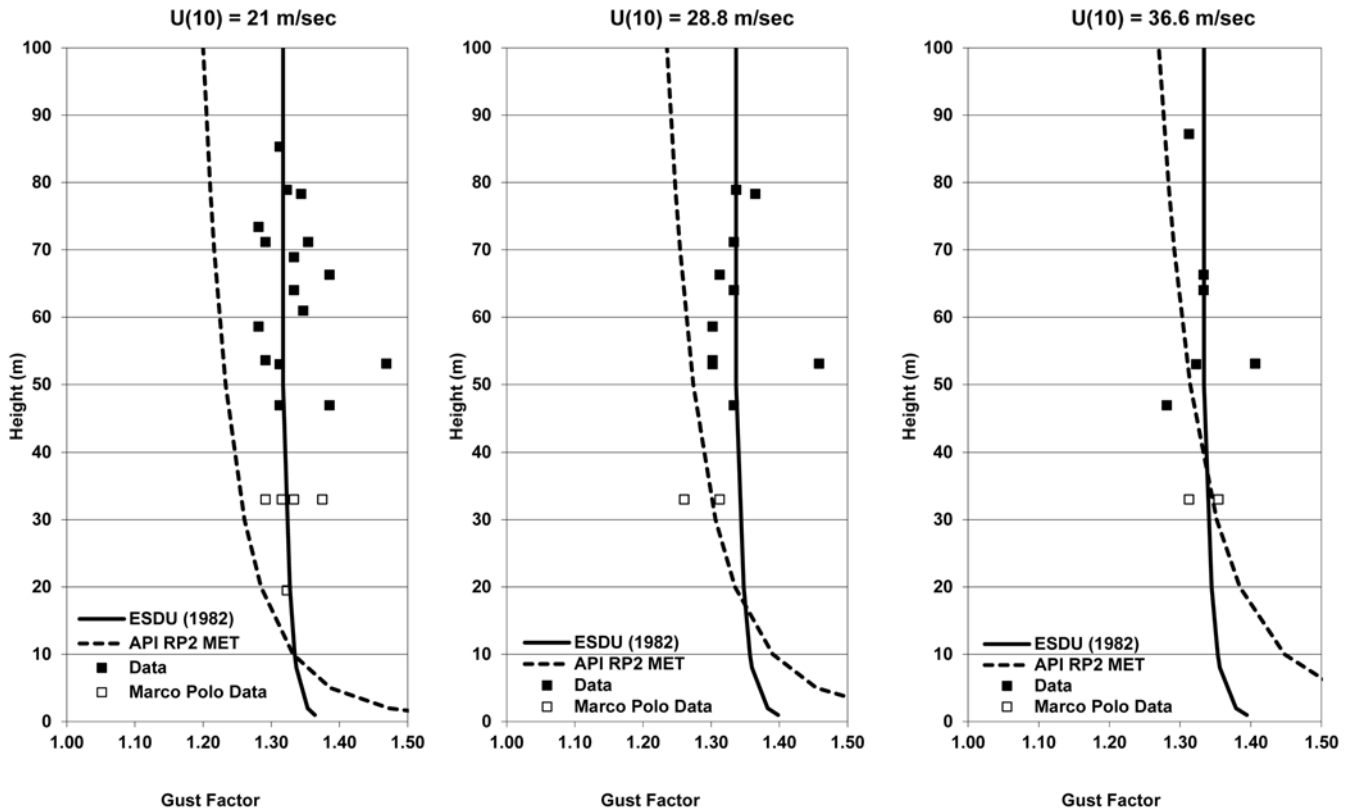


FIGURE 10

Comparison of measured gust factors with recommended factors from API and ESDU for three different wind speeds.



flow of the Loop Current through the Yucatan Straits—fundamental information that had never been gathered. This was followed by measurements of turbulence in the Loop Current; a study driven by concerns about resonance in tendons, moorings, and risers. Field measurements were completed in 2003, which dismissed that concern. In 2004, attention was turned to finding the best available forecast model of the Loop Current, a tool that could save the Industry millions of dollars by helping it avoid downtime during drilling and installation of large facilities like spars. Two studies were done comparing the ability of eight existing forecast models. Results showed that many of the models were much worse than simply assuming that the Loop remained unchanged (persistence) and revealed that the models were primarily limited by the accuracy of their initial conditions. This knowledge has been used in other Industry efforts to improve forecast models. In 2004, a six-phase effort was begun to quantify Topographic Rossby Waves (TRW)—a wave with a length of 200 km first measured in the Gulf in 1998 and capable of generating currents of 1 m/s (2 kt) near the sea floor. Phases 1 and 2 deployed arrays of current meters that recorded several TRWs. These measurements were then used to develop and validate a numerical model—the first to successfully simulate the full strength of these powerful waves. Phase 5 used the TRW model to develop a 50-year hindcast database that provides accurate operational and extreme current criteria throughout much of the deepwater Gulf. Phase 6 is using the model to develop a probabilistic forecast that can warn drill rigs and installation operations of an approaching TRW. Most recently, DeepStar has funded

work to analyze the wealth of wind data collected during the recent extreme hurricanes. This study has revealed that the present Industry standard for hurricane wind spectra, profiles, and gusts can be improved, so revisions will soon be adopted.

Corresponding Author:

Cortis Cooper
Chevron Energy Technology Co.
Email: CortCooper@Chevron.com

References

- Abascal, A.J., Sheinbaum, J., Candela, J., Ochoa, J., & Badan, A.** 2003. Analysis of flow variability in the Yucatan Channel. *J Geophys Res.* 108(C12):3381. doi:10.1029/2003JC001922.
- American Petroleum Institute.** 2012. Derivation of metocean design and operating conditions, API RP 2MET, First Edition.
- Engineering Sciences Data Unit, ESDU.** 1974. Characteristics of atmospheric turbulence near the ground, Item No. 74031, London.
- Engineering Sciences Data Unit, ESDU.** 1982. Strong winds in the atmospheric boundary layer, Part 1: Mean hourly wind speed, Item No. 82026, London.
- Engineering Sciences Data Unit, ESDU.** 1983. Strong winds in the atmospheric boundary layer, Part 2: discrete gust speeds, Item No. 83045, London.
- Dukhovskoy, D.S., Morey, S.L., Martin, P.J., O'Brien, J.J., & Cooper, C.** 2009. Application of a vanishing, quasi-sigma, vertical coordinate for simulation of high-speed, deep currents over the Sigsbee Escarpment in the Gulf of Mexico, *Ocean Model.* 28(4):250-65.
- Hamilton, P., & Lugo-Fernandez, A.** 2001. Observations of high speed deep currents in the northern Gulf of Mexico. *Geophys Res Lett.* 28:2867-70.
- Mitchell, T.M., Lueck, R.G., Vogel, M.J., & Forristall, G.Z.** 2007. Turbulence measure-

ments in a Gulf of Mexico warm-core ring. In: Proc. 26th Int. Conf. on Offshore Mech. and Arctic Eng., OMAE2007-29231. New York: American Society of Mechanical Engineers.

Morey, S.L., Dukhovskoy, D.S., & Cooper, C. 2010. Measurement and modeling of topographically trapped waves along the Sigsbee Escarpment. In: Proc. Offshore Tech. Conf., 20694. doi:10.4043/20694-MS.

Recent Development in IR Sensor Technology for Monitoring Subsea Methane Discharge

AUTHORS

Mark Schmidt

Peter Linke

GEOMAR Helmholtz Centre for Ocean Research Kiel, Kiel, Germany

Daniel Esser

CONTROS Systems & Solutions GmbH, Kiel, Germany

Introduction

Natural marine hydrocarbon seeps are important sources of methane (CH_4) to the surface sediments, the benthic boundary layer, and eventually to the water column and atmosphere. CH_4 is a potent greenhouse gas that warms the Earth about 23 times more than carbon dioxide (CO_2) when averaged over 100 years. Quantifying the discharge of CH_4 from the seabed, its fate in the water column and its flux to the atmosphere has been the subject of ongoing research on many different fronts (e.g., Clark et al., 2000; McGinnis et al., 2006; Judd & Hovland, 2007; Westbrook et al., 2009; Faure et al., 2010). Furthermore, a natural subsea hydrocarbon seep can serve as an ideal analogon for studying gas leakage scenarios from subsea constructions like gas/oil transport lines, active or abandoned wellheads, etc. (Leifer et al., 2006). Moreover, the dissolution behavior and transport of gas in the water column at variable oceanographic conditions, like currents, horizontal/vertical eddies, tidal changes, or stratified water columns can be studied at natural seepage sites (e.g., Leifer et al., 2006; McGinnis et al., 2006,

ABSTRACT

Recently developed methane sensors, based on infrared (IR) absorption technology, were successfully utilized for subsea methane release measurements. Long-term investigation of methane emissions (fluid flux determination) from natural methane seeps in the Hikurangi Margin offshore New Zealand were performed by using seafloor lander technology. Small centimeter-sized seep areas could be sampled at the seafloor by video-guided lander deployment. *In situ* sensor measurements of dissolved methane in seawater could be correlated with methane concentrations measured in discrete water samples after lander recovery. High backscatter flares determined by lander-based Acoustic Doppler Current Profiler (ADCP) measurement indicate bubble release from the seafloor. Highest methane concentrations determined by the IR sensor coincided with periods of high ADCP backscatter signals. The high fluid release cannot be correlated with tidal changes only. However, this correlation is possible with variability in spatial bubble release, sudden outbursts, and tidal changes in more quiescent seepage phases.

A recently developed IR sensor (2,000 m depth-rated) with a detection limit for methane of about 1 ppm showed good linearity in the tested concentration range and an acceptable equilibration time of 10 min. The sensor was successfully operated offshore Santa Barbara by a small work-class ROV at a natural methane seep (Farrar Seep). High background methane concentration of 50 nmol L^{-1} was observed in the coastal water, which increases up to 560 nmol L^{-1} in dissolved methane plumes south of the seepage area. ROV- and lander-based sensor deployments have proven the applicability of IR sensor technology for the determination of subsea methane release rates and plume distribution. The wide concentration range, low detection limit, and its robust detection unit enable this technology for both subsea leak detection and oceanographic trace gas investigations.

Keywords: methane, sensor development, natural hydrocarbon seeps, subsea leak detection

2011; Schneider von Deimling et al., 2010). Here, we report on the development and deployment of novel methane sensors, based on infrared absorption technology, which were tested in two different subsea settings. The first setting was a long-term multisensor deployment with a benthic lander, which was placed for 41 h at a 670-m-deep CH_4 cold-seep at the seafloor in the Hikurangi Margin,

New Zealand. The second one was a shallow water test of ROV-operated sensor measurement at a natural hydrocarbon seep offshore Santa Barbara, California.

CH_4 Sensor Deployment on a Deep Sea Lander

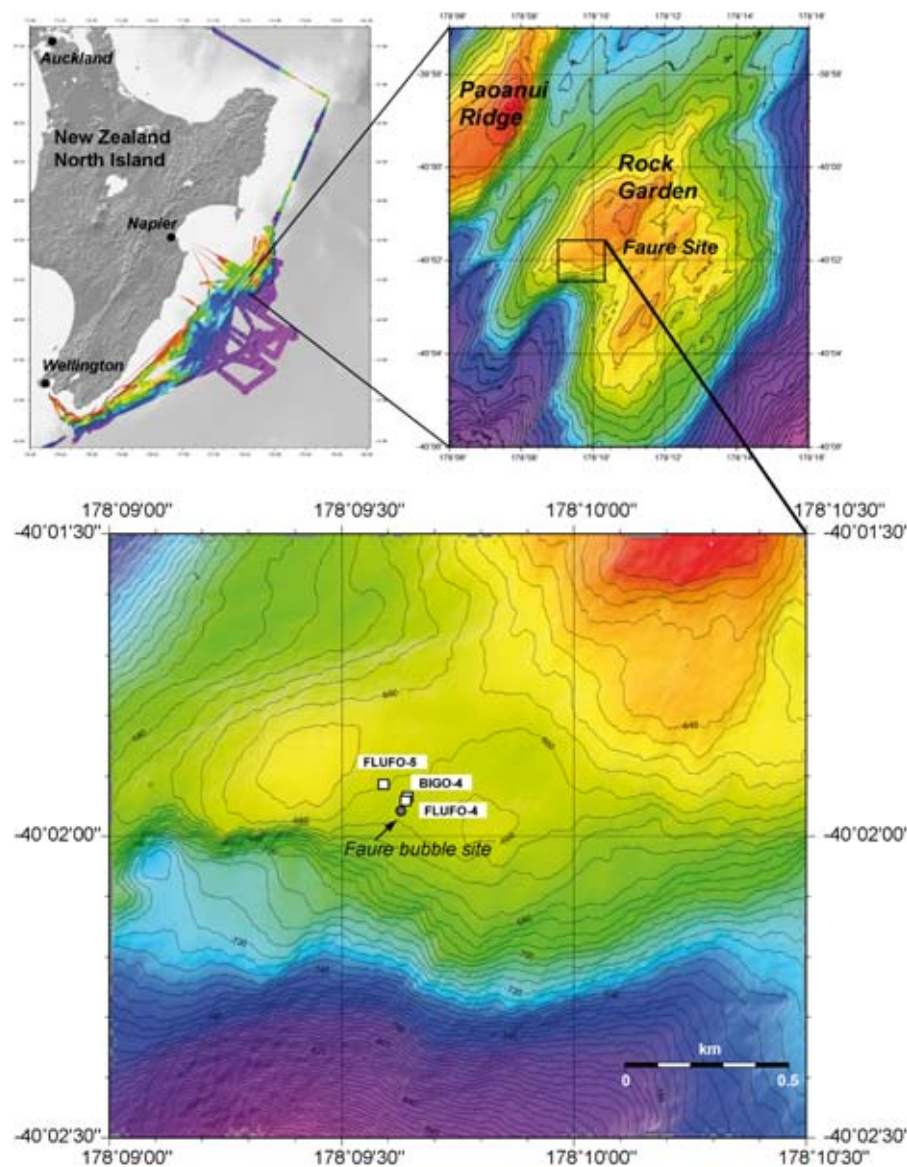
A novel methane sensor HydroC™ of CONTROS System & Solutions

GmbH, Germany, was deployed on a benthic lander equipped with a wide range of instrumentation to study the role of physical parameters on exchange processes in the benthic boundary layer. Benthic landers provide a stationary study platform decoupled from the movement of the ship and simultaneously measure several physical, chemical, and biological parameters across the sediment water interface. The Fluid Flux Observatory (FLUFO) was deployed for *in situ* flux measurements of methane and oxygen in about 670-m water depth at a methane seep setting known as Rock Garden by local fishermen (Figure 1). This area is situated at the southern termination of Ritchie Ridge and is uplifted by the subduction of a seamount beneath the outer Hikurangi Margin at the east coast of New Zealand's North Island. Townend (1997) estimated that more than 20 m³ of fluids are being squeezed from accreted and subducted sediments along each meter of the Hikurangi Margin every year, which results in abundant evidence of escaping gas offshore (Faure et al., 2010; Linke et al., 2010; Naudts et al., 2010) and onshore (Campbell et al., 2008). The deployment was part of a large campaign involving a large range of equipment and scientific disciplines to study the methane seeps at the Hikurangi Margin (Greinert et al., 2010).

The observatory consists of a titanium tripod frame that carries 21 Benthos glass spheres for buoyancy and ballast weights attached to each leg (Figure 2a). The release of the ballast weights is controlled by two acoustic releasers. FLUFO is equipped with two circular benthic chambers, each covering a sediment area of 651.4 cm². A video-guided launching system (LAUNCHER) allowed smooth placement of the observatory on a

FIGURE 1

Overview map showing the bathymetry of the Hikurangi Margin at the east coast of New Zealand, mapped during R/V SONNE cruise SO191 in 2007 (modified from Linke et al., 2010). The enlarged bathymetric maps depict the Rock Garden area with stations relevant for this paper; for example, the site of vigorous gas discharge (Faure bubble site) discovered during a ROV dive (Naudts et al., 2010) and two other lander stations (FLUFO-4 and BIGO-4) described in Linke et al. (2010). (Color version of figures are available online at: <http://www.ingentaconnect.com/content/mts/mts/2013/00000047/00000003>.)

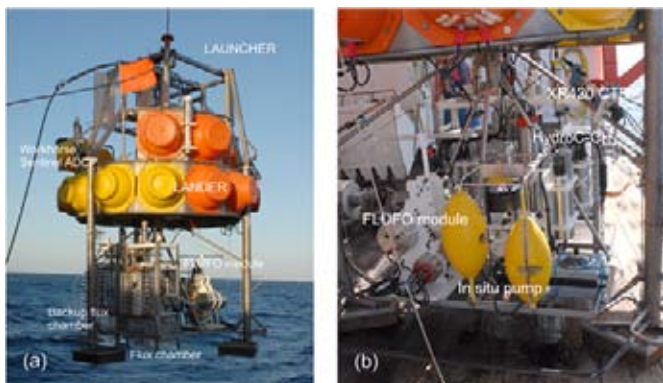


selected site at the seafloor (Pfannkuche & Linke, 2003). Two to three hours after deployment, the benthic flux chambers were slowly driven into the sediment. Seabed methane emission was monitored with eight sequentially water samples taken from each cham-

ber by means of glass syringe samplers. Sampling (monitoring) periods were about 34 (FLUFO-5) and 40 h (FLUFO-4, BIGO-4), respectively. After the *in situ* incubation, the bottom of the chambers was closed with a shutter to recover the sediments for further

FIGURE 2

Launch of the Fluid Flux Observatory (FLUFO) with the video-guided launcher on top showing the different scientific modules integrated in the back (a) and in the front (b) of the lander (modified from Linke et al., 2010).



analyses. After recovery, syringe water samples retrieved during lander deployment were immediately transferred into the cold room, where subsamples were obtained for the determination of oxygen and methane (Linke et al., 2010).

Next to the chambers, the lander carried the HydroC™ methane sensor for *in situ* measurements up to 4,000 m water depths (Figure 2b). The high-pressure seawater side is separated by a permeable membrane from the internal infrared detection unit. An internal pump system increases equilibration of internal partial pressure of, for example, methane with the dissolved methane in seawater. Concentrations of methane were determined by using optical NDIR absorption technique. Large quantities of methane accumulated in the internal gas circuit can actively be removed with a patented exhaust system. The sensor was calibrated to detect CH₄ concentrations as low as approximately 100 nmol L⁻¹, and data were logged by a 24-bit SmartDI controller.

The HydroC™ methane sensor was mounted upright at the lander frame to avoid any trapping of gas bubbles in front of the membrane inlet. Beside the methane sensor, FLUFO was equipped with an upward-looking

Acoustic Doppler Current Profiler (ADCP; 300 kHz Workhorse Sentinel ADCP, Teledyne RD Instruments, USA) and a small stand-alone memory CTD (Conductivity, Temperature, Depth; XR420, RBR Ltd., Ottawa, Canada). The CTD was also equipped with an optical backscatter sensor (SeaPoint), which measures light scattered by particles suspended in water.

The lander was deployed in the vicinity of a methane gas vent named Faure bubble site (FLUFO-5; Figure 2). Here, bubble release occurs from differently sized depressions, which are often aligned in NW-SE direction; the largest depression observed by a ROV was 50 cm in diameter and 15 cm deep (Naudts et al., 2010). These observations clearly showed that the depressions are formed by the often violent release of bubbles. Naudts and coworkers observed that the bubbles entrained sediment particles, which then get carried away by the water currents, creating the depressions and a sediment outfall away from the venting hole. The data obtained with the HydroC™ sensor depict pulses of CH₄ emission (Figure 3a), ranging between 150 and 200 nmol L⁻¹. Water samples obtained from the ambient bottom water during

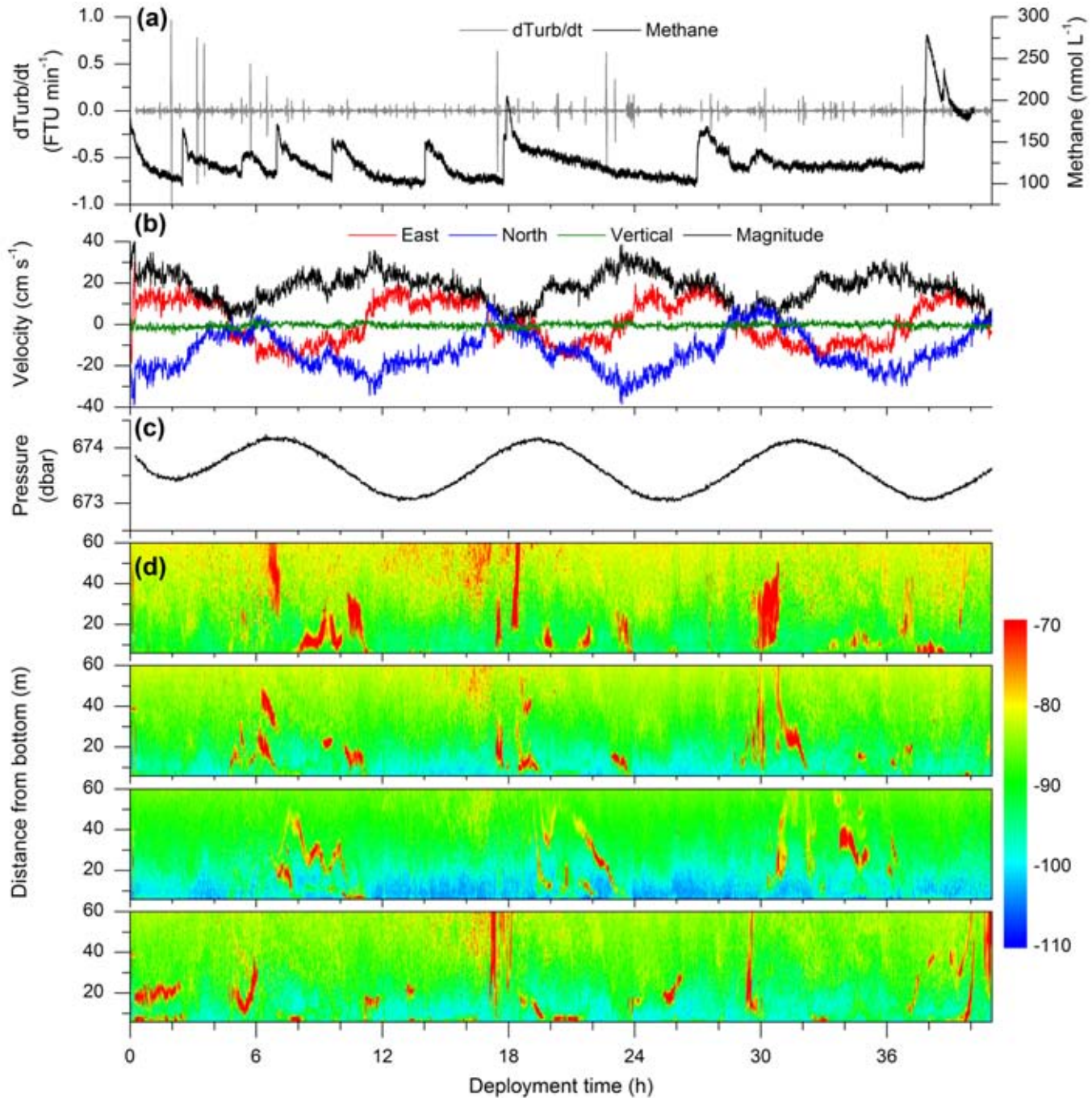
a parallel deployment of another lander (BIGO-4; Figure 2) at the same height above the sediment water interface like the sensor showed two distinct peaks with CH₄ concentrations of 189 and 190 nmol L⁻¹, respectively (Linke et al., 2010), which are in the same range of the measurements obtained with the HydroC™ sensor. On the other hand, the data shown here depict that the sensor needed some time of relaxation after it had experienced high a peak of CH₄ before it was able to record another sudden increase.

However, the pulses seen in the HydroC™ sensor data correspond with increases in the backscatter strength detected in all four beams of the upward-looking ADCP (Figure 3d). The “flares” (presumed to be bubbles) persisted for 10–60 min, and some of them covered almost the whole acoustic depth range (100 m) of the ADCP. No associated signal was observed in the turbidity data obtained from the CTD (Figure 3a). The occurrence of the flares does not seem to be related to a sudden or tidal hydrostatic pressure drop (Figure 3c). In fact, some of the outburst occurred during high tide and at maximum current velocities of more than 20 cm s⁻¹ (Figure 3b). This is in agreement with results of Linke et al. (2010) from another lander deployment next to the Faure Site (FLUFO-4; Figure 2). They found CH₄ concentration fluctuations in both the ambient bottom water and the chamber water, which coincided with tidally induced fluctuations of currents and acoustic backscatter flares in the ADCP record.

Furthermore, these measurements agree very well with ROV observations in the area reporting highly variable spatial bubble release rates and bubble sizes, with periods of low activity, alternating with periods of violent outbursts (Naudts et al., 2010).

FIGURE 3

Physical measurements obtained simultaneously to the changes in CH₄ concentration during deployment of FLUFO-5. Top to bottom: (a) turbidity changes and CH₄ concentration, (b) depth-averaged velocity time series, (c) local hydrostatic pressure, and (d) ADCP backscatter (all four beams).



High-Sensitive Methane Sensor (HISEM) Development

A new methane sensor, which should fulfill the needs for scientific

trace gas (i.e., CH₄) investigations in the oceans and for subsea leak detection, is currently under development (www.martec-era.net). The sensor technology is based on laser diode IR absorption technology that provides

excellent detection limits at good signal-to-noise ratios. The actual configuration is a 2,000-m depth-rated version with a (Contros HydroC™) membrane-inlet configuration. The system was tested in the laboratory

against various partial pressures of methane dissolved in water in a temperature controlled (4–15°C) water-filled calibration tube. The water is continuously equilibrated at atmospheric pressure with standard gas mixtures of methane (3–200 mol-ppm) in synthetic air pressure bottles (~200 bar).

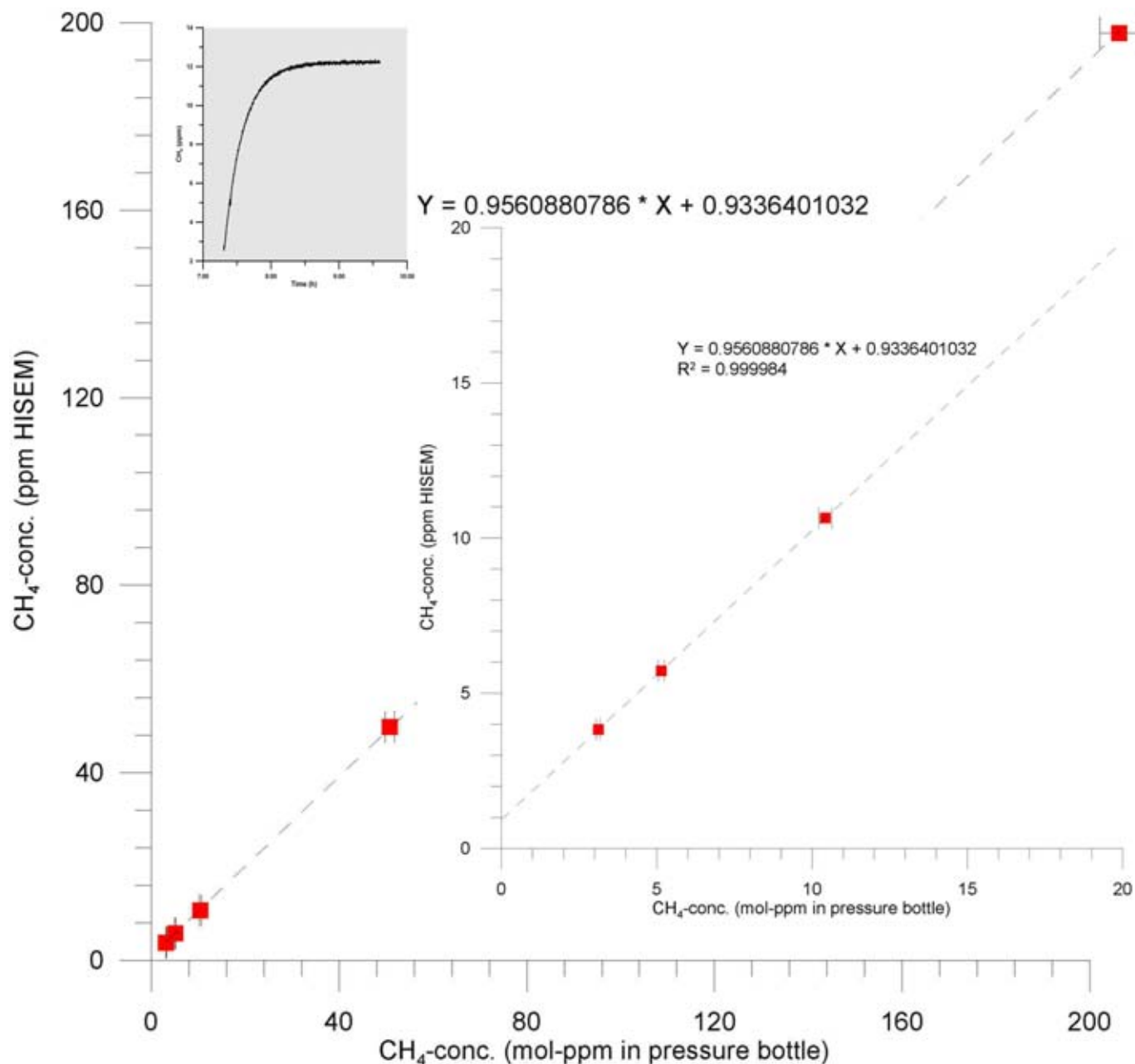
Gas exchange with atmosphere is prevented in the semiclosed system. The response of the sensor signal is continuously recorded during testing, and equilibration of the signal is established with a response time (t_{65}) of about 10 min after partial methane pressures have been changed in the tube (Figure 4).

The detection limit of the HISEM of about 1 ppm could be determined with a signal-to-noise ratio of 5.

The sensor output (ppm unit) shows good linearity ($R^2 = 0.99998$) against the known pressure bottle concentrations given in mol-ppm with an offset of ~1 ppm (Figure 4). The correlation

FIGURE 4

Methane concentrations determined with the HISEM system, which was placed in a water-filled calibration tube at 4°C. The water is equilibrated with methane by using different gas mixtures (3, 5, 11, 50, 100, and 200 mol-ppm CH₄ in pressure bottles).



was confirmed by parallel determination of dissolved methane concentrations sampled from the calibration tube. These methane analyses were conducted by using head space sampling technique and subsequent gas chromatographic analysis.

HISEM Offshore Test Site

To test the sensor performance for methane plume detection and its offshore practicability in operating the system with a small work-class remotely operated vehicle (i.e., HYSUB 20 ROV), a 3-day offshore campaign was performed in November 2012 near Santa Barbara, Southern California. The offshore test site that was chosen is named *Farrar Seep* and is located within the Coal Oil Point seep area in the inner Santa Barbara Channel (Figure 5a) about 1,300 m east of the University of California, Santa Barbara area (Figure 5b). The *Farrar Seep* is a natural hydrocarbon seep that is indicated by gas bubble release from the seafloor at about 22 mbsl. Natural gas seeps in the area of the inner Santa Barbara Channel can be charac-

FIGURE 6

(a) Deployment of the HYSUB 20 ROV from the starboard site of M/V *Danny C.* (b) The HISEM prototype (marked by white rectangle) was mounted behind the bumper bar of the ROV.

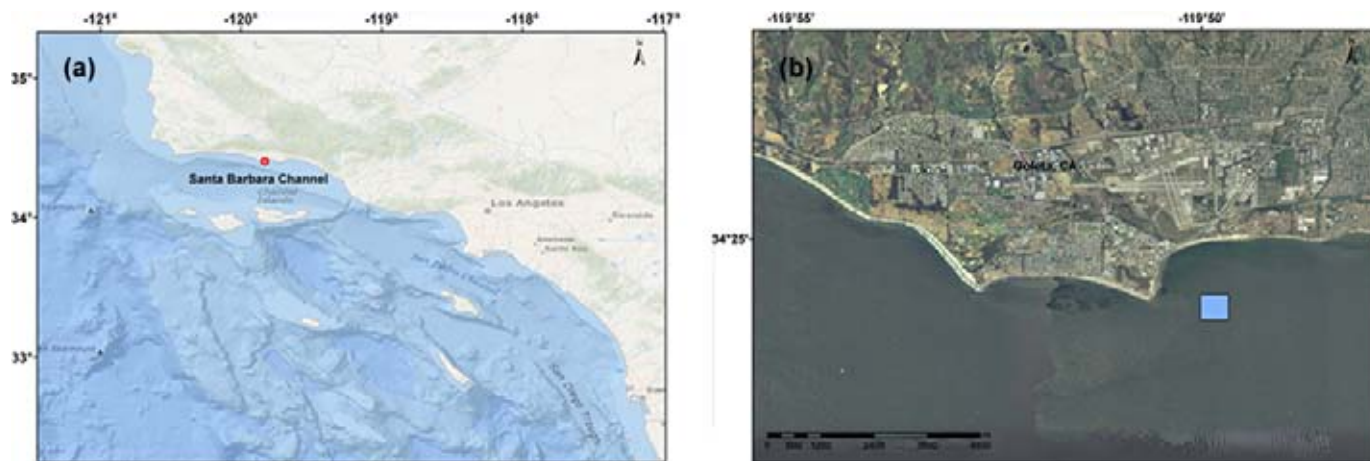


terized by low seepage activity, and the gas composition of bubbles emanating from the seafloor consists of up to 90% of methane and 10% of higher hydrocarbons (e.g., Leifer et al., 2006). As gas bubbles dissolve and exchange their gas content during uplift in seawater, dissolved gas plumes are formed in the water column and the initial hydrocarbon content of the bubbles decreases (e.g., Leifer & Patro, 2002; Clark et al., 2003; McGinnis et al., 2006). Numerous natural gas and oil seeps exist in the inner Santa Barbara channel, which lead to general high background concentrations of dissolved methane in the area (e.g., ~20–100 nmol L⁻¹; Clark et al., 2000).

To measure dissolved methane concentrations during ROV dives, the HISEM system was mounted parallel behind the upper bumper bar of the HYSUB 20 (Figure 6). The head (membrane inlet) of the HISEM prototype was connected with a plastic tube to a suction inlet at the front of the ROV. A metal filter was mounted to the suction inlet, and the inlet area was monitored permanently by cameras. A second tube connected the suction inlet by a y-adapter with a CTD and a commercial leak detection device (Combination of HydroC-CH₄, Fluorometer). A constant water flow through the tubing was guaranteed by two Seabird pumps, which operated inline the tubes.

FIGURE 5

(a) Map of the overall area of the Santa Barbara channel in Southern California. The test site is marked as a small open circle. (b) *Farrar Seep* offshore test site (shaded rectangle), about 1,300 m east of the University of California Santa Barbara area.



ROV-Based Sensor Measurements

Two N-S and four W-E ROV dives were conducted at the 28th and 29th of November 2012 at the estimated location of the Farrar Seep (Figure 5b). The average length of a ROV dive track was about 250 m. Furthermore, one vertical dive track was conducted at the estimated center of the seep (Figure 5b). During all dives, water depth, temperature, conductivity (SV48 CTD, Sea and Sun Technology) and methane sensor data (HISEM) were recorded continuously. However, the ROV stopped every 15 m for 1–2 min to increase the total measuring time. The homogeneous temperatures of about 15.8°C and salinities of about 33.4 PSU measured during the ROV dives indicate a well-mixed water column in this coastal area during November 2012. The water depth of the test area is about 16–30 mbsl and ROV dive tracks plotted in Figure 7 were performed above seafloor at elevations of 2 and 12 m, respectively. Due to strong currents in the area and especially a current direction and current speed change between the 28th and 29th of November 2012 (Goleta Point buoy data, SCCOOS.org), navigating the ROV was challenging and deviations from predefined track lines were about 15 m. The Farrar Seep location could be verified at 119°49.836'W and 34°24.157'N (WGS84) by measuring a CH₄ concentration maximum (up to 260 ppm and 334 nmol L⁻¹, respectively) while crossing the central seepage site with the ROV at 2 m elevation above seafloor (Figure 8). The minimum concentration of dissolved methane, which was determined in water masses in the test area, was ~50 nmol L⁻¹.

The center of the main seepage activity of the Farrar Seep was also

FIGURE 7

ROV dive tracks conducted in the test area “Farrar Seep.”

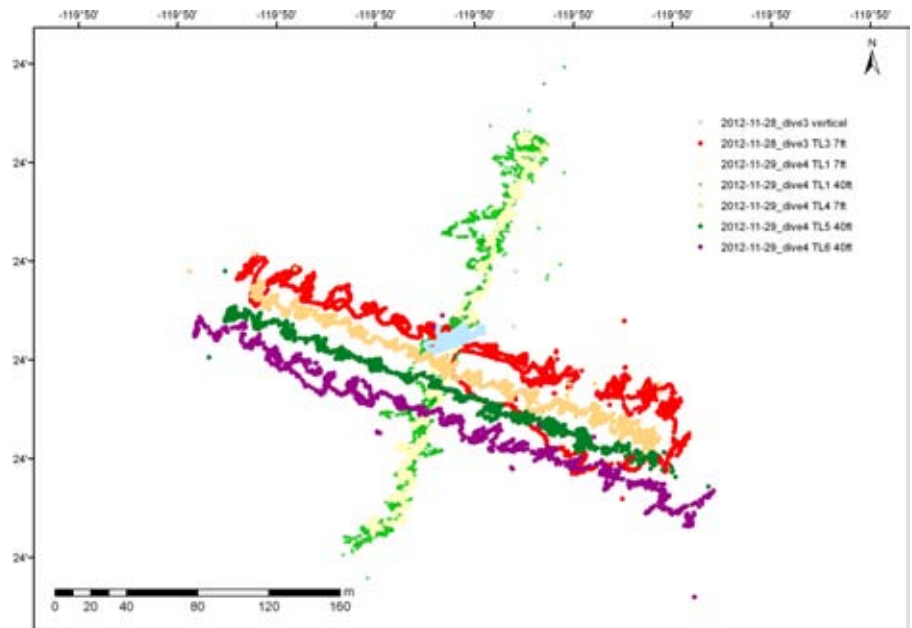


FIGURE 8

Methane sensor signal recorded with HISEM about 2 m above the seafloor during ROV track line 1 at the 28th and 29th of November 2012. Track line 1 is the N-S profile and crosses the Farrar Seep (Figure 3).

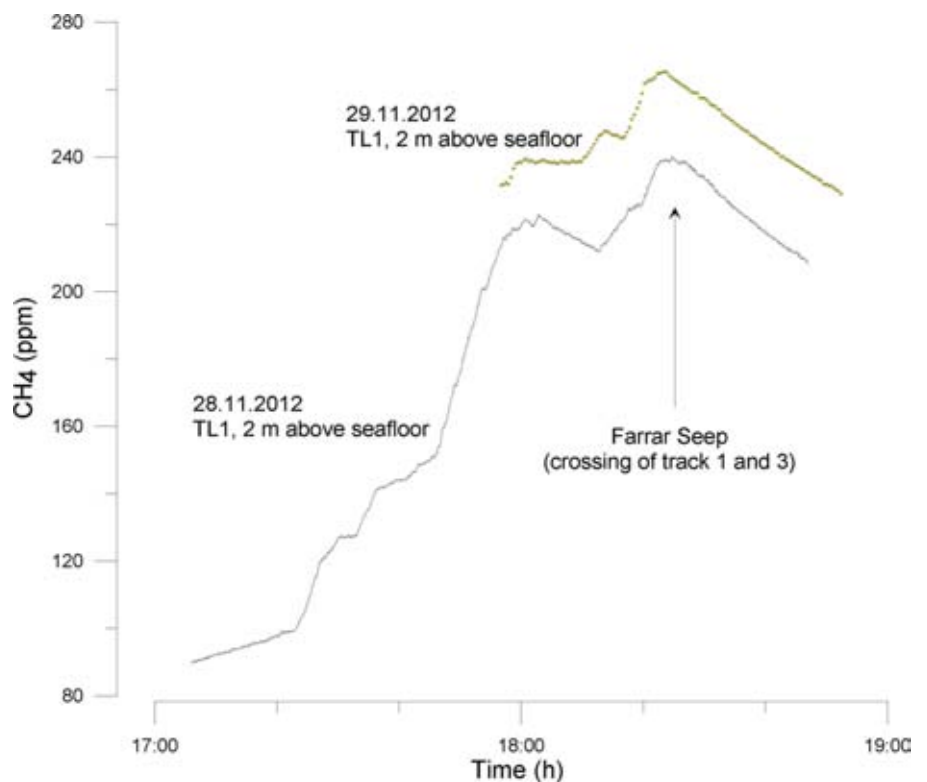
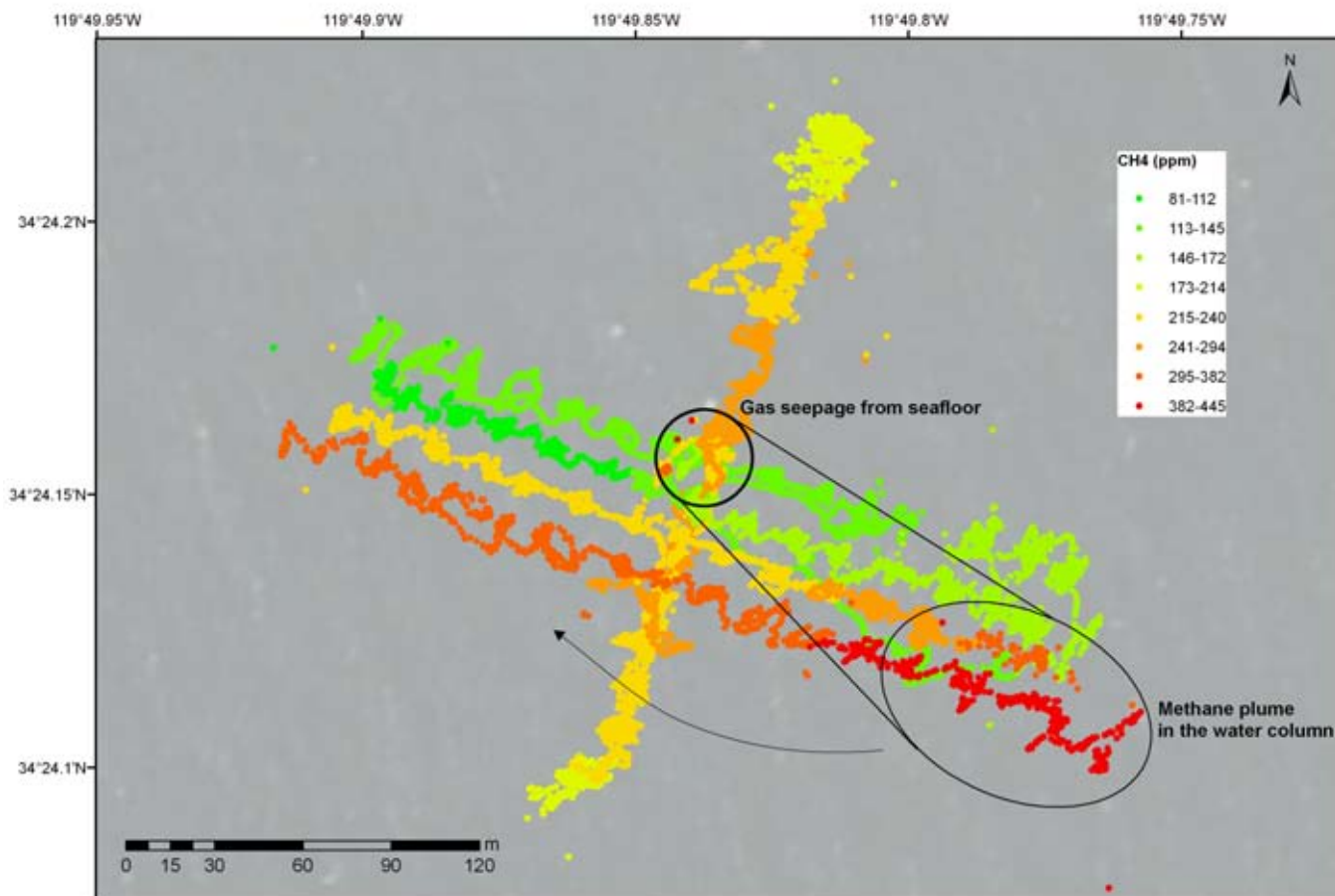


FIGURE 9

Spatial methane concentrations at Farrar Seep measured by HISEM during ROV dives. The concentration of methane is given in ppm. The total range measured by HISEM corresponds to dissolved methane concentrations of 50–560 nmol L⁻¹ in the test area.



indicated by the ship's echo-sounder (acoustic blanketing by gas bubbles) and ground-truthing by ROV (video observations). Note that measuring the dissolved gas content within the bubble streams emanating from the seafloor did not increase the HISEM sensor concentration signal. The concentration pattern of November 28th could be verified by following the same track on the 29th (Figure 8). The deviation of methane concentration data of about 25 nmol L⁻¹ measured within the central seep area is possibly related to a weakening of the local current regime on the 29th (<http://sccoos.org/>).

The dimensions of the main (dissolved) methane plume were about

50–150 m around the seepage site (Figure 9). However, dissolved gas plumes with high methane concentrations (up to 560 nmol L⁻¹) were also examined towards the east and south at about 12 m above the seafloor (Figure 9). In general, the dissolved methane concentrations are highest towards the south, which could indicate a preferred rotation of the methane plume direction from east to south and then west (Figure 9).

Conclusions

Subsea determination of dissolved methane concentration can be conducted by using infrared absorption

technology. The technology, measuring the partial pressure of methane in a separated gas chamber, is combined with a membrane inlet, which separates high-pressure conditions of the deep sea from the gas chamber at normal pressure. Recent advances in laser diode technology led also to cost-effective and high-sensitive infrared absorption units. The newly designed high-sensitive methane sensor (HISEM), which combines laser diode infrared absorption with membrane inlet technology, closes a gap between the needs of small and less sensitive methane sniffers used for offshore leak detection (Oil & Gas Industry) and oceanographic trace gas

determinations down to 1–2 nmol L⁻¹ of CH₄ (equilibrium concentration of seawater with the atmosphere).

Membrane-inlet IR absorption sensors can be used for long-term measurements at the seafloor (e.g., lander-based deployment). The determination of, for example, varying methane concentrations in the vicinity of a methane seep have to be combined with determination of temperature, salinity, and pressure variations, as well with current measurements (i.e., using ADCPs). This combination is the basic information used to determine (dissolved) gas fluxes from natural seeps or leaking constructions at the seafloor.

Focused release of methane from subsea seeps and of rising plumes of dissolved methane can be monitored with ROV-based IR sensor technology. However, the quantification of methane release also needs some basic oceanographic information about the local current regime and physical parameters (T, S, P) along the ROV dive tracks. This could be realized during onboard CTD measurements and an upward-looking ADCP deployed at the seafloor. A miniaturization of the recently developed high sensitive methane sensor (HISEM) is prerequisite to use this technology onboard inspection class ROVs.

Acknowledgments

The HISEM system development is funded by the German Ministry BMWi (Project No. 03SX301) within the European funding initiative MARTECH (ERA-NET, Maritime Technologies). Wintershall Noordzee is kindly acknowledged for supporting the offshore operations and ROV adaptations.

Corresponding Author:

Mark Schmidt
GEOMAR Helmholtz Centre for
Ocean Research Kiel
Wisshofstr. 1-3,
24148 Kiel, Germany
Email: mschmidt@geomar.de

References

- Campbell**, K.A., Francis, D.A., Collins, M., Gregory, M.R., Nelson, C.S., Greinert, J., & Aharon, P. 2008. Hydrocarbon seep-carbonates of a Miocene forearc (East Coast Basin), North Island, New Zealand. *Sediment Geol.* 204:83-105. <http://dx.doi.org/10.1016/j.sedgeo.2008.01.002>.
- Clark**, J.F., Leifer, I., Washburn, L., & Luyendyk, B.P. 2003. Compositional changes in natural gas bubble plumes; Observations from the Coal Oil Point marine hydrocarbon seep field. *Geo-Mar Lett.* 23:187-93. <http://dx.doi.org/10.1007/s00367-003-0137-y>.
- Clark**, J.F., Washburn, L., Hornafius, J.S., & Luyendyk, B.P. 2000. Dissolved hydrocarbon flux from natural marine seeps to the Southern California Bight. *J Geophys Res.* 105(11):509-11,522.
- Faure**, K., Greinert, J., Schneider von Deimling, J., McGinnis, D.F., Kipfer, R., & Linke, P. 2010. Methane seepage along the Hikurangi Margin of New Zealand: Geochemical and physical data from the water column, sea surface and atmosphere. *Mar Geol.* 272:170-88. <http://dx.doi.org/10.1016/j.margeo.2010.01.001>.
- Greinert**, J., Lewis, K.B., Bialas, J., Pecher, I.A., Rowden, A., Bowden, D.A., ... Linke, P. 2010. Methane seepage along the Hikurangi Margin, New Zealand: Overview of studies in 2006 and 2007 and new evidence from visual, bathymetric and hydroacoustic investigations. *Mar Geol.* 272:6-25. <http://dx.doi.org/10.1016/j.margeo.2010.01.017>.
- Judd**, A.G., & Hovland, M. 2007. *Seabed Fluid Flow: The Impact on Geology, Biology, and the Marine Environment*. New York: Cambridge Univ. Press. 475 pp. <http://dx.doi.org/10.1017/CBO9780511535918>.
- Leifer**, I., Clark, J., & Luyendyk, B. 2006. Simulation of a Subsurface Oil Spill by a Marine Hydrocarbon Seep. MMS OCS Study 2006-050. Santa Barbara, CA: Coastal Research Center, Marine Science Institute, University of California. MMS Cooperative Agreement Number 14-35-01-00-CA-31063. 81 pp.
- Leifer**, I., & Patro, R.K. 2002. The bubble mechanism for methane transport from the shallow sea bed to the surface: A review and sensitivity study. *Cont Shelf Res.* 22:2409-28. [http://dx.doi.org/10.1016/S0278-4343\(02\)00065-1](http://dx.doi.org/10.1016/S0278-4343(02)00065-1).
- Linke**, P., Sommer, S., Rovelli, L., & McGinnis, D.F. 2010. Physical limitations of dissolved methane fluxes: The role of bottom-boundary layer processes. *Mar Geol.* 272:209-22. <http://dx.doi.org/10.1016/j.margeo.2009.03.020>.
- McGinnis**, D.F., Greinert, J., Artemov, Y., Beaubien, S.E., & Wuest, A. 2006. Fate of rising methane bubbles in stratified waters: How much methane reaches the atmosphere? *J Geophys Res.* 111:C09007. <http://dx.doi.org/10.1029/2005JC003183>.
- McGinnis**, D.F., Schmidt, M., DelSontro, T., Themann, S., Rovelli, L., Reitz, A., & Linke, P. 2011. Discovery of a natural CO₂ seep in the German North Sea: Implications for shallow dissolved gas and seep detection. *J Geophys Res (Oceans).* 116:C03013. <http://dx.doi.org/10.1029/2010JC006557>.
- Naudts**, L., Greinert, J., Poort, J., Belza, J., Vangampelaere, E., Boone, D., ... De Batist, M. 2010. Active venting sites on the gas-hydrate-bearing Hikurangi Margin, Off New Zealand: Diffusive versus bubble-released methane. *Mar Geol.* 272:233-50. <http://dx.doi.org/10.1016/j.margeo.2009.08.002>.
- Pfannkuche**, O., & Linke, P. 2003. GEOMAR landers as long-term observatories. *Sea Technol.* 44(9):50-5.
- Schneider von Deimling**, J., Greinert, J., Chapman, N.R., Rabbal, W., & Linke, P. 2010. Acoustic imaging of natural gas seepage

in the North Sea: Sensing bubbles controlled by variable currents. *Limnol Oceanogr Meth.* 8:155-71. <http://dx.doi.org/10.4319/lom.2010.8.155>.

Townend, J. 1997. Subducting a sponge: minimum estimates of the fluid budget of the Hikurangi margin accretionary prism. *Geol Soc N Zeal Newsl.* 112:14-6.

Westbrook, G.K., Thatcher, K.E., Rohling, E.J., Piotrowski, A.M., Pålke, H., Osborne, A.H., ... Aquilina, A. 2009. Escape of methane gas from the seabed along the West Spitsbergen continental margin. *Geophys Res Lett.* 36:L15608. <http://dx.doi.org/10.1029/2009GL039191>.

Development of the *Jiaolong* Deep Manned Submersible

AUTHOR

Weicheng Cui
Hadal Science and Technology
Research Center,
Shanghai Ocean University,
Shanghai, China and
China Ship Scientific Research
Center, Wuxi, Jiangsu, China

Introduction

The deep seas have fascinated humans for centuries. The flow of new ideas has traveled through the centuries and inspired people to dive below the surface and explore the forms of life that exist in the abyss. A detailed historical account of human beings' deep dives into the oceans and discovery of its true mysteries can be found in, for example, Forman (2009), Kohnen (2009), and Sagalevitch (2009). Deep sea explorations are indispensable, not only for the investigation of marine creatures, microorganisms, minerals, and other resources hidden under the deep water but also for geophysical research into the structure and behavior of the earth. Deep sea exploration and exploitation are of increasing interest to people in the 21st century, and both manned and unmanned deep submergence research vehicles are necessary means for deep sea exploration (Momma, 1999; Committee on Future Needs in Deep Submergence Science [CFNDSC], 2004; Committee on Evolution of the National Oceanographic Research Fleet, 2009; Fletcher et al., 2009; Barry & Hashimoto, 2009).

Although unmanned submersibles such as autonomous underwater vehi-

ABSTRACT

Deep sea exploration and exploitation are of increasing interest to 21st century scientists, and both manned and unmanned deep submergence vehicles are necessary means for deep sea exploration. To fulfill the requirements of deep sea exploration for China Ocean Mineral Resources R&D Association (COMRA), a deep manned submersible was in the process of development in China from 2002 to 2012 and was named *Jiaolong* in 2010. The purpose of this paper is to introduce the development process from a historical point of view, including the design, realization of components, assembly, open-water tank test, and sea trials of the *Jiaolong* deep manned submersible. The technical difficulties encountered at each stage, and their solutions are briefly described. The future development trends for deep manned submersibles are pointed out.

Keywords: deep manned submersible, *Jiaolong*, development process, design, realization of components

cles (AUVs) and remotely operated vehicles (ROVs) have advantages in certain aspects, Human operated vehicles (HOVs) remain the central element in the selection of modern tools at the service of knowledge acquisition (Kohnen, 2009; CFNDSC, 2004; Rona, 2000) because the sense of vision is the most important of all the five human senses.

In the 1970s and 1980s, the U.S. manned submersible DSV *Alvin*, made a number of important discoveries in marine scientific research (<http://www.whoi.edu/>). This promoted an upsurge in the international community to develop deep manned submersibles. The first 6,000 m submersible was the U.S. Navy's *Sea Cliff*. France, the former Soviet Union and Japan then developed another four 6,000-m deep manned submersibles, namely, *Nautilie* (Jarry, 1986), *MIR I & II* (Sagalevitch, 2009), and *Shinkai 6500* (Nanba et al., 1990; Takagawa et al., 1995),

respectively. In the 1990s, Russia started to develop two more 6,000-m submersibles, *Rus* and *Consul*, that were to be fully built in country. Due to lack of funding, the sea trials of these two submersibles were not completed until 2011, and both are now in service of the Russian Navy (<http://www.rusnavy.com/news/>).

The first proposal to develop a 6,000-m deep manned submersible in China was submitted by the China Ship Scientific Research Center (CSSRC) to the then State Commission of Science and Technology (now the Ministry of Science and Technology) in 1992. Because the public demand for deep manned submersibles was not urgent and the technical risk was high, the proposal was not approved.

In 1999, the China Ocean Mineral Resources R&D Association (COMRA) submitted a new proposal for a deep manned submersible, substantiating a pressing need for such technology

to fulfill their duties. This renewed proposal was approved by the Ministry of Science and Technology of the Chinese Government and marked the beginning of the deep manned submersible project now named *Jiaolong*. COMRA was appointed as the project coordinator and final owner of this submersible. The development formally began in June 2002, and on June 30, 2012, the *Jiaolong* successfully completed the final dive of its sea trials program.

The purpose of this paper is to examine the development process from a historical point of view, including design, realization of components, assembly, open-water tank test and sea trials of the *Jiaolong* deep manned submersible. The paper will be divided into four sections. After the first introduction section, the entire development process of the submersible is described in Development Process of the Deep Manned Submersible *Jiaolong*. This process includes the three stages of design, realization of components and assembly, as well as open-water tank test and sea trials. The technical difficulties encountered at each stage and their respective solutions are also briefly described. Latest Technical Specifications of the *Jiaolong* are listed and Future Development Trends for Deep Manned Submersibles are briefly discussed in section 3. The last Section is a summary, and some conclusions from the development process have been drawn.

Development Process of the Deep Manned Submersible *Jiaolong* Design

The main purpose of the project is to develop a usable submersible, which is of comparative performance with

existing submersibles, so the technical innovations and the application of the latest immature technologies were not the emphasis of the project. Our design team began its formal design work in June 2002. According to the requirements of the quality control manual of CSSRC, the design was divided into three phases: preliminary design, technical design, and detailed design.

Having made an in-depth summary of the missions and the overall technical indicators specified in the contract, the following five essential key performance factors were proposed:

- (1) the ability to reach a depth of 7,000 m;
- (2) good maneuverability;
- (3) the capability of real-time communication and microtopography detection;
- (4) the capability to sample in a hovering state at a designated position; and
- (5) safety and reliability.

After developing the five key performance factors, a list of technical challenges was identified for the research and production of the *Jiaolong* submersible. This resulted in a selection of key techniques for each of the performance requirements. The chief designer then divided the vehicle into 12 subsystems according to the requirements of the overall technical indicators and characteristics of the participating research units and personnel. The 12 subsystems were (1) the overall performance and general arrangement; (2) structure system; (3) outfitting; (4) ballast and trim adjustment system; (5) propulsion system; (6) electric power and distribution system; (7) lighting, video, and VHF communication system; (8) control system; (9) acoustic system; (10) hydraulic and operation system; (11) life support system;

(12) underwater emergency jettison system. The principal challenge for such a division is the handling of interface relations among numerous subsystems. The interface relations between any two subsystems should not be repeated or omitted, and this cannot be guaranteed simply by the chief designer's experience. Therefore, a four-element method was developed to solve this problem (Cui et al., 2008a, 2008b). All the parameters of each subsystem were divided into four categories: input, output, support, and restraint. The designers were asked to draw a four-element diagram for each subsystem to check the consistency (shown in Figure 1). This allowed us to successfully handle and reconcile the interface relationship among all 12 subsystems in an orderly and systematic process, thus solving the first and most fundamental problem for the development of the manned submersible.

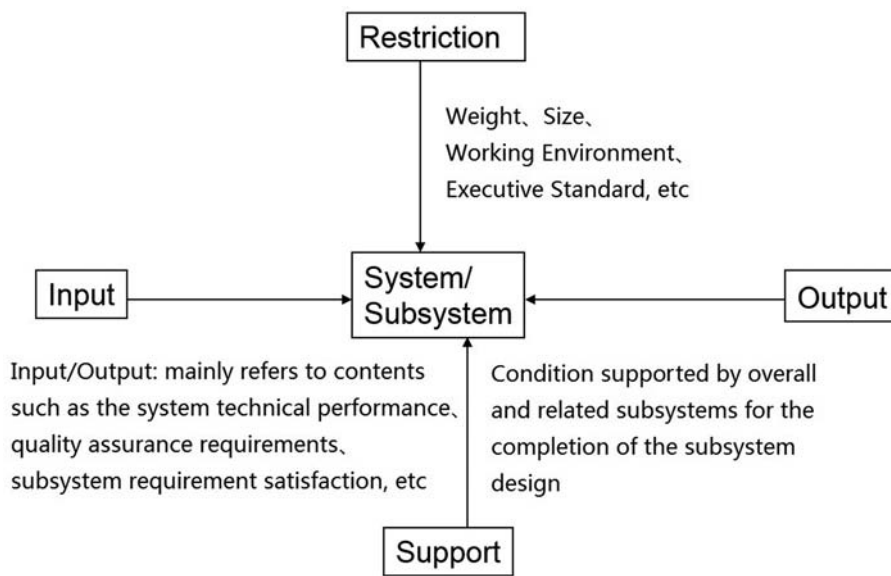
The preliminary design was a significant challenge for the design team, since nobody had any personal experience with a real deep manned submersible. The components selection, how to arrange them to form a coordinated and functional vehicle, and the weight and displacement of each component were all unknown.

Almost all the important pieces of equipment for the *Jiaolong* ended up being custom parts, which needed to be developed specifically for us by the producers. Through communication and discussion with the relevant producers, the performance, weight, and volume of each piece of equipment gradually became clear.

In order to make each subsystem work effectively and form a complete entity, able to complete its missions and tasks, the general arrangement of the manned submersible was developed with a modularized structure

FIGURE 1

The four-element diagram of the system/subsystem.



and function as a guideline. The key point of the design process was to ensure the reliability and maintainability of the submersible.

On February 26–27, 2003, the “Preliminary Design of the *Jiaolong* Manned Submersible” was submitted to an experts’ review organized by the State Oceanic Administration, and the project entered into the phase of technical design. The research and design at this stage were focused on feasibility, reliability, and maintainability considerations. A mature design state was reached, in which the main technical indicators of the submersible were fixed, through modeling and prototype testing.

Designing the manned cabin was technically difficult because it was directly related to the safety of the crew. If the design was too conservative, the submersible would be very heavy, undermining its maneuverability and increasing the operational cost. To find a safe balance, a series of problems needed to be solved, such as calculating the stress concentration

factors at openings, analyzing the ultimate strength, choosing the appropriate safety factors, determining the fatigue load spectrum, and analyzing the fatigue life.

Due to time constraints, the team chose to follow the rules of the China Classification Society (CCS, 1996) and the Russian Maritime Register of Shipping (RS, 2004). Our objective was to concurrently meet the two sets of rules. In addition, the finite element method was used to analyze and calculate the ultimate strength of the manned cabin (Lu et al., 2004). Specific attention was paid to stress concentrations near large openings, such as personnel access hatches, observation windows, and penetrators. The use of the finite element method with contact elements to analyze this problem was particularly helpful (Li & Cui, 2004).

The fatigue design load spectrum was first proposed through a statistical analysis of the *Alvin* manned submersible’s historical dive data (Li et al., 2004). Based on this, we analyzed the fatigue life of the stress-concentrated

areas of the manned cabin, using the simple analysis method of fatigue life according to CCS rules (Li et al., 2006). This then provided the main structural parameters of the manned cabin. Next, a Russian company was contracted to produce the manned cabin using the “melon petals welding into a semi-sphere” method. After that, a pressure test was carried out in Russia. The pressure vessel was instrumented with strain gauges, and measured stress values were found to be in good agreement with the finite element analysis results. Based on this test data, we determined that our design was reasonable, the manufacturing quality was guaranteed, and the ultimate strength and fatigue life of the manned cabin of the *Jiaolong* was ensured.

However, we clearly knew that only a small number of manned submersibles had been produced in the world, and most of them had been developed by the navy and not classified by classification societies. Therefore, strictly speaking, the design standards and safety assessment standards of any classification society lacked practical experience. Thus, the rationality and scientific foundation of the design standards needed to be investigated.

In the development of the *Jiaolong* submersible, 40% of the equipment was procured from international companies. In order to expand deep sea technology development in China, a new project to construct a domestically produced 4,500 m manned submersible was started in 2009. The main objectives of this project were to reduce the operational cost and to further increase the reliability, in addition to the technology development.

This compelled the team to compare the design standards of all major classification societies; they found that

the strength requirements of these design standards varied widely. In fact it was noted that most existing deep manned submersibles could not meet the requirements of the published standards, see Table 1 and Table 2 (Pan & Cui, 2011a, 2011b). Considering that all these submersibles operated safely in the past years, most classification societies' standards can be considered overly conservative for hadal depth designs.

Hence, we reviewed the analysis method of the buckling and ultimate strength of spherical pressure hull under external pressure (Pan & Cui, 2010), unified the description methods of the initial defects, made a series of calculations about all the parameters affecting the ultimate strength of the manned cabin within the range of possible variations by finite element analyses, and, finally, proposed a more rational ultimate strength formula (Pan et al., 2010). By absorbing

TABLE 2

Check of actual designs of existing pressure hulls to the existing design rules.

Submersible	Alvin	Consul (Rus)	Nautile ^a	Shinkai 6500	New Alvin	Jiaolong
DNV1988	X	X	X	X	X	X
BV1989	X	X	X	X	X	X
LR1989	X	X	X	X	X	X
RS2004	X	√	√	√	X	X
CCS1996	X	√	√	X	X	X
ABS2009	X	X	X	X	X	X
GL2009	X	X	X	X	X	X

^aNote: Due to the lack of detailed material data for each submersible, the average material properties for Titanium TA6V4 have been employed in the calculations made in Table 1. Dr. Jean-Francois Drogou from IFREMER pointed out in the review process that, for Nautile, the TA6V4 alloy is forged in beta phase that gives a resistance $R_{e0.2}$ of more than 950 MPa and the design of Nautile hull satisfied with the ABS requirements.

the U.S. Navy's requirements for the control methods of macro stress levels and stress concentration (NSSC, 1998), a set of complete design standards for a manned cabin was proposed (Pan & Cui, 2011a, 2011b). These were adopted by CCS and writ-

ten into their "Principles of Check of Drawing and Inspection of Deep-Sea Manned Submersible" (CCS, 2011) as the classification standard for the *Jiaolong*. The new design standard of the manned cabin is as follows (Pan & Cui, 2011a, 2011b).

TABLE 1

Calculation results of existing titanium pressure hulls.

Actual Design of Existing Pressure Hull						
Submersible	Alvin	Consul (Rus)	Nautile	ShinKai 6500	New Alvin	Jiaolong
Depth (m)	4,500	6,000	6,000	6,500	6,500	7,000
Operating pressure from GL2009 (MPa)	45.45	60.6	60.6	65.65	65.65	70.7
Internal diameter (m)	2.0	2.1	2.1	2.0	2.1	2.1
Design thickness (mm)	49	71	62–73	75	71–72	76–78
Safety factor	1.5	1.5	1.5	1.55	1.5	1.5
Minimum proof thickness calculated by design rules (mm)						
DNV1988	59.7	78.2	78.2	79.5	83.5	88.7
BV1989	62.6	86.9	86.9	90.4	94.9	103.0
LR1989	75.6	99.0	99.0	101.0	106.1	113.4
CCS1996	51.5	72.7	72.7	77.8	78.9	85.2
RS2004	51.1	68.9	68.9	72.7	74.0	79.2
GL2009	59.4	83.2	83.2	86.1	90.2	97.8
ABS2010	72.0	97.6	97.6	103.3	105.1	112.9

The ultimate strength of the titanium alloy spherical pressure hull of deep manned submersible is calculated by the following equations:

$$P_u = \left(1 - k \frac{\Delta}{R}\right) \left(\frac{\sigma_u t}{R} + \frac{\sigma_u t}{R_m}\right) \quad (1)$$

$$k = a + b \times \exp\left(-c \left(\frac{\Delta}{R}\right) - d \left(\frac{t}{R}\right) + e \left(\frac{\Delta}{R}\right)^2 + f \left(\frac{t}{R}\right)^2 - g \left(\frac{\Delta}{R}\right)^3 - h \left(\frac{t}{R}\right)^3\right) \quad (2)$$

where $a = -15.63$; $b = 606.6$; $c = 264.6$; $d = 72.72$;
 $e = 3 \times 10^4$; $f = 882.5$; $g = 1.2 \times 10^6$; $h = 3969$;

σ_u = the guaranteed minimum tensile strength of titanium alloy used;

t = thickness of the pressure hull;

R = internal radius of the spherical pressure hull;

R_m = mean radius of the hull.

Δ = the deviation between actual spherical surface and regular spherical surface.

The application range of this empirical equation is $0.025 \leq t/R \leq 0.08$ and $\Delta/R \leq 0.01$. The safety factor for this equation is 1.5.

Besides the above ultimate strength formulae, additional stress limitations that control the overall stress level and local stress concentrations need to be considered in the makeup of a safety standard. The stress limitations are suggested to be as follows:

- The average shell membrane stress at maximum operating pressure shall be limited to two thirds of the minimum specified yield strength of the material.
- The highest combined value of average shell membrane stress and bending stress (excluding effects of local stress concentrations) at maximum operating pressure shall be limited to 3/4 of the minimum specified yield strength of the material.
- The maximum compressive peak stress at any point in the hull, including effects of local stress concentrations, shall be limited to 4/3 of the minimum specified tensile yield strength and shall not exceed the compressive ultimate strength of the material. The maximum tensile peak stress at any point in the hull, including effects of local stress concentrations, shall be limited to the minimum specified yield strength of the material.
- Currently, there is no condition to set a reliable standard for fatigue strength assessment. It is recommended that designers and users of the submersible should pay attention to this issue and carry out the fatigue analysis at all stress concentration areas using the commonly accepted approaches.

This newly established safety standard was used to optimize the structural design of the 4,500 m manned cabin (Pan & Cui, 2012).

To solve the problem of a comprehensive optimized design for *Jiaolong's* hydrodynamic layout and lines, we systematically collected a comprehensive amount of relevant data of all the submersibles in the world, analyzed their characteristics of shape and hydrodynamic performance, proposed assessment indicators of the submersible's maneuverability, established theoretical and experimental forecasting methods for its hydrodynamic performance (including speed and maneuverability), clarified the main design variables of the manned submersible's

hydrodynamic performance, determined the properties of judging its comprehensive hydrodynamic performance, and provided an optimized design method for the manned submersible's hydrodynamic performance under constraints. When studying the spatial hydrodynamic characteristics of a deep manned submersible in a complex nonlinear deep sea environment, the submersible's hydrodynamic characteristic of a 6 degree-of-freedom motion was obtained. An equation of a 6 degree-of-freedom spatial motion was derived, the corresponding hydrodynamic coefficients were determined from wind tunnel tests, rotating arm basin tests, towing tank model tests, and a mathematical model was established, which can be used to forecast and analyze the submersible's maneuverability (Ma & Cui, 2004, 2005, 2006a, 2006b; Cui & Ma, 2009; Pan et al., 2010).

The ballast and trim regulating system consists of a variable ballast system with a flow rate of up to 3 L/min, one ballast tank with displacement of up to 1,500 kg and a set of trim regulating systems with a flow rate of up to 15 L/min. The variable ballast system consisted of a titanium sphere 840 mm in diameter, a hydraulically operated super-pressure pump, driven by an 8-kW DC motor, oil-immersed solenoid valve, pressure balance valve, etc. Commercial companies were commissioned to produce a super-pressure pump and DC motor. The trim regulating system mainly consisted of tanks located at the bow and aft, an oil control box (containing oil pump, oil motor and valves) and a piping system. The trim regulating system's power came from the submersible's hydraulic source; the oil motor used the power of the hydraulic source to drive the low-pressure oil pump to provide

low-pressure oil of 1.5 MPa, which pumped the mercury back and forth between the bow and aft, thereby adjusting the trim angle.

The propulsion system was composed of four main ducted propellers at the stern, two rotatable ducted propellers midship, and one tunnel propeller at the bow. According to the contract, the submersible had to have a maximum speed of up to 2.5 km and a cruising speed up to 1 km.

The electrical power and distribution system supplied electrical power to the whole submersible. Thus, it should have the following functions: providing 110 V DC to the thruster motors, hydraulic source motor, and various lights outside the submersible; providing 24 V DC to underwater acoustic equipment, motion control system, sensors and instruments in the cabin, etc.; having the ability to supply sufficient power for the whole submersible according to the requirements of the power consumption of all the equipment and time history of typical missions; offering a distribution switch and protection for the main power supply circuit. According to the requirements of the sub-contract's technical specifications, the electrical power and distribution system needed to equip a set of oil-immersed silver-zinc batteries and a set of corresponding distribution systems.

Based on the statistics of the load diagram, the load of the main battery was 86.7 kwh; that of the secondary battery was 24.2 kwh; thus, the total output capacity of the main and secondary batteries should be not less than 110.9 kwh. The emergency battery is used if both the main and secondary batteries fail and mainly provides power to emergency lighting, the underwater acoustic phone, and

the life support system. In addition, when the submersible is floating at the surface, the spare battery provides a VHF radio transmitter and strobe lights. The emergency battery electric capacity is 5.4 kwh.

Lighting and video equipment serve to provide a source of underwater lighting for operators and observers when sailing, operating and observing. Video equipment serves to photograph underwater targets and then stores the videos and photos. The main role of the VHF communication system is to offer radio voice communication on the surface. Originally, the *Jiaolong* was equipped with one 3CCD color video camera, two 1CCD color video cameras, one black-and-white low-light level video camera, one underwater camera, two HMI lamps, two HID lamps, four quartz halogen lamps, one pan and tilt, and one set of video cameras in the cabin. After the 3000-m-depth class sea trials, the lighting and camera systems were upgraded. The *Jiaolong* is now equipped with 10 LED lamps, 4 HMI lamps, 2 HID lamps, 1 quartz halogen lamp, 2 HD video cameras, 2 1CCD video cameras, 1 camera, 1 black-and-white low-light level camera, 2 pan and tilts, 1 HD video recording system, and 1 video camera in the cabin.

The hydraulic system is the *Jiaolong's* most important source of auxiliary power, since it supplies hydraulic power for buoyancy adjustment, trim adjustment, and underwater sampling. The hydraulic system has rate of pressure up to 21 MPa, rate of flow up to 25 L/min, and a maximum input power up to 10 kW.

The *Jiaolong's* design requirements also included the function of a sampling system, to accomplish a series of tasks relying on the power from the hydraulic system. The sampling

system included two hydraulic manipulator arms, a hydrothermal sampler to keep high-pressure liquid, a sediment sampler, underwater drilling equipment, and a sampling basket.

The main function of the control system is to collect information from sensors on the submersible, display and record the data and then control the implementation mechanisms. This makes the submersible competent to cruise, observe, and perform tasks.

The acoustic system is mainly composed of an underwater acoustic communicator, high-resolution side-scan sonar, acoustic Doppler speedometer, obstacle avoidance sonar, imaging sonar and long-distance ultra-short baseline positioning sonar. Installed on both sides of the submersible, the high-resolution side-scan sonar is used to measure the seabed's micro-topography and targets in the water or on the seabed and draw real-time three-dimensional maps of the scene. The mechanical scanning imaging sonar is located at the bow of the submersible and serves to detect the surrounding environment and forward targets in the water for the pilot's observation. On one hand, it helps the pilot to search for targets; on the other hand, it prevents the submersible from running into obstacles, thus ensuring its safety.

Seven anticollision sonars are installed at the bow and on both sides of the submersible. They are able to measure the distances between the submersible and obstacles in six directions, helping the pilot to avoid obstacles to ensure safety. They also measure the distance from the submersible to the seabed to control the submersible.

The *Jiaolong* is equipped with a transponder at its top; thus, it can be positioned by the long-distance

ultra-short baseline positioning sonar installed on the mother ship. Further, the combination of this and the GPS is able to provide the absolute position of the submersible. In addition, a long baseline system was added after the 3000-m-depth sea trial.

The life support system provides oxygen (O₂) in three ways: normal operation, emergency operation and oxygen masks. Each oxygen subsystem is independent of the others in order to ensure the system's reliability. There is one set of normal life support systems providing O₂ for 12 h, one set of emergency life support systems providing O₂ for 60 h, and one set of mask breathing systems provide O₂ for 12 h. These systems use high-pressure oxygen cylinders to produce oxygen and high-efficiency lithium hydroxide to absorb carbon dioxide.

The *Jiaolong* is China's first deep manned submersible. Consequently, during the period of sea trials, China did not have a rescue capability. Therefore, safety was the most important concern for the *Jiaolong* at that time. In the design phase, we proposed "able to dive downward, able to come back" as the design principle. The overall guiding philosophy was that the *Jiaolong* should be fitted with all the existing emergency means of existing manned submersibles. In addition, we would ensure that the emergency jettison system was sufficiently reliable through numerous prototype evaluations and sea trials. Having learnt from the successful experience of existing manned submersibles, the following self-rescue measures were implemented based on the idea of a "redundant design":

(1) A ballast jettisoning mechanism: the maximum weight of the solid ballast is 1.3 tons. As long as it jettisons all of them, the submersible

will certainly become positively buoyant and thus can go upward. The emergency jettison system was designed to be able to drop ballasts using two independent mechanisms, one electromagnetic and the other hydraulic. Ballasts can be jettisoned by a single action. What is more, as soon as a power failure starts, the ballast will be automatically discarded.

- (2) A main battery box jettisoning mechanism: in a situation in which solid ballasts cannot be discarded, the main battery box that weighs 1.2 tons will be discarded so that the submersible can become positively buoyant. This function is realized through the use of two electrical-explosive bolts (one of them offers redundancy) with a series connection. As long as one of them works, the main battery box can be dropped.
- (3) A mercury jettisoning mechanism: all the mercury weighs 480 kg and can easily be jettisoned. However, jettisoned mercury will pollute the environment; therefore, this is not encouraged unless in an emergency. In many cases, even if everything else cannot be jettisoned, jettisoning the mercury will be able to provide sufficient buoyancy to make the submersible go upward.
- (4) A mechanism used to jettison the hydraulic manipulator arms: if the manipulators are bound, they can be completely released.
- (5) A ballast tank system: when the submersible goes up to only 10 meters below the sea surface, the pilot should start the ballast tank system to drain off water. This is capable of providing 1.5 tons of buoyancy, ensuring that the *Jiaolong* has a relatively large freeboard on the water.

- (6) A rescue buoy: if the submersible is trapped on the seabed, the rescue buoy will be released by detonating electrical-explosive bolts. The strobe light on the buoy will lead the mother ship to find this buoy, and then mother ship can catch the buoy and drag the submersible up by a cable, as long as 9,000 m, linking the submersible and the buoy.
- (7) A mechanism used to jettison the sampling basket: The sampling basket is also connected with the submersible by an electrical-explosive bolt, so that if it is bound, it can be jettisoned.

On the basis of the general arrangement drawings of the preliminary design, a 1:1 model was made to test and confirm the maintainability and rationality of the general arrangements. The final configuration of the *Jiaolong's* general architecture and the preliminary determination of its hydrodynamic performances were firmed up through repeated attempts and modifications.

On August 29–30, 2003, the "7000 m Manned Submersible's Technical Design" was submitted to the expert review organized by the State Oceanic Administration and received positive confirmation.

The detailed design phase involved mainly the generation of construction drawings on the basis of the technical design, establishing a reliable supply channel of each piece of equipment and doing model tests for critical pieces. In this phase, the team also established a joint debugging test process and implementation method, technical principles of assembly and an overall testing process.

On April 13–14, 2004, the "Detailed Design of the 7000 m Manned Submersible" was submitted to the expert review set by the State

Oceanic Administration and received acceptance.

Realization of Components

It was very difficult for China to produce some of the equipment for the *Jiaolong*. The project team also knew that the manned cabin could not be produced in-country. However, Russia had developed two manned submersibles (*Rus* and *Consul*) and produced three titanium alloy manned cabins, and the Russians were willing to produce one for China. Thus, a Russian institution was commissioned to produce the *Jiaolong's* manned cabin, and the pressure acceptance test was done at the Krylov Shipbuilding Research Institute. On January 29, 2003, COMRA signed a contract with the Russian Krylov Institute to produce a 7,000-m manned submersible's titanium alloy structure.

The buoyancy foam was originally planned to be procured from Russia but its specific weight was around 0.65. This would have brought the submersible's total weight up to 25 tons, which exceeded the technically allowed limit of 22 tons. Later, an American company, Emerson & Cuming, Inc., was willing to supply buoyancy material, DS32, with a specific gravity of 0.525. A contract was signed and sent to the U.S. government for approval. The U.S. government agreed but added restrictions on the DS32 foam and only authorizing Emerson to provide its DS35 foam, a type of buoyancy material with a specific gravity of 0.561.

Contracts for other imported equipment were signed with foreign firms, in most cases, following the technical design. The imported equipment reached Shanghai Customs in succession from March 2005 until November 2005. However, since

China's exemption policy was not clear, the customs formalities for our imported equipment were not completed until September 2006. On September 25, 2006, the last piece of imported equipment reached CSSRC from Shanghai Customs, and a pressure acceptance test was done on each piece of pressurized equipment.

Assembly

Domestically produced equipment arrived in steady succession from the end of 2004. The submersible's titanium alloy frame was made in Russia but was not delivered until November 2005. Therefore, a temporary steel frame was produced locally based on the detailed design drawings for the trial installation at the end of 2004 in order to shorten the installation time. In September 2006, when all the equipment and components, imported or domestically produced, had reached CSSRC, we started the general assembly of the submersible's hull, bracket, equipment, outfitting, piping, cable, etc., into a complete submersible, in order to experiment a complete integration on a 1:1 steel frame and made preliminary interfaces debugging tests.

After receiving the submersible's final titanium frame at the final assembly site, we first measured the frame's geometric dimensions and then determined the reference position of the installation. A laser was used during the installation process to monitor any changes in the reference position.

Unfortunately, the Russian-made titanium frame's mounting dimensions were beyond the permissible tolerance, causing significant problems with the installation of brackets for light shells and equipment brackets. Because these brackets were made on the basis of the drawings and thus

matched the steel frame, they did not match the titanium frame. Hence, the interface between the brackets and titanium frame needed to be repeatedly modified. What is more, oxygen cutting cannot be used for the titanium alloy and this resulted in a tremendous amount of sanding work. This was not estimated beforehand, and thus, it delayed the schedule of the final assembly.

When installing brackets welded to the frame, we first drew hanging lines or, if necessary, made installation templates. The parts were then sanded to make them match each other, weighed, and then spot welded. Relevant work fixtures were installed to ensure an accurate installation and reduce welding distortion. Later, we inspected the assembly, and if it passed, we finally welded it for a further inspection.

Firstly, 37 pieces of buoyancy blocks were installed externally in the 10 sections of the titanium frame; 43 pieces of buoyancy blocks were installed internally (including 13 pieces at the head); and then 161 brackets which connected the buoyancy blocks and titanium frame were welded or bolted to the titanium frame and bolted to the buoyancy blocks. It should be noted that, when installing the buoyancy blocks on the titanium frame, we had to ensure a fair shape of the submersible.

Since the distortion tolerance of the welded titanium frame was far more than that of the machined buoyancy blocks, the thickness of each correction gasket had to be modified several times during the installation; this was extremely cumbersome and heavy work.

If the installation of the buoyancy blocks contradicted the arrangement of the frame or interfered with

equipment or cables, modified lines would be drawn on the buoyancy blocks and they would be modified by hand. All these buoyancy blocks had to be hand modified on site until they dimensionally fitted the frame and other interfaces representing a lot of added assembly work had to be done on the site.

Having installed the external buoyancy blocks and adapted them to the required positions, welders welded the blocks' brackets to the frame. The welding distortion of the external buoyancy blocks had to be considered carefully, otherwise the bolts on the external buoyancy blocks could not be screwed into the nuts on the brackets. Our welders attempted to resolve this problem again and again, and then decided to control the welding distortion by reducing the welding current and discontinuously welding on both sides.

The acoustic equipment such as the bathymetric side-scan sonar, Doppler speedometer and motion sensors required very high installation accuracy, and trial and error methods with special tools were used to meet the accuracy requirement.

The onshore combined debugging was carried out after the final assembly. The main purpose of the onshore combined debugging was to ensure our work could enter the next phase, the open-water tank test, by checking whether the interfaces between the equipment and subsystems were accurate, whether their communications were right, and whether they were able to perform their required functions. The onshore combined debugging was a bridge between the final assembly and the open-water tank test; it marked a step forward from equipment to system. The following aspects were the focus of the onshore combined debugging:

- (1) We confirmed that connections were correct and reliable by repeatedly checking the cable connections among the equipment.
- (2) The onshore debugging check. All the electrical circuits and signal transmission paths were checked with battery power.
- (3) The results of onshore debugging were determined by the complete operating equipment checkpoints. The final assembly and onshore combined debugging tests altogether took 1 year and lead to the open-water tank test phase that followed.

Open-Water Tank Test

CSSRC has an open-water tank shaped like a circular basin, with a diameter of 85 m and a maximum depth of 15 m, which is equipped with an indoor dock. This dock is 30 m × 8 m × 8 m and has a 30-ton bridge crane (shown in Figure 2). Thanks to this facility, we could add an open-water

FIGURE 2

Open-water tank (a) and corresponding dock (b).



tank test to *Jiaolong's* Technical Test Plan process to identify problems in water and solve them, before going to sea trials.

The open-water tank test included (1) underwater system verification, (2) checking the operation and integration performances of each subsystem and their required functions, (3) confirming the practicability of the designed work procedure of each mission, (4) examining the accuracy and reliability of the exchange of information flow and control flow, and (5) accumulating the relevant data.

The main tasks of the open-water tank test completed include the following:

1. measuring the submersible's weight and center of gravity;
2. determining drainage volume and coordination of the center of buoyancy by a balancing test;
3. determining the mooring propulsive force and the relationship between the rotation rates of each propeller;
4. evaluating the submersible's ability to regulate the trim angle, accumulating experience by rehearsing according to "Operating Rules of Each Post of Sea Trials (draft)" and the rules of implementation compiled for each dive in a sea trial;
5. debugging the control performance of a 6 degree-of-freedom motion of the submersible and submersible's comprehensive performance of landing on the seabed;
6. debugging the submersible's automatic control function;
7. simulating the task of sampling;
8. debugging the interfaces between the submersible and tools; and
9. debugging the comprehensive operational capability of the submersible.

The open-water tank test lasted for 110 days, from October 3, 2007 to

January 20, 2008. Underwater tests were performed 53 times during this period, and 18 staff members entered the manned cabin. A series of malfunctions were discovered during these tests, such as the malfunctions of the propellers, trim pump, high-pressure air relief valve, anti-collision sonar, hydraulic source, and seawater valves, as well as the rupture of the compensation film of the main and secondary battery boxes. These were all detected and corrected on site.

Another task of the open-water tank test was to train the pilots and operational team for the sea trials. Several staff members participated in the training program and dove the *Jiaolong* during the tank tests. This included Mr. Cong Ye, who was the chief designer of the general arrangements of *Jiaolong*. He was also a member of the team that participated in a Sino-U.S. joint deep diving voyage, and he was the only member who obtained two chances to dive with *Alvin*. He was consequently selected to be the chief pilot of the *Jiaolong* in the sea trials. At the same time, the two future professional pilots, Mr. Wentao Fu and Mr. Jialing Tang, continued their training and would be given as many operational chances as possible.

On January 17, 2008, an expert panel organized by COMRA came to CSSRC to test the *Jiaolong*. The test program consisted of a wide variety of functional tests which included (1) displacing water from ballast tank, (2) executing the automatic directional navigation, (3) sample hovering at a designated position, (4) operating the life support system, and (5) jettisoning the solid ballast. The results of this test sequence demonstrated to the satisfaction of the expert panel that the submersible's functions and performance met

the relevant requirements. Two months later, on March 2, 2008, in Wuxi, the State Oceanic Administration held a Pre-Delivery Inspection and Confirmation meeting. It was concluded that the submersible had met all the technical qualifications required by the sea trials' outline and that the *Jiaolong* was ready for ocean sea trials. More detailed introduction about open-water tank tests can be found in Hu et al. (2008) and Cui et al. (2009).

Sea Trials

The sea trials were the final phase of the *Jiaolong*'s development but also represented the greatest risk. Success or failure of the entire project depended on the results of these tests. The purpose of the sea trials was to comprehensively examine the technical performance, operation efficiency, safety and reliability of the completed submersible, to determine whether its performance met all contract requirements, design files and relevant norms, to ultimately decide if it could be delivered, accepted and declared in operational activity.

The *Jiaolong*'s sea trial was a complex system engineering process, which not only concerned the submersible itself and the technical state of the surface support system but also involved preparation of the sea area for the trial, organizing the testing personnel, preparing the relevant vessels, preparing a contingency plan for the sea trial, and many logistics factors. Our project team began to do the relevant preparation work in 2005, including drawing up sea trial files, purchasing spare parts, refitting the mother ship, selecting and preliminarily training pilots and operators, and selecting the appropriate sea areas for the trial. At the end of 2007, an outline of the sea trial was approved by the

State Oceanic Administration, and the organization of the sea trial was formally established.

The supporting ship was clearly identified as a very important element for the sea trials test as well as for all future utilization. However, due to restricted project funding, it was impossible to develop a specific mother-ship for *Jiaolong* in a parallel effort, so a temporary ship had to be selected and refitted for the sea trials test. After various efforts, an older oceanographic survey ship, the *Xiangyanghong-09*, was chosen (Figure 3). A series of modifications and updates were necessary such as adding an A frame at the stern and modernization of the living quarters. In the aft deck, a special platform was constructed for the storage and maintenance of the submersible.

The main technical characteristics of the ship are given below.

Length overall:	112.05 m
Breadth moulded:	15.2 m
Draft:	5.5 m
Displacement:	4,435 tons
Endurance:	60 days
Cruising speed:	12 km, maximum speed: 15 km
Deck equipment:	6,000 m electrical winch for geology, 2,000 m hydraulic winch for acoustic communication.
Scientific investigation equipment:	Sub-bottom profiler, Acoustic Doppler

FIGURE 3

Xiangyanghong-09 and its main facilities.



Current Profiler (ADCP), Conductivity, Temperature, and Depth (CTD), Ultra-short Baseline (USBL)

Laboratories: e.g., dry lab, wet lab, biology lab, submergence control center, network center

Total space for crew aboard the ship: 96, including 45 ship operators, 2 medical staff and a maximum of 49 for the test team.

Figure 3 shows a picture of *Xiangyanghong-09* and its main facilities. The main challenge for the test team was the ship's lack of a dynamic positioning system (DPS). All station-keeping had to rely on the ship master's expertise to maintain safe operating distances between the supporting ship and the submersible. Close tracking of the submersible's position was critical in order to maintain reliable acoustic communication during test dives. Otherwise, we would lose sight of the submersible after surfacing at the end of a dive.

The 1,000-m-level sea trials were formally started in 2009, and this proved the most difficult time in all the sea trials. Firstly, the season was not appropriate as it was typhoon season in the South China Sea. Secondly, problems due to the lack of experience, improper design and assembly errors occurred in almost every dive and this continuously accrued the perception of project risk. Thirdly, overall support for the project was precarious and the team understood that there was no route of retreat. If this initial sea trial phase failed, the whole project would be canceled. Consequently, the only option was to solve these problems on site and complete the necessary sea trial objectives. A brief summary for all the test dives of *Jiaolong* submersible is given in Table 3.

In the 1,000-m class tests, the most challenging technical problem was the communication system. Both the sur-

face VHF and underwater acoustic communication systems did not work. The second problem was caused by having to use expired silver-zinc batteries due to funding problems. The batteries failed in most of the dives and this added a significant maintenance work load on the crew. Another major problem encountered during the 300-m sea trial was the leakage of watertight cables and connectors. Through the joint efforts of the test team, we successfully finished the 1,000-m class test and a new Chinese record of 1,109 m was achieved.

With this hard won initial sea trials success, the ministry of science and technology approved the follow-on project of "Improvement of Jiaolong Manned Submersible's Key Techniques and Research of 3,000-m-Level Sea Trial." The new project was aimed at completely and comprehensively resolving the problems revealed in the 1,000-level sea trial, including the sitting on bottom ability, convenience and reliability of the grounding detection system, reliability of the hydraulic system, contacts between the stabilizers and the seabed, reliability of the video system, reliability of the control system, and the reliability of the acoustic system.

From May 31 to July 18, 2010, the *Jiaolong's* 3,000-m-level sea trial was performed in the South China Sea, in which the *Jiaolong* made 17 dives and the maximum dive depth of 3,759 m was reached.

All required test missions were successfully completed in this sea trial, and the results even exceeded our expectations, especially since the submersible had run without any anomaly in the last two dives. The ministry of science and technology saw a great possibility of success from this sea trial, and the research project was opened to the media

and the public. More detailed information on the first two phases of sea trials can be found in Liu et al. (2010) and Cui et al. (2010).

After the success of the 3,000-m-level sea trial, the ministry of science and technology directly approved the "Technical Improvement of the *Jiaolong* Manned Submersible and 5,000–7,000 m Sea Trials." This contract required that all improvements, the 5,000–7,000 m sea trial and the full classification work of the *Jiaolong* should be done within 2 years. Classification work had not been included in the initial contract for the development. Before the 5,000-m-level sea trial, some comprehensive technical improvements were made in five aspects, including (1) the upgrade of the video system, (2) the improvement of the operation system, (3) grounding detection system, (4) positioning system and (5) acoustic system. These improvements were all focused to enhance the *Jiaolong's* safety and capacity for work.

China's contracted sea area of polymetallic nodules was deliberately chosen as the test site for the 5,000-m-level sea trials. This would simultaneously conduct an investigation into the natural resources and do scientific research in this area, as required of COMRA by the International Seabed Authority. This sea trial was done from July 1 to August 18, 2011. Since the test area was far away from China, the working time was just 2 weeks, because the travel time was almost one month. The weather conditions remained terrible throughout the entire sea trials. We were only able to make five dives with depths of 4,027 m, 5,057 m, 5,188 m, 5,184 m, and 5,180 m, respectively. Apart from the first dive, each of the other four dives successfully landed the submersible on the seabed several times and all systems functioned well.

TABLE 3Dive log of *Jiaolong* sea trials.

Dive No.	Date	Test Site	Depth (m)	Brief Description
1	2009.8.3	Dock 1	2.4	Carried out the launch and recovery exercise with no persons in the cabin.
2	2009.8.3	Dock 1	2.4	Carried out the launch and recovery exercise with persons in the cabin. Carried out the ground detection.
3	2009.8.4	Dock 1	2.4	Finished the launch and recovery test and the grounding detection.
4	2009.8.15	Dock 2	2.4	Finished the launch and recovery test and the check of submersible functions; Finished the grounding detection.
5	2009.8.15	Dock 2	2.4	Finished the launch and recovery test. Debugging the VHF system and acoustic communication system.
6	2009.8.16	A1	2.4	Finished the VHF communication test but the acoustic communication system did not work.
7	2009.8.17	A1	2.4	Carried out the functional test for the main ballast system and due to high positive buoyancy, the submersible did not dive.
8	2009.8.18	A1	38	Finished the diving test by thrusters.
9	2009.8.20	A1	2.4	Finished the test of the acoustic communication system with the main engines of the mothership stopped or operated.
10	2009.8.21	A1	41	Finished the functional test of filling and draining of the main ballast water tank; Finished the check of navigational functions; Finished functional test for the variable ballast system and the trim adjustment system.
11	2009.8.23	A1	44	Finished the releasing test of the emergency buoy.
12	2009.8.30	B1	2.4	Debugging of the acoustic communication system.
13	2009.8.31	B1	213	Balance test in 200-m depth; Debugging the acoustic communication system.
14	2009.9.7	B1	100	Established the Morse code communication. Test terminated due to severe weather.
15	2009.9.12	Dock 2	2.4	Finished grounding detection; Debugging the acoustic communication system.
16	2009.9.13	B1	335	Finished the functional check for manual navigation with and without computer. Finished functional test for automatic orientation, depth, height and hovering; Finished the functional test for trim adjustment; Finished the functional test for the variable ballast system; Finished sitting on bottom.
17	2009.9.18	B1	268	Finished functional test for automatic orientation, depth, height and hovering; Finished the test for payload; Finished the functional test for side scan sonars and hydrothermal samplers; Finished the functional check for manual navigation without computer.
18	2009.9.20	B1	292	Finished sitting on bottom and placing markers; Finished functional test of the acoustic communication system; Testing the automatic height function.
19	2009.9.30	Dock 2	2.4	Finished grounding detection and functional test for the variable ballast system; Debugging the acoustic communication system.
20	2009.10.3	C2	1,109	Finished un-powered diving and floating; Finished the whole process of submersible diving operation.
21	2010.5.29	Dock 1	2.4	Finished the launch and recovery training for the operators; Finished the functional check for the ground inspection system.
22	2010.6.8	A1	2.4	Submersible turning when launched in water and one towing rope cut the cable of one transducer. Fortunately the transducer was saved by the persons in the rubber boat. Underwater filming test terminated.

continued

TABLE 3

Continued

Dive No.	Date	Test Site	Depth (m)	Brief Description
23	2010.6.9	A1	37	Finished the balance test; Finished underwater filming by a diver; Finished functional check for side scan sonars, the acoustic communication system; Finished navigational function check.
24	2010.6.11	B1	291	Finished solid blast weight check in 300-m depth; Finished the navigational function check; Finished the functional test for automatic depth, orientation and height; Finished the functional check for the acoustic communication system; Finished sitting on bottom.
25	2010.6.12	B1	291	Finished the navigational function check; Finished the functional test for automatic depth; Finished sitting on bottom; Finished operational exercise for one pilot-in-training.
26	2010.6.20	D2	2,068	Finished un-powered diving and floating; Finished solid blast weight check in 2,000-m depth; Finished the functional check for the acoustic communication system.
27	2010.6.22	D2	3,039	Finished un-powered diving and floating; Finished functional test for the acoustic communication system; Finished the functional check for the ground inspection system.
28	2010.6.27	D2	2.4	Diving test terminated when the leakage alarm of the backup battery box was sounding.
29	2010.6.28	D2	2,104	Finished un-powered diving and floating; Finished functional check for the ground inspection system; Finished operational exercise for one pilot-in-training.
30	2010.6.29	B1	286	Finished bathymetric bottom mapping with two side-scan sonars; Finished navigational function check; Finished sitting on bottom and placing the marker; Carried out target search exercise.
31	2010.6.30	B1	286	Finished the search of the marker placed in the previous dive; Finished sitting on bottom and placing the new marker; Finished operational skill test for two pilots-in-training.
32	2010.7.6	A1	33	Finished video recording and photo taking of the whole sea trial scene by the helicopter; Finished functional check for ground inspection system and the updated video system of the submersible.
33	2010.7.8	D2	2,088	Diving terminated due to the high short-circuit current value displayed by the ground inspection system; Finished functional test for the hydraulic system.
34	2010.7.9	D2	3,757	Finished un-powered diving and floating; Finished sitting on bottom 5 times; Operated the hydrothermal sampler but without obtaining water samples.
35	2010.7.11	D2	1,134	Diving test terminated when the leakage alarm of the backup battery box was sounding.
36	2010.7.12	D2	3,757	Finished un-powered diving and floating; Finished sitting on bottom, taking hydrothermal samples and placing markers.
37	2010.7.13	D2	3,759	Finished un-powered diving and floating; Finished sitting on bottom and taking samples; Finished bathymetric bottom mapping with two side-scan sonars. Finished operational skill test for two pilots-in-training.
38	2011.6.28	Dock 1	2.4	Finished launch and recovery training for the operators; Finished functional check for the ground inspection system.
39	2011.6.29	Dock 1	2.4	Finished launch and recovery training for the operators; Finished functional check for the ground inspection system.
40	2011.7.20	E3	4,027	Finished un-powered diving and floating; Finished solid blast weight check in 4,000-m depth; Finished functional check for ultra-short baseline and ground inspection system; Finished submersible functional check.

continued

TABLE 3

Continued

Dive No.	Date	Test Site	Depth (m)	Brief Description
41	2011.7.25	E3	5,057	Finished un-powered diving and floating; Finished solid blast weight check in 5,000-m depth; Finished functional check for ultra-short baseline; Finished submersible functional check; Finished sitting on bottom and taking videos and photos.
42	2011.7.27	E2	5,188	Finished unpowered diving and floating; Finished navigational function check in 5,000-m depth; Finished sitting on bottom and taking videos and photos; Finished bathymetric bottom mapping of 3 km with two side-scan sonars.
43	2011.7.29	E1	5,184	Finished un-powered diving and floating; Finished navigational function check in 5,000-m depth; Finished sitting on bottom, placing markers; Finished sampling of manganese nodules and biologies; Recorded many videos and photos. Finished the whole process of submersible diving operation.
44	2011.7.31	E1	5,180	Finished un-powered diving and floating; Finished functional check in 5,000-m depth; Finished sitting on bottom, placing markers; Finished biological sampling; Recorded many videos and photos. Finished the whole process of submersible diving operation.
45	2012.6.1	Dock 1	2.4	Finished launch and recovery training for the operators.
46	2012.6.15	G1	6,671	Finished un-powered diving and floating; Finished functional check in 5,000 m and 6,000-m depths; Obtained 405 ml water sample in normal pressure and 430 ml water sample in high pressure of 28 MPa.
47	2012.6.19	G1	6,965	Finished unpowered diving and floating; Finished functional check in 6,000-m depth; Finished sitting on bottom, placing markers, micro topography survey by side-scan sonar; Obtained a sediment sample of 14 cm length; Obtained 435 ml water sample in normal pressure; Finished the whole process of submersible diving operation.
48	2012.6.22	G1	6,963	Finished un-powered diving and floating; Finished functional check and safety verification in 6,000-m depth; Finished sitting on bottom, placing markers; Obtained three sediment samples whose lengths are 21 cm, 16 cm and 18 cm, respectively; Obtained 400 ml and 435 ml water samples in normal pressure and 123 ml water sample in high pressure of 15 MPa; Caught one white sea cucumber and two pieces of nodular mineral samples. Finished the whole process of submersible diving operation.
49	2012.6.24	G1	7,020	Finished un-powered diving and floating; Finished functional check in 7,000-m depth; Finished sitting on bottom, placing markers; Finished submersible tele-communication test with the person in Beijing office; Obtained 440 ml and 445 ml water samples in normal pressure and 345 ml water sample in high pressure of 35 MPa; Finished the whole process of submersible diving operation.
50	2012.6.27	G1	7,062	Finished unpowered diving and floating; Finished functional check and safety verification in 7,000-m depth; Finished sitting on bottom, placing markers; Obtained two sediment samples whose lengths are 21 cm and 27 cm, respectively; Obtained 440 ml and 435 ml water samples in normal pressure; Caught one white sea cucumber. Carried out the biological trapping experiment with bait. Finished the whole process of submersible diving operation.
51	2012.6.30	G1	7,035	Finished unpowered diving and floating; Finished submersible functional check and safety verification in 7,000-m depth; Finished sitting on bottom and sample taking exercise; Finished functional verification of two domestic propellers by long distance cruise. Finished the whole process of submersible diving operation.

Note: Dock 1 = The Jiangyin International Container Terminal; Dock 2 = The mooring site near Sanya; A1 = South China Sea (109°09'E, 18°01'N); B1 = South China Sea (112°36'E, 19°01'N); C2 = South China Sea (110°26.8'E, 17°28.45'); D2 = South China Sea (116°28'E, 18°36'N); E1 = China poly metallic nodules contract area in the northeast Pacific (154°12'W, 10°08'N); E2 = China poly metallic nodules contract area in the northeast Pacific (154°11'W, 8°40'N); E3 = The northeast Pacific (151°7'W, 4°48'N); G1 = The exclusive economic zone (EEZ) of the Federated States of Micronesia in the southern Mariana Trench (141°58'E, 10°59'N).

Furthermore, each dive completed its mission, including reaching the position with the required depth, and no invalid dives occurred as in the previous two years (Table 3). This indicated that the improved submersible's technical state was stable, our test team had matured, and the sea trial's plan and content proved to be reasonable and scientific. As a difference from the previous trials, this sea trial was completely open to the media, and several dives were broadcast live on CCTV. A detailed introduction to the 5,000-m depth class test can be found in Cui et al. (2011a, 2011b).

The final 7,000-m depth class test was carried out from June 3 to July 16, 2012. Although it faced the unique challenges of 7,000 m sea trials, the team was now fully prepared, carried out very careful operations at sea, and could analyze and solve all the problems that occurred on-site. After very strict inspection by the on-site acceptance group of experts, it was concluded that the test team completed the 7,000 m sea trials safely and successfully. The details are reported in Cui et al. (2013). The sea trials tests showed that all the design requirements were fully realized. This 7,000-m sea trials test is the deepest of the same type of deep manned submersibles in the world. The success of the *Jiaolong* submersible demonstrates that China's manned submersible technology has entered the club of the countries of the highest international standard.

Latest Technical Specifications of the *Jiaolong* and Future Development Trends for Deep Manned Submersibles

Although the technical specifications of the *Jiaolong* submersible have

been reported in several references (Cui et al., 2008a, 2008b, 2009; Liu et al., 2008), some of them changed during the technical improvements made in the sea trials period. The latest technical specifications of the *Jiaolong* are as follows:

Maximum operational depth:	7,000 m
Main dimensions:	8.4 × 4.2 × 3.4 m
Inner diameter of manned cabin:	2.1 m
Weight in air:	22 tons
Crew:	1 pilot, 2 scientists
Power supply:	Silver-zinc battery, >110 kWh
Control mode:	Automatic fixed height, fixed direction, fixed depth, hovering and manual operations
Navigation system:	Ultra-short baseline system, long baseline system motion sensors + acoustic Doppler speedometer
Operation:	Two seven-function hydraulic manipulator arms
Lighting and video system:	HD video camera system, LED lights
Communication:	Underwater acoustic communication, underwater acoustic telephone, VHF communication + GPS positioning

Figure 4 is a photo of the latest design. Although the *Jiaolong* is the deepest and latest manned submersible within the second generation of three-crew operational submersibles, it cannot be claimed to represent the latest state-of-the-art technology for deep manned submersibles.

When comparing our *Jiaolong* with the U.S.'s new *Alvin* (<http://www.whoi.edu/alvin/>), it can be found that, on the one hand, the inner diameters of their manned cabin are the same; their payload, battery power, lighting and imaging systems, maneuverability and

ability to sample hovering at an accurate position are almost equivalent. Their respective underwater working time on the bottom are within the limit of manned submersibles. The *Jiaolong* also possesses similar performances in the aspects of automatic drive, underwater acoustic communication, capabilities of navigation and positioning.

On the other hand, based on a great deal of operational experience, the new *Alvin* has a more outstanding design of viewports, in-cabin man-machine interface, data acquisition and instrument interfaces.

The future technical trends of manned submersibles mainly focus on the aspects of economy, comfort and environmental protection (Cui et al., 2011a, 2011b). Two requirements will bring revolutionary changes to the design of manned submersibles. One is to significantly reduce the running costs, making manned submersibles comparable with unmanned submersibles in this aspect (Hawkes, 2009). The other is to miniaturize the in-cabin facilities, making a more comfortable in-cabin

FIGURE 4

Jiaolong deep manned submersible.



environment (Taylor & Lawson, 2009). Concerning environmental protection, this mainly relies on elimination of mercury as the substance to adjust the trim, or modify the substance used in the emergency jettison system. Solid ballast iron would not be used, or only if necessary.

These two last requirements primarily depend on the technique of a large-flow high-pressure sea water pump. The new *Alvin*'s design team once considered making a breakthrough in this aspect at the very beginning of their design; however, they ultimately had to give up this idea due to tremendous technical difficulties and lack of funds. In spite of their failure to make such a breakthrough, it ought to have attracted sufficient attention as a direction of technical development. Another improvement direction of great potential importance is the manipulator. Current seven function manipulators obtained commercially are far away from the capabilities of human hands and discovering how to develop a manipulator simulating the human hand would bring a revolutionary change to the submersible community. At the same time, another direction of great interest to human beings is challenging the full ocean depth, which needs a breakthrough in improving submersibles' speed of descending and ascending. In this direction, James Cameron completed his record-breaking Mariana Trench dive in March 26, 2012, with his Solo sub Deepsea Challenger (<http://deepseachallenge.com/>). Another two full ocean depth manned submersibles are under development (<http://www.doermarine.com/>; <http://deepflight.com/>).

Summary and Conclusions

This paper is the first one describing the development process of the *Jiaolong*

deep manned submersible from a historical point of view, including the design, realization of components, assembly, open-water tank test and sea trials. The main technical challenges met at each stage are briefly explained, supplemented by the many references published during the process for interested readers. The *Jiaolong* submersible is briefly compared with the new *Alvin*, which is regarded as being the best in the deep sea community, and it is concluded that, except for the design of the viewports, in-cabin man-machine interface, data acquisition and instrument interfaces, most of the performances and functions are equivalent in addition to the *Jiaolong*'s ability to dive 500-m deeper. This indicates that the *Jiaolong* can also be regarded as one of the most advanced deep manned submersibles for scientific operations. The 7,000-m depth capability is the deepest of the same type of deep manned submersibles in the world. The success of the *Jiaolong* submersible demonstrates that China's manned submersible technology has entered the realm of countries with the highest international standard. Finally, future technical trends of manned submersibles were also discussed.

Acknowledgments

The development of the *Jiaolong* submersible was sponsored by the Ministry of Science and Technology under the contracts of Development of a 7,000-m Deep Manned Submersible (Project No. 2002AA401000); 1,000-m Depth Class Sea Trials of *Jiaolong* Submersible (Project No. 2009AA093201); Key Technology Improvements and 3,000-m Depth Class Sea Trials of *Jiaolong* Submersible (Project No. 2010AA094001); Operational Technology Improvement and 5,000–7,000 m Sea Trials

(Project No. 2011AA09A101). The State Oceanic Administration (SOA) is the organization department of the sea trials of *Jiaolong*. China Ocean Mineral Resources R&D Association (COMRA) of SOA is specifically responsible for organizing the sea trials. In total, 96 members from 18 domestic organizations jointly completed the sea trial tests. The author of this paper is very grateful to all the team members. Comments, suggestions and language improvements from Dr. Don Walsh, Dr. Kurt Uetz, Dr. William Kohlen and another two reviewers to this paper are greatly appreciated. My M.Sc. student, Mr. Hao Li did some translation for this paper and his help is also appreciated. The work reported in this paper was completed in my former organization China Ship Scientific Research Center, and now this author has been moved to Shanghai Ocean University.

Author:

Weicheng Cui

China Ship Scientific Research Center,
Jiangsu, 214082, China
Currently with Hadal Science and
Technology Research Center, Shanghai
Ocean University, Shanghai, China
Email: wccui@shou.edu.cn

References

- Barry, J.P., & Hashimoto, J. 2009. Revisiting the Challenger Deep using the ROV *Kaiko*. *Mar Technol Soc J.* 43(5):77-8.
- China Classification Society. 1996. Classification and Construction Rules for Diving Systems and Submersibles [S]. Beijing: People's Transportation Press (in Chinese).
- China Classification Society. 2011. Principles for plan approval and inspection of deep-sea manned submersible. A supplement to CCS1996, Internal document (in Chinese).

- Committee on Evolution of the National Oceanographic Research Fleet.** 2009. Science at Sea: Meeting Future Oceanographic Goals with a Robust Academic Research Fleet, National Research Council, ISBN: 0-309-14558-9, 120 pages, The National Academies Press. This free PDF was downloaded from <http://www.nap.edu/catalog/12775.html>.
- Committee on Future Needs in Deep Submergence Science.** 2004. Future Needs in Deep Submergence Science: Occupied and Unoccupied Vehicles in Basic Ocean Research, National Research Council, ISBN: 0-309-52917-4, 152 pages, The National Academies Press. This PDF is available from the National Academies Press at: <http://www.nap.edu/catalog/10854.html>.
- Cui, W.C., Hu, Z., Ye, C., & Pan, B.B.** 2011a. Current status and future trends for deep manned submersibles. *J Cent South Univ T.* 42(Suppl. 2):13-20 (in Chinese).
- Cui, W.C., Hu, Z., Ye, C., & Xu, Q.N.** 2010. First two phases of sea trials of deep manned submersible "Jiaolong." In: Ocean Innovation Conference (OI2010), October 17-20, 2010. St. John's, Canada: The Marine Institute of Memorial University, Marketing & Business Development Division.
- Cui, W.C., Liu, F., Hu, Z., Zhu, M., Guo, W., & Liu, C.G.** 2013. On 7000 m sea trials of the manned submersible "JIAOLONG." *Mar Technol Soc J.* 47(1):67-82. <http://dx.doi.org/10.4031/MTSJ.47.1.2>.
- Cui, W.C., Liu, F., Hu, Z., Zhu, M., Guo, W., & Wang, C.S.** 2011b. 5000 m sea trials test of the deep manned submersible "JIAOLONG." *Shipbuilding of China.* 52(3)(Serial No. 197): 1-14 (in Chinese).
- Cui, W.C., Liu, Z.Y., & Xu, Q.N.** 2008a. The four-element method for the design of large complex engineering system. *Shipbuilding of China.* 49(2)(Serial No. 181):1-12 (in Chinese).
- Cui, W.C., & Ma, L.** 2009. Hydrodynamic problems involved in submersible design. In: Proceedings of the 9th National Congress on Hydrodynamics and 22nd National Conference on Hydrodynamics, 9-29 (in Chinese). Beijing: Ocean Press.
- Cui, W.C., Xu, Q.N., Liu, F., Hu, Z., Wang, X.H., & Zhu, M.** 2009. Design, construction and open water tank test of the deep manned submersible "Harmony." In: Keynote paper presented in the Sixth International Symposium on Underwater Technology UT2009, Wuxi, China, April 2009. Wuxi: China Ship Scientific Research Center.
- Cui, W.C., Xu, Q.N., Liu, T., Hu, Z., Yang, Y.N., Hu, Y., & Ma, L.** 2008b. Design and construction of the deep manned submersible "Harmony." *J Ship Sci Technol.* 30(1):17-25 (in Chinese).
- Fletcher, B., Bowen, A., Yoerger, D.R., & Whitcomb, L.L.** 2009. Journey to the Challenger Deep: 50 years later with the *Nereus* hybrid remotely operated vehicle. *Mar Technol Soc J.* 43(5):65-76. <http://dx.doi.org/10.4031/MTSJ.43.5.26>.
- Forman, W.** 2009. From Beebe and Barton to Piccard and Trieste. *Mar Technol Soc J.* 43(5):27-36. <http://dx.doi.org/10.4031/MTSJ.43.5.14>.
- Hawkes, G.** 2009. The old arguments of manned versus unmanned systems are about to become irrelevant: New technologies are game changers. *Mar Technol Soc J.* 43(5): 164-8. <http://dx.doi.org/10.4031/MTSJ.43.5.21>.
- Hu, Z., Wang, X.H., Zhu, M., Xu, Q.N., & Cui, W.C.** 2008. Tank test of the deep manned submersible "Harmony"[C]// In: the 3rd Asian-and Pacific Diving and Underwater Technology Conference, Shanghai, June 13-15, 2008. Shanghai: Shanghai Society of Naval Architects and Marine Engineers.
- Jarry, J.** 1986. SAR, NAUTILE, SAGA, ELIT-four new vehicles for underwater work and exploration: The IFREMER approach. *IEEE J Oceanic Eng.* OE-11(3):413-7. <http://dx.doi.org/10.1109/JOE.1986.1145192>.
- Kohnen, W.** 2009. Human exploration of the deep seas: Fifty years and the inspiration continues. *Mar Technol Soc J.* 43(5):42-62. <http://dx.doi.org/10.4031/MTSJ.43.5.30>.
- Liu, F., Cui, W.C., & Li, X.Y.** 2008. Introduction to design and construction of deep manned submersible "Harmony." In: Paper presented in International Conference of INMARTECH2008, All Seasons Hotel, Toulon, France, October 8-10, 2008. Toulon: Ifremer.
- Liu, F., Cui, W.C., & Li, X.Y.** 2010. China's first deep manned submersible. *Jiaolong. Science China—Earth Sci.* 53(10):1407-10. <http://dx.doi.org/10.1007/s11430-010-4100-2>.
- Li, X.Y., & Cui, W.C.** 2004. Contact finite element analysis of a spherical hull in the deep manned submersible. *J Ship Mech.* 8(6):85-94.
- Li, X.Y., Cui, W.C., & Zhang, W.M.** 2006. Fatigue life reliability analysis of titanium manned spherical shell. *J Ship Mech.* 10(2):82-6 (in Chinese).
- Li, X.Y., Liu, T., Huang, X.P., & Cui, W.C.** 2004. Determination of fatigue load spectrum for pressure hull of a deep manned submersible. *J Ship Mech.* 8(1):59-70 (in Chinese).
- Lu, B., Liu, T., & Cui, W.C.** 2004. Ultimate strength of pressure spherical hull in deep-sea manned submersibles. *J Ship Mech.* 8(1): 51-8 (in Chinese).
- Ma, L., & Cui, W.C.** 2004. Simulation of dive motion of a deep manned submersible. *J Ship Mech.* 8(3):31-8.
- Ma, L., & Cui, W.C.** 2005. Path following control of a deep-sea manned submersible based upon NTSM. *China Ocean Eng.* 19(4):625-36.
- Ma, L., & Cui, W.C.** 2006a. Heading control study of a deep manned submersible at a low speed and large drift angles based on fuzzy sliding mode control. *Ocean Eng.* 24(3):74-8 (in Chinese).
- Ma, L., & Cui, W.C.** 2006b. Dynamic system identification of manned submersible in horizontal plane. *Shipbuilding of China.* 47(2):76-81 (in Chinese).
- Momma, H.** 1999. Deep ocean technology at JAMSTEC. *Mar Technol Soc J.* 33(4):49-64. <http://dx.doi.org/10.4031/MTSJ.33.4.6>.
- Nanba, N., Morihana, H., Nakamura, E., & Watanabe, N.** 1990. Development of deep submergence research vehicle "SHINKAI

6500." Technical Review of Mitsubishi Heavy Industries, Ltd. 27(3):157-68.

Naval Sea Systems Command (NSSC). 1998. System Certification Procedures and Criteria Manual for Deep Submergence Systems. Revision A, SS800-AG-MAN-010/P-9290. Published by Direction of Commander, Naval Sea Systems Command, 0910-LP-018-2840.

Pan, B.B., & Cui, W.C. 2010. An overview of buckling and ultimate strength of spherical pressure hull under external pressure. *Mar Struct.* 23(3):227-40. <http://dx.doi.org/10.1016/j.marstruc.2010.07.005>.

Pan, B.B., & Cui, W.C. 2011. A comparison of different rules for the spherical pressure hull of deep manned submersibles. *J Ship Mech.* 15(3):276-85.

Pan, B.B., & Cui, W.C. 2011. On an appropriate design and test standard for spherical pressure hull in a deep manned submersible. In: *Proceeding of 2011 IEEE Symposium on Underwater Technology (UT 2011) and 2011 Workshop on Scientific Use of Submarine Cables and Related Technologies (SSC 2011)*, Tokyo, Japan, 5-8 April 2011, IEEE Catalog Number: CFP11UTS-PRT, ISBN: 978-1-4577-0165-8, pp. 436-442. Tokyo: Institute of Industrial Science, University of Tokyo

Pan, B.B., & Cui, W.C. 2012. Structural optimization for a spherical pressure hull of a deep manned submersible based on an appropriate design standard. *IEEE J Oceanic Eng.* 37(3):564-71. Color versions of one or more of the figures in this paper are available online at <http://ieeexplore.ieee.org>. Digital Object Identifier. 10.1109/JOE.2012.2190809.

Pan, B.B., Cui, W.C., Shen, Y.S., & Liu, T. 2010. Further study on the ultimate strength analysis of spherical pressure hulls. *Mar Struct.* 23(4):444-61. <http://dx.doi.org/10.1016/j.marstruc.2010.11.001>.

Rona, P.A. 2000. Deep diving manned research submersibles. *Mar Technol Soc J.* 33(4):13-25. <http://dx.doi.org/10.4031/MTSJ.33.4.3>.

Russian Maritime Register of Shipping.

2004. Rules for the Classification and Construction of Manned Submersibles, Ship's Diving Systems and Passenger Submersibles [S]. Moscow: RS Press.

Sagalevitch, A. 2009. From the bathyscaph *Trieste* to the submersibles *Mir*. *Mar Technol Soc J.* 43(5):79-86. <http://dx.doi.org/10.4031/MTSJ.43.5.3>.

Taylor, L., & Lawson, T. 2009. Project Deepsearch: An innovative solution for accessing the oceans. *Mar Technol Soc J.* 43(5):169-77. <http://dx.doi.org/10.4031/MTSJ.43.5.28>.

Takagawa, T., Momma, H., & Hotta, H. 1995. Advanced technology used in Shinkai 6500 and full ocean depth ROV Kaiko. *Mar Technol Soc J.* 29(3):15-25.

Reliability-Centered Development of Deep Water ROV ROSUB 6000

AUTHORS

Vedachalam Narayanaswamy
 Ramesh Raju
 Muthukumaran Durairaj
 Aarthi Ananthapadmanabhan
 Subramanian Annamalai
 Gidugu Ananada Ramadass
 Malayath Aravindakshan Atmanand
 National Institute of Ocean
 Technology, Chennai, India

Introduction

The remotely operable submersible ROSUB 6000 for deep sea operation is an electric work class Remotely Operable Vehicle (ROV), equipped with two manipulators and having an additional payload capability of 150 kg for mounting scientific and mission-oriented subsystems. The ROSUB system comprises the main components, namely the ROV, Tether Management System (TMS), Launching and Recovery System (LARS), ship systems, control console, instrumentation, control and electrical system, Hydro Acoustic Navigation System (HANS), and the control and operational system (Manecius et al., 2010; Ramesh et al., 2010). Figure 1 shows the overall view of the ROV with LARS in the ship.

Figure 2 shows the system launching phase, where the work class ROV and the TMS are docked together and launched from the mother vessel using the LARS. The storage winch houses the 7,000-m-long umbilical cable, and its operation is synchronized with the LARS and other deck gear.

ABSTRACT

This paper presents the reliability-centered development of a deep water Remotely Operable Vehicle (ROV) ROSUB 6000 by the National Institute of Ocean Technology (NIOT), India. ROV operations are required during deep water interventions, such as well head operations, emergency response situations, bathymetric surveys, gas hydrate surveys, poly-metallic nodule exploration, and salvage operations. As per our requirements, the system needs to be capable of deep water operation for a period of 300 h/year and to be extremely reliable. Methodologies applied during the development and enhancement phases of electrical and control systems, taking into consideration the cost, space, and time constraints to attain the best possible reliability are detailed. Reliability, availability, and maintainability (RAM) studies are carried out to identify possible failure cases. It is found that ROV-Tether Management System (TMS) docking failure could be detrimental to the ROV system, and manipulator system failure could be detrimental to subsea operations. It has been calculated and found that the improved design has a mean time between failure (MTBF) of 4.9 and 6.2 years for ROV-TMS docking and manipulator system operations, respectively. The importance of monitoring tether cable healthiness during normal and winding operations and the systems implemented for effectively monitoring and maintaining the tether cable operational and functional healthiness, using the tether cable pay-out, vehicle heading, electric insulation, and optical performance sensors with the aid of a sea battery, are discussed. Maintenance decision support tables, which detail the operational personnel for the upkeep of the systems during the indicated interval so that the highest possible reliability is maintained during the mission period, are also presented. Keywords: remotely operated vehicle, reliability, probability of failure, mean time between failure, FMECA analysis

The umbilical is an electro-optic interface between the TMS and the ship and is used to carry the weight of the TMS and the ROV.

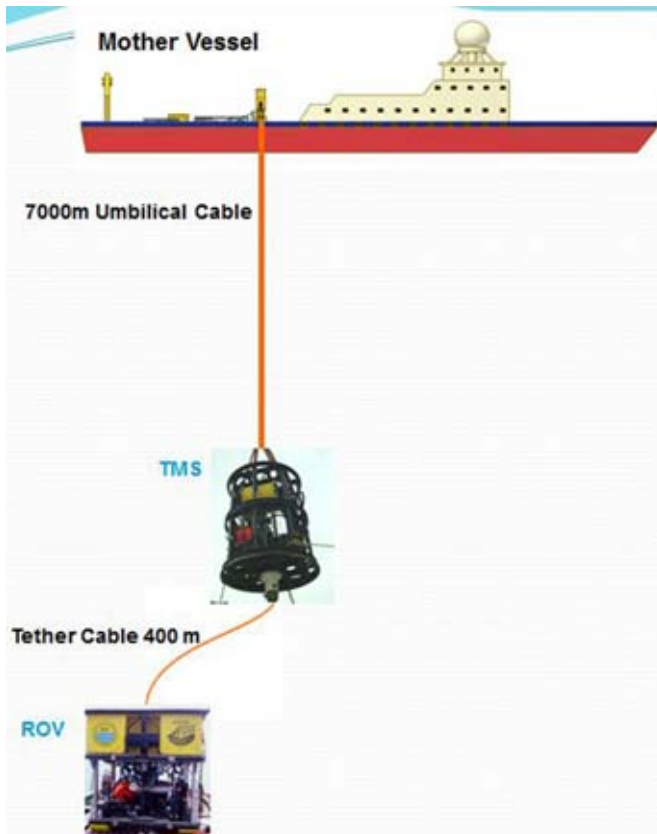
The LARS takes the ROV-TMS docked system below the splash zone and undocks it. The ROV-TMS system is lowered to the location of interest. As the docked system gets closer to the target of interest, the ROV is released from the TMS. The ROV is equipped with thrusters and can be operated on the pilot's command

from the launching vessel. Manipulators mounted on the ROV are used to carry out the required subsea operation. After completion of the task, the ROV is docked back to the TMS in the subsea location, and the system is taken back to the ship.

Figure 3 indicates the electrical and control system architecture in the TMS, ROV, and the ship. The ship power at 415 V at 50 Hz is converted into 6,600 V at 460 Hz, using a combination of a standard frequency converter

FIGURE 1

View of the system architecture of ROSUB 6000.

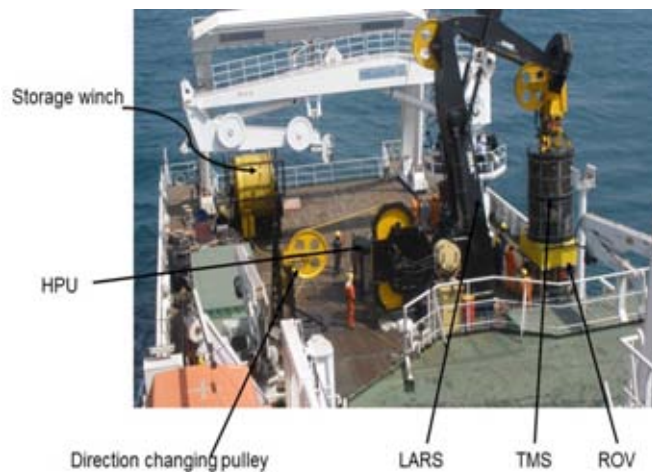


and a step-up transformer. The electro-optical connectivity between the ship and the TMS is achieved by a 7,000-m umbilical cable (Manecius et al., 2010;

Ramesh et al., 2010), while the connectivity between the TMS and the ROV is obtained by a 400-m-long tether cable. Subsea power converters

FIGURE 2

View of the ROSUB 6000 system ready to be launched.



in the TMS and the ROV convert power at 6,600 V at 460 Hz to the power level requirements of the subsystems. The voltage of 6,600 V is selected as a tradeoff between the size of the umbilical/tether cables, while the voltage drop is managed in the 6,000 m transmission cable and the power requirements of the system. A frequency of 460 Hz is used to reduce the size and weight of the magnetic components in the ROV and TMS.

Electronic controllers with input-output modules are used for interfacing with the field devices in the TMS and the ROV. Data formats are managed by using multiplexers and media converters. The ROV and TMS systems communicate with the ship system using the fiber optic Ethernet link through the slip rings located in the TMS and deck storage winches. The manipulators can be operated from the control console, and the control is interfaced to the ROV and the ship side controllers at either end.

RAM Methodology and the Standards Followed

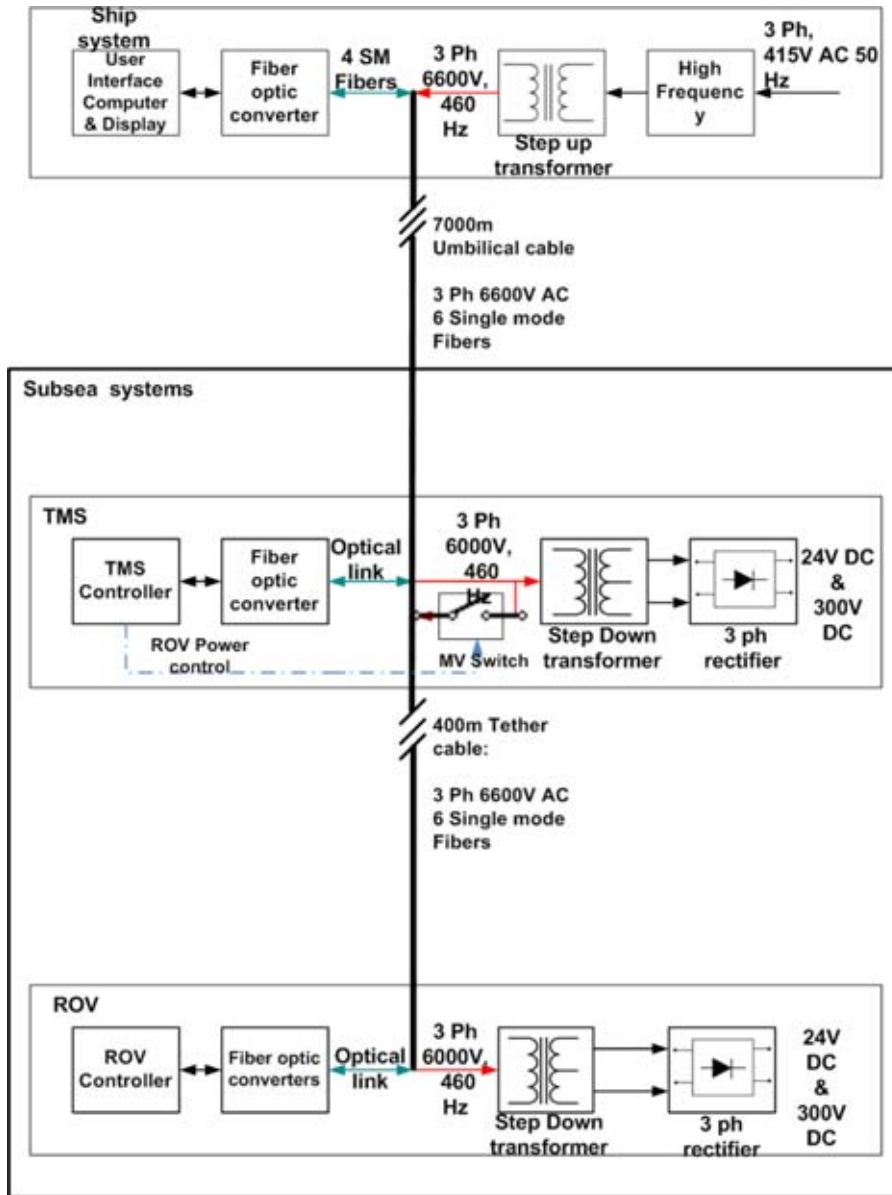
As the ROSUB 6000 system is to be involved in mission critical applications, reliability, availability, and maintainability (RAM) are of utmost importance. As part of the RAM studies, Failure Mode Effects Analysis (FMECA) studies were done to identify the possible failures.

Failures were classified into four categories based on their impact on the overall system, and the most critical failure surfacing in each category is taken up for improvements.

- a. Type 1 failures that have a minimal impact on the mission objective and the system, e.g., failure of one of the lamps or cameras in the ROV.
- b. Type 2 failures that could defeat the mission objective, but not damaging

FIGURE 3

Electrical and control architecture of the ROSUB 6000 system.



- c. Type 3 failures that cause damage to the system itself, e.g., ROV-TMS docking failure.
- d. Type 4 failures that could cause damage to the system as well as the subsea installation, e.g., manipulator failure while in operation.

The following Types 3 and 4 failures are described in this paper:

1. Failure of the ROV to dock with the TMS underwater.
2. Failure of the manipulator when carrying out a subsea task.

Reliability trees are drawn to find out the probability of failure for the identified two critical operations. Calculations were performed to find out the mean time between failure (MTBF) for a 5-year period, with the system clocking deep water operation for a period of 300 h/year.

The following are the list of the major standards followed:

1. FIDES Guide for Reliability Methodology (FIDES Guide, 2009) for electronic systems, which deals with the mission and environment specific analysis.
2. MIL HDBK 217F Military Handbook for Reliability Estimation (U.S. Department of Defense, 1991) of the Electronics Equipment.
3. OREDA Handbook (OREDA AUTOR, 2003) for Offshore Reliability Data.
4. IEEE 493 IEEE Recommended Practices (IEEE Standard, 1997) for the Design of Reliable Industrial and Commercial Power Systems.
5. Reliability of Valve Regulated Lead Acid Batteries (DeAnda et al., 2004), a study by the U.S. Department of Energy, Energy Storage Systems program.

Failure rate determination is done by the following methods:

- a. Based on the manufacturer's data and interpretation suitable for the mission profile.
- b. For systems and circuit boards, where schematics are available, using component failure data from the respective standards, and calculating the failure rates taking the mission profile, operating conditions and stresses into consideration.
- c. For commercially sourced circuit boards, where there is no adequate information, based on the functional specification, the failure rate for the mission profile is calculated using standards.

The FIDES approach is based on physics and the failures supported by the analysis of test data, feedback from operations and existing models, along with the statistical interpretations over the normal operating life period of the involved systems.

The standard considers the influence of the operating temperature, amplitude and frequency of the temperature changes, vibration amplitude, humidity and operating stress factors. For example, the impact on the lifetime due to the operating temperature, thermal cycling and vibration stresses are based on the Arrhenius, Norris and Basquin laws (FIDES, 2009). The standards make provision to account for manufacturing and integrating quality factors into the calculations, taking into account the environmental conditions and stresses during different mission profiles. The standard also provides the commercial off-the-shelf approach for calculating the failure rates of commercially available circuit boards for the defined mission profile with the functional requirements and mission profile as an input from the user.

The failure rate of the components is not a linear function with time. Failure rates are usually mentioned in terms of the number of failures per billion hours (FIDES, 2009), abbreviated as failure-in-time (FIT). As an example, Table 1 populates the calculated failure rate of a thruster

TABLE 1

Failure-in-time date for brushless direct current (BLDC) motor power electronics controller.

Hours of Operation per Year	Failure-In-Time (FIT)
1	64
100	68
300	77
500	85
3,000	195
5,000	282
8,000	413
8,760	446

motor power electronic controller. It can be seen that the device has a failure rate of 77 and 446 FIT for a mission profile of 300 and 8,760 h/year, respectively.

The failure rates of the components are calculated at the circuit component level and incorporated in the reliability trees. Table 2 gives the standards followed for the major systems and components.

The TOTAL-SATODEV's GRIF software is used for realizing the trees for calculating the probability of failure for a specific time period, with provisions to incorporate the mean time to repair (MTTR), and the options to select the reliability laws based on the availability of field failure data. In this study, exponential laws are applied, as the field failure data are very limited for subsea and similar systems.

Reliability and Availability Type 3 Failure Scenario: ROV-TMS Docking Failure; *Normal ROV-TMS Recovery*

When the ROV completes the identified mission, it has to be docked with the TMS, and the docked system has to be brought to the subsurface close to the ship, so that the ROV-TMS system can be docked with the LARS in the splash-free subsurface

region and then recovered to the deck. Figure 4 shows the pilot view of the ROV-TMS docking, captured by the illuminated camera located in the TMS during ROV deep water operations in 2008, where the navigation parameters are displayed on the pilot screen in the ship's control console.

The camera and lights located in the TMS will aid the pilot in carrying out the ROV-TMS docking. Given below is the process sequence in carrying out a successful subsea docking process.

- Pilot the ROV close to the TMS location.
- Wind the already released tether cable back in the TMS by operating the winch in the TMS.
- Pilot the ROV vertically down the TMS and operate the top thrusters to produce a downward thrust (normally ROV is upward buoyant by 20 kg) in such a way that the tether cable is held under minimum tension.
- With the minimum tension in the cable, operate the TMS winch and wind the tether cable in a way that the cable is without any slack.
- Continue the winding at a slower pace until the ROV enters the TMS cone and gets onto the latches (which will be indicated by the limit switches inside the latches).

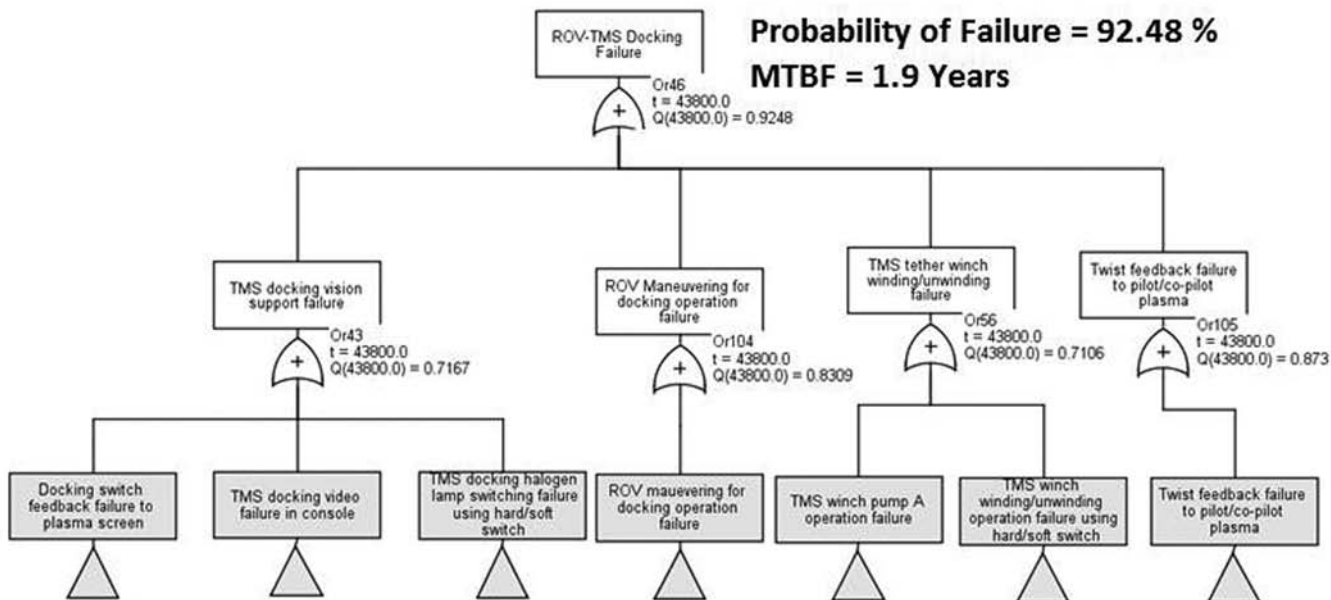
TABLE 2

Major standards followed for study.

Component	Standards
CPU, AC-DC converters, DC-DC converters, fuses, electronics and optical connectors, Ethernet converters, data and video multiplexers, input and output modules for data acquisition cards	FIDES
HF converters and transformers, isolators, motors	MIL and IEEE
Power contactors, halogen lamps	MIL
Umbilical and tether cables, terminations, subsea sensors	OREDA

FIGURE 6

Tree for calculating the docking failure MTBF for the base design case.



- f. Real-time controller
- g. Photonic inertial navigation system
- h. BLDC motor controller

By means of having spares in the ship, the probability of failure of the power supply input to the TMS can be reduced from 64.65% to 1.38%. Hence, the MTBF can be increased to 3.3 years.

c. By introducing black-dock sensors

As shown in Figure 4, the ROV-TMS docking operation is supported by a camera, lights, associated controls and power systems located in the TMS. It is calculated that the TMS docking vision support has a probability of failure of 20.51%. When this support system fails, the pilot cannot dock back the ROV to the TMS, even if the other conditions required for proper docking are maintained. To overcome this, black-dock sensors are introduced. The sensors are used to measure the following:

- a. Tether cable tension.

- b. Cable winding counter to ensure that the already released cable is wound back.

The black-dock sensors enable the pilot to carry out the docking operation in the event of vision system failure. From the failure trees in Figure 7, it can be seen that, by using the black-dock system, the probability of failure is reduced to 16.71% from 20.51%.

By means of this, the MTBF of the ROV-TMS docking process can be increased to 3.6 years.

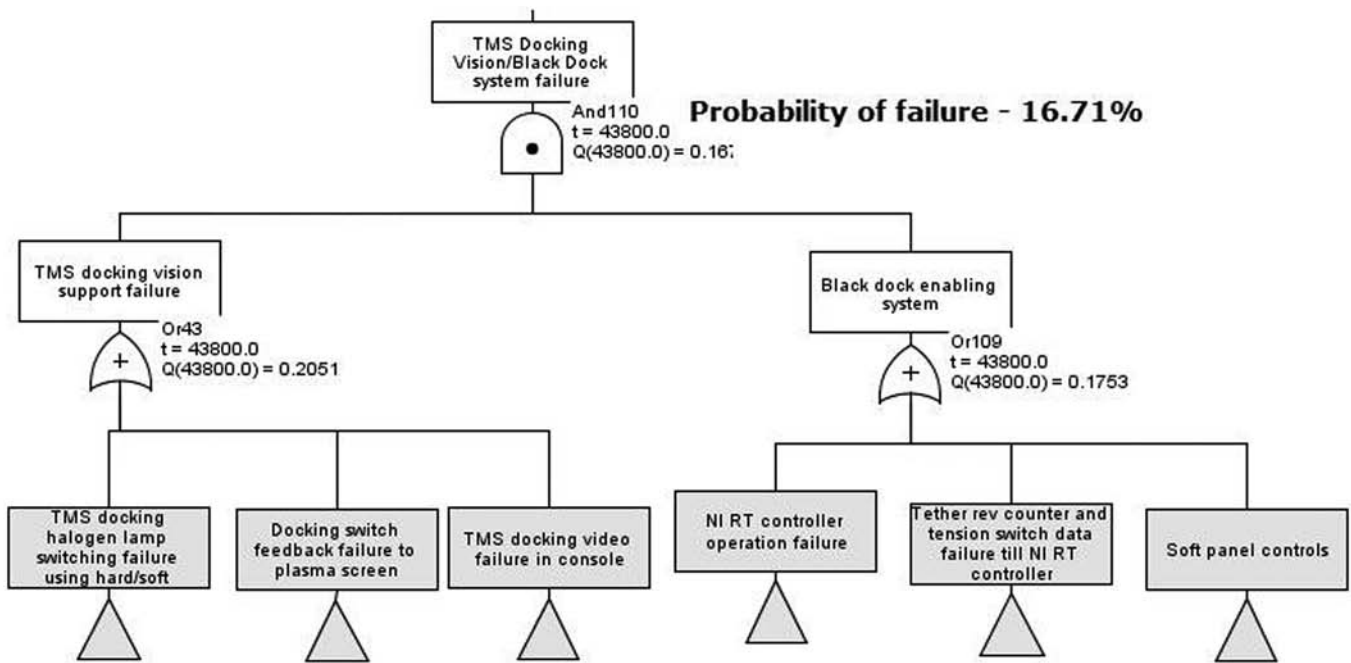
d. By operating the ROV isolation switchgear in the TMS as a switch

From standards (U.S. Department of Defense, 1991), the FIT of the electric power contactor opening under load is 10 times higher than when it is operated without load. The ROV operates with a power of nearly 60 kW at near unity power factor for propulsion and control systems. The remotely operable isolating device in the TMS has to handle a maximum current of 10 A at 6,600 V. Using the conventional

industrial standard vacuum circuit breaker (VCB) is not an attractive solution as a typical VCB of minimum rating of 400 A at 7.2 kV weighs around 25 kg and has a dimension of approximately 0.4 m (L) × 0.21 m (W) × 0.32 m (H). In addition to their huge footprints, such circuit breakers should be operated inside pressure-rated enclosures with feed through. This increases the size, weight, and cost of the assembly, which are not preferred solutions. As a solution to this challenge, an industrial standard 660 V, 100 A motor air break low voltage contactor is selected and used in an oil-filled, pressure-compensated environment. As the dielectric capacity of oil is 10 times that of air, this encourages the use of the 660 V air contactor at 6,600 V in a pressure compensated mode. The dimension of the selected contactor used to carry out the medium voltage (MV) switching operation is approximately 0.2 m (L) × 0.11 m (W) × 0.1 cm (H).

FIGURE 7

MTBF improvement by incorporating black-dock sensors.



The reliability of the MV switch-gear is of utmost importance in the overall system, as the failure of this contactor leads to the paralysis of the whole system. When the switchgear opens, an electrical arc is produced, and this is extinguished by the arc-chute mechanism and insulating oil.

As the arc generates high temperature, it decomposes a portion of the oil into gases (Thomas, 2008) composed of 70% hydrogen, 20% acetylene and carbon particles. Carbon particles are conductive in nature. The quantity of decomposed carbon is a function of the arc intensity, duration of the arc and the temperature of the arc plasma. As the switchgear is in a closed oil system, prolonged usage or excessive generation of carbon particles leads to oil contamination and subsequent failures. Therefore, the longevity and hence the reliability of the assembly can be improved by ensuring that the switchgear opens under a no-load con-

dition, resembling the required condition of a MV switch.

FMECA studies revealed that possible situations leading to the opening of the MV switch TMS located under load are as follows:

1. Input power failure in the TMS alone.
2. Control system failure in the TMS alone.
3. Accidental open command to the MV switch.

To overcome the above situations, a possible solution would be to delay the opening of the switch by a few seconds, during which time the electrical load on the MV switch will be reduced. This requires reliable localized energy storage in the TMS system. Even though batteries could be attractive in terms of size, they are not so attractive in terms of reliability and safety. Super capacitors are found to be the best trade-off (Lemofouet & Rufer, 2006; Mallika & Saravanakumar, 2011;

Paulo et al., 2001; Shukla et al., 2001). They are electrochemical, double layer capacitors (Barrade et al., 2003; Rufer, Hotellier, & Barrade, 2004; Weddell et al., 2011; DeAnda et al., 2004), which are preferable because they offer high power and energy densities.

The MV switch operates on 24 VDC supply and requires a maximum coil current of 0.2 A. The design criteria (Al-Ramadhan & Abido, 2012) involve ensuring a minimum voltage of 12 V for continuous holding of the coil for duration of 60 s. Based on these parameters, we have calculated the requirements of energy (W) and minimum capacitance (C). Twelve capacitors are connected in a series to get the effective capacitance of 0.833 F that can hold the MV switch up to 60 s. The designed circuit incorporating the required protection circuits is integrated into the TMS control system. When a 24-V control command from the TMS is given, the MV switch coil gets energized. The

super capacitor is charged through a 50 Ω , 10-W resistor. In the event of the 24 V control command failure, the super capacitors will continue to hold the MV switch coil by supplying the stored energy through the diode. The super capacitors shall continue to energize the contactor coil and, in turn, hold the power contacts of the switch in a closed condition for a period of 60 s. The control system utilizes this period to reduce the electrical load on the MV switch, so that it operates at no-load. The required logic is implemented in the logic controllers in the ROV, the TMS and the ship. By means of this, the probability of power failure to the ROV is reduced from 26.4% to 12.8%.

By means of this, the MTBF of the ROV-TMS docking process can be increased to 3.8 years.

e. By having redundancy in the Ship-ROV optic link and a serial link between the ROV and the TMS

The ROV and TMS communicate with the ship system through the optical-based Ethernet network. The topology in the base and improved cases is shown in Figure 8.

In the base case, the ROV-Ship network spans through the optical core in the tether cable and in the umbilical cable, with one pass in the TMS winch slip ring, and one in the deck storage winch slip ring and to the ship console. The TMS-Ship network spans through one pass in the TMS winch slip ring and in the deck storage winch slip ring and one core in the umbilical cable and then to the ship console.

The improved design incorporates the following:

- a. Redundancy is introduced in the ROV-Console communication link, by having an additional optical pass in the TMS tether and deck

storage winch slip rings, and additional optical cores in the tether and umbilical cables.

- b. A new RS485 link between the ROV and the TMS processors using the twisted pair electric cable in the tether cable is established.

From Figure 9, it can be seen that the ROV-Ship Console communication failure probability is 2.59%. By means of the improved architecture, the probability of failure is reduced from 2.59% to 0.434%.

With this improvement, the MTBF of the ROV-TMS docking process is increased to 4.6 years.

f. With voltage control devices on the top side and back-emf capacitors in TMS and ROV 300 V circuits

Thruster motors are operated using BLDC motor electronic controllers located in the ROV. Tether winch hydraulic motors are also operated by the BLDC motor controllers located in the TMS. The controllers are energized by 300-V power supplies in the ROV and the TMS. The BLDC motor power electronic systems are sensitive to excess voltage. To improve the reliability of the electronic controllers and subsequently the system reliability, voltage management systems are required.

Voltage management from the ship side is implemented as follows:

In the ROSUB 6000 system, the ship power at 415 V at 50 Hz is converted to 6,600 V at 460 Hz and transmitted through the 7,000-m-long umbilical cable and further to the ROV through the 400-m-long tether cables. The voltages are stepped down and rectified so as to obtain 300 V and 24 V DC, suitable for operating the propulsion thrusters and control systems. The ROV has an electrical load of 70 kW and the TMS has a total load of 20 kW.

When the ROV and TMS operate at full electric load, the system is designed in such a way that the shipside voltage is 6,600 V and the ROV and TMS end voltage is 6,000 V, with an umbilical cable voltage drop of 600 V. At no load condition, the TMS and the ROV systems experience a voltage of 6,600 V. This results in 10% increase in the 300 V circuits, which is not a healthy condition for the thruster motor power electric speed controller system.

This overvoltage condition is managed by implementing the automatic voltage compensation system on the ship side, using a high-frequency (hF) power converter, which works on the principle of v/f control philosophy. The control methodology is implemented using a proportional-integral-derivative (PID) controller, and the same is shown in Figure 10. At no load condition, the system draws only the reactive current required to charge the cable capacitance. When the ROV system gets loaded, there is an increase in the active component of the load current. The PID controller is tuned to provide the control input to the gate driver of the HF converter in such a way that 300 V is maintained constant at the ROV and TMS ends.

Voltage management on the subsea side is implemented as follows:

Thrusters and pump motors in the ROV and TMS are operated with brushless DC motors, which are controlled by power electronics. The controllers help in operating the systems at the required speeds. A BLDC motor in operation produces back-emf voltage (Brushless Direct Current Motor manufacturer recommendations for thruster Power System reference), at the pulse width modulation (PWM) frequency. This back-emf has the tendency to raise the overall 300 V DC

FIGURE 8

Schematic of the network.

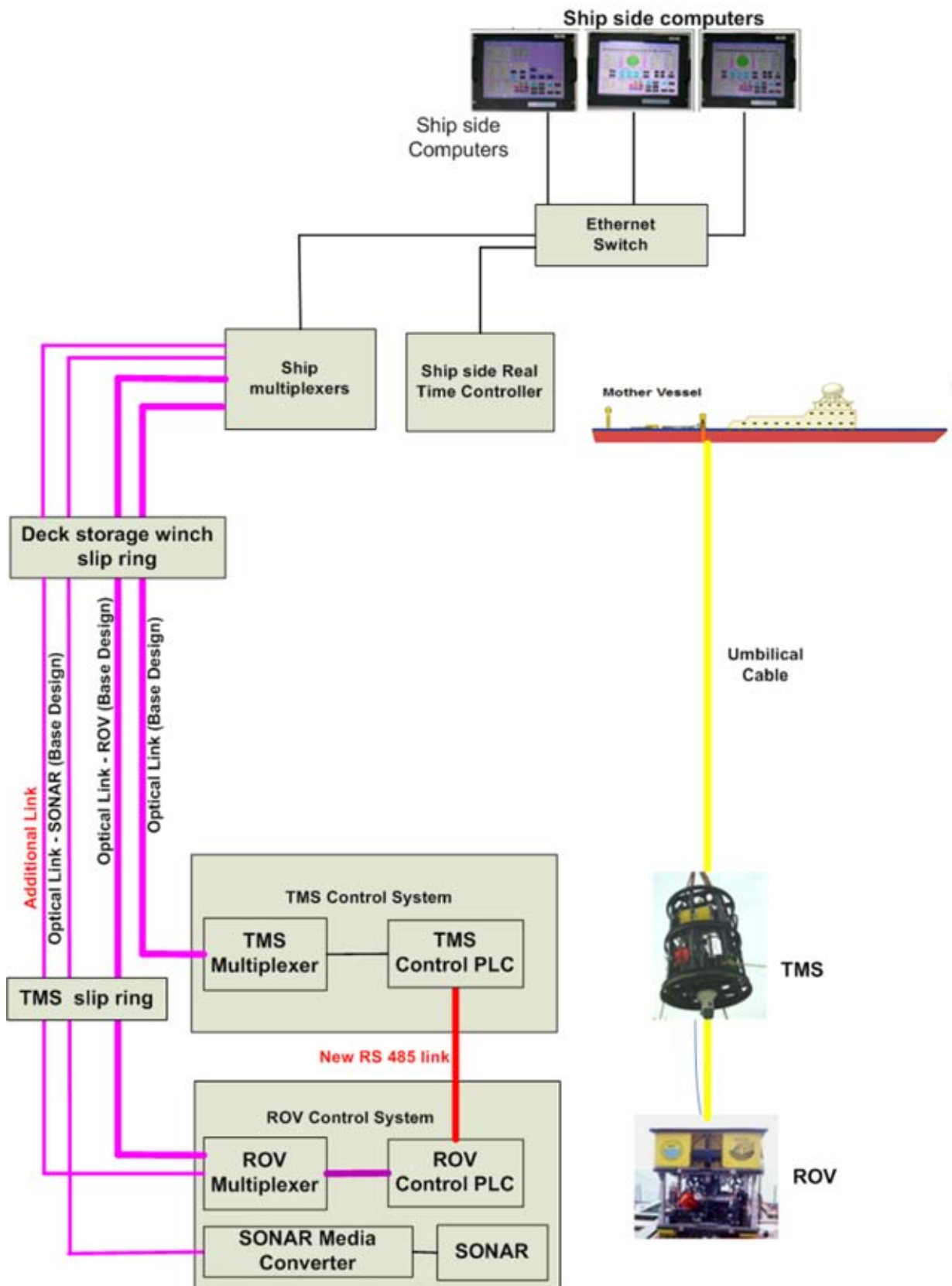
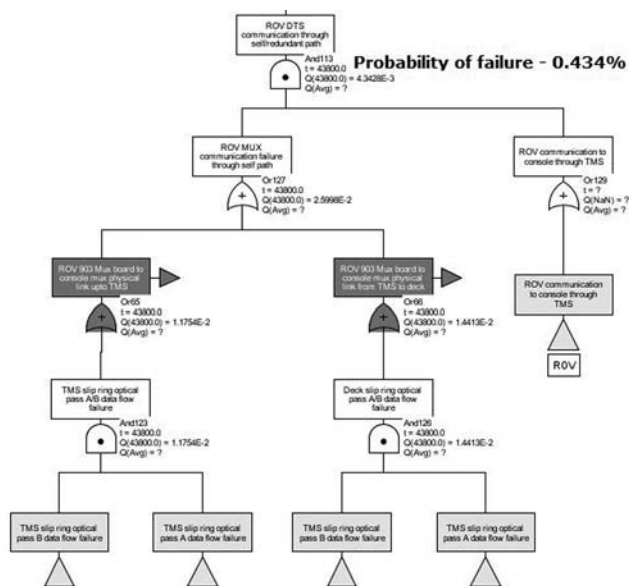


FIGURE 9

Tree indicating improvements in TMS-Console.



bus voltages to more than 600 V. This is detrimental to all the power electronics controllers connected to the 300 V DC network. To counter this back-emf, the DC capacitor banks of

80 and 20 mF are connected across the DC buses permanently in the ROV and TMS. In the base case, each BLDC motor power electronics controller has a probability of failure

of 19.52%. By ensuring proper operating voltage with the aid of the described voltage management devices the probability of failure for each BLDC motor controller is reduced to 16%. With this improvement, the MTBF of the ROV-TMS docking process is increased to 4.8 years.

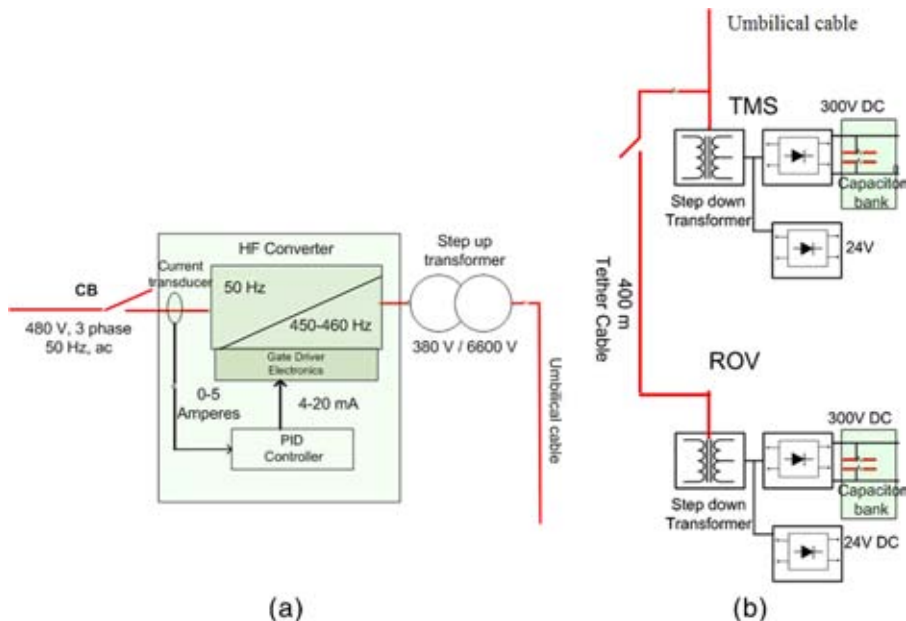
g. With redundant TMS pump

In the base case, the TMS system is equipped with one electric motor driven hydraulic pump, which is used for operating the tether cable winch drum. With a redundant pump, the winch operation due to the electrical and corresponding control system failure is reduced from 9.96% to 1%. The same can be seen from the failure trees in Figure 11.

With this improvement, the MTBF of the ROV-TMS docking process is increased to 4.9 years. The same can be seen from Figure 12. The stage by stage improvement in the probability of failure and the corresponding MTBF can be found from Table 3.

FIGURE 10

(a) Automatic Voltage Compensation implementation methodology. (b) Location of capacitors in the subsea side.



Type 4 Failure Scenario: Manipulator Operation Failure

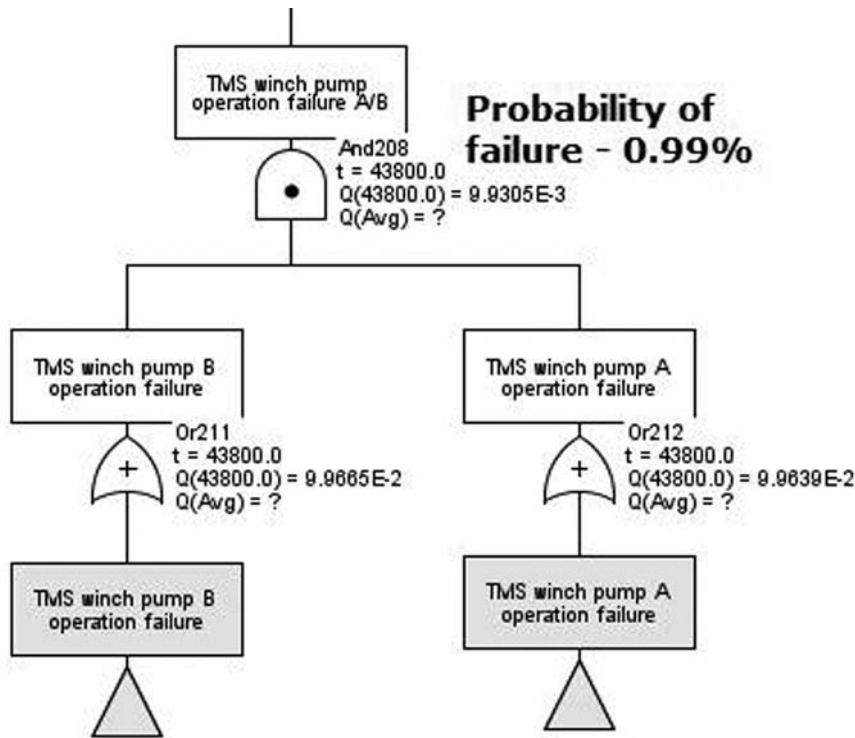
Normal Working Scenario

The ROV in the ROSUB 6000 is equipped with two manipulator arms with five and seven functions for carrying out subsea operations. The manipulators are operated by the personnel from the control console using joysticks. In addition to other vision systems, manipulator arms are equipped with a camera, which will give a real-time video feedback to the operating personnel. Figure 13 shows the work class ROVs with manipulators involved in different kinds of tasks.

The subsea operations depend on the mission objective and may involve tasks such as electric wet mate connector mate/de-mate, pipe line valve

FIGURE 11

Improvement in the failure rate with redundant pump improved case.



operations and pipe line sacrificial anode fixing.

Failure Scenario

The risk involved in these subsea operations varies widely (API RP14B, 2012; NORSOK standard, 2001). Figure 12 shows the ROV holding one end of the wet mate cable connector for mating with the fixed ROV panel. The other end of the cable could be a part of the permanent subsea installation. When the manipulator operation fails in this condition, the forced retrieval of the ROV by winding back the tether or main umbilical winch could damage the subsea installation. Such damages could turn disastrous for subsea oil and gas well-heads and manifolds. Thus, the ROV will be anchored to the subsea installation, with other systems connected to the ROV deployment vessel. To mitigate this situation, another intervention

FIGURE 12

Tree indicating improvement in the overall MTBF after introducing the redundant pump.

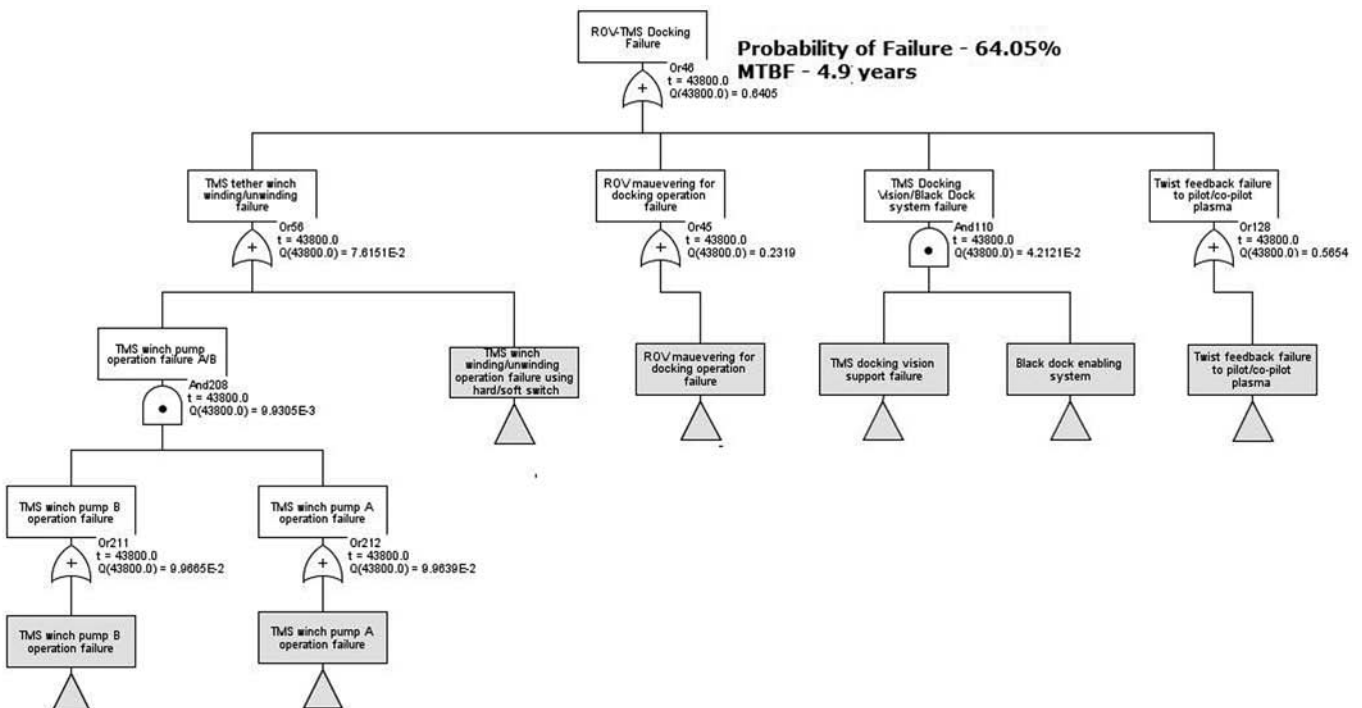


TABLE 3

MTBF Improvements with modifications for TMS-ROV docking failure case.

Improvement	Probability of Failure	MTBF
Base design case	92.48%	1.9 years
By means maintaining spares for ship based electric systems	78.9%	3.3 years
By operating ROV isolation circuit breaker as a switch	73.13%	3.8 years
By having redundancy in Ship-ROV optic link and a serial link between ROV and TMS	66.64%	4.6 years
With voltage control devices in top side and back-emf capacitors in ROV 300 V circuits	64.97%	4.8 years
With redundant TMS pump	64.05%	4.9 years

vehicle has to be dispatched for crisis management. A similar condition could occur if the ROV operates an oil pipe line isolation valve, which leads to valve damages and consequent oil leakages, if double barrier isolation is not provided. The same could be risks involved during salvage operations. Therefore, the reliability of the manipulator system has to be high.

Base Case

The following could lead to manipulator operations failure:

- Manipulator functional failure.
- Hydraulic pump motor electric system failure.
- Manipulator operation vision support failure.

In the base case, the ROV manipulator control failure is calculated to be

90.27% with a corresponding MTBF of 2.1 years. The network and hardware used for the ROV-TMS docking function is shared by the manipulator system. Therefore, the system improvements discussed for Type 3 ROV-TMS docking failure apply equally for reducing the manipulator operation failure.

It can be seen from Figure 14 that the manipulator operation failure probability is reduced to 55% with a corresponding MTBF of 6.2 years. The improvement with each change is listed in Table 4.

Maintainability Importance of Cable Twist Monitoring Mechanism

When the ROV is undocked from the TMS, the pilot will maneuver the

ROV to the location of interest. During the process, based on the ROV heading with respect to the TMS, the Kevlar-armored, torsionally balanced tether cable will be subjected to twisting, and the number of twists depend on the skill of the pilot, nature of the operation and the condition of the sea water currents. Further, as the TMS is connected to the deployment vessel, which is maintained in a dynamic positioning mode, it may also create heading changes for the TMS with respect to the ROV. Thus, the number of twists depends on the relative 360 deg. heading counts. When the ROV has completed the mission, it will be docked back to the TMS after winding back all the reeled out cable. Tether cables are designed to withstand specific twists per meter length (Buckham et al., 2003; Sakamoto et al., 2008). When the number of twists/meter exceeds the design limit, the cable sheath and, hence, the cable will be damaged. Thus, to avoid cable damage, the pilot has to ensure that there is no residual twist on the cable before docking.

To aid in a hassle free dock, the following parameters are monitored by the control system:

- ROV heading counts provided by the heading sensor in the ROV.
- TMS heading counts provided by the heading sensor mounted in the TMS.
- Length of the cable reeled out of the drum, which is provided by the tether cable layer counter.
- Cable tension which is provided by the load cell sensor mounted in the winch.

As the heading sensors and electronic counting are done in the ROV and TMS, a power interruption to the ROV and TMS will result in the loss of twist count information. Even

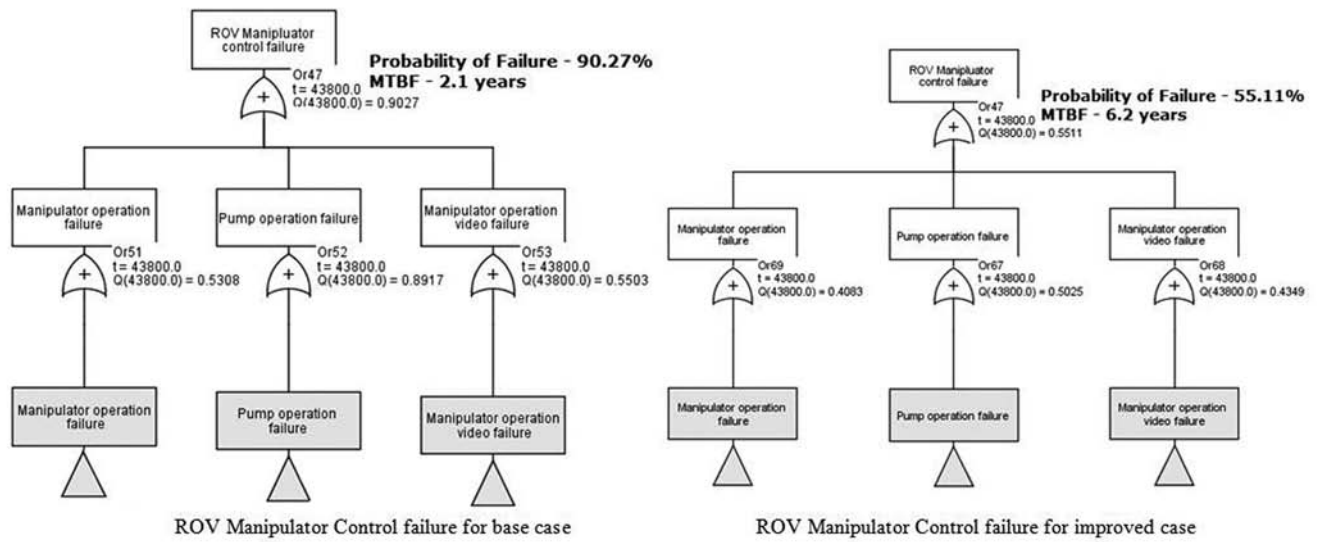
FIGURE 13

Typical ROV manipulator in operation (Courtesy: WHOI and MBARI websites).



FIGURE 14

ROV manipulator control failure for the base and improved cases.



though the last logged value could be made available in the shipside, once the power resumes, the number of heading changes undergone by the ROV during the interruption period will not be known. Therefore, the residual twists on the cable will not be available to the pilot during the final docking stage. To overcome this problem and to avoid power interruption to the heading sensor and monitoring electronics, a sea battery is used as a backup power in the ROV.

Figure 15 shows the heading counts monitoring mechanism and the sea battery in the ROV.

By means of introducing the sea battery, the probability of power failure to the ROV control systems is reduced from 15% to 5%. Thus, the twist feedback information failure probability to the pilot is reduced from 60% to 55%.

Table 5 shows the MTBF of the ROV-TMS docking process and manipulator operation with different

failure rates of the tether cable. This is given to indicate the impact of the tether cable failure on the overall system MTBF.

As it is understood that the tether cable is an important component having a significant role in the MTBF, systems are incorporated that can measure the cable electric insulation and optical losses in the system online. As the cable performance depends on the operating ambient condition, the inclusion of this mechanism will be useful for the system safety as well as for preventive maintenance action.

TABLE 4

MTBF improvements with modifications for manipulator function failure case.

Improvement	Probability of Failure	MTBF
Base design case	90.27%	2.1 years
By means of maintaining spares for ship based electric systems	71%	4.1 years
By operating ROV isolation circuit breaker as a switch	64.7%	4.8 years
By having redundancy in Ship-ROV optic link and a serial link between ROV and TMS	64%	5.0 years
With voltage control devices in top side and back-emf capacitors in ROV 300 V circuits	55.11%	6.2 years

Preventive Maintenance Decision Support

Table 6 shows the probability of failure in percentage for the ROV-TMS docking process for different periods. The table also details the role of the subcomponents.

The cells with data in bold fonts indicate the failure rates of the components whose failure probabilities are higher.

FIGURE 15

ROV and TMS having independent heading sensing systems and the location of the sea battery in the ROV.

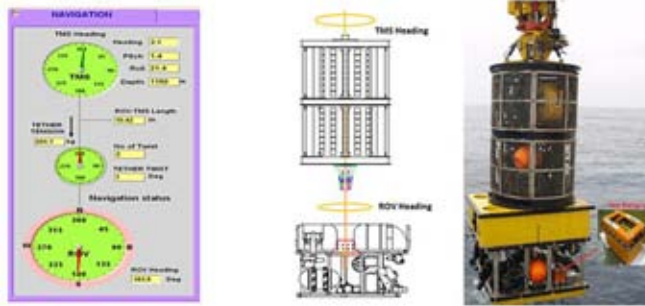


TABLE 5

Impact of tether cable failure in failure cases under study.

Times Tether Failure FIT	ROV-TMS Docking		Manipulator Operation	
	Probability of Failure (%)	MTBF (years)	Probability of Failure (%)	MTBF (years)
×1	64	4.9	55	6.3
×2	65	4.8	56	6.1
×5	67	4.5	58.5	5.7
×10	70	4.1	62.4	5.1
×20	75	3.6	67	4.5

TABLE 6

Maintenance decision support table.

System/Component	Probability of Failure in %				
	1 year	3 years	5 years	10 years	15 years
ROV-TMS docking	18.1	45.4	64.0	87.6	93.5
Subcomponents					
Cable termination	0.064	0.18	0.30	0.60	0.90
Tether cable	0.38	1.14	1.9	3.76	5.59
Umbilical cable	0.21	0.63	1.06	2.11	3.15
HF converter	16.1	41.1	58.6	82.9	92.9
LV isolator	0.32	0.98	1.6	3.24	4.82
HV transformer	0.58	1.7	2.9	5.72	8.46
BLDC motors	0.39	1.18	2.01	3.9	5.8
Electrical slip ring	1.54	4.56	7.48	14.4	20.8
Power contactor	0.4	1.3	2.2	4.28	6.35
Plasma display	0.44	1.2	2.31	3.18	4.73

continued

Preventive Maintenance

Schedule Summary

Umbilical and Tether Cables

The longevity of the tether cable depends on the handling and electrical stresses. Handling stresses are due to twisting and can be optimized by skilled piloting. The failure rates of the umbilical and tether cables were obtained from OREDA and are used for the calculations. Andrew Bowen et al of Woods Hole Oceanographic Institution (WHOI) and Ed Mellinger et al. of Monterey Bay Aquarium Research Institute (MBARI) performed the insulation life testing of field-aged samples of cables used in MBARI Tiburon ROV and WHOI Jason ROVs, which have an accumulated time of 6,700 h in 230 dives. The tests identified factors affecting the insulation stress at the operating voltage and high hydrostatic pressures. It was calculated that the cable could survive for 22.8 years under dry aging conditions but would survive only for 7.6 years when operated at 400 Hz

TABLE 6

Continued

System/Component	Probability of Failure in %				
	1 year	3 years	5 years	10 years	15 years
Computers	0.45	1.35	2.2	4.45	6.6
PLC processor with memory	0.3	0.71	1.05	1.8	2.5
NI CPU IO modules	0.021	0.06	0.1	0.2	0.31
Thrusters BLDC motor power electronic controller	0.37	0.82	1.03	2.03	2.31
Fuses	0.008	0.026	0.043	0.087	0.13
Halogen lamp	0.017	0.052	0.087	2.13	2.59
Multiplexer power board	0.025	0.076	0.12	0.025	0.38
Multiplexer data board	0.079	0.23	0.39	0.79	1.18
Multiplexer video board	0.007	0.02	0.03	0.07	0.1
Real-time controller	1.11	3.31	5.46	10.64	15.53
Sea battery	8.8	24	37	60	75
Proximity sensor	0.052	0.15	0.26	0.52	.78
Fiber optic rotary joint	1.92	5.66	9.26	17.6	25.3
Photonic inertial navigation sensor	25.3	58.4	76.7	96.4	98.8

in a continuous deep water environment. Based on this experience, we have estimated the tether cable replacement period for the ROSUB6000 as 10 years.

Sea Battery

A sea battery has a failure rate of 8.8% in the first year of operation.

The failure rates are used from a standard obtained from the studies made for the U.S. Department of Energy-Energy Storage Studies program (DeAnda et al., 2004), which considers battery failure rates, when used in an UPS and similar applications. Lead acid battery life depends highly on the

number of charge-discharge cycles and the depth of discharge. In our application, the battery is subjected to very minimal stresses in terms of the depth of discharge and duty cycle. Based on this experience, we have estimated the sea battery replacement period for the ROSUB 6000 as 3 years.

TABLE 7

Summary of failures with probabilities of failure.

Failure Type	Failure Description	Base Case		Improved Case	
		Probability of Failure	MTBF	Probability of Failure	MTBF
1	Camera not available for operation in ROV	83.51%	2.8 years	7.25%	>10 years
1	Halogen Lamp not available for operation in ROV	83.40%	2.8 years	7.12%	>10 years
2	Visual survey failure	98.86%	1.1 years	53.34%	6.6 years
2	SONAR bathymetric survey failure	97.87%	1.2 years	78.05%	3.3 years
2	Gas hydrate survey failure	98.89%	1.1 years	53.73%	6.5 years
3	ROV-TMS subsea docking failure	92.48%	1.9 years	64.05%	4.9 years
4	ROV manipulator operation failure	90.27%	2.1 years	55.11%	6.2 years

Summary and Conclusions

This paper describes the methodology of RAM studies carried on the ROSUB 6000 deep water work class ROV system. Table 7 summarizes all types of failures studied, the probability of failures and the MTBF in the base case and improved cases.

The technical challenges in achieving the best possible MTBF for the critical failures are explained in detail. The maintenance decision support table details the operational personnel for the upkeep of the systems during the indicated maintenance interval, so that the highest possible reliability is maintained during the mission period. The importance of monitoring the tether cable healthiness during normal and winding operations, and the systems implemented for effectively monitoring and maintaining the tether cable's operational and functional healthiness, using the tether cable pay-out, vehicle heading, electric insulation and optical performance sensors with the aid of a sea battery, is also discussed.

Acknowledgments

The authors gratefully acknowledge the support extended by the Ministry of Earth Science, Government of India in funding this research. The authors also wish to thank the other staff involved in the project for their contribution and support.

Corresponding Author:

Narayanaswamy Vedachalam
National Institute of Ocean Technology
Chennai, India
Email: veda1973@gmail.com

References

Al-Ramadhan, M., & Abido, M.A. 2012. Design and simulation of super capacitor en-

ergy storage system. In: International Conference on renewable energies and power quality (ICREPQ), Spain, 28–30 March 2012, pp. 1-4. Spain: European Association for the Development of Renewable Energies, Environment and Power Quality (EA4EPQ).

API RP14B, American Petroleum Institute. 2012. API Recommended Practices for Design, Installation, Repair and Operation of Sub-surface System. Pennsylvania: American Petroleum Institute. 30 pp.

Barrade, P., & Ruffer, A. 2003. Current capability and power density of supercapacitors: Considerations on energy efficiency, ref. ISBN 90-75815-07-7. Pages 3,4.

Buckham, B.J., Driscoll, R.F., Nahon, M., & Radanovic, B. 2003. Three dimensional dynamic simulation of slack tether cable in an ROV system. In: Proceedings of ISOPE 2003, Hawaii, USA, Department of Mechanical Engineering, Vol. 2, pp. 2-3. Victoria BC, Canada: University of Florida.

DeAnda, M.F., Miller, J., Moseley, P., & Butler, P. 2004. Reliability of Valve-Regulated Lead-Acid Batteries for Stationary Applications. California: Sandia National Laboratories. 68 pp. <http://dx.doi.org/10.2172/918779>.

FIDES Guide. 2009. Reliability Methodology for Electronic Systems. FIDES group. 465 pp.

IEEE. 1997. IEEE Standard 493-1997, Recommended Practice for the Design of Reliable Industrial and Commercial Power Systems, IEEE Standards Boards. Available at: <http://standards.ieee.org/findstds/standard/493-2007.html>.

Lemofouet, S., & Rufer, A. 2006. Hybrid Energy Storage system based on compressed air and supercapacitors with maximum efficient point tracking. IEEE T Ind Electron. 53(4):1105-15.

Mallika, S., & Saravanakumar, S. 2011. Review of ultracapacitor—Battery interfaces for energy management system. Int J Eng Technol. 3(1):2-3.

Manecius, S., Ramesh, R., Subramanian, A.N., Sathianarayanan, D., Harikrishnan, G., Jayakumar, V.K., ... Amiragov, A. 2010. Technology tool for deep ocean exploration—remotely operated vehicle. In: Twentieth

International Offshore (Ocean) and Polar Engineering Conference, pp. 206-212. Beijing, China: International Society of Offshore and Polar Engineering (ISOPE).

Mellinger, E., Aabo, T., Bowen, A., Katz, C., & Petitt, R.A., Jr. 2010. High Voltage Testing of an ROV electro-optic tether cable. MTS. 28(9):4-5.

NORSOK standard. 2001. Risk and Emergency Preparedness Analysis. Norway: Norwegian Technology Centre.

OREDA AUTOR. 2003. OREDA. SINTEF. 835 pp.

Paulo, F.R., Brian, K.J., Maiiesia, L.C., Ayşen Basa, A., & Yilu, L. 2001. Energy Storage Systems for Advanced Power Applications. IEEE Proceedings. 89(12):3-4.

Ramesh, R., Jayakumar, V.K., Manecius, S., Doss Prakash, V., Ramadass, G.A., & Atmanand, M.A. 2010. Distributed Real Time control systems for deep water ROV (ROSUB 6000). In: 7th International Conference on Computational Intelligence, Robotics and Autonomous Systems (CIRAS) in 13th FIRA Robot World congress, Proceedings, pp. 33-40. New York: Springer.

Rufer, A., Hotellier, D., & Barrade, P. 2004. A super capacitor based energy storage substitution for voltage compensation in Weak Transportation networks. IEEE T Power Deliv. 19(2):629-36.

Sakamoto, K., Fujimoto, Y., & Osawa, H. 2008. Development of fatigueless umbilical cable for full ocean depth 12000 m. In: Marine cable Development Section Engineering Department, Furukawa Electric Co. Ltd, Japan, Advanced Underwater Vehicle R and D Group, JAMSTEC, Japan in International wire and cable 57th Symposium proceedings, pp. 2-4. Eatontown, NJ: IWCS Inc.

Shukla, A.K., Sampath, S., & Vijayamohanan, K. 2001. Electro-chemical capacitors: Energy Storage and beyond batteries. Curr Sci. 79(12):37-38,41.

Tecnadyne Application Note AN601. 2006. General Power System Wiring Practices

Applied to Tecnydyne DC Brushless Motors.
San Diego, CA: Tecnydyne, Inc.

Thomas, A.P. 2008. Oil Circuit Breaker
Diagnostics. In: 7th Annual Weidmann
Technical conference, pp. 1-2, 5. New Orleans:
Weidmann Inc.

U.S. Department of Defense. 1991. Military
Handbook, Reliability Prediction of Elec-
tronic Equipment. Washington, DC: Author.

Weddell, A.S., Merrett, G.V., Kazmierski,
T.T., & Al-Hashimi, B.M. 2011. Accurate
supercapacitor modeling for Energy harvesting
wireless sensor nodes. IEEE T Circuits-II.
58(12):2. [http://dx.doi.org/10.1109/TCSII.
2011.2172712](http://dx.doi.org/10.1109/TCSII.2011.2172712).

Anchor Drop Tests for a Submarine Power-Cable Protector

AUTHORS

Han-Sam Yoon

Research Center for Ocean Industry and Development, Pukyong National University, Busan, South Korea

Won-Bae Na

Department of Ocean Engineering, Pukyong National University, Busan, South Korea

Introduction

Anchoring activities—colliding and dragging—have become the largest cause of submarine cable faults in recent years (International Cable Protection Committee, 2009). To prevent power cable failures from this cause, the International Cable Protection Committee (ICPC) suggests the use of automatic identification systems (AISs) for vessels. Nevertheless, the use of AISs is not applicable to small ships, and their use has not spread rapidly in some developing and even industrialized countries (Coffen-Smout & Herbert, 2000; International Cable Protection Committee, 2009; Wagner, 1995). This is a serious issue, because cable failures can lead to significant inconvenience to residents, cutting communications, power, and water supplies. For example, in 2010 the submarine power cable linking Shanghai and Shengsi Island, Zhejiang, was fouled and broken completely as a result of ship anchoring. The island lost its power supply for 4 days, and then electricity was only partially restored to about 90,000 residents using diesel generators (Jie &

ABSTRACT

Submarine power cables are widely used for power transmission, such as between mainlands and offshore islands and from offshore wind farms to on-land substations. There are several ways to protect power cables from accidental loads. Protection includes concrete blankets, sand bags, bundles, tunnel-type protectors, and trenching. However, no design standard for power-cable protectors is currently available because of the varieties of cable protection solutions and man-made or natural hazards to submarine power cables. Thus, this paper presents anchor drop tests for a newly designed, matrix-type submarine power-cable protector assembled with reinforced concrete blocks, to make a safety assessment. Marine environments were surveyed at the target site and simulated in the test set-up. A 2-ton stock anchor was selected as the colliding object, and a 25-ton crane was prepared to drop the anchor. Preliminary tests were performed to investigate the effect of soil composition and protector arrangements on the test results. Finally, four field anchor drop test scenarios were designed, carried out, and analyzed, and a safety assessment was made for the submarine power cable. From the tests, it was found that, in addition to falling distances, the soil composition and saturation were significant factors for the settlement depth and damaged areas. Considering the settlement depth of soils, the damaged areas of the concrete blocks, and the damaged state of the pipes (safety zone), all of the test results showed that the mattress failed to protect the power cable from the anchor collision. The deformation, damage, and breakage of the pipe, which simulated the safety zone of the power cable, gave clues as to the reasons for the failure.

Keywords: anchor drop, field test, submarine power-cable protector, stock anchor

Yao-Tian, 2012). Similarly, in 2006, one of two submarine power cables connecting the main Korean Peninsula to Jeju Island was damaged by ship anchoring activities. This event caused a power-supply blackout for the whole of Jeju Island, resulting in severe inconvenience to nearly 570,000 residents and 30,000 tourists. Fortunately, no loss of human life was reported during that period, likely because the outage lasted only 2.5 h during the daytime (Woo et al., 2009). However, it was certainly undesirable because tourism is important to the

island, and the power-supply blackout caused a simultaneous suspension of water availability.

Such accidents are also applicable to the power cables transporting offshore wind power to a national grid on land. Moreover, given the current increasing trends in offshore wind-energy projects, offering security against many energy-supply emergencies—whether natural or man-made—is a significant issue. Thus, there has been much work to assess the causes of damage and to improve cable protection. The possible causes—anchor collision

and dragging—have been investigated and design criteria for submarine power-cable protectors have been improved in South Korea (Woo et al., 2009). This extensive research has included computer simulations of anchor collision and dragging on cable protectors (Woo & Na, 2010). However, numerical simulations alone are not fully reliable because it is not easy to make definite safety or failure assessments based solely on numerical results, such as stress contour and deformation patterns.

Thus, in this study, field anchor drop tests of a newly designed submarine power-cable protector were investigated. For this purpose, the following works were carried out: (1) material preparation and test set-up, (2) field anchor drop tests, and (3) safety assessment. For material preparation, a mattress-type power-cable protector was selected, designed to allow adjustment of its horizontal and vertical lengths by controlling the number of reinforced concrete blocks used. This adjustability allows the blocks to be assembled in the field, using hooks and links, into different sizes of protectors in a designated field environment after installing the power cables on the seabed. In the field tests, first, the terminal velocity of a 2-ton stock anchor in water was calculated and converted the velocity into a corresponding falling distance in air. Second, the soil properties were surveyed at the target site—Haenam, in the Southwest corner of the Korean Peninsula. Third, by recognizing the fundamental behaviors of the protector, an experimental set-up was designed.

This study should be relevant to the offshore wind power industry, where submarine cables take power to an offshore transformer and the offshore transformer converts the elec-

tricity to a high voltage (about 33 kV) and sends it 8–16 km to a national or international grid at a substation on land (Byrne & Houlsby, 2012; Esteban et al., 2011; Yamabuki & Kubori, 2012). Because wind speeds tend to increase significantly with distance from land, the offshore wind resources can generate more electricity than wind resources at adjacent land-based sites. This means the length of the power cables will increase, and so will the need for cable protection. The test process and results can provide a valuable checkpoint for managing the electrical power supply from the mainland to an island and from an offshore wind farm to an on-land station.

Current Practice

In South Korea, there is no a specific design guideline and standard for power cable protectors. After KT Submarine (a Korean company) was established in 1994, submarine power cable installation and maintenance have been practiced under the supervision of the Korea Electric Power Corporation (KEPC). However, the design practice has not yet been established because of the lack of data and studies. Although all of the power cables in South Korea have been operated and maintained by KEPC since 1979, the first major issue on power cable design came up in 2006, after the failure of the cable between Henam and Jeju. From the accident, it was found that the concrete mattresses installed were not good enough to endure current anchor specifications and activities. That is why this study investigated the newly designed cable protector. With the series of field anchor collision and dragging tests, the Korean government is focusing on a

safety evaluation guideline for submarine power cable protection, and associated projects will launch in 2013. The safety guideline will be completed in 2015.

There is no international design guideline and standard. At the Subsea Power Cables Conference in London (April 2012), a roundtable discussion dealt with the necessities of international standards set for cable installation projects. The burial protection index was suggested as a power cable protection solution, but this method is conceptual. Sharples (2011) emphasized the fact that different cable protection technologies developed over time lend themselves to specific conditions and scenarios. These include rock dumping, preformed concrete mattress, assisting natural sedimentation with frond mats, durable padding or grout-filled bags, external plastic (polyurethane) or metal sheathing on the cable, heavy armoring built into the cable itself, and custom solutions. Det Norske Veritas (DNV) published the recommended practice DNV-RP-F401 (Electrical Power Cables in Subsea Applications, 2012). The recommended practice (RP) focuses not on cable protection but on the electrical power cables themselves. Because of the varieties in cable protection solutions and man-made or natural hazards to submarine power cables, it is hard to set the design guideline and standard. Therefore, at the moment, most work focuses on mitigating the risk of cable damage through cable protection solutions and planning the best cable route, etc.

However, Det Norske Veritas published a related recommended practice DNV-RP-F107 (Risk Assessment of Pipeline Protection, 2010). This recommended practice has a chapter called “Pipeline and Protection Capacity,”

which deals with steel pipeline, flexible pipeline, umbilicals, and different protection methods. Here, umbilicals are typically a complex compound of tubing, electrical wires, reinforcement, and protective layers. In other words, umbilicals consist of hydraulic lines used to transfer chemicals and fluids and electric and fiber optic components to monitor pressure, temperature, flow and vibration, while submarine power cables are used for transmission of electric power. Therefore, the recommended practice can be useful to develop the design practice of submarine power cable protection.

Material Preparation and Test Set-up

A dimensional description of the power-cable protector is shown in Figure 1. The proposed mattress-type protector was assembled from 70 blocks (5 EA \times 14 EA), as shown in Figure 2a. Here, the first notation (5 EA) indicates the number of blocks in the y direction (width), and the second notation (14 EA) indicates the number of blocks in the x direction (length). There were three types of blocks—left, basic, and right—meaning that each column consisted of one left, one right, and three basic

FIGURE 1

Dimensional description of the mattress-type power-cable protector.

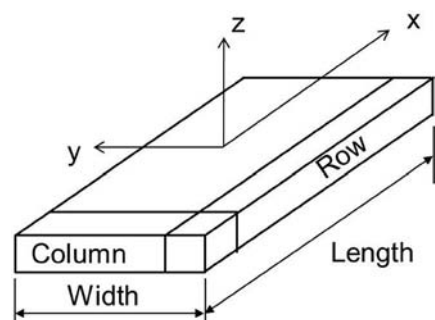
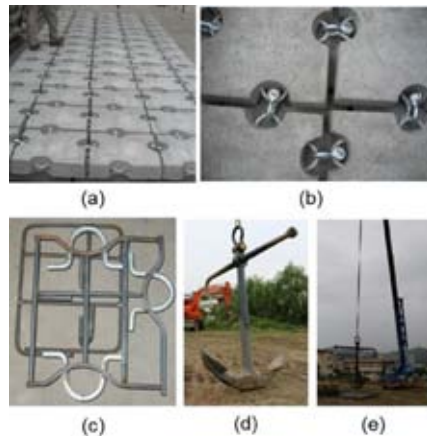


FIGURE 2

Materials and facilities: (a) assembly of 70 blocks (5 EA \times 14 EA), (b) circular links and arch hooks used to assemble each block, (c) array of reinforcing bars and hooks in each concrete block, (d) 2-ton stock anchor, and (e) 25-ton crane.



blocks between the left and right blocks. These arrangements were designed to change the size of the protector. The assembly could be performed on a vessel using circular links and arch hooks (Figure 2b).

Each block was 0.5 m (length) \times 0.5 m (width) \times 0.1 m (depth) and was manufactured from reinforced concrete to increase its compressive and tensile strengths. The design concrete compressive strength was 52 MN/m². The reinforcement array is shown in Figure 2c. Here, the tensile strength of the reinforcing bars (SD 400) was 560 MN/m², the diameter was 13 mm, and the entire length of the reinforcing bars was 6.274 m in each concrete block. The hooks were zinc-coated, cold-drawn, round steel bars with a tensile strength of 686 MN/m² and a diameter of 16 mm. Once the reinforced concrete blocks were manufactured, these arch-shaped hooks were linked by the circular links (Figure 2b) so that the blocks were assembled and extended to the mattress. These arch-

shaped hooks were connected to the reinforcing bars (Figure 2c).

Concrete is often considered to be the ultimate construction material, because of its considerable strength, relatively low cost, and virtually limitless design capabilities. When subjected to an impact or collision, concrete is generally submitted to both a multi-axial state of stress characterized by a high mean stress and high strain rates. It is known that the only material parameter governing impact resistance of concrete structures is based on the uniaxial unconfined compressive strength of concrete (Daudeville & Malécot, 2011). Therefore, it is necessary for concrete to have a significant increase in its toughness, hence impact resistance (Liu et al., 2012).

Field drop tests on the protector were carried out in an open space. For the field-test set-up, a 2-ton stock anchor (KS V3311, 2006) and a 25-ton crane (Figures 2d and 2e) were prepared. To analyze the movements of the protector and anchor, a camcorder was used.

It should be noted here that, instead of a water environment, tests were carried out on land because otherwise it would be quite difficult to observe the state of the protector during the anchor drop process. To accommodate the water environment, the effect of water resistance on the anchor was considered in the test by facilitating the soil conditions of the target sites and converting the terminal velocity of the anchor in water into a falling distance of the anchor in air.

To simulate the soil conditions on the target seabed (Haenam), the soils were surveyed and the soil compositions were obtained using the American Association of State Highway and Transportation Officials (AASHTO) soil classification method (Table 1).

TABLE 1

Soil composition at the target site.

Ground	Sediment Texture (%)		
	Gravel	Sand	Silt and Clay
Case 1	49.62 (≈ 50)	49.88 (≈ 50)	0.5 (≈ 0)
Case 2	2.89 (≈ 3)	96.81 (≈ 97)	0.3 (≈ 0)

However, in the field tests, approximate values were used instead of the exact percentage of each sediment texture (Table 1). Case 1 had 50% gravel and 50% sand, while Case 2 had 3% gravel and 97% sand. In addition to the composition, the soils were classified into dry and saturated states by adjusting their water content. However, the degree of saturation was not recorded in detail; only rough descriptions—dry and saturated—were used in the tests.

Considering the tidal effects on the water depths at the target site, it was assumed that the terminal velocity was the design velocity of the stock anchor. However, in the calculations, it was not easy to determine the drag coefficient of the stock anchor because of its unusual shape. Thus, a range of drag coefficients, from 0.7 to 1.7 (Table 2), was introduced to investigate a range of terminal velocities. By making use of the principle of energy conservation, the falling distances in air were calculated, ranging from 1.78 to 4.32 m. Because of the maximum value of 4.32 m (4.96 m in water), a falling distance of 5 m was considered in the field tests. This selection was conservative in the sense that the corresponding drag coefficient to the maximum falling distance was 0.7, which is much smaller than the drag coefficients of a C-section (2.30 or 1.20), square prism (2.05 or 1.05), and disk (1.17) (Fox et al., 2004). However, it should be emphasized here that the protector was designed

to be located not only at the target site but also at other sites. Thus, in addition to 5 m, 9 m was used as a falling distance in the tests.

Considering the added mass effects on the tests, it should be noted that the stock anchor reaches the falling state with a constant falling velocity (the terminal velocity) in the target sites. In other words, the anchor is not accelerating before colliding. As this happens, the effect of the added mass on the anchor is not significant. Therefore, the effects of the added mass on the test results were not considered in the test. In addition, because of the presence of water, pressure effects in deep water and the resulting soil behavior are other factors to be considered in the tests. However, their effects on

the test results were assumed minor; hence, these were not considered in the tests.

Before carrying out the field tests, two preliminary tests were performed, designed as shown in Table 3, to pinpoint the measuring points and deformation patterns. The effects of variations in the soil composition (Case 1 and Case 2) and mattress specifications (3 EA \times 3 EA and 5 EA \times 14 EA) were also investigated. Other factors, such as the soil condition and falling distance, were fixed as dry and 10 m, respectively. In the preliminary tests, the safety assessment was made through the failure of blocks and the resulting settlement depth and shape. Unlike the main test program, a plastic pipe under the mattress was not installed.

Finally, a criterion was decided for the safety or failure assessment of the protector after collision with the 2-ton stock anchor for the main test program. For the assessment, a safety zone was introduced along the center of the power-cable location. To simulate this, a plastic pipe was embedded below the

TABLE 2

Terminal velocity and falling distance with respect to drag coefficient.

Drag Coefficient	Terminal Velocity (m/s)	Energy (J)	Falling Distance (m)
0.7	9.856	84755	4.32
0.8	9.219	74153	3.78
0.9	8.692	65918	3.36
1.0	8.246	59326	3.03
1.1	7.682	53930	2.75
1.2	7.528	49445	2.52
1.3	7.232	45633	2.33
1.4	6.969	42374	2.16
1.5	6.733	39553	2.02
1.6	6.519	37078	1.89
1.7	6.324	34893	1.78

TABLE 3

Preliminary drop tests.

Identity	Soil Condition	Soil Composition	Falling Distance	Mattress Specifications	
				No. of Rows	No. of Columns
P1	Dry	Case 1	10 m	3	3
P2	Dry	Case 2	10 m	5	14

TABLE 4

Anchor drop test scenarios.

Identity	Soil Condition	Soil Composition	Falling Distance	Mattress Specifications	
				No. of Rows	No. of Columns
T1	Dry	Case 1	5 m	5	14
T2	Dry	Case 1	9 m	5	14
T3	Saturated	Case 2	5 m	5	14
T4	Saturated	Case 2	9 m	5	14

mattress. The mattress was assumed to have failed if the anchor and broken concrete blocks delivered a compressive force to the pipe. In total, four scenarios were designed to provide a safety assessment of the protector under anchor drops with the two-ton stock anchor (Table 4).

Drop Test Results

The field tests, described in Tables 3 and 4, were carried out on open land at Pukyong National University, located in Busan. As described earlier, a 25-ton crane was used to drop the two-ton stock anchor to the protector. Before carrying out the four drop scenarios (Table 4), preliminary drop tests were performed to investigate damage patterns, determine measuring points, and assess the effects of soil compositions. Figure 3 shows a typical colliding sequence or process. In all of the tests, the same colliding process occurred, as follows.

A detailed description of P1 is provided in Table 3. For the test, first, the dry soil composition of Case 1 was prepared below the mattress and the stock anchor was dropped from 10 m. In this case, a 3 EA × 3 EA mattress was prepared instead of a 5 EA × 14 EA. As a result (Figure 4), the blocks near the collision area were broken, and three blocks were crushed (Figure 4a). After removing the protector (Figure 4b), the measured maximum vertical soil settlement was 7 cm. Despite the relatively shallow settlement, the protector failed to protect the power cable be-

FIGURE 3

A typical anchor drop process between the anchor and protector.

**FIGURE 4**

Test result P1 (falling distance: 10 m, soil: Case 1, mattress 3 EA × 3 EA).

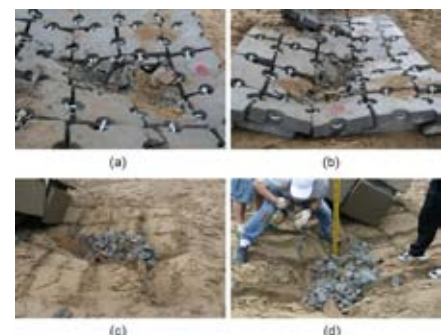


cause of the broken blocks under the mattress and because of the settlement depth and shape.

A detailed description of P2 is provided in Table 3. For the test, the dry soil composition of Case 2 was prepared below the mattress and the stock anchor was dropped from 10 m. Here, a 5 EA × 14 EA mattress was prepared. The protector was damaged (Figure 5), and the blocks near the collision area were broken. Two blocks were totally crushed (Figures 5a and 5b). After removing the protector (Figures 5c and 5d), the measured maximum vertical soil settlement was 37 cm. The vertical settlement differed from that in P1, although the falling distance of T1 and T2 was the same. It happened because of the difference in the soil composition between T1 and T2. That is, the soil composition of Case 2 (gravel 3% and sand 97%) was much weaker than

FIGURE 5

Test result P2 (falling distance: 10 m, soil: Case 2, mattress 5 EA × 14 EA).



that of Case 1 (gravel 50% and sand 50%). For Case 2, the mattress protector also failed to protect the power cable because of the broken blocks under the mattress and the settlement depth and shape.

Considering T1 (Table 4), the dry soil composition of Case 1 was prepared below the mattress and the stock anchor was dropped from 5 m (Figure 6a). The mattress arrangement was 5 EA × 14 EA. Blocks near the collision area were broken (Figure 6b), resulting in a damaged area that was 90-cm long and 17-cm wide, for a total area of 1,530 cm² (Figure 6c). After removing the protector, it was found that the measured maximum vertical soil settlement was about 5 cm and the embedded pipe was damaged (Figure 6d).

Considering T2 (Table 4), the dry soil composition of Case 1 was prepared below the mattress and the stock anchor was dropped from 9 m (Figure 7a). In this case, a 5 EA × 14 EA mattress was prepared. The blocks near the collision area were broken (Figure 7b), resulting in a damaged area that was 90-cm long and 28-cm wide, for a total area of 2,520 cm² (Figure 7c). After removing the protector, it was found that the measured maximum vertical soil settlement was 7 cm and the embedded pipe was severely damaged (Figure 7d).

FIGURE 6

Test result T1 (falling distance: 5 m, soil: Case 1, mattress 5 EA × 14 EA).

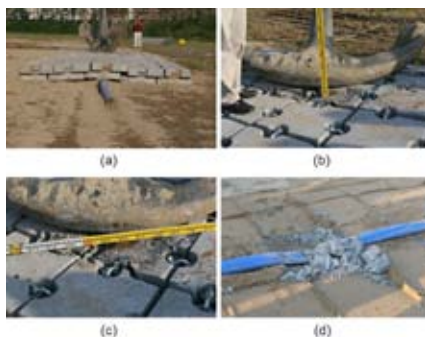
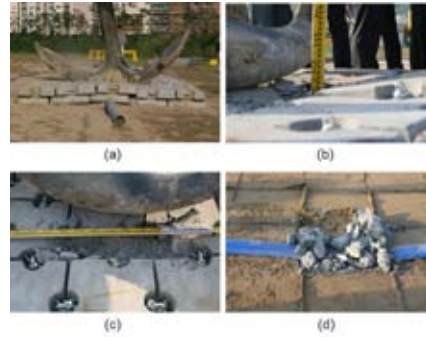


FIGURE 7

Test result T2 (falling distance: 9 m, soil: Case 1, mattress 5 EA × 14 EA).



maximum vertical soil settlement was 7 cm and the embedded pipe was severely damaged (Figure 7d).

Considering T3 (Table 4), the saturated soil composition of Case 2 was prepared below the mattress and the stock anchor was dropped from 5 m (Figure 8a). The mattress arrangement was 5 EA × 14 EA. The blocks near the collision area were broken (Figure 8b), resulting in a damaged area that was 96-cm long and 32-cm wide, for a total area of 3,072 cm² (Figure 8c). After removing the protector, it was found that the measured maximum vertical soil settlement was 13 cm and the embedded pipe was severely damaged (Figure 8d).

FIGURE 8

Test result T3 (falling distance: 5 m, soil: Case 2, mattress 5 EA × 14 EA).



Considering T4 (Table 4), the saturated soil composition of Case 2 was prepared below the mattress and the stock anchor was dropped from 9 m (Figure 9a). The mattress arrangement was 5 EA × 14 EA. The blocks near the collision area were broken (Figure 9b), resulting in a damaged area that was 130-cm long and 50-cm wide, for a total area of 6,500 cm² (Figure 9c). After removing the protector, it was found that the measured maximum vertical soil settlement was 35 cm and the embedded pipe was severely damaged (Figure 9d).

Safety Assessment

The anchor drop test results are summarized in Table 5. As shown in the table, all of the test results showed the failure of the mattress power-cable protector under the anchor drop scenarios tested. This failure assessment was due to the excessive compressive force on the pipe under the mattress, with permanent deformation and breakage of the pipe. The collision forces on the reinforced concrete blocks transferred to the soil and obviously to the pipe. To help assess the test results, Figure 10 shows the settlement depth and damaged area, respectively, versus

FIGURE 9

Test result T4 (falling distance: 9 m, soil: Case 2, mattress 5 EA × 214 EA).



TABLE 5

Failure assessment.

Identity	Soil Description	Falling Distance (m)	Damaged Area (cm ²)	Settlement Depth (cm)	Pipe State	Failure Assessment
T1	Dry Case 1	5	1,530	5	Damaged	Failed
T2	Dry Case 1	9	2,520	7	Damaged	Failed
T3	Sat. Case 2	5	3,072	13	Damaged	Failed
T4	Sat. Case 2	9	6,500	35	Damaged	Failed

the falling distances (5 and 9 m). From the figures, the increase in falling distance increased the settlement depth and damaged area, although the slopes differed. Considering the effect of the soil conditions and composition, the saturated Case 2 (gravel 3% and sand 97%) gave deeper settlement depths and wider damaged areas than the dry Case 1 (gravel 50% and sand 50%) did. It was shown that this was mainly due to the soil composition effect in addition to soil saturation because, in the preliminary tests, Case 2 gave a deeper depth (37 cm) than Case 1 (7 cm) did, although the soil conditions were dry.

In the anchor drop tests, anchor velocity is the most important factor

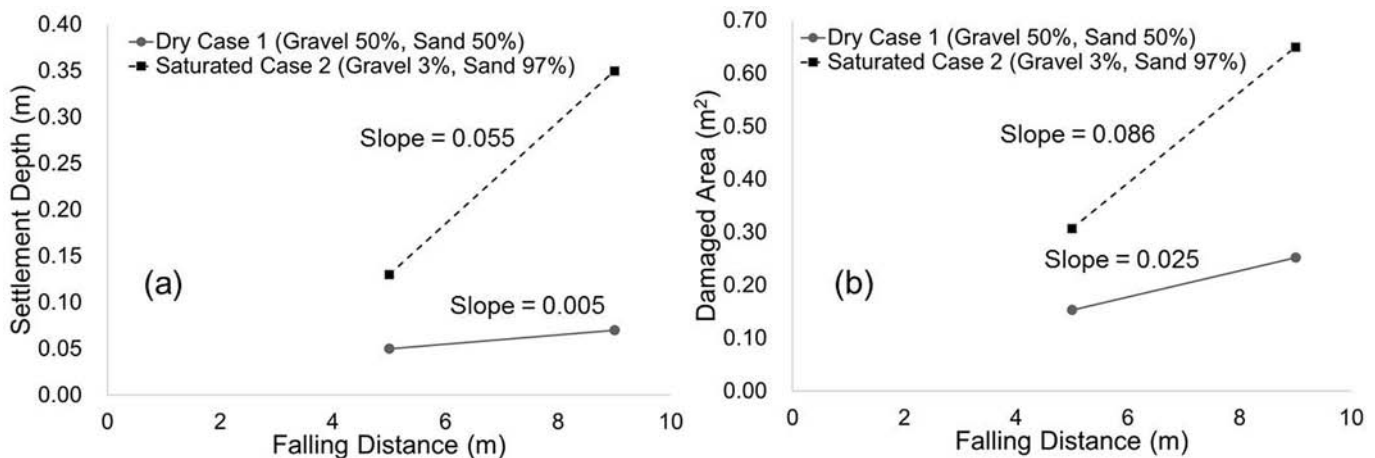
because it is directly related to the impact energy. The anchor velocity in water was converted to the velocity in air (Woo & Na, 2010). In that sense, the water effect on the impact was considered. In tunnel-type protectors, power cables do not have to be embedded in the seabed. In most cases, the protectors cover the power cable, which is located on the seabed. Thus, the main energy dissipation is according to the toughness of the concrete mattress. However, as shown in the test results, soil composition and soil saturation had effects on the test results. In that sense, the water effect on the soil was partially considered in the tests. Regarding to the water effect on the mattress, it should be empha-

sized here that reinforced concrete structures in water generally deteriorate as time goes. Thus, it is expected that the protector in water will have different reaction to anchor collision during its service life. However, Kim et al. (2008) reported that reinforced concrete reefs, immersed in seawater for 18–25 years, have sound physical and chemical properties. Nonetheless, in this field study, there were only limited test cases to distinguish the effects of soil composition and saturation on the test results.

Considering the test results, the newly designed protector should be modified and the burial condition of the power cable should be specified to dissipate impact energy. A series of

FIGURE 10

Settlement depth (a) and damaged area (b) versus falling distance obtained from T1 to T4.



field anchor drop and dragging tests will be scheduled to investigate the mechanism and accordingly to establish a safety evaluation guideline of submarine power cable protection in the near future. The associated projects in South Korea will be launched in 2013 and are expected to be done in 2015.

Conclusions

This study presents anchor drop tests on a newly designed matrix-type submarine power-cable protector assembled from reinforced concrete blocks to make a safety assessment. For the study, the conditions of the marine environments, such as water depths and soil specifications, were surveyed at the target site and simulated in the test set-up. A 2-ton stock anchor was selected as the colliding object, a 25-ton crane was prepared to drop the anchor, and recording units were set up to capture the collision process and damage patterns. Before carrying out designated test scenarios, preliminary tests were performed to investigate the effects of the soil composition and mattress arrangement on the test results. Finally, four anchor drop test scenarios were designed, carried out, and analyzed, and then a safety assessment was made for the matrix-type submarine power-cable protector.

From the tests, in addition to the falling distance, it was found that soil composition was a significant factor in the settlement depth and damaged area. Case 2 (3% gravel and 97% sand) gave deeper settlement depths and wider damaged areas than Case 1 (50% gravel and 50% sand) did. This observation was also made in the preliminary tests; thus, in addition to the soil conditions (dry and saturated), it

was shown that soil composition did provide a representative effect on the settlement depth and damaged area. Considering the settlement depth of the soils, the damaged areas of the concrete blocks, and the damaged state of the pipes (safety zone), all of the test results showed that the mattress failed to protect the power cable from the anchor collision forces. The deformation, damage, and breakage of the pipe, simulating the safety zone of the power cable, gave clues as to the failure. However, it should be noted here that the failure assessment in this study does not necessarily ideally represent the real failure of the power cables in the target marine environment because of real power cable specifications, such as the presence of armor layers. Also, in the calculations of falling distances, a conservative selection would result in a worse failure assessment. Nevertheless, this study shows the collision process of the stock anchor on the mattress, damaged patterns of the concrete blocks, soil settlement, and effect of soil composition on the test results. Thus, it was shown that the test process and results provide valuable information to design further anchor drop tests, specify the soil conditions, and establish a safety evaluation guideline of submarine power cable protection in the near future.

Acknowledgments

This study was supported financially by the Singangjin Power Station of the Korea Electric Power Corporation (KEPCO). We sincerely thank Dr. Hongjin Kim for his technical support. Additionally, material preparation by Samsung Industry is greatly appreciated. It should be noted here that this paper does not necessarily represent the views of the funding

agency or its officers, agents, and employees.

Corresponding Author:

Won-Bae Na
Department of Ocean Engineering,
Pukyong National University,
Busan, South Korea
Email: wna@pknu.ac.kr

References

- Byrne, B.W., & Houlby, G.T.** 2012. Foundations for offshore wind turbines. *Philos Trans R Soc A*. 361:2909-30. <http://dx.doi.org/10.1098/rsta.2003.1286>.
- Coffen-Smout, S., & Herbert, G.J.** 2000. Submarine cables: A challenge for ocean management. *Mar Policy*. 24:441-8. [http://dx.doi.org/10.1016/S0308-597X\(00\)00027-0](http://dx.doi.org/10.1016/S0308-597X(00)00027-0).
- Daudeville, L., & Malécot, Y.** 2011. Concrete structures under impact. *Eur J Environ Civil Eng*. 15:101-40. <http://dx.doi.org/10.1080/19648189.2011.9695306>.
- DNV-RP-F107.** 2010. Risk Assessment of Pipeline Protection. Katy, TX: Det Norske Veritas.
- DNV-RP-F401.** 2012. Electrical Power Cables in Subsea Applications. Katy, TX: Det Norske Veritas.
- Esteban, M.D., Diez, J.J., López, J.S., & Negro, V.** 2011. Why offshore wind energy? *Renew Energ*. 36:444-50. <http://dx.doi.org/10.1016/j.renene.2010.07.009>.
- Fox, R.W., McDonald, A.T., & Pritchard, P.J.** 2004. Introduction to Fluid Mechanics. Hoboken, NJ: Wiley.
- International Cable Protection Committee.** 2009. Damage to submarine cables caused by anchors. *Loss Prevention Bull*. Available at: http://www.iscpc.org/publications/Loss_Prevention_Bulletin_Anchor_Damage.pdf.
- Jie, W., & Yao-Tian, F.** 2012. Study on safety monitoring system for submarine power cable on the basis of AIS and radar technology.

Phys Proc. 24:961-5. <http://dx.doi.org/10.1016/j.phpro.2012.02.144>.

Kim, H.S., Kim, C.G., Na, W.B., Woo, J., & Kim, J.K. 2008. Physical and chemical deterioration of reinforced concrete reefs in Tongyeong coastal waters, Korea. *Mar Technol Soc J.* 42(3):110-8.

KS V3311. 2006. Anchor. Korean Standards Association.

Liu, F., Chen, G., Li, L., & Guo, Y. 2012. Study of impact performance of rubber reinforced concrete. *Constr Build Mater.* 36:604-16. <http://dx.doi.org/10.1016/j.conbuildmat.2012.06.014>.

Sharples, M. 2011. Offshore electrical cable burial for wind farms: state of the art, standards and guidance & acceptable burial depths, separation distances and sand wave effect. Washington, DC: Bureau of Safety and Environmental Enforcement.

Wagner, E. 1995. Submarine cables and protections provided by the law of the sea. *Mar Policy.* 19:127-36. [http://dx.doi.org/10.1016/0308-597X\(94\)00002-A](http://dx.doi.org/10.1016/0308-597X(94)00002-A).

Woo, J., Na, W.B., & Kim, H.T. 2009. Numerical simulation of arch-type submarine cable protector under anchor collision. *J Ocean Eng Technol.* 23:96-103.

Woo, J., & Na, W.B. 2010. Analyses of the maximum response of cylinders-connected protector under anchor colliding and dragging. *J Ocean Eng Technol.* 24:81-7.

Yamabuki, K., & Kubori, K. 2012. A transient analysis of a scaled model for a submarine cable connected with an offshore wind farm. *Electr Pow Syst Res.* 85:59-63. <http://dx.doi.org/10.1016/j.epsr.2011.07.009>.

Elements of Underwater Glider Performance and Stability

AUTHORS

Shuangshuang Fan

The State Key Lab of Fluid Power Transmission and Control, Zhejiang University

Craig Woolsey

Department of Aerospace and Ocean Engineering, Virginia Tech

1. Introduction

For at least two decades, experimental ocean scientists have envisioned a dense distribution of mobile ocean sensor platforms to provide persistent and pervasive ocean monitoring (Curtin et al., 1993). Within this vision, there is an economic argument for using underwater gliders to sample the deep ocean over large spatial and temporal scales (Rudnick et al., 2004). The first generation of underwater gliders, such as *Slocum* (Webb et al., 2001), *Seaglider* (Eriksen et al., 2001), and *Spray* (Sherman et al., 2001), were designed for such long-endurance, deep ocean sampling missions. More recent development efforts have produced variants that are suitable for both deeper (Osse & Eriksen, 2007) and shallower (Teledyne Webb Research, 2013) operations. Although glider endurance suffers in shallower water, it compares well with that of conventional underwater vehicles, and gliders are more robust to biological fouling and debris. Moreover, advanced perception, planning, and control algorithms that exploit natural vehicle and environmental dynamics can improve performance. A shallow-water glider developed recently

ABSTRACT

Underwater gliders are winged autonomous underwater vehicles (AUVs) that can be deployed for months at a time and travel thousands of kilometers. As with any vehicle, different applications impose different mission requirements that impact vehicle design. We investigate the relationship between a glider's geometry and its performance and stability characteristics. Because our aim is to identify general trends rather than perform a detailed design optimization, we consider a generic glider shape: a cylindrical hull with trapezoidal wings. Geometric parameters of interest include the fineness ratio of the hull, the wing position and shape, and the position and size of the vertical stabilizer. We describe the results of parametric studies for steady wings-level flight, both at minimum glide angle and at maximum horizontal speed, as well as for steady turning flight. We describe the variation in required lung capacity and maximum lift-to-drag ratio corresponding to a given vehicle size and speed; we also consider range and endurance, given some initial supply of energy for propulsion. We investigate how the turning performance varies with wing and vertical stabilizer configuration. To support this analysis, we consider the glider as an 8-degree-of-freedom multibody system (a rigid body with a cylindrically actuated internal moving mass) and develop approximate expressions for turning flight in terms of geometry and control parameters. Moving from performance to stability and recognizing that a glider's motion is well described in terms of small perturbations from wings-level equilibrium, we study stability as an eigenvalue problem for a rigid (actuators-fixed) flight vehicle. We present a number of root locus plots in terms of various geometric parameters that illuminate the design tradeoff between stability and control authority.

Keywords: multibody dynamics, design analysis, range and endurance, buoyancy propulsion

at Virginia Tech provides unique new capabilities for testing such algorithms (Wolek et al., 2012).

Earlier studies have addressed various stability and performance tradeoffs involved in underwater glider design. A sweeping 2003 analysis sponsored by the U.S. Office of Naval Research provided insightful comparisons between the propulsive efficiency of underwater gliders and both biological and engineered flyers (Jenkins et al., 2003). One conclusion of that study

was that a blended wing-body glider would yield greater flight efficiency than “legacy” configurations. The primary focus of the 2003 glider study was performance; earlier investigations had considered stability. Graver et al. (1998) investigated the stability of wings-level flight with respect to a “bottom-heaviness” parameter related to the glider's metacentric height. Galea (1999) provided a general static stability analysis for glider wings-level flight and turning motion. Graver

(2005) analyzed scaling rules for steady glide performance (e.g., the glide speed versus ballast loading, glide angle and glider volume), and he provided a preliminary overview of glider design requirements, including sizing, body, and wing geometry. Graver (2005) also discussed longitudinal stability, focusing especially on the role of the phugoid mode, a mode that had been recognized in aircraft motion a century before by Lanchester (Lanchester, 1908; Mises, 1959). Nonlinear gliding stability is discussed in Bhatta and Leonard (2008), where a composite Lyapunov function is constructed to prove gliding stability. One advantage of Lyapunov analysis is that it provides a tool for estimating the region of attraction for asymptotically stable equilibria; such information can be useful in scheduling transitions between steady motions.

In any flight vehicle design effort, it is important to understand the relationship between vehicle geometry and performance and stability (Pamadi, 2004). To simplify our parametric analysis, we describe the hull and wing geometry using several nondimensional parameters: the hull fineness ratio, wing aspect ratio, wingspan ratio, and wing thickness ratio. In addition to these parameters, the wing and vertical stabilizer configurations (shape, size, and location) are also considered. As hydrodynamic coefficients are determined by the glider geometry and the flow characteristics, it is necessary to obtain a hydrodynamic model for the glider. For generic vehicle shapes, there are well-known semi-empirical expressions relating geometry to aerodynamic (or hydrodynamic) coefficients (Etkin & Reid, 1996; USAF Stability and Control DATCOM). Because our focus is to identify general trends rather than perform a detailed

design optimization, we use simple methods such as these to develop a generic glider hydrodynamic model that supports performance and stability analysis. We consider two wings-level flight conditions (minimum glide angle and maximum horizontal speed) as well as turning motion. To support our analysis of turning motion for a vehicle with a cylindrically actuated internal moving mass, we follow the regular perturbation method described in Mahmoudian et al. (2010). The performance analysis covers preliminary design considerations, such as sizing, range and endurance, and turning capability. For stability analysis, we view the glider as a rigid body and investigate the effect of geometric parameters on the longitudinal and lateral-directional eigenmodes. Specifically, we consider the effect of changes in wing shape, wing longitudinal location, and vertical stabilizer size and location.

In this paper, we consider a conventional glider configuration comprising a cylindrical hull with a trapezoidal wing and vertical stabilizer. The analysis makes use of a new multibody dynamic model for a glider with a cylindrically actuated moving mass. This actuation scheme matches that of several existing gliders including *Seaglider*, *Spray*, and the Virginia Tech underwater glider (Wolek et al., 2012). The paper is organized as follows. Section 2 presents the derivation of an 8-degree-of-freedom underwater glider dynamic model with a cylindrically actuated moving mass. In Section 3, we define the nomenclature associated with glider geometry and with vehicle motion and we review relevant glider hydrodynamic characteristics. Section 4 presents some analytical results concerning performance in steady wings-level flight and in steady turning motion. Section 5 describes how the longitudinal

and lateral-directional eigenmodes for a rigid glider vary with certain geometric parameters. We summarize and conclude in Section 6.

2. Underwater Glider Dynamics With a Cylindrically Actuated Moving Mass

The 8-degree-of-freedom glider is modeled as a rigid body (mass m_{rb}) with a single moving point mass (m_p) that is offset from the centerline. The point mass can move longitudinally and can revolve around the vehicle centerline. Earlier multibody dynamic models incorporated one or more rectilinear mass particles for attitude control, but the cylindrical actuation scheme better reflects the actual control mechanism in several existing gliders.

The vehicle also includes a variable ballast actuator whose effect is represented by a point mass (m_b) with variable volume (V_b), which is fixed at the body frame origin. In modeling a buoyancy control system, one may assume either that the mass varies or the displacement, depending on whether the “control volume” that contains the vehicle is fixed or deformable. In either case, the net effect is a change in the vehicle’s density. Thus, in our model, when the variable ballast actuator decreases the vehicle’s volume sufficiently, the vehicle becomes denser than the surrounding water and descends. Conversely, when the actuator increases the displaced volume, the vehicle becomes less dense than the surrounding water and ascends.

The total vehicle mass, which remains fixed, is

$$m = m_{rb} + m_p + m_b$$

2.1. Kinematics

Define a body-fixed, orthonormal reference frame centered at the geometric center of the vehicle (the center of buoyancy) and represented by the unit vectors \mathbf{b}_1 , \mathbf{b}_2 , and \mathbf{b}_3 . The vector \mathbf{b}_1 is aligned with the longitudinal axis of the vehicle, \mathbf{b}_2 points out the right wing, and \mathbf{b}_3 completes the right-handed triad (see Figure 1). Define another orthonormal reference frame, denoted by the unit vectors \mathbf{i}_1 , \mathbf{i}_2 , and \mathbf{i}_3 , which is fixed in inertial space such that \mathbf{i}_3 is aligned with the force due to gravity. The relative orientation of these two reference frames is given by the proper rotation matrix \mathbf{R}_{IB} , which maps free vectors from the body-fixed reference frame into the inertial reference frame. Let \mathbf{e}_i represent the standard basis vector for \mathbb{R}^3 , where $i \in \{1, 2, 3\}$, and let the character $\hat{\cdot}$ denote the 3×3 skew-symmetric matrix satisfying $\hat{\mathbf{a}}\mathbf{b} = \mathbf{a} \times \mathbf{b}$ for vectors \mathbf{a} and \mathbf{b} . Then, in terms of conventional Euler angles

(roll angle φ , pitch angle θ , and heading angle ψ), we have

$$\mathbf{R}_{\text{IB}}(\varphi, \theta, \psi) = e^{\hat{\mathbf{e}}_3\psi} e^{\hat{\mathbf{e}}_2\theta} e^{\hat{\mathbf{e}}_1\varphi}$$

where $e^{(\cdot)}$ denotes the matrix exponential.

The origin of the body frame sits at the vehicle's center of buoyancy (CB), which remains fixed under our assumptions. The center of mass (CM) of the glider (neglecting the contribution of m_p) is located at \mathbf{r}_{rb} (see Figure 1). Let the inertial vector $\mathbf{X} = [x, y, z]^T$ represent the position vector from the origin of the inertial frame to the origin of the body frame. Let $\mathbf{v} = [u, v, w]^T$ and $\boldsymbol{\omega} = [p, q, r]^T$ represent the translational and rotational velocity of the body with respect to the inertial frame, but expressed in the body frame. The kinematic equations are

$$\dot{\mathbf{X}} = \mathbf{R}_{\text{IB}}\mathbf{v} \quad (1)$$

$$\dot{\mathbf{R}}_{\text{IB}} = \mathbf{R}_{\text{IB}}\hat{\boldsymbol{\omega}} \quad (2)$$

In addition to the 6 degrees of freedom associated with the vehicle's translation and rotation, there are 2 degrees of freedom associated with the moving mass, which is modeled as a particle. To describe the point mass position, we define a third orthonormal "actuator" triad $\{\mathbf{a}_1, \mathbf{a}_r, \mathbf{a}_\mu\}$, where \mathbf{a}_1 is parallel with \mathbf{b}_1 (see Figure 1). The vector \mathbf{a}_r points in the radial direction from the vehicle centerline through the point mass. The vector \mathbf{a}_μ completes the right-handed frame. The proper rotation matrix \mathbf{R}_{BP} maps free vectors from this particle-fixed frame to the body frame,

$$\mathbf{R}_{\text{BP}} = \begin{pmatrix} 1 & 0 & 0 \\ 0 & -\sin\mu & -\cos\mu \\ 0 & \cos\mu & -\sin\mu \end{pmatrix}$$

where μ is the rotation angle of the moving mass about the longitudinal axis of the vehicle. Let

$$\bar{\mathbf{r}}_p = r_{p_x}\mathbf{a}_1 + R_p\mathbf{a}_r = \begin{pmatrix} r_{p_x} \\ R_p \\ 0 \end{pmatrix}_p$$

denote the particle's position with respect to the body frame origin, expressed in the particle frame. Correspondingly, define the body vector

$$\mathbf{r}_p = \mathbf{R}_{\text{BP}}\bar{\mathbf{r}}_p = \begin{pmatrix} r_{p_x} \\ -R_p \sin\mu \\ R_p \cos\mu \end{pmatrix}_b$$

Then the kinematics of the moving mass particle relative to inertial space is

$$\mathbf{v}_p = \mathbf{v} + (\boldsymbol{\omega} + \dot{\mu}\mathbf{b}_1) \times \mathbf{r}_p + (\dot{r}_{p_x}\mathbf{b}_1) \quad (3)$$

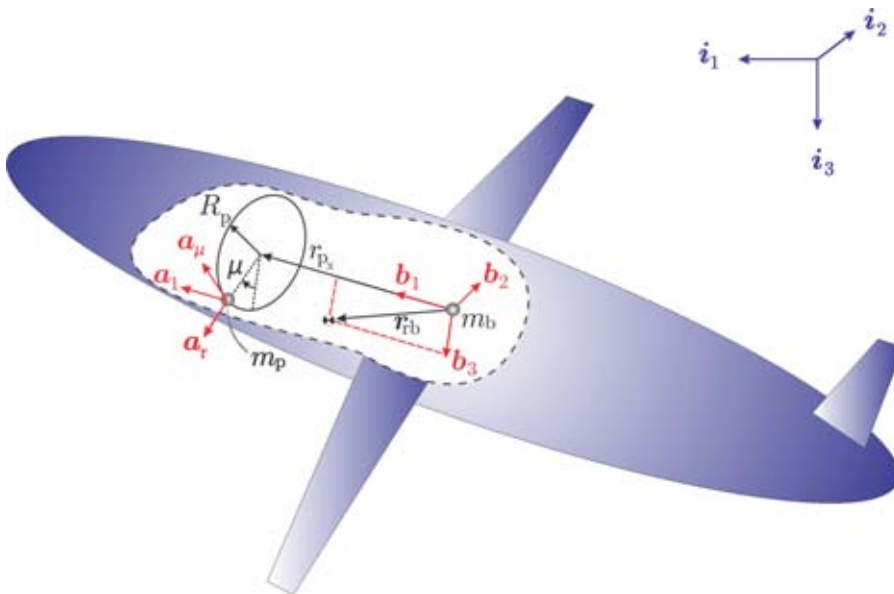
Note that we may also write

$$\mathbf{v}_p = \begin{pmatrix} \mathbf{I} & -\hat{\mathbf{r}}_p & \mathbf{e}_1 & -\hat{\mathbf{r}}_p\mathbf{e}_1 \end{pmatrix} \boldsymbol{\eta}$$

$$\text{where } \boldsymbol{\eta} = \begin{pmatrix} \mathbf{v} \\ \boldsymbol{\omega} \\ \dot{r}_{p_x} \\ \dot{\mu} \end{pmatrix}.$$

FIGURE 1

An underwater glider with a cylindrically actuated moving point mass.



2.2. Dynamics

To derive the equations of motion, one first defines the total kinetic energy of the body/particle/fluid system,

$$T = T_p + T_b + T_{tb} + T_f = \frac{1}{2} \boldsymbol{\eta}^T \mathbb{M}(\mathbf{r}_p) \boldsymbol{\eta}$$

where

$$\mathbb{M}(\mathbf{r}_p) = \mathbb{M}_p(\mathbf{r}_p) + \mathbb{M}_b + \mathbb{M}_{tb} + \mathbb{M}_f$$

Explicit expressions for the generalized inertia matrices are given in Appendix A.

The generalized momentum is

$$\begin{pmatrix} \mathbf{p} \\ \mathbf{h} \\ p_{p_x} \\ h_{p_x} \end{pmatrix} = \frac{\partial T}{\partial \boldsymbol{\eta}}$$

where \mathbf{p} is the total body translational momentum, \mathbf{h} is the total body angular momentum, and p_{p_x} and h_{p_x} appear in the point mass momentum as follows:

$$\mathbf{p}_p = \mathbf{R}_{BP} \begin{pmatrix} p_{p_x} \\ p_{p_z} \\ h_{p_x}/R_p \end{pmatrix}$$

The dynamic equations in the body frame are

$$\dot{\mathbf{p}} = \mathbf{p} \times \boldsymbol{\omega} + \tilde{\mathbf{m}}\mathbf{g}\boldsymbol{\zeta} + \mathbf{f}_v \quad (4)$$

$$\begin{aligned} \dot{\mathbf{h}} &= \mathbf{h} \times \boldsymbol{\omega} + \mathbf{p} \times \mathbf{v} + m_{rb} \mathbf{g} \mathbf{r}_{rb} \times \boldsymbol{\zeta} \\ &+ m_p \mathbf{g} \mathbf{r}_p \times \boldsymbol{\zeta} + \mathbf{m}_v \end{aligned} \quad (5)$$

$$\begin{aligned} \dot{p}_{p_x} &= \mathbf{e}_1 \cdot \left(\mathbf{R}_{BP}^T (\mathbf{p}_p \times (\boldsymbol{\omega} + \dot{\boldsymbol{\mu}} \mathbf{b}_1) \right. \\ &\left. + m_p \mathbf{g} \boldsymbol{\zeta} \right) + u_{p_x} \end{aligned} \quad (6)$$

$$\begin{aligned} \dot{h}_{p_x} &= R_p \mathbf{e}_3 \cdot \left(\mathbf{R}_{BP}^T (\mathbf{p}_p \times (\boldsymbol{\omega} + \dot{\boldsymbol{\mu}} \mathbf{b}_1) \right. \\ &\left. + m_p \mathbf{g} \boldsymbol{\zeta} \right) + \tau_{p_x} \end{aligned} \quad (7)$$

where

$$\boldsymbol{\zeta} = \mathbf{R}^T \mathbf{i}_3$$

is the ‘‘tilt vector,’’ the body frame unit vector in the direction of gravity, \mathbf{f}_v and \mathbf{m}_v are the viscous force and moment acting on the glider, expressed in the body frame, and u_{p_x} and τ_{p_x} are the input force and moment, which adjust the moving point mass location to control vehicle attitude.

Letting u_b denote the rate of change of displaced volume, an input, we have

$$\dot{V}_b = u_b \quad (8)$$

Equations (4) through (8) describe the dynamics of the cylindrically actuated glider. Together with the kinematic equations (1), (2), and (3), these equations completely describe the motion of the vehicle in still water.

Having obtained a multibody dynamic model, one may compute steady motions, examine their stability, develop feedback control schemes, and implement them in simulation. For example, one may investigate flight control methods that involve stitching together sequences of stable gliding motions, as in Mahmoudian and Woolsey (2013).

3. Glider Geometry and Hydrodynamic Characteristics

3.1. Geometry and Nomenclature

Motivated by the challenge of designing an underwater glider to meet particular mission requirements, we investigate the general relationship between glider geometry and the stability and performance characteristics. In doing so, we consider a generic wing-and-cylinder configuration, where the

cylindrical fuselage has diameter d and length l . The wingspan (tip to tip) is b . We consider an untapered, trapezoidal wing with a constant cross-sectional shape. The wing planform area is denoted S . The mean aerodynamic chord length (i.e., the average width of a rectangular wing with equivalent aerodynamic properties) is \bar{c} and $S = b \cdot \bar{c}$. Another important geometric parameter is the maximum wing thickness t .

The hull and wing geometry can be characterized by several nondimensional parameters: the hull fineness ratio (f), the wing aspect ratio (AR), the wingspan ratio (κ), and wing thickness ratio (\tilde{t}).

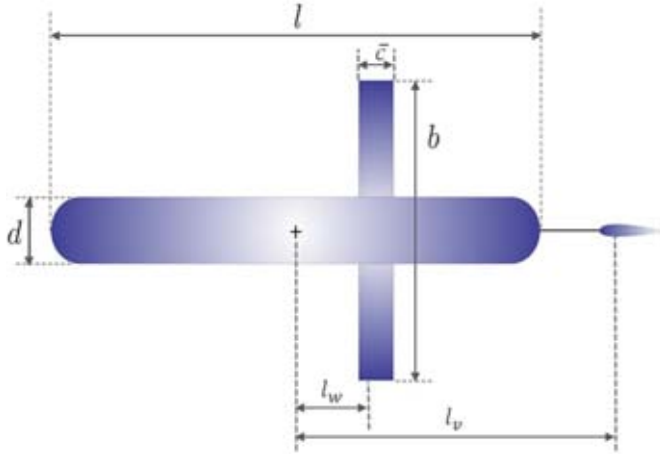
$$f = \frac{l}{d}, \quad AR = \frac{b^2}{S}, \quad \kappa = \frac{b}{d}, \quad \text{and} \\ \tilde{t} = \frac{t}{c}$$

We also consider a few other configuration parameters for the wing and vertical stabilizer, including wing longitudinal position l_w , vertical stabilizer longitudinal position l_v and area of the vertical stabilizer S_v . The aerodynamic center of the wing and the vertical stabilizer, which is located near the quarter-chord line, are \tilde{l}_w and \tilde{l}_v (normalized by the fuselage length l) aft of the center of buoyancy, respectively, while the area of the vertical stabilizer S_v is normalized by the fuselage frontal area S_f . All of the geometric parameters that we consider are indicated in Figure 2.

A critical parameter for performance analysis is the *buoyant lung capacity* $\bar{\eta}$, given as a percentage of the neutrally buoyant displacement. Buoyancy actuators include piston-cylinder arrangements, oil-filled bladders, and pneumatic bladders. For simplicity, we consider the case of a piston-cylinder actuator and assume a

FIGURE 2

Geometric parameters of the underwater glider model.



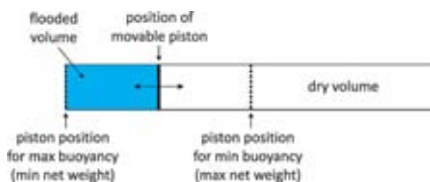
cylindrical hull with constant cross-sectional area (see Figure 3). Recall that the dynamic model presented earlier assumes changes in buoyant volume occur at the origin of the body frame. Although a change in buoyancy generated with the arrangement shown in Figure 3 would induce a moment, we do not account for it here; our aim is merely to relate changes in buoyancy to the vehicle geometry. Let $\bar{\eta}$ denote the percentage difference between the displacement required for neutral buoyancy (V_{NB}) and the maximum displacement (V). That is,

$$V = (1 + \bar{\eta})V_{NB} \text{ and } \bar{\eta} = V/V_{NB} - 1$$

where $V_{NB} = W/(\rho g)$ and W is the vehicle's dry weight. The "net weight" of the glider is denoted $\tilde{W} = W - B$, where B is the buoyant force.

FIGURE 3

Notional schematic of the buoyancy actuation system.



Let η denote the fractional displacement from neutral buoyancy, $\eta \in [-\bar{\eta}, \bar{\eta}]$, defined such that $\eta > 0$ corresponds to an increase in buoyancy. Then

$$B = \rho g(1 + \eta)V_{NB}$$

Thus,

$$\begin{aligned} \tilde{W} &= W - B = \rho g V_{NB} - \rho g(1 + \eta)V_{NB} \\ &= -\eta \rho g V_{NB} \\ &= -\left(\frac{\eta}{1 + \bar{\eta}}\right) \rho g V \end{aligned}$$

3.2. Hydrodynamic Characteristics

To assess glider performance and stability, it is necessary to develop a hydrodynamic model. The hydrodynamic forces (lift, side force, and drag) are expressed in the "current" reference frame, defined such that the 1-axis is aligned with the velocity vector. Let $\alpha = \arctan(w/u)$ denote the vehicle's "angle of attack" and let $\beta = \arcsin(v/|\mathbf{v}|)$ denote the "sideslip angle." The current frame is related to the body frame through the proper rotation matrix

$$\mathbf{R}_{BC}(\alpha, \beta) = e^{-\hat{e}_2 \alpha} e^{\hat{e}_3 \beta}$$

The hydrodynamic force and moment are typically represented using non-dimensional coefficients as follows:

$$\mathbf{f}_v = \mathbf{R}_{BC} \begin{pmatrix} L \\ SF \\ D \end{pmatrix} = \frac{1}{2} \rho V^2 S \begin{pmatrix} C_L \\ C_{SF} \\ C_D \end{pmatrix}$$

$$\mathbf{m}_v = \begin{pmatrix} K \\ M \\ N \end{pmatrix} = \frac{1}{2} \rho V^2 S \begin{pmatrix} b C_l \\ \bar{c} C_m \\ b C_n \end{pmatrix}$$

The nondimensional coefficients depend on the vehicle geometry and the flight condition. Based on physical considerations, such as left/right symmetry of the outer mold line, we assume these coefficients have the following dependencies

$$C_L = C_L(\alpha, \bar{q}), \quad C_{SF} = C_{SF}(\beta, \bar{p}, \bar{r}),$$

$$C_D = C_D(\alpha, \bar{q}), \quad C_l = C_l(\beta, \bar{p}, \bar{r}),$$

$$C_m = C_m(\alpha, \bar{q}) \text{ and } C_n = C_n(\beta, \bar{p}, \bar{r})$$

Here, $\bar{p}, \bar{q}, \bar{r}$ are nondimensional roll, pitch and yaw rates, which are defined as

$$\bar{p} = p/(2V_0/b), \quad \bar{q} = q/(2V_0/\bar{c})$$

$$\text{and } \bar{r} = r/(2V_0/b)$$

where V_0 is the nominal velocity of the vehicle. (Please note that while V represents volume, V represents speed.) For aircraft flight dynamic models, dependence of the forces and moments on vehicle acceleration is typically included in these nondimensional coefficients as well (e.g., dependence of C_m on $\dot{\alpha}$). Here, these effects are instead included in the added mass and inertia terms. Dependence of the moments on inertial attitude, due to the metacentric moment, is also incorporated elsewhere in the formulation.

Following convention, we assume that the nondimensional hydrodynamic forces and moments above depend *linearly* on their arguments (e.g., $C_n = C_{n\beta}\beta + C_{n\tilde{p}}\tilde{p} + C_{n\tilde{r}}\tilde{r}$), with the exception of the drag coefficient, which varies quadratically with lift,

$$C_D = C_{D_0} + KC_L^2$$

The parameter C_{D_0} represents the parasitic drag due, for example, to skin friction. The parameter K accounts for drag that is induced when the wing generates lift. It scales inversely with the aspect ratio AR ; induced drag vanishes for a wing of infinite span.

The hydrodynamic coefficients (such as $C_{n\beta}$) are determined in part by the glider geometry, such as the slenderness of the fuselage, the shape and location of the wing, the size and location of the vertical stabilizer, etc. For generic flight vehicle shapes, there are well-known semiempirical expressions relating geometry to aerodynamic (or hydrodynamic) coefficients (Etkin & Reid, 1996; USAF Stability and Control DATCOM), although these methods are imprecise. One can obtain higher fidelity approximations using computational fluid dynamics methods, ranging from simple vortex lattice methods to full Navier-Stokes solvers. However, semiempirical methods provide a simple way to investigate the first-order effect of changes in vehicle geometry on performance and stability.

While hydrodynamic coefficients depend on glider geometry, they also depend on the flow characteristics, which correlate to the *Reynolds number*

$$Re = \frac{Vx_{length}}{\nu}$$

where x_{length} is some characteristic linear dimension (e.g., vehicle length,

hull diameter, or wing chord). In fact, the hydrodynamic coefficients are especially sensitive to Reynolds number for speeds at which underwater gliders typically operate. For motion through water, these speeds correspond to a critical Reynolds number range in which flow over the vehicle may (or may not) transition from laminar to turbulent.

4. Performance Analysis

4.1. Steady Motions

In this section, we discuss two types of underwater glider steady motions: wings-level flight and steady turning motion.

4.1.1. Wings-Level Flight

Our discussion of wings-level performance begins with a general overview and then focuses on two specific flight conditions: flight at minimum glide angle and flight at maximum horizontal speed.

Figure 4 shows the free body diagram for a flight vehicle in wings-level gliding flight. In this sketch, \tilde{W} denotes the vehicle's *net weight* (weight minus buoyant force). Here, we adopt a "performance model"—we treat the vehicle as a point mass, ignoring rotational dynamics. As explained earlier, the lift and drag force are typically expressed in terms of nondimensional

coefficients C_L and C_D . The coefficients C_L and C_D are related to the *descent angle* ξ as shown in the triangle at the right in Figure 4. Summing forces in Figure 4 along the velocity direction gives

$$C_D \left(\frac{1}{2} \rho V^2 S \right) = \tilde{W} \sin \xi$$

The descent angle is the angle from the inertial horizontal plane down to the velocity vector; it is the negative of the *flight path angle* γ that is commonly used in aircraft flight dynamics (Etkin & Reid, 1996). Solving for speed, one finds that

$$V = \sqrt{\frac{2\tilde{W} \sin \xi}{\rho S C_D}} \quad (9)$$

The horizontal and vertical components of speed are

$$V_x = V \cos \xi$$

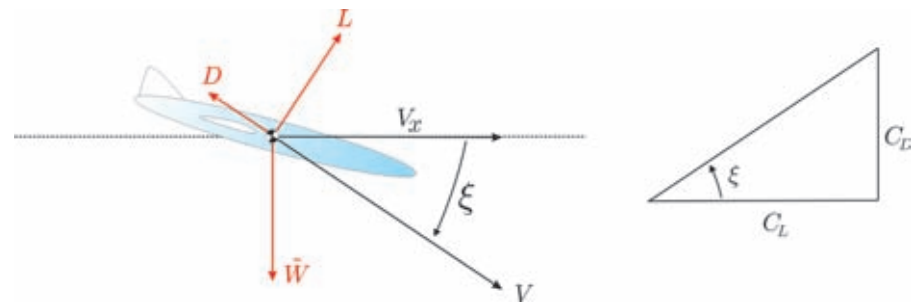
$$V_z = V \sin \xi$$

Referring to Figure 4, we note the following relationships:

$$\begin{aligned} \sin \xi &= \frac{C_D}{\sqrt{C_D^2 + C_L^2}} \quad \text{and} \\ \cos \xi &= \frac{C_L}{\sqrt{C_D^2 + C_L^2}} \end{aligned} \quad (10)$$

FIGURE 4

Free body diagram for wings-level gliding flight.



Recall that

$$\tilde{W} = -\left(\frac{\eta}{1 + \bar{\eta}}\right)\rho g V$$

As mentioned earlier, we assume that buoyancy is controlled by a single-stroke (piston-cylinder) actuator. We take the piston diameter to be the hull diameter, and we assume the buoyancy actuation is concentrated at the origin of the body frame (i.e., we ignore moments due to changes in buoyancy). When the vehicle's net weight is maximum, we have $\eta = -\bar{\eta}$ so that

$$\begin{aligned}\tilde{W} &= \left(\frac{\bar{\eta}}{1 + \bar{\eta}}\right)\rho g V \\ &= \left(\frac{\bar{\eta}}{1 + \bar{\eta}}\right)\rho g \left(\frac{\pi}{4}d^2 l\right)\end{aligned}\quad (11)$$

Substituting equation (11) into equation (9), we find that

$$\begin{aligned}V^2 &= \frac{2\tilde{W} \sin \xi}{\rho S C_D} \\ &= \frac{\pi g l d^2}{2 S} \left(\frac{\bar{\eta}}{1 + \bar{\eta}}\right) \frac{\sin \xi}{C_D} \\ &= \frac{\pi g l A R}{2 \kappa^2} \left(\frac{\bar{\eta}}{1 + \bar{\eta}}\right) \frac{1}{\sqrt{C_D^2 + C_L^2}}\end{aligned}\quad (12)$$

Thus, we find that speed scales with the square root of linear dimension l and inversely with the wingspan ratio κ . The dependence of speed on aspect ratio is more subtle, since AR affects C_D through the induced drag parameter K .

A. Minimum Glide Angle Flight. In still water, flight at the shallowest glide path angle results in the maximum horizontal range. Referring to Figure 4, the minimum glide angle occurs when the lift-to-drag ratio is maximum. In powered flight (e.g., for aircraft flying

at a constant altitude), this flight condition corresponds to the minimum drag force; the values of the drag and lift coefficient in this condition are

$$C_{D_{\text{md}}} = 2C_{D_0} \quad \text{and} \quad C_{L_{\text{md}}} = \sqrt{\frac{C_{D_0}}{K}}$$

(Adopting aircraft nomenclature, the subscript “md” stands for “minimum drag.”) These expressions can be obtained by differentiating the right-hand side of $\tan \xi = (C_{D_0} + KC_L^2)/C_L$ with respect to C_L and finding the roots. Referring to equation (12), we find that the speed for minimum drag (the “speed-to-fly”) is

$$\begin{aligned}V_{\text{md}} &= \sqrt{\frac{\pi g l A R}{2 \kappa^2} \left(\frac{\bar{\eta}}{1 + \bar{\eta}}\right) / \sqrt{C_{D_{\text{md}}}^2 + C_{L_{\text{md}}}^2}} \\ &= \sqrt{\frac{\pi g l A R}{2 \kappa^2} \left(\frac{\bar{\eta}}{1 + \bar{\eta}}\right) / \sqrt{\frac{C_{D_0}}{K} (1 + 4KC_{D_0})}}\end{aligned}\quad (13)$$

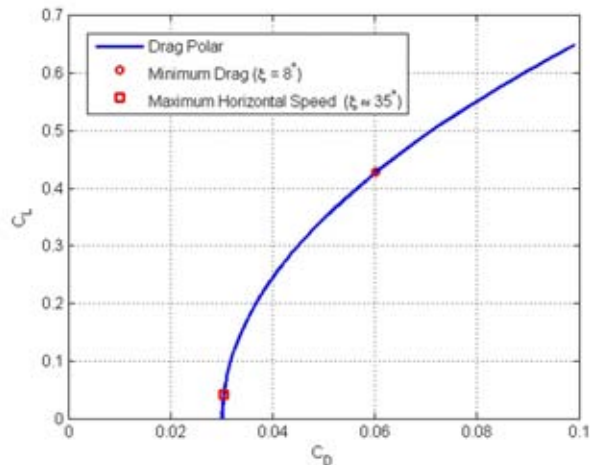
The minimum glide angle condition is illustrated in the plot of C_L versus C_D in Figure 5, a curve sometimes called the *drag polar*. Note that the lift-to-drag ratio is maximum when a line extending from the origin is just tangent the drag polar. This flight condition corresponds to the shallowest achievable glide angle, which is 8° in the case of the *Slocum* model given in (Graver, 2005; Bhatta, 2006).

B. Maximum Horizontal Speed. Using the lift-and-drag triangle in Figure 4, we find that

$$V_x = \sqrt{\frac{2\tilde{W}}{\rho S} \frac{C_L}{[C_L^2 + C_D^2]^{3/4}}}$$

FIGURE 5

Drag polar for a model of the *Slocum* glider.



The value is maximum when

$$f(C_L) = \frac{C_L}{[C_L^2 + C_D^2]^{3/4}}$$

is maximum. Defining $\sigma = 2KC_{D_0}$, one finds (after some effort) that

$$C_{L_{\max V_x}} = \sqrt{\frac{2}{4K}} \sqrt{-(1+\sigma) + \sqrt{(1+\sigma)^2 + 8\sigma^2}}$$

$$C_{D_{\max V_x}} = C_{D_0} + \frac{1}{8K} \left[-(1+\sigma) + \sqrt{(1+\sigma)^2 + 8\sigma^2} \right]$$

Noting from Figure 4 that

$$\tan \xi = \frac{C_D}{C_L},$$

we find that for wings-level gliding flight at maximum horizontal speed,

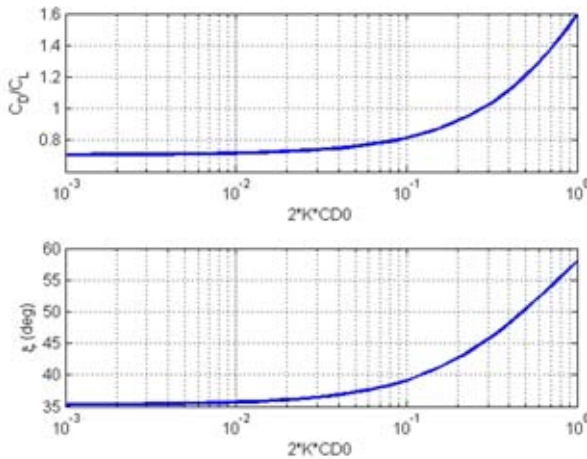
$$\tan \xi = \frac{C_{D_{\max V_x}}}{C_{L_{\max V_x}}} = \frac{\sqrt{2}\sigma + \frac{1}{\sqrt{8}} \left[-(1+\sigma) + \sqrt{(1+\sigma)^2 + 8\sigma^2} \right]}{\sqrt{-(1+\sigma) + \sqrt{(1+\sigma)^2 + 8\sigma^2}}}$$

Figure 6 shows the drag-to-lift ratio and the descent angle. Note that in the limit $\sigma \rightarrow 0$, we have $\xi \rightarrow \arctan(1/\sqrt{2}) \approx 35^\circ$.

For well-designed flight vehicles, for which the product KC_{D_0} is reasonably small, the descent angle for maximum downrange speed is well approximated

FIGURE 6

Drag-to-lift ratio and descent angle versus $2KC_{D_0}$.



by its theoretical limit $\arctan(1/\sqrt{2})$. Further, one may verify that in the limit $KC_{D_0} \rightarrow 0$, the lift and drag coefficients for maximum horizontal speed are

$$C_{L_{\max V_x}} \approx \sqrt{2}C_{D_0} \quad \text{and}$$

$$C_{D_{\max V_x}} \approx C_{D_0}(1 + 2KC_{D_0})$$

4.1.2. Turning Motion

Mahmoudian et al. (2010) developed analytical approximations for steady turning motion of an underwater glider using regular perturbation theory, with the vehicle turn rate as the perturbation parameter. The analysis assumed rectilinear motion of the moving point mass. Using the same approach, we rederive the steady turning flight approximation with a cylindrical moving point mass actuator. We treat turning flight as a small perturbation from a nominal, wings-level equilibrium flight condition at speed V_0 and pitch angle θ_0 , at some corresponding angle of attack α_0 . In wings-level flight, the moving mass rotation angle $\mu = 0$, so that the roll angle ϕ and the sideslip angle β are both zero. We hold the pitch angle constant at θ_0 and perturb the steady wings-level flight such that the body angular velocity vector ω is vertical with a small magnitude $\varepsilon\omega_n$ where ω_n is some characteristic frequency (e.g., $\sqrt{g/l}$ or V_0/l), and ε is the perturbation parameter. To first order in ε , one finds

$$V \approx V_0, \quad \varphi \approx \varepsilon\varphi_1,$$

$$\alpha \approx \alpha_0, \quad \beta \approx \varepsilon\beta_1,$$

$$\tilde{m} \approx \tilde{m}_0 \quad \text{and} \quad \mu \approx \varepsilon\mu_1$$

Explicit expressions for φ_1 , β_1 , and μ_1 are given in equations (14), (15),

and (16); these analytical expressions enable one to investigate the role of vehicle parameters in a vehicle's turning performance.

$$\begin{aligned}
\xi_1 = & (1/(2gm_p\tilde{m}_0R_p))V_0\omega_n((C_n l^2\tilde{m}_0S\rho + 2(\tilde{m}_0N_v + m_p r_{p_x}(m - X_u))\cos\alpha_0)\cot\theta_0 \\
& - 2(\tilde{m}_0M_{\dot{w}} + m_p r_{p_x}(-m + Z_{\dot{w}}))\sin\alpha_0 - ((S(C_{n_\beta}l\tilde{m}_0 + m_p r_{p_x}(C_{D_0} + C_{S_\beta} + C_{L_\alpha}^2 K\alpha_0^2))\rho \\
& + 2\tilde{m}_0(-X_u + Y_v)\cos\alpha_0)\csc\theta_0((C_n l^2\tilde{m}_0S\rho + 2(\tilde{m}_0N_v + m_p r_{p_x}(m - X_u))\cos\alpha_0)\cos\theta_0^2 \\
& + (C_{l_p}l^2\tilde{m}_0S\rho + 2(m_{tb}r_{tb_z} + m_p R_p)(m - Z_{\dot{w}})\sin\alpha_0)\sin\theta_0^2 + ((m_{tb}r_{tb_z} + m_p R_p)(m - X_u)\cos\alpha_0 \\
& + (\tilde{m}_0N_v + m_p r_{p_x}(m - Z_{\dot{w}}))\sin\alpha_0)\sin 2\theta_0)) / ((S(C_{n_\beta}l\tilde{m}_0 + m_p r_{p_x}(C_{D_0} + C_{S_\beta} + C_{L_\alpha}^2 K\alpha_0^2))\rho \\
& + 2\tilde{m}_0(-X_u + Y_v)\cos\alpha_0)\cos\theta_0 + (S(-C_{l_\beta}l\tilde{m}_0 + (m_{tb}r_{tb_z} + m_p R_p)(C_{D_0} + C_{S_\beta} + C_{L_\alpha}^2 K\alpha_0^2))\rho \\
& + 2\tilde{m}_0(Y_v - Z_{\dot{w}})\sin\alpha_0)\sin\theta_0))
\end{aligned} \tag{14}$$

$$\begin{aligned}
\varphi_1 = & (1/(2g\tilde{m}_0))V_0\omega_n\sec\theta_0(2(m + \tilde{m}_0 - X_u)\cos\alpha_0\cos\theta_0 + 2(m + \tilde{m}_0 - Z_{\dot{w}})\sin\alpha_0\sin\theta_0 \\
& - (S(C_{D_0} + C_{S_\beta} + C_{L_\alpha}^2 K\alpha_0^2)\rho((C_n l^2\tilde{m}_0S\rho + 2(\tilde{m}_0N_v + m_p r_{p_x}(m - X_u))\cos\alpha_0)\cos\theta_0^2 \\
& + (C_{l_p}l^2\tilde{m}_0S\rho + 2(m_{tb}r_{tb_z} + m_p R_p)(m - Z_{\dot{w}})\sin\alpha_0)\sin\theta_0^2 + ((m_{tb}r_{tb_z} + m_p R_p)(m - X_u)\cos\alpha_0 \\
& + (\tilde{m}_0N_v + m_p r_{p_x}(m - Z_{\dot{w}}))\sin\alpha_0)\sin 2\theta_0)) / ((S(C_{n_\beta}l\tilde{m}_0 + m_p r_{p_x}(C_{D_0} + C_{S_\beta} + C_{L_\alpha}^2 K\alpha_0^2))\rho \\
& + 2\tilde{m}_0(-X_u + Y_v)\cos\alpha_0)\cos\theta_0 + (S(-C_{l_\beta}l\tilde{m}_0 + (m_{tb}r_{tb_z} + m_p R_p)(C_{D_0} + C_{S_\beta} + C_{L_\alpha}^2 K\alpha_0^2))\rho \\
& + 2\tilde{m}_0(Y_v - Z_{\dot{w}})\sin\alpha_0)\sin\theta_0))
\end{aligned} \tag{15}$$

$$\begin{aligned}
\beta_1 = & -(\omega_n((C_n l^2\tilde{m}_0S\rho + 2(\tilde{m}_0N_v + m_p r_{p_x}(m - X_u))\cos\alpha_0)\cos\theta_0^2 \\
& + (C_{l_p}l^2\tilde{m}_0S\rho + 2(m_{tb}r_{tb_z} + m_p R_p)(m - Z_{\dot{w}})\sin\alpha_0)\sin\theta_0^2 + ((m_{tb}r_{tb_z} + m_p R_p)(m - X_u)\cos\alpha_0 \\
& + (\tilde{m}_0N_v + m_p r_{p_x}(m - Z_{\dot{w}}))\sin\alpha_0)\sin 2\theta_0)) / (V_0((S(C_{n_\beta}l\tilde{m}_0 + m_p r_{p_x}(C_{D_0} + C_{S_\beta} + C_{L_\alpha}^2 K\alpha_0^2))\rho \\
& + 2\tilde{m}_0(-X_u + Y_v)\cos\alpha_0)\cos\theta_0 + (S(-C_{l_\beta}l\tilde{m}_0 + (m_{tb}r_{tb_z} + m_p R_p)(C_{D_0} + C_{S_\beta} + C_{L_\alpha}^2 K\alpha_0^2))\rho \\
& + 2\tilde{m}_0(Y_u - Z_{\dot{w}})\sin\alpha_0)\sin\theta_0))
\end{aligned} \tag{16}$$

4.2. Parametric Performance Analysis

Here, we examine performance in steady wings-level and turning flight.

4.2.1. Performance Analysis of Wings-level Flight

A vehicle's geometry defines its performance. We first consider the effect of various geometric parameters on the speed at minimum glide angle (also called the "speed to fly") and the maximum lift-to-drag ratio. We also consider range, endurance, and number of dives, for a given propulsive energy budget. We focus on a few key parameters such as hull length and fineness ratio, wing aspect ratio, the wingspan ratio, and also the buoyant lung capacity $\bar{\eta}$.

Size Analysis. Because underwater gliders operate at conditions where the flow over the vehicle and its components may be laminar or turbulent, it is important to keep track of the Reynolds number, which characterizes the flow over a body. We define

$$\text{Re}_l = \frac{Vl}{\nu} \quad \text{and} \quad \text{Re}_{\bar{c}} = \frac{V\bar{c}}{\nu} = \text{Re}_l \frac{\bar{c}}{l} = \text{Re}_l \frac{\kappa}{fAR}$$

Referring to equation (12), we may write

$$\text{Re}_l^2 = \left(\frac{l}{\nu}\right)^2 \frac{\pi g l AR}{2 \kappa^2} \left(\frac{\bar{\eta}}{1+\bar{\eta}}\right) \frac{1}{\sqrt{C_D^2 + C_L^2}}$$

Note that the Reynolds number Re_l affects the parasitic drag coefficient C_{D_0} and thus appears on both sides of the equation above. Solving for $\bar{\eta}$ we find

$$\bar{\eta} = \frac{1}{\Phi - 1} \quad \text{where} \quad \Phi = \frac{1}{\text{Re}_l^2} \frac{\pi g l^3 AR}{2 \nu^2 \kappa^2} \frac{1}{\sqrt{C_D^2 + C_L^2}} \quad (17)$$

For flight at the shallowest descent angle, the parameters C_D , C_L , and Re_l are

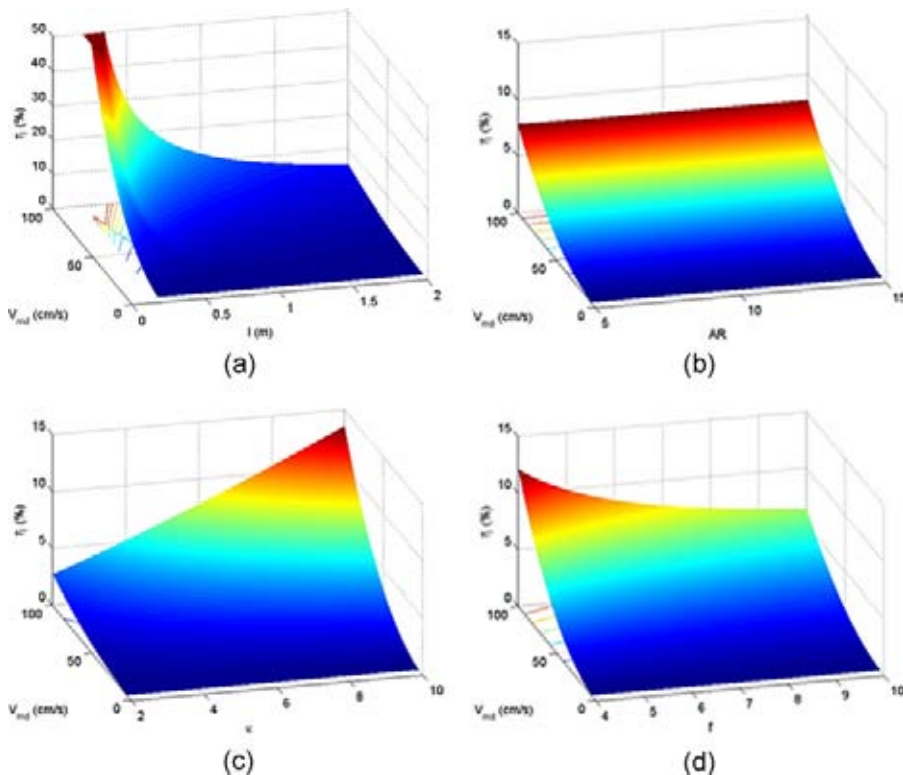
$$C_{D_{\text{md}}} = 2C_{D_0}, \quad C_{L_{\text{md}}} = \sqrt{\frac{C_{D_0}}{K}} \quad \text{and} \quad \text{Re}_{l_{\text{md}}} = \frac{V_{\text{md}} l}{\nu}$$

The maximum lift-to-drag ratio at this flight condition can be described as

$$\frac{L}{D} = \frac{C_{L_{\text{md}}}}{C_{D_{\text{md}}}} = \sqrt{\frac{1}{4KC_{D_0}}}$$

FIGURE 7

Variation of the required lung capacity with the given minimum glide angle speed and size. (a) Variation of lung capacity with V_{md} and l . (b) Variation of lung capacity with V_{md} and AR . (c) Variation of lung capacity with V_{md} and κ . (d) Variation of lung capacity with V_{md} and f .



Referring to (Hoerner, 1965; Stengel, 2004), one finds that C_{D_0} depends on Reynolds number, so C_{D_0} varies with speed and length.

Figures 7 and 8 present surface plots of the variation in required lung capacity and the maximum lift-to-drag ratio for a glider with the following parameter values

$$l = 1.5 \text{ m}, \quad AR = 11, \quad \kappa = 6,$$

$$f = 7, \quad \text{and} \quad \bar{i} = 0.02$$

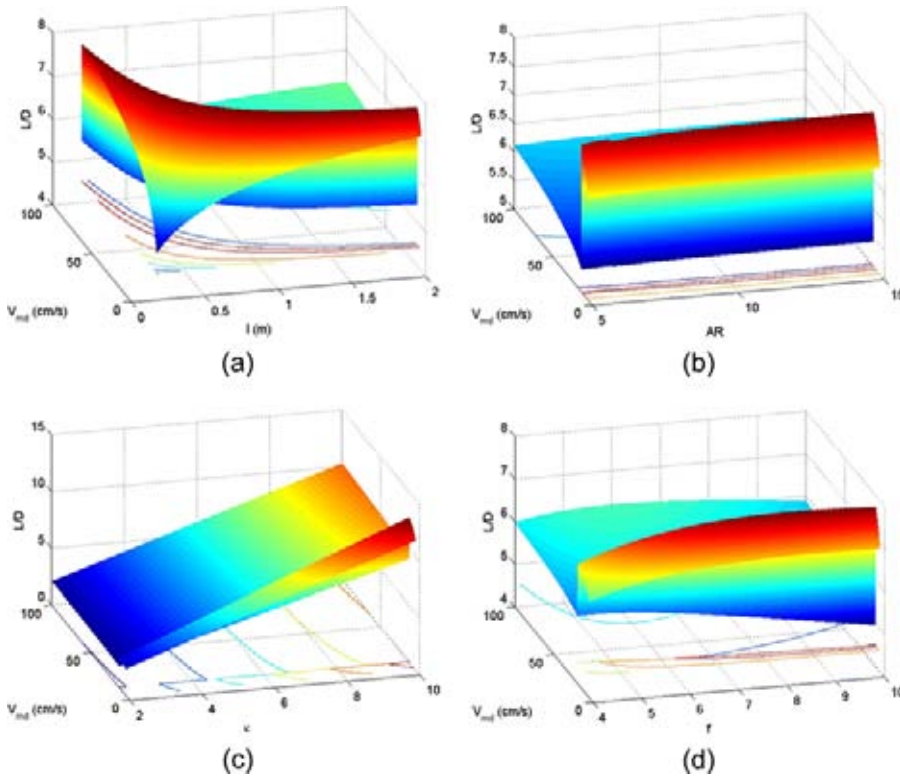
These parameter values are based on a model of *Slocum* used in earlier studies (Graver, 2005; Bhatta, 2006).

Figure 7 shows the variation in lung capacity required for flight of a 52-kg glider over a range of minimum glide angle speeds, given variations in one of the four geometric parameters l , AR , κ , or f . (In each plot, the nonvarying parameters take the nominal values given earlier.) To reduce the lung capacity required for a given speed at the minimum glide angle, one should increase the vehicle size (parameterized by hull length l) and fineness ratio f , and decrease the wingspan ratio κ . The required lung capacity does not vary with the wing aspect ratio AR .

Figure 8 shows the variation in maximum lift-to-drag ratio of a 52-kg glider over a range of minimum glide angle speeds, given variations in one of the four geometric parameters l , AR , κ , or f . (Again, the nonvarying parameters take the nominal values given earlier.) The apparent discontinuities occur when the flow over the wings transitions between laminar and turbulent. To increase the lift-to-drag ratio for a given speed to fly within a given flow regime (laminar or turbulent), one should increase the vehicle size (i.e., the hull length l) and the wingspan ratio κ . The lift-to-drag ratio appears less sensitive to changes in hull

FIGURE 8

Variation of maximum lift-drag ratio with the given minimum glide angle speed and size. (a) Variation of maximum lift-to-drag ratio with V_{md} and l . (b) Variation of maximum lift-to-drag ratio with V_{md} and AR . (c) Variation of maximum lift-to-drag ratio with V_{md} and κ . (d) Variation of maximum lift-to-drag ratio with V_{md} and f .



fineness ratio or wing aspect ratio, within a given flow regime.

Figure 9 shows the variation in displaced mass (for neutral buoyancy) with length, for the nondimensional parameter values above.

Range and Endurance. Referring to Figure 4 and considering saw-tooth profiles to a depth Δz at the minimum glide angle flight condition, the per-dive range is approximately

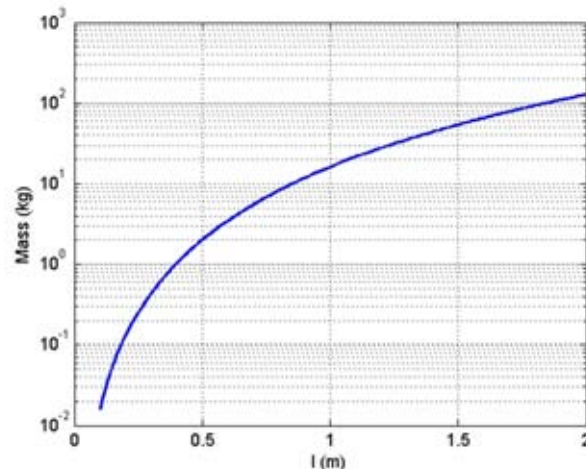
$$\Delta x = 2 \frac{C_{L_{md}}}{C_{D_{md}}} \Delta z = \frac{\Delta z}{\sqrt{KC_{D_0}}}$$

Note that we are ignoring the effects of transition between gliding flight conditions, on the assumption that such transitions can be effected quickly compared with the total dive time and

depth. The energy required to execute a single saw-tooth dive is given (approximately) by the pressure-volume work required at depth. Assume that

FIGURE 9

Neutral displacement versus length, at $f = 7$.



the vehicle displacement varies from minimum to maximum

$$2\bar{\eta}V_{NB} = 2 \left(\frac{\bar{\eta}}{1 + \bar{\eta}} \right) V$$

Correspondingly, the piston of the buoyancy actuator is moved from its maximally retracted position to its maximally extended position. The piston must counter a hydrostatic pressure $\rho g \Delta z$ acting on the piston face, which has area $\pi d^2/4$. Thus, we find that

$$\Delta E = \frac{\pi}{2} (\rho g \Delta z) \left(\frac{\bar{\eta}}{1 + \bar{\eta}} \right) \left(\frac{l^3}{f^2} \right)$$

In keeping with other simplifying assumptions, we ignore the variation in pressure within the dry volume due to the piston displacements. The time required to execute this dive, assuming the symmetrical flight condition in ascent, is

$$\Delta T = \frac{2\Delta z}{\dot{z}}$$

where, recalling equations (10) and (13),

$$\dot{z} = V_{md} \sin \xi_{md}$$

$$= \sqrt{\frac{\pi g l AR}{2 \kappa^2} \left(\frac{\bar{\eta}}{1 + \bar{\eta}} \right)} \frac{C_{D_{md}}}{(C_{D_{md}}^2 + C_{L_{md}}^2)^{3/4}}$$

Given an amount of stored energy E_p allocated for propulsion, the total

number of dives that can be executed to depth Δz is

$$N = \text{floor}\left(\frac{E_p}{\Delta E}\right)$$

where “floor” indicates the greatest lower integer. The total range that can be traversed (in still water) is

$$R = N\Delta x$$

and the total endurance is

$$E = N\Delta T.$$

Figure 10 shows contour plots indicating range and endurance and number of dives for a glider of given size and geometry when repeatedly diving to a given depth at a given nominal speed. In these plots, the vehicle length is 1.5 m, which corresponds to a mass of 52 kg. The total power available

for propulsion is 540 kJ, equivalent to a single 5 Ah, 30 VDC battery. In generating Figure 10, we assumed flight at the minimum glide angle speed with the net weight (or buoyancy) fixed at the maximum value, as determined from equation (17).

As indicated in Figure 10(a), the number of dives that can be executed involves a tradeoff between nominal speed and dive depth. Range and endurance diminish nonlinearly with increasing nominal speed but are independent of dive depth, a consequence of our assumptions that hydrostatic pressure is linear in depth (i.e., the water density is constant) and that pump efficiency does not vary with depth. Deep diving gliders typically modulate their buoyancy using a pump-driven, oil-filled bladder whose efficiency varies with ambient pressure.

Moreover, for deep dives, variation in water density is significant (Osse & Eriksen, 2007); ocean stratification and hull compressibility have a marked effect on glider performance (Jenkins et al., 2003). Considering these and other factors, such as the time spent in transition between equilibrium flight conditions, would alter the range and endurance contours, but the qualitative trends would persist.

4.2.2. Performance Analysis of Turning Motion

Based on the approximate expressions of turning motion presented in Section 4.1.2, we examine how the wing geometry (sweep angle, dihedral angle, and vertical placement) and the vertical stabilizer geometry (location l_v and area S_v) affect turning capability here. Variations in the wing sweep angle, dihedral angle, and vertical placement affect the roll moment due to sideslip, as expressed by the hydrodynamic coefficient $C_{l\beta}$ (Etkin & Reid, 1996). Therefore, we vary the coefficient $C_{l\beta}$ to investigate the effect of wing configuration parameters on turning motion. Note that the vertical stabilizer parameters l_v and S_v do not appear explicitly in equations (14), (15), and (16). However, they do affect the hydrodynamic coefficients, such as $C_{S\beta}$, C_{n_r} and $C_{n\beta}$ (Nelson, 1998) and thus influence turning performance.

Recalling that turning motions are parameterized by the moving mass rotation angle (μ), the glider roll angle (φ), and the sideslip angle (β), we examine the variation in the first-order sensitivities μ_1 , φ_1 , and β_1 with l_v , S_v , and $C_{l\beta}$ for a given turn rate. Recall that approximate values of μ , φ , and β may be obtained by multiplying the parameters μ_1 , φ_1 , and β_1 by the turn rate. In Figures 12(a), 11(b), and 11(c), which were generated using expressions

FIGURE 10

Contours of range (in km), endurance (in days), and number of dives for a 540-kJ glider. (a) Dive contours. (b) Range contours (km). (c) Endurance contours (days).

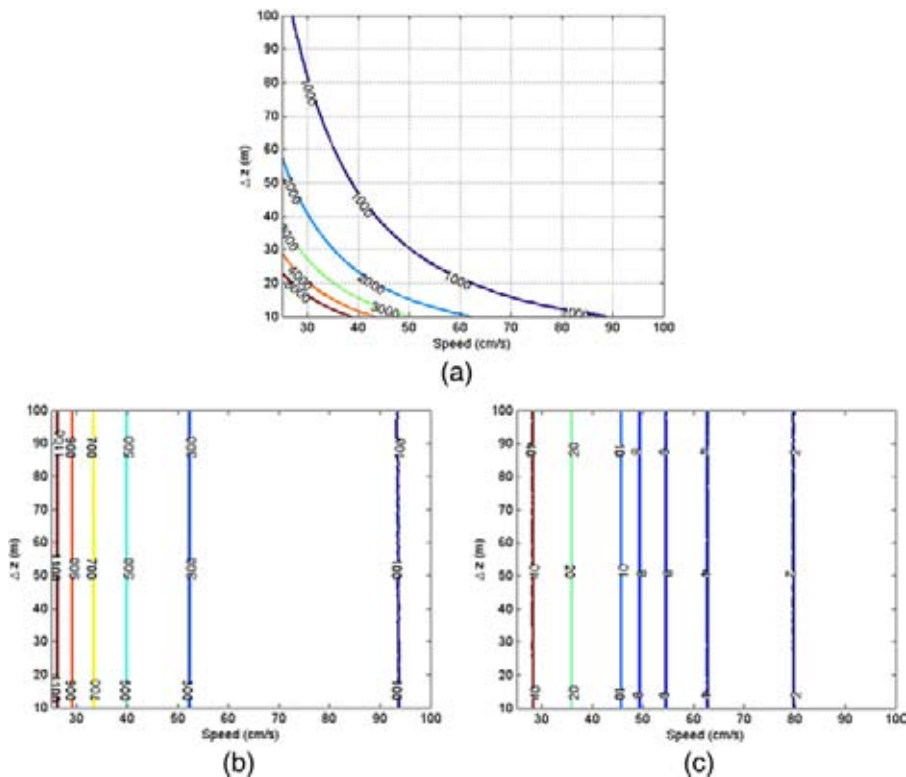
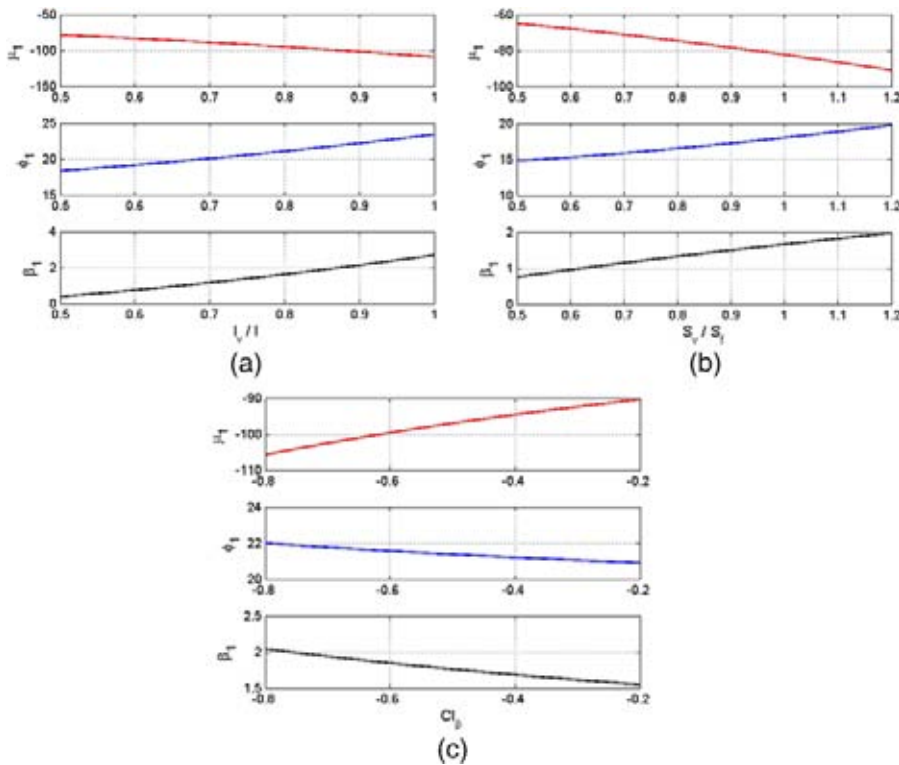


FIGURE 11

Variation in turning parameters μ_1 , φ_1 and β_1 with l_v , S_v and $C_{l\beta}$. (a) Variation of turning parameters with l_v . (b) Variation of turning parameters with S_v . (c) Variation of turning parameters with $C_{l\beta}$.



(14), (15), and (16), we see that when l_v or S_v (or their product, the “vertical stabilizer volume”) is small and/or the dihedral parameter $C_{l\beta}$ is less negative, a smaller moving mass rotation μ and roll angle φ are required to establish a given steady turn rate. Correspondingly, however, the vehicle’s steady turn rate is more sensitive to errors in the roll angle. While Figure 11 describes the effect of wing and vertical stabilizer geometry on the steady turning flight condition, it says nothing of stability, which is the topic of Section 5.

5. Stability Analysis

A glider’s geometry affects the hydrodynamic coefficients that appear in stability analysis. In this section, we consider the natural modes of glider motion and use root locus analysis to

examine the effects of a few critical parameters on glider stability.

5.1. Eigenmode Analysis

Considering a glider with fixed actuators as a rigid body, we linearize the dynamic equations about a wings-level equilibrium condition. Specifically, we consider the case of steady flight at maximum horizontal speed. Given a dynamic model, one may obtain an equilibrium flight condition with the help of a numerical trim solver. In our case, using Matlab’s *fsolve* subroutine, we found the following equilibrium:

$$V_{eq} = 0.77 \text{ m/s}, \quad \tilde{m}_{eq} = 0.2130 \text{ kg},$$

$$\gamma_{eq} = -35^\circ, \quad r_{pxeq} = 0.2826 \text{ m} \quad \text{and}$$

$$\alpha_{eq} = 1.2^\circ$$

Linearizing the dynamic equations about the above wings-level equilibrium, one finds that the resulting equations decompose into longitudinal and lateral-directional components. Ignoring certain kinematic variables, one obtains two sets of four, first-order equations,

$$\dot{X}_{long} = A_{long}X_{long} + B_{long}u_{long} \quad \text{and}$$

$$\dot{X}_{lat} = A_{lat}X_{lat} + B_{lat}u_{lat}$$

where

$$X_{long} = [\Delta u, \Delta w, \Delta q, \Delta \theta]^T \quad \text{and}$$

$$X_{lat} = [\Delta v, \Delta p, \Delta r, \Delta \varphi]^T$$

and where the elements of the state and input matrices depend on the steady flight condition and on the glider geometry, through the stability derivatives. Eigenvalues λ and non-dimensional eigenvectors v (in amplitude and phase form) for the state matrices A_{long} and A_{lat} are listed in Tables 1 and 2.

For the maximum horizontal-speed flight condition considered here, the longitudinal eigenvalues shown in Table 1 include two real eigenvalues and a complex conjugate pair. Examination of the eigenvectors associated with these eigenvalues indicates the following characteristic modes:

- a quickly converging pitch rate mode,
- a slowly converging speed mode, and
- an underdamped mode in which the pitch angle is coupled with the angle of attack.

The lateral-directional eigenvalues shown in Table 2 also include two real eigenvalues and a complex conjugate pair. Examination of the eigenvectors associated with these eigenvalues

TABLE 1

Eigenvalues and eigenvectors of longitudinal motion.

Longitudinal	$\lambda_1 = -3.28$	$\lambda_2 = -0.85 + 0.27i$	$\lambda_3 = -0.85 - 0.27i$	$\lambda_4 = -0.06$
Δu	$v_{11} = 0.0315 \angle 0^\circ$	$v_{21} = 0.0661 \angle -126^\circ$	$v_{31} = 0.0661 \angle 126^\circ$	$v_{41} = 1 \angle 0^\circ$
Δw	$v_{12} = 0.0631 \angle 0^\circ$	$v_{22} = 0.6694 \angle 0^\circ$	$v_{32} = 0.6694 \angle 0^\circ$	$v_{42} = 0.0231 \angle 180^\circ$
Δq	$v_{13} = 1 \angle 180^\circ$	$v_{23} = 1 \angle 84.5^\circ$	$v_{33} = 1 \angle -84.5^\circ$	$v_{43} = 0.0005 \angle 180^\circ$
$\Delta \theta$	$v_{14} = 0.1306 \angle 0^\circ$	$v_{24} = 0.4793 \angle -78^\circ$	$v_{34} = 0.4793 \angle 78^\circ$	$v_{44} = 0.0038 \angle 0^\circ$

TABLE 2

Eigenvalues and eigenvectors of lateral-directional motion.

Lateral-directional	$\lambda_1 = -1.33 + 1.75i$	$\lambda_2 = -1.33 - 1.75i$	$\lambda_3 = -1.81$	$\lambda_4 = -0.17$
Δv	$v_{11} = 0.0363 \angle -131^\circ$	$v_{21} = 0.0363 \angle 131^\circ$	$v_{31} = 0.1313 \angle 0^\circ$	$v_{41} = 0.7647 \angle 0^\circ$
Δp	$v_{12} = 1 \angle 0^\circ$	$v_{22} = 1 \angle 0^\circ$	$v_{32} = 0.9125 \angle 0^\circ$	$v_{42} = 0.4 \angle 0^\circ$
Δr	$v_{13} = 0.5026 \angle 150^\circ$	$v_{23} = 0.5026 \angle -150^\circ$	$v_{33} = 1 \angle 0^\circ$	$v_{43} = 0.0235 \angle 180^\circ$
$\Delta \varphi$	$v_{14} = 0.1969 \angle -127^\circ$	$v_{24} = 0.1969 \angle 127^\circ$	$v_{34} = 0.2125 \angle 180^\circ$	$v_{44} = 1 \angle 180^\circ$

indicates the following characteristic modes:

- a slowly converging, coupled roll and yaw rate mode,
- a slowly converging mode involving roll angle and side velocity, and
- an underdamped mode in which the roll rate and yaw rate are strongly coupled.

5.2. Glider Stability Varied With Geometry

Here, we investigate the effect of specific geometric parameters on the eigenvalue distribution. We consider two specific flight conditions: maximum horizontal speed and minimum glide angle. We present root locus plots for the longitudinal modes, in terms of the longitudinal wing location l_w , and for the lateral-directional modes, in terms of vertical stabilizer location l_v and area S_v , as well the dihedral parameter C_{lp} (which accounts for the effect of wing sweep, dihedral angle, and vertical placement). The variation of parameters l_w , l_v , and S_v

changes the hydrodynamic coefficients, which affects the eigenmodes of the glider dynamics. There are several methods to obtain hydrodynamic coefficients, including analytical, experimental, and computational approaches (Geisbert, 2007). For analysis of general trends, as described here, a semiempirical approach is sufficient (Nelson, 1998).

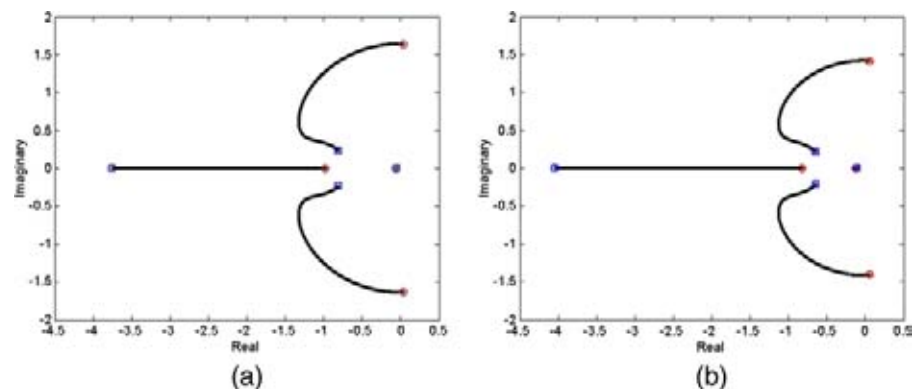
Again, the physical and hydrodynamic characteristics used in this

analysis are based on the *Slocum* model used in earlier studies (Graver, 2005; Bhatta, 2006). Stability of steady motion is obviously affected by vehicle speed; in order to make reasonable comparisons between different flight conditions, we fix the flight speed at $V = 0.77$ m/s, as in previous studies.

Figure 12 shows root locus plots for longitudinal modes in wings-level flight at maximum speed (left) and at

FIGURE 12

Root locus plots for longitudinal modes with the parameter l_w . (Root locus branches begin at red circles and end at blue squares.) (a) Maximum speed. (b) Minimum glide angle.



minimum glide angle (right) in terms of the parameter l_w . In these plots, l_w varies from zero (in which case the wing is aligned with the center of buoyancy) to $0.2 l$. Note that the farther aft the wing is located, the more stable the glider longitudinal dynamics become, due in part to the increased pitch damping.

Figure 13 shows root locus plots for the lateral-directional modes in wings-level flight at maximum speed (left) and at minimum glide angle (right) in terms of the parameter l_v . In these plots, l_v varies from $0.5 l$ to l , that is, from the stern of the hull to a half-vehicle length aft of the stern. The farther aft the vertical stabilizer is located, the more stable the glider lateral-directional dynamics become, due to increasing yaw stiffness and damping. Figure 14 shows root locus plots for the lateral-directional modes in wings-level flight at maximum speed and at minimum glide angle in terms of the parameter S_v , which varies from half the hull frontal area to 1.2 times the hull frontal area. Note that a larger vertical stabilizer area yields more stable lateral-directional modes, by increasing yaw stiffness and damping. Figure 15 shows root locus plots for the lateral-directional modes in wings-level flight at maximum speed and at minimum glide angle in terms of the parameter $C_{l\beta}$, which varies from “more negative” (-0.8) to “less negative” (-0.2). Note that larger negative values of this parameter (corresponding to wings with larger sweep angle, larger dihedral angle, or higher vertical placement) yield more stable lateral-directional dynamics. Of course, greater stability implies that greater control authority is required to effect a maneuver, such as a turn. Tradeoffs between control authority and stability are fundamental in vehicle design

FIGURE 13

Root loci for lateral-directional modes with parameter l_v . (Root locus branches begin at red circles and end at blue squares.) (a) Maximum speed. (b) Minimum glide angle.

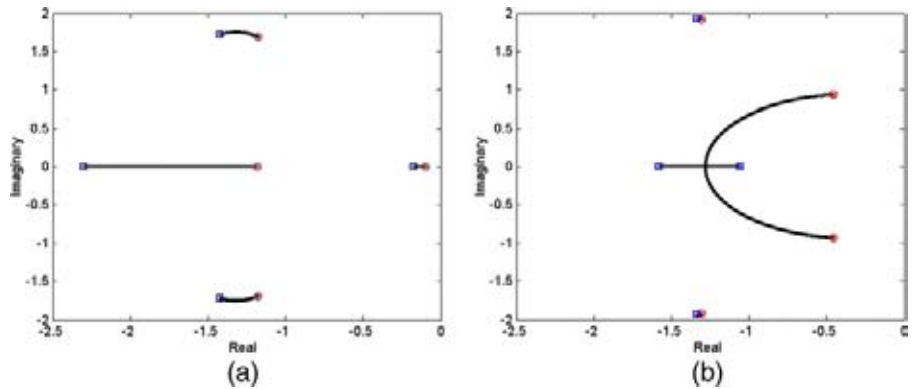


FIGURE 14

Root loci for lateral-directional modes with parameter S_v . (Root locus branches begin at red circles and end at blue squares.) (a) Maximum speed. (b) Minimum glide angle.

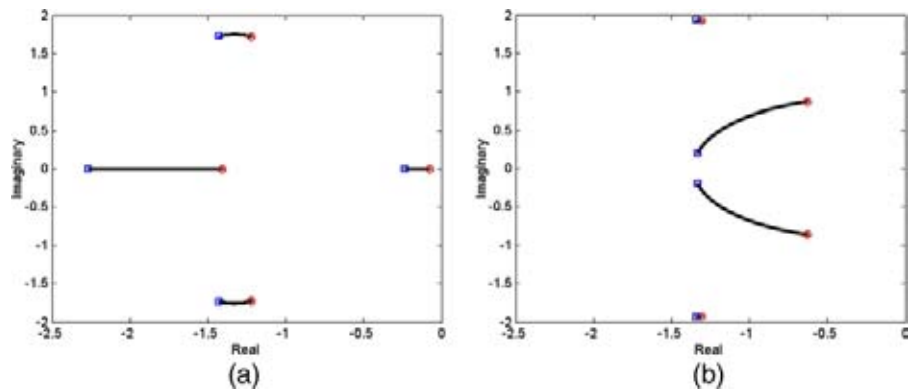
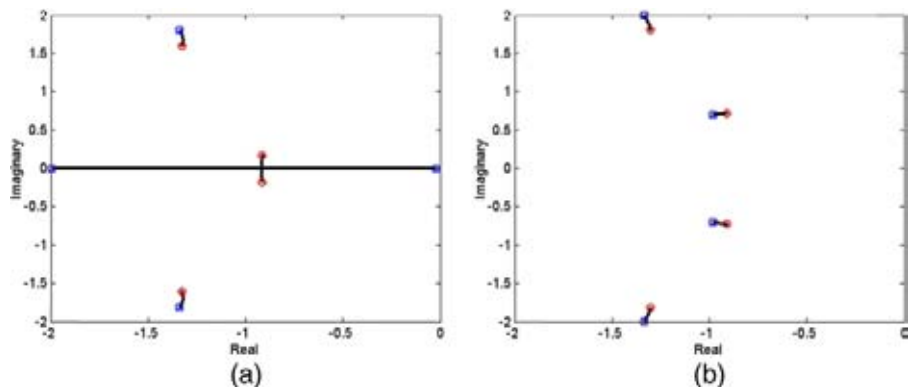


FIGURE 15

Root loci for lateral-directional modes with parameter $C_{l\beta}$. (Root locus branches begin at red circles and end at blue squares.) (a) Maximum speed. (b) Minimum glide angle.



and they suggest the need for guidelines. For manned vehicles, such guidelines are obtained based on crew and passenger comfort, but for unmanned vehicles they must be derived from other considerations such as payload motion.

6. Conclusion

Considering a conventional underwater glider configuration comprising a cylindrical hull, a simple trapezoidal wing and a vertical stabilizer, we have provided analysis to describe the effect of a few important geometric parameters on steady wings-level flight and steady turning flight. Starting from an 8-degree-of-freedom model that incorporates a cylindrically actuated moving point mass, we considered two important wings-level gliding conditions: minimum glide angle and maximum horizontal speed. We also developed approximate analytical expressions for steady turning motion in terms of the cylindrical actuation scheme and investigated the relationship between glider geometric parameters and the vehicle's performance and stability characteristics. The geometric parameters characterized the slenderness of the hull, the position and shape of the wing, and the size and position of the vertical stabilizer. We found, for example, that for a glider of given mass and buoyant lung capacity, higher speeds are attainable using longer hull lengths, smaller wing spans, larger hull fineness ratios, and higher wing aspect ratios. To maximize the lift-drag ratio at a given minimum glide angle speed, on the other hand, one should decrease the hull length and increase the wingspan ratio. Adapting a regular perturbation approach to develop analytical expressions for steady turning flight, we

found that a smaller roll angle is required to effect a steady turn at a given rate when the vertical tail volume and/or the dihedral effect is smaller. We also provided simple methods to estimate range and endurance; a more sophisticated analysis would incorporate details of the buoyancy lung mechanization as well as the variation of water density and hull compressibility. Turning to stability, we used root locus analysis to examine the variation in longitudinal and lateral-directional eigenvalues with changes in wing location, wing shape, and vertical stabilizer size and location. We found that the farther aft the wing is located, the more stable the glider longitudinal dynamics become, due in part to the increased pitch damping. The farther aft the vertical stabilizer is located and/or the larger the vertical stabilizer area is, the more stable the glider lateral-directional dynamics become, due to the increasing yaw stiffness and damping. Also, a larger dihedral effect yields more stable lateral-directional modes; dihedral effect can be increased by increasing sweep or dihedral angle and by placing the wings higher on the hull. Increased stability may provide better response to disturbances, but may also limit control authority, a tradeoff that must be considered in vehicle design.

Acknowledgments

The authors gratefully acknowledge the sponsorship of the Office of Naval Research under Grant #N00014-08-1-0012. The first author would like to thank the China Scholarship Council (CSC) for financial support during her visit to Virginia Tech.

Corresponding Author:

Shuangshuang Fan
 The State Key Lab of Fluid Power Transmission and Control,
 Zhejiang University, Hangzhou, China
 Email: fanshuangshuang@163.com

Appendix A. Body/Particle/Fluid System Energy

To derive the equations of motion for an underwater glider with a moving mass particle, one first determines the kinetic energy of the body/particle/fluid system in order to compute the momenta. The particle kinetic energy is

$$T_p = \frac{1}{2} m_p \mathbf{v}_p^T \mathbf{v}_p = \frac{1}{2} \boldsymbol{\eta}^T \mathbb{M}_p(\mathbf{r}_p) \boldsymbol{\eta}$$

where

$$\mathbb{M}_p(\mathbf{r}_p) = m_p \begin{pmatrix} \mathbb{I} \\ \hat{\mathbf{r}}_p \\ \mathbf{e}_1^T \\ \mathbf{e}_1^T \hat{\mathbf{r}}_p \end{pmatrix} \begin{pmatrix} \mathbb{I} \\ \hat{\mathbf{r}}_p \\ \mathbf{e}_1^T \\ \mathbf{e}_1^T \hat{\mathbf{r}}_p \end{pmatrix}^T = \begin{pmatrix} m_p \mathbb{I} & -m_p \hat{\mathbf{r}}_p & m_p \mathbf{e}_1 & -m_p \hat{\mathbf{r}}_p \mathbf{e}_1 \\ m_p \hat{\mathbf{r}}_p & -m_p \hat{\mathbf{r}}_p \hat{\mathbf{r}}_p & m_p \hat{\mathbf{r}}_p \mathbf{e}_1 & -m_p \hat{\mathbf{r}}_p \hat{\mathbf{r}}_p \mathbf{e}_1 \\ m_p \mathbf{e}_1^T & -m_p \mathbf{e}_1^T \hat{\mathbf{r}}_p & m_p & \mathbf{0} \\ m_p \mathbf{e}_1^T \hat{\mathbf{r}}_p & -m_p \mathbf{e}_1^T \hat{\mathbf{r}}_p \hat{\mathbf{r}}_p & \mathbf{0} & -m_p \mathbf{e}_1^T \hat{\mathbf{r}}_p \mathbf{e}_1 \end{pmatrix}$$

Here and elsewhere in the text, $\mathbf{0}$ represents a matrix of zeros whose dimensions are clear from context.

The kinetic energy T_b of the mass particle representing the buoyancy control system is defined similarly. The generalized mass matrix is

$$\mathbb{M}_b = \begin{pmatrix} m_b \mathbb{I} & -m_b \hat{\mathbf{r}}_b & \mathbf{0} \\ m_b \hat{\mathbf{r}}_b & -m_b \hat{\mathbf{r}}_b \hat{\mathbf{r}}_b & \mathbf{0} \\ \mathbf{0} & \mathbf{0} & \mathbf{0} \end{pmatrix}$$

Where \mathbf{r}_b denotes the location of the mass particle in the body frame. Since we have assumed the buoyancy control system is at the body frame origin, however, $\mathbf{r}_b = [0, 0, 0]^T$.

The kinetic energy of the rigid body portion of the glider is also quadratic in $\boldsymbol{\eta}$, with the generalized mass matrix

$$\mathbb{M}_{rb} = \begin{pmatrix} m_{rb} \mathbb{I} & -m_{rb} \hat{\mathbf{r}}_{rb} & \mathbf{0} \\ m_{rb} \hat{\mathbf{r}}_{rb} & \mathbf{J}_{rb} & \mathbf{0} \\ \mathbf{0} & \mathbf{0} & \mathbf{0} \end{pmatrix}$$

where \mathbf{J}_{rb} is the matrix of rigid body moments of inertia.

Finally, define the generalized added mass matrix

$$\mathbb{M}_f = \begin{pmatrix} \mathbf{M}_f & \mathbf{C}_f^T & \mathbf{0} \\ \mathbf{C}_f & \mathbf{J}_f & \mathbf{0} \\ \mathbf{0} & \mathbf{0} & \mathbf{0} \end{pmatrix}$$

where the component submatrices \mathbf{J}_f , \mathbb{M}_f , and \mathbf{C}_f represent added inertia, added mass, and hydrodynamic coupling between the translational and rotational motion of the rigid body.

The total kinetic energy of the rigid body/particle/fluid system is

$$T = T_p + T_b + T_{rb} + T_f = \frac{1}{2} \boldsymbol{\eta}^T \mathbb{M}(\mathbf{r}_p) \boldsymbol{\eta}$$

where

$$\mathbb{M}(\mathbf{r}_p) = \mathbb{M}_p(\mathbf{r}_p) + \mathbb{M}_b + \mathbb{M}_{rb} + \mathbb{M}_f.$$

References

- Bhatta**, P. 2006. Nonlinear stability and control of gliding vehicles. Ph.D. thesis, Princeton University. 206 pp.
- Bhatta**, P., & Leonard, N.E. 2008. Nonlinear gliding stability and control for vehicles with hydrodynamic forcing. *Automatica*. 44(5):1240-50. <http://dx.doi.org/10.1016/j.automatica.2007.10.006>.
- Curtin**, T.B., Bellingham, J.G., Catipovic, J., & Webb, D. 1993. Autonomous oceanographic sampling networks. *Oceanography*. 6(3):86-94. <http://dx.doi.org/10.5670/oceanog.1993.03>.
- Eriksen**, C.C., Osse, T.J., Light, R.D., Wen, T., Lehman, T.W., Sabin, P.L., ... Chiodi, A.M. 2001. Seaglider: A long-range autonomous underwater vehicle for oceanographic research. *IEEE J Oceanic Eng.* 26(4):424-36. <http://dx.doi.org/10.1109/48.972073>.
- Etkin**, B., & Reid, L.D. 1996. Dynamics of Flight: Stability and Control. New York: John Wiley and Sons. 400 pp.
- Galea**, A.M. 1999. Optimal path planning and high level control of an autonomous gliding underwater vehicle. Master thesis, Massachusetts Institute of Technology. 67 pp.
- Graver**, J., Liu, J., Woolsey, C.A., & Leonard, N.E. 1998. Design and analysis of an underwater vehicle for controlled gliding. In: Proc CISS. pp. 801-6. Princeton, NJ: IEEE.
- Graver**, J.G. 2005. Underwater gliders: Dynamics, control and design. Ph.D. thesis, Princeton University. 273 pp.
- Geisbert**, J.S. 2007. Hydrodynamic modeling for autonomous underwater vehicle using computational and semi-empirical methods. Master thesis, Virginia Tech. 87 pp.
- Hoerner**, S.F. 1965. Fluid Dynamic Drag. Midland Park, NJ: Author. 452 pp.
- Jenkins**, S.A., Humphreys, D.E., Sherman, J., Osse, J., Jones, C., Leonard, N.E., ... Wasyly, J. 2003. Underwater glider system study. Technical Report 53, Office of Naval Research (ONR). 240 pp.
- Lanchester**, F.W. 1908. Aerodnetics. London: A. Constable and Co. 468 pp.
- Mahmoudian**, N., Geisbert, J., & Woolsey, C.A. 2010. Approximate analytical turning conditions for underwater gliders and implications for path planning. *IEEE J Oceanic Eng.* 35(1):131-43. <http://dx.doi.org/10.1109/JOE.2009.2039655>.
- Mahmoudian**, N., & Woolsey, C.A. 2013. An efficient motion control system for underwater gliders. *Nonlinear Engineering: Modeling and Application*, 2013. (To appear.)
- Mises**, R.V. 1959. Theory of Flight. New York: Dover. 672 pp.
- Nelson**, R.C. 1998. Flight Stability and Automatic Control. New York: McGraw-Hill Higher Education. 441 pp.
- Osse**, T.J., & Eriksen, C.C. 2007. The deepglider: A full ocean depth glider for oceanographic research. In: Proc MTS/IEEE OCEANS. pp. 1-12. Vancouver, BC: IEEE.
- Pamadi**, B.N. 2004. Performance, Stability, Dynamics and Control of Airplanes. Reston, VA: AIAA. 780 pp. <http://dx.doi.org/10.2514/4.862274>.
- Rudnick**, D.L., Davis, R.E., Eriksen, C.C., Fratantoni, D.M., & Perry, M.J. 2004. Underwater glider for ocean research. *Mar Technol Soc J.* 38(1):48-59.
- Sherman**, J., Davis, R.E., Owens, W.B., & Valdes, J. 2001. The autonomous underwater glider "Spray". *IEEE J Oceanic Eng.* 26(4):437-46. <http://dx.doi.org/10.1109/48.972076>.
- Stengel**, R.F. 2004. Flight Dynamics. Princeton, NJ: Princeton University Press. 845 pp.
- Teledyne Webb Research**. 2013. Electric glider. <http://www.webbresearch.com/electricglider.aspx>, April 2013.
- USAF Stability and Control Datcom**. 1978. Flight Control Division, Air Force Flight Dynamics Laboratory. Fairborn, OH: Wright Patterson Air Force Base.
- Webb**, D.C., Simonetti, P.J., & Jones, C.P. 2001. SLOCUM: An underwater glider

propelled by environmental energy. IEEE J Oceanic Eng. 26(4):447-52. <http://dx.doi.org/10.1109/48.972077>.

Wolek, A., Burns, J., Woolsey, C.A., Techy, L., Quenzer, J., & Morgansen, K. 2012. A maneuverable, pneumatic underwater glider. In: Proc MTS/IEEE OCEANS. October 14–19, 2012. Virginia Beach, VA: IEEE.

Analysis of Underwater Acoustic Communication Channels

AUTHORS

Sadia Ahmed

Huseyin Arslan

Department of Electrical Engineering, University of South Florida

Introduction

The underwater acoustic communication (UAC) channel is vast and varying in nature. The existing UAC channel models may not be sufficient to represent every single UAC channel scenario. Moreover, the choice of models from the existing ones may not be accurate to represent the true channel environment. Thus, the varying nature of the UAC channel requires representing of such channel according to its channel environment, which in turn is specified by sets of channel parameters. If the channel parameters and hence the channel environment is accurately determined, the environment can be mapped onto the appropriate UAC channel representation (Ahmed & Arslan, 2009a, 2009b). The same channel representations can be reapplied in same or similar environments. The parameter values can be adaptively measured/estimated or derived according to the UAC environment. Therefore, the relationship between UAC channel representations and the UAC environments allows wider representation and coverage of the varying UAC channels. A high level classification of the UAC channel environments according to literature is presented in Figure 1.

ABSTRACT

The underwater acoustic communication (UAC) channel presents many difficulties such as high frequency, space, and time selectivity, frequency-dependent noise, and significant range and band limitation on transmission. Traditional UAC channel models that model such channels primarily include environmental models based on experimental data; models that are developed using mathematical equations such as wave equations, modal methods, and parabolic equations; and using statistical distributions. These methods/models are often limited in their coverage and accurate representations of every possible UAC channel environment. It is also physically impractical and cost ineffective to try to measure/estimate each channel to determine its model. In this paper, the authors will present the analysis of UAC channels according to the UAC channel environments classified and presented in a prior work by the authors, in which cognitive intelligence is used in the selection of the appropriate channel representations according to each sensed environment. To the best knowledge of the authors, this type of analysis and representation of UAC channels with respect to each UAC environment has not been addressed in the literature to date and therefore presents a significant contribution.

Keywords: channel representation, deep channel, shallow channel, underwater channel environment

The contributions of this paper are as follows:

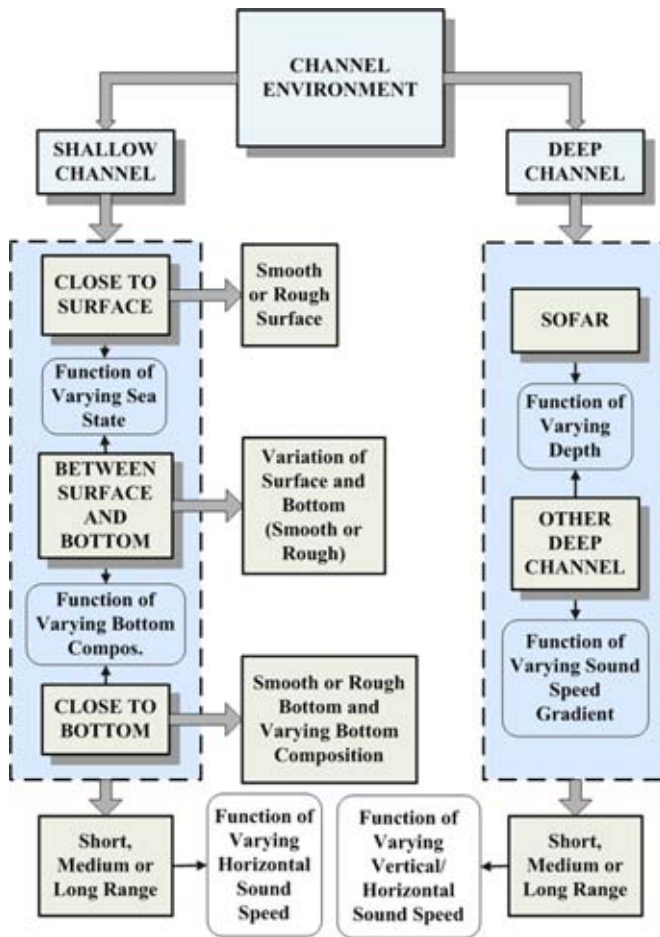
- This paper presents an analysis of UAC channel impulse response according to each broadly categorized UAC channel environment (Figure 1).
- Fading characteristics of the received signal and signal-to-noise ratio (SNR) of UAC channel in each channel environment and the relationship between environment parameters and different types of fading are analyzed and discussed.
- The channel representations are generated using the AcTUP software module.

The rest of the paper is organized as follows. Related Works presents

a brief literature review of UAC channel models. Mapping of UAC Channel Parameters to UAC Channel Environments discusses the mapping of UAC channel environment parameters onto UAC channel environments. UAC Channel Representation According to Environment presents the analysis of channel impulse response and fading characteristics of UAC channels according to channel environments. SNR Analysis provides the SNR analysis of the channel representations. Benefits of Channel Classification and Selection of Channels briefly presents the benefits of channel selection and the channel selection methods. Simulation Results presents the simulation results, and Conclusion addresses the concluding remarks.

FIGURE 1

Identification and high-level classification of UAC channel environments.



Related Works

The UAC channels are presented using stochastic models in some literature. In Galvin and Coats (1996), the amplitude and phase fluctuation of received signal is presented first by linear and then nonlinear transformations of Gaussian variables. In Morozov (1995), the estimation of slow phase fluctuations of channel impulse response is described as Markov's process, and the accumulation of impulse channel responses is decided by the Viterbi algorithm. In Byun et al. (2007), a channel model is proposed to present the time-varying UAC channel, where the time variation is produced by trans-

mitter and receiver motion. In this model, the eigen rays corresponding to direct/reflected multipaths are determined using ray tracing while the random diffusive multipaths are modeled using Rayleigh fading.

In the current paper, the random fluctuation due to diffusive paths are represented as Rayleigh or Rician variables according to the environment.

In Appleby and Davies (1998), time and frequency dispersion of UAC channel is represented by a model, which encompasses two separate modeling stages. First, the environment model is developed using the environmental data such as wind speed, sound speed profile, bottom

loss characteristics and incorporates features such as surface wave model, internal wave model, tidal currents model, two-layer bottom interactions, and ambient noise. Second, 3-D ray tracing is used to develop the propagation model that includes effects such as range dependent bathymetry, branching at the water/sediment interface, propagation through the sediment layer, range-dependent sound speed, caustics, reflection from the moving sea surface, and motion of transmitter/receiver platforms.

In the current paper, the effect of environment parameters and the propagation characteristics are incorporated in the deterministic and stochastic components of the arrived paths.

In Geng and Zielinski (1995), the random fluctuation of dominant eigen paths between transmitter and receiver is represented by the presence of smaller sub-eigen paths. The combination of eigen and sub-eigen paths is represented by Rician fading. In Bjerrum-Niese and Lutzen (2000), signal-to-multipath ratio and signal fading statistics is presented. Turbulence of water causes change in signal phase and amplitude. Ray tracing is used to determine the deterministic component and phase and amplitude variation is placed on top of the deterministic components.

In the current paper, the deterministic eigen components are first derived using Ray tracing and then the random fluctuation causing sub-eigen components are placed on top of the deterministic components. The combined effect of eigen and sub-eigen is represented as Gaussian, Rayleigh, or Rician variables.

In Walree et al. (2008) and Socheleau et al. (2011), data are measured and the measured data are interpolated to determine channel impulse response (CIR). Both uncorrelated and

correlated taps are considered. Pseudo-random binary signal is used as probe signal in the measurements.

Mapping of UAC Channel Parameters to UAC Channel Environments

The cognitive intelligence (CI) algorithms to map UAC channel parameters to environments and to map UAC environments to channel models have been presented in Ahmed and Arslan (2009a, 2009b), respectively.

All possible UAC channel environments may be determined from the sensed channel environment parameters. The channel representations, once mapped from the environments, will be more accurate since they are derived from the actual channel environments.

UAC Channel Representation According to Environment

In the proposed channel analysis, the following assumptions are made.

Channel Assumptions

- The channel equations are derived in the time domain. The transmission frequency and bandwidth are considered as parameters defining the UAC environment (Ahmed & Arslan, 2009a).
- Power in terms of path loss in dB is considered for each path in the power delay profile.
- Time variation of channel is applied on top of the power delay profile.
- The individual scatters are assumed to be independent and identically distributed (i.i.d.) Gaussian random variables in the case of uncorrelated taps.
- Each dominant and its corresponding sub-eigen paths arrive at the receiver at the same time.

- Line-of-sight (LOS) path is considered to be present in each UAC environment.

The rest of this section is organized as follows. Channel Impulse Response of UAC Channels presents the CIR and Fading Characteristics, Probability Distribution, Relationship Between Fading and Channel Parameters for Wide Sense Stationary (WSS) Uncorrelated Tap Channel presents the fading characteristics of different UAC channels according to each UAC environment. Frequency Dependent and Independent Noise briefly touches on the noise components and Fading Characteristics, Distribution, Relationship Between Fading and Channel Parameters for Quasi-stationary Channels on quasistationarity of UAC channels.

Channel Impulse Response of UAC Channels

Let the transmitted signal be denoted by an impulse, $\delta(t)$, where δ represents a Dirac delta function. The UAC channel will produce multipaths that may vary in time. In a time invariant channel, the channel impulse response can be expressed as $h(\tau_{REF}) = \sum_{l=0}^{L-1} \alpha_l \delta(\tau_{REF} - \tau_l)$.

The variables α_l and τ_l denote the attenuation coefficient and the time delay of the l th path respectively. The variable L denotes the total number of multipaths, τ_{REF} is a time reference. In a time variant channel, this equation can be modified as below,

$$h(\tau_{REF}, t) = \sum_{l=0}^{L-1} \alpha_l(t) \delta(\tau_{REF} - \tau_l(t)). \quad (1)$$

In an UAC channel, group of multipaths may consist of dominant paths, for examples, originating from reflections on the boundaries, also known as eigen paths (Gutierrez et al., 2005;

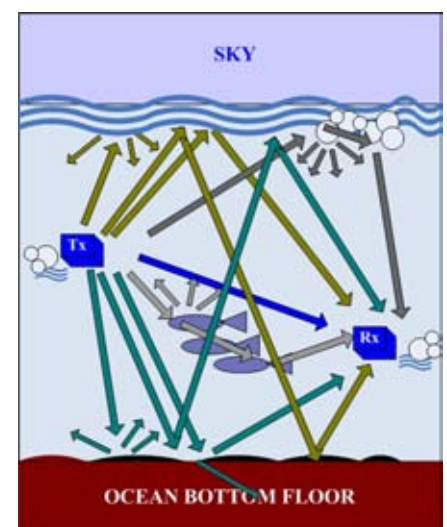
Geng & Zielinski, 1995) accompanied by less dominant paths or sub-eigen paths, for example, originating from various scatters.

Shallow Channel Representation According to Environment

A generic shallow water channel is illustrated in Figure 2. The shallow water UAC channel multipaths can be grouped according to their origination. In a shallow UAC channel environment, there may be five groups of eigen and sub-eigen paths. The first group of paths may result from surface only reflection and scatter, while the third group may result from bottom only reflection, bottom refraction, and scatter. The second group may include paths that reflect on both surface and bottom but the first reflection is on the surface. The fourth group may also include paths reflecting on both surface and bottom but the first reflection is on the bottom. There may be scatters associated with these paths as well. Depending on the transmission range and depth, sound refraction through water layers may result in

FIGURE 2

Underwater acoustic shallow water channel.



another group of eigen and sub-eigen paths. This fifth group may also include paths resulting from reflection, refraction, and scatter on marine life and other objects in the water medium. In addition, there may be a direct LOS that may depend on transmission range and depth. Equation (1) can be expanded to represent channel impulse response for all these five groups of paths as below.

$$\begin{aligned}
 h(t) = & \alpha_0(t)\delta(t) + \underbrace{\sum_{i=1}^I [\alpha_i(t)\delta(t - \tau_i(t))]}_{\text{GROUP1}} + \underbrace{\sum_{ii=II+1}^L [\alpha_{ii}(t)\delta(t - \tau_{ii}(t))]}_{\text{GROUP2}} \\
 & + \underbrace{\sum_{j=I+1}^{JJ} [\alpha_j(t)\delta(t - \tau_j(t))]}_{\text{GROUP3}} + \underbrace{\sum_{jj=JJ+1}^J [\alpha_{jj}(t)\delta(t - \tau_{jj}(t))]}_{\text{GROUP4}} \\
 & + \underbrace{\sum_{k=J+1}^{L-1} [\alpha_k(t)\delta(t - \tau_k(t))]}_{\text{GROUP5}}. \tag{2}
 \end{aligned}$$

Table 1 presents examples of dominant paths in these groups.

Each group of (2) can be expanded into many eigen paths and their corresponding sub-eigen paths as in (3). Each eigen and its sub-eigen paths arrive at the same time at each delay.

$$\begin{aligned}
 \text{GROUP}_1 = & \left[\alpha_1(t)\delta(t - \tau_1) + \sum_{m_1=2}^{M_1-1} \alpha_{1m_1}(t)\delta(t - \tau_1) \right] \\
 & + \left[\alpha_2(t)\delta(t - \tau_2) + \sum_{m_2=2}^{M_2-1} \alpha_{2m_2}(t)\delta(t - \tau_2) \right] \dots \\
 & \dots + \left[\underbrace{\alpha_{II}(t)\delta(t - \tau_{II})}_{\text{Eigenpath}} + \underbrace{\sum_{m_{II}=2}^{M_{II}-1} \alpha_{II m_{II}}(t)\delta(t - \tau_{II})}_{\text{Sub-eigenpaths}} \right]. \tag{3}
 \end{aligned}$$

Figure 3 illustrates one single dominant path originating in each group along with less dominant paths due to scatters.

In an ideal scenario, with a smooth surface and a smooth bottom boundary, the channel generated multipaths can be described as arriving from image sources (Lurton, 1996). Under this scenario, the range traversed by each path from source to destination denoted by $Range_{wv}$ can be expressed in terms of the distance between

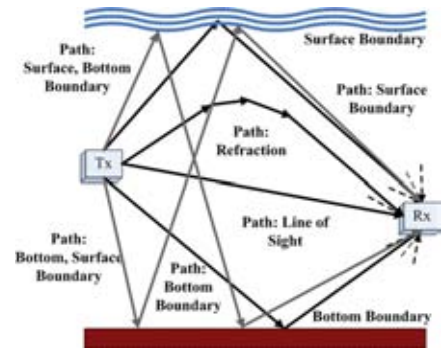
TABLE 1

Shallow water channel: The five groups and their respective paths.

Group	Paths in the Group
GROUP1	
GROUP2	
GROUP3	
GROUP4	
GROUP5	

FIGURE 3

Single path originated from each group in UAC shallow channel. Solid line represents eigen paths, and dashed line represents sub-eigen paths.



source and destination denoted by D , source and destination depth from surface denoted by z_s and z_r respectively, and water column height between surface and bottom denoted by H . There are four such image sources and are given by Lurton (1996).

$$\begin{aligned}
 z_{1v} &= 2(v-1)H + z_s - z_r \\
 z_{2v} &= 2(v-1)H + z_s + z_r \\
 z_{3v} &= 2vH - z_s - z_r \\
 z_{4v} &= 2vH - z_s + z_r. \tag{4}
 \end{aligned}$$

Then the time delay of each multipath at the destination can be expressed as

$$\tau_{wv} = \frac{Range_{wv}}{c}, \tag{5}$$

where $w = 1, 2, 3, 4$ denotes the image source types and c denotes the sound velocity. The values of v can be $v = 1, 2, 3, \dots$. If only path loss is considered and the sound velocity is considered constant (the value is provided in simulation), each multipath from individual image source will go through path loss given by Lurton (1996),

$$TL_{wv} = 20\log Range_{wv} + \beta Range_{wv}, \tag{6}$$

where β is the water absorption coefficient with units of dB/Km . In this ideal scenario, in the absence of scatters, each

path arriving from each image source will only consist of a dominant path. The amplitude of each path derived from (6) can be expressed as

$$A_{uv} = 10^{\frac{TL_{uv}}{10}}. \quad (7)$$

In case of a smooth surface and a smooth bottom and in the absence of sub-eigen paths, there will only be dominant paths; the CIR will consist of one LOS, one surface reflected path (GROUP1), one bottom reflected path (GROUP3), multiple paths in GROUP2, and multiple reflected paths in GROUP4. Therefore, in the absence of sub-eigen paths, (2) becomes

$$\begin{aligned} h(t) = & \alpha_0(t)\delta(t) + \underbrace{[\alpha_1(t)\delta(t - \tau_1)]}_{GROUP1} + \underbrace{\sum_{ii=II+1}^I [\alpha_{ii}(t)\delta(t - \tau_{ii}(t))]}_{GROUP2} \\ & + \underbrace{[\alpha_{JJ}(t)\delta(t - \tau_{JJ}(t))]}_{GROUP3} + \underbrace{\sum_{jj=JJ+1}^J [\alpha_{jj}(t)\delta(t - \tau_{jj}(t))]}_{GROUP4} \\ & + \underbrace{\sum_{k=J+1}^{L-1} [\alpha_k(t)\delta(t - \tau_k(t))]}_{GROUP5} \end{aligned} \quad (8)$$

The above ideal scenarios generate *deterministic path components*.

Now, let the smooth surface and smooth bottom be replaced by surface waves and a rough bottom, respectively. Let the following conditions be assumed: (a) the transmitter and the receiver are stationary; (b) the water column height (vertical distance between surface and bottom) remain the same for both transmitter and receiver; (c) the acoustic wave length is much larger than the wave surface and bottom reflector elements; (d) the dominant paths arrive at the receiver; and (e) the delays of dominant paths are calculated using image sources, although the surface movement due to surface waves and the presence of rough bottom may vary these dominant path delays.

The scatters induced by surface waves and rough bottom may produce sub-eigen paths that can be represented as *stochastic path components* along with each dominant path. Then (8) becomes

$$\begin{aligned} h(t) = & \alpha_0(t)\delta(t) + \underbrace{[\alpha_1(t)\delta(t - \tau_1) + \sum_{m_1=2}^{M_1-1} \alpha_{1m_1}(t)\delta(t - \tau_1)]}_{GROUP1} \\ & + \underbrace{\sum_{ii=II+1}^I [\alpha_{ii}(t)\delta(t - \tau_{ii}(t)) + \sum_{mm_{ii}=2}^{MM_{ii}-1} \alpha_{iimm_{ii}}(t)\delta(t - \tau_{ii}(t))]}_{GROUP2} \\ & + \underbrace{[\alpha_{JJ}(t)\delta(t - \tau_{JJ}) + \sum_{p_{JJ}=2}^{P_{JJ}-1} \alpha_{JJp_{JJ}}(t)\delta(t - \tau_3)]}_{GROUP3} \\ & + \underbrace{\sum_{jj=JJ+1}^J [\alpha_{jj}(t)\delta(t - \tau_{jj}(t)) + \sum_{pp_{jj}=2}^{PP_{jj}-1} \alpha_{jjpp_{jj}}(t)\delta(t - \tau_{jj}(t))]}_{GROUP4} \\ & + \underbrace{\sum_{k=J+1}^{L-1} [\alpha_k(t)\delta(t - \tau_k(t)) + \sum_{q_k=2}^{Q_k-1} \alpha_{kq_k}(t)\delta(t - \tau_k)]}_{GROUP5}. \end{aligned} \quad (9)$$

Let the combination of each dominant and its corresponding sub-eigen paths be denoted as $R'_{index}(t)$. Using (9), $h(t)$ can be expressed as the sum of variables as below,

$$\begin{aligned}
 h(t) = h_{S_{BET}}(t) = & \alpha_0(t)\delta(t) + \underbrace{R_1(t)}_{GROUP1} \\
 & + \underbrace{R_{II+1}(t) + R_{II+2}(t) + \dots + R_I(t)}_{GROUP2} + \underbrace{R_{JJ}(t)}_{GROUP3} \\
 & + \underbrace{R_{JJ+1}(t) + R_{JJ+2}(t) + \dots + R_J(t)}_{GROUP4} + \underbrace{R_{J+1}(t) + R_{J+2}(t) + \dots R_{L-1}(t)}_{GROUP5},
 \end{aligned} \tag{10}$$

where $GROUP_1$ denotes the surface only reflected/scattered paths, $GROUP_3$ denotes bottom only reflected/scattered paths, and $GROUP_5$ denotes paths corresponding to refraction in the medium and refraction/reflection/scatter on other objects. The $GROUP_2$ represents the surface/bottom reflected/scattered paths, while $GROUP_4$ represents the bottom/surface reflected/scattered paths. It is to be noted that arrival time of groups of paths and paths within the groups may vary.

According to Figure 1, the shallow channel can be classified into three broad categories. They are close to surface, close to bottom, and in between channels. The surface and bottom roughness dictates further classification of shallow channel environment. The channel representations for these environments are given below.

A channel that represents a shallow channel communication environment in between surface and bottom can be expressed by (10), where $h_{S_{BET}}(t)$ denotes the channel impulse response. Depending on how close to the surface and/or to the bottom the source and destination are, both CIR, h_{S_S} and h_{S_B} , for close to surface and close to bottom environment respectively, may have paths in $GROUP1$ through $GROUP4$.

1) **Shallow Channel Close to Rough Surface:** Similar to a channel somewhere in between surface and bottom, a close to rough surface shallow channel can be expressed as (10). If however the bottom is far away from the surface in a close to rough surface communication environment, strictly *ideally*, the bottom reflected dominant paths may disappear due to higher loss and/or longer delay in arriving. Under such scenario, $GROUP3$ will be empty, and in $GROUP2$ and $GROUP4$ only surface scattered sub-eigen paths will dominate. Let the combination of scattered sub-eigen paths generated only from the surface corresponding to each negligible surface/bottom reflected dominant paths be denoted by the variables R'_{index} . In that case, (10) will reduce to $h_{S_S}(t)$ as below,

$$\begin{aligned}
 h_{S_S}(t) = & \alpha_0(t)\delta(t) + \underbrace{R_1(t)}_{GROUP1} + \underbrace{R'_{II+1}(t) + R'_{II+2}(t) + \dots + R'_I(t)}_{GROUP2} \\
 & + \underbrace{R'_{JJ+1}(t) + R'_{JJ+2}(t) + \dots + R'_J(t)}_{GROUP4} + \underbrace{R_{J+1}(t) + R_{J+2}(t) + \dots R_{L-1}(t)}_{GROUP5}.
 \end{aligned} \tag{11}$$

The CIR in a close to a rough surface for long, short, and medium range transmission can be expressed as $h_{S_{RS/L}}(t)$, $h_{S_{RS/S}}(t)$, and $h_{S_{RS/M}}(t)$, respectively. The expressions for these are derived from (11).

In a long range close to rough surface transmission, the sub-eigen paths due to scatter are negligible and hence may result in $GROUP2$ and $GROUP4$ of (11) to be empty. Surface reflected dominant paths may dominate over the surface scattered sub-eigen paths. Let $R''_1(t)$ denote the combination of surface reflected dominant path and negligible sub-eigen scatters. There may be horizontal variation of sound speed resulting in scatter and/or dominant paths due to refraction. Even though some reflection and scatters may occur due to objects in the medium, in a long range these may/may not be negligible. Hence $GROUP5$ may not be empty. Using (11), the CIR for transmission can be written as

$$h_{S_{RS/L}}(t) = \alpha_0(t)\delta(t) + \underbrace{R''_1(t)}_{GROUP1} + \underbrace{R_{J+1}(t) + R_{J+2}(t) + \dots R_{L-1}(t)}_{GROUP5}. \tag{12}$$

In a short range close to rough surface transmission, surface scattered sub-eigen paths will be dominating. Therefore, $GROUP2$ and $GROUP4$ will not be empty. Due to short range, there may not be horizontal sound velocity variation

but the presence of other objects in the water may result in reflection and scatters. If the range is short, the reflection/scatter on objects in the medium may be significant. Therefore, GROUP5 may not be empty. The resulting CIR, $h_{S_{RS/S}}(t)$ will be as same as (11) with $R_1(t)$ having more dominant sub-eigen paths.

In a medium range transmission, there may be dominant paths due to reflection and sub-eigen paths due to scatter. If the range is medium, the reflection/scatter on objects in the medium may be significant. The CIR of such a channel, $h_{S_{RS/M}}(t)$ will be as same as (11).

2) **Shallow Channel Close to Smooth Surface:** In case of smooth surface, there will be no sub-eigen paths due to scatters on surface or bottom. Hence when the bottom is far away from the surface, ideally, GROUP2 and GROUP4 will be empty. For medium range transmission, (11) can be expressed as,

$$h_{S_{SS/M}}(t) = \alpha_0(t)\delta(t) + \underbrace{R_1''(t)}_{GROUP1} + \underbrace{R_{J+1}(t) + R_{J+2}(t) + \dots R_{L-1}(t)}_{GROUP5}, \quad (13)$$

where R_1'' denotes surface only reflected dominant path without any sub-eigen paths. Equation (13) also represents short range and long range close to smooth surface channels.

3) **Shallow Channel Close to Rough Bottom:** Similar to channels close to the surface, a close to rough bottom channel can be expressed as (10). If the surface is far away from the bottom, *ideally*, the surface reflected dominant paths will disappear due to higher loss and/or due to delay in arriving and (10) will reduce to $h_{S_B}(t)$ as shown in (14). Variable $R'_{Bindex}(t)$ denotes the combination of sub-eigen scatters generated only from the bottom corresponding to each negligible surface/bottom reflected dominant path.

$$\begin{aligned} h_{S_B}(t) = \alpha_0(t)\delta(t) + & \underbrace{R'_{BII+1}(t) + R'_{BII+2}(t) + \dots + R'_{BI}(t)}_{GROUP2} \\ & \underbrace{R_{JJ}(t)}_{GROUP3} + \underbrace{R'_{BJJ+1}(t) + R'_{BJJ+2}(t) + \dots + R'_{BJ}(t)}_{GROUP4} \\ & + \underbrace{R_{J+1}(t) + R_{J+2}(t) + \dots R_{L-1}(t)}_{GROUP5}. \end{aligned} \quad (14)$$

The CIR in a close to a rough bottom for long-, short-, and medium-range transmission can be expressed as $h_{S_{RB/L}}$, $h_{S_{RB/S}}$, and $h_{S_{RB/M}}$, respectively. In a close to rough bottom shallow channel, in addition to bottom reflection, different bottom composition may produce refracted scatters in GROUP2, GROUP3, and GROUP4.

In long-range transmissions, these scatters may not have significant contribution and so, GROUP2 and GROUP4 may be empty. Then (14) becomes

$$h_{S_{RB/L}}(t) = \alpha_0(t)\delta(t) + \underbrace{R''_{JJ}(t)}_{GROUP3} + \underbrace{R_{J+1}(t) + R_{J+2}(t) + \dots R_{L-1}(t)}_{GROUP5}, \quad (15)$$

where $R''_{JJ}(t)$ denotes combination of bottom reflected dominant path and negligible sub-eigen scatters.

Different marine life and other objects on the ocean floor may produce scatters due to reflection and refraction. In long-range transmission, these scatters may not be significant but in short- and medium-range transmission, these scatters may be dominant. In short and medium range transmissions, strong bottom reflected/refracted scatters may also be dominant. Therefore, short range close to rough bottom transmission can be expressed as (14), denoted by $h_{S_{RB/S}}(t)$, where $R_{JJ}(t)$ will contain more dominant sub-eigen paths. A medium range close to rough bottom transmission can also be expressed as (14) and denoted by $h_{S_{RB/M}}(t)$.

4) **Shallow Channel Close to Smooth Bottom:** In case of smooth bottom, there will be no sub-eigen paths due to scatters on the bottom. Hence for medium range transmission, (14) can be expressed as

$$h_{S_{SB/M}}(t) = \alpha_0(t)\delta(t) + \underbrace{R''_{JJ}(t)}_{GROUP3} + \underbrace{R_{J+1}(t) + R_{J+2}(t) + \dots R_{L-1}(t)}_{GROUP5}, \quad (16)$$

where $R_{JJ}'''(t)$ denotes bottom only reflected dominant path without any sub-eigen paths. Equation (16) also represents short range and long range close to smooth bottom channels denoted by $h_{S_{SB/S}}(t)$ and $h_{S_{SB/L}}(t)$, respectively.

Deep Channel Representation According to Environment

If only path loss is considered, in a deep channel, each multipath will go through path loss given by Lurton (1996) and will arrive at various delays.

In a deep channel, when the sound velocity is not constant, the first group of multipaths represents the steepest paths, the second group represents grazing paths for isothermal channel or axis paths for SOFAR channel, and the third group represents bottom reflected multipaths (Lurton, 1996). These paths are presented below.

$$\begin{aligned}
 h_D(t) = & \underbrace{\sum_{i_D=1}^{I_D} [\alpha_{i_D}(t)\delta(t - \tau_{i_D}) + \sum_{m_{D_{i_D}}=2}^{M_{D_{i_D}}-1} \alpha_{i_D m_{D_{i_D}}}(t)\delta(t - \tau_{i_D})]}_{\text{GROUP1}} \\
 & + \underbrace{\sum_{j_D=I_D+1}^{J_D} [\alpha_{j_D}(t)\delta(t - \tau_{j_D}) + \sum_{p_{D_{j_D}}=2}^{P_{D_{j_D}}-1} \alpha_{j_D p_{D_{j_D}}}(t)\delta(t - \tau_{j_D})]}_{\text{GROUP2}} \\
 & + \underbrace{\sum_{k_D=J_D+1}^{L_D-1} [\alpha_{k_D}(t)\delta(t - \tau_{k_D}) + \sum_{q_{D_{k_D}}=2}^{Q_{D_{k_D}}-1} \alpha_{k_D q_{D_{k_D}}}(t)\delta(t - \tau_{k_D})]}_{\text{GROUP3}}. \quad (17)
 \end{aligned}$$

Although (17) considers both eigen and sub-eigen components, the existence of a fewer number of scatters in a deep channel may only cause dominant eigen components to exist. The deep channel can be broadly categorized into SOFAR and other types of deep channels.

1) **SOFAR Channel:** The CIR in a SOFAR channel for long-, medium-, and short-range transmission can be derived from (17). For long-, medium-, and short-range transmission, not close to surface or bottom, the scatters may be insignificant resulting in only dominant components as below,

$$\begin{aligned}
 h_{D_{SOFAR/L,M,S}}(t) = & \underbrace{\sum_{i_D=1}^{I_D} [\alpha_{i_D}(t)\delta(t - \tau_{i_D})]}_{\text{GROUP1}} \\
 & + \underbrace{\sum_{j_D=I_D+1}^{J_D} [\alpha_{j_D}(t)\delta(t - \tau_{j_D})]}_{\text{GROUP2}} \\
 & + \underbrace{\sum_{k_D=J_D+1}^{L_D-1} [\alpha_{k_D}(t)\delta(t - \tau_{k_D})]}_{\text{GROUP3}}. \quad (18)
 \end{aligned}$$

However, for SOFAR channels close to surface or bottom, there may be some significant scatters that would result in (17). In both cases, GROUP1 denotes the

steepest paths, GROUP2 denotes the axis paths, and GROUP3 denotes the bottom reflected paths.

2) Other Deep Channels:

Isothermal Deep Channel: The CIR in isothermal channels for long-, medium-, and short-range transmission can be expressed as $h_{D_{ISO/L,M,S}}(t)$. For long-, medium-, and short-range transmission, not close to surface or bottom, the scatters may be insignificant resulting in mostly dominant eigen paths similar to (18). For channels close to surface or bottom, the presence of significant scatters may result in an equation similar to (17). The first group of paths denotes the steepest paths, the second one denotes grazing paths, and the third one denotes the bottom reflected paths.

Fading Characteristics, Probability Distribution, Relationship Between Fading and Channel Parameters for Wide Sense Stationary (WSS) Uncorrelated Tap Channel

In determining the fading characteristics and probability distribution of various UAC channels, the following assumptions are made:

Assumptions:

- Channel paths are considered at each sample time.
- In the absence of a natural path at any sample, a path is generated by interpolating neighboring paths.
- The symbol period is considered large enough to encapsulate all the significant arrived multipaths.

After convolving with the channel the received signal, using (1), can be expressed as

$$\begin{aligned}
 r(t) = & \alpha_0(t)s(t) + \sum_{l=1}^{L-1} \alpha_l(t)s(t - \tau_l), \\
 & + n_1(t) + n_2(t), \quad (19)
 \end{aligned}$$

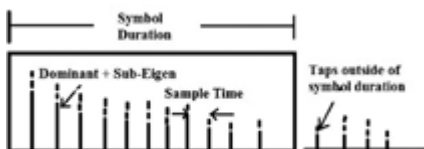
where the variables $s(t)$, $n_1(t)$ and $n_2(t)$ denote the transmitted signal, frequency-independent and frequency-dependent noise, respectively.

When each arrived path is i.i.d. Gaussian, the following conditions may occur. Case a) When the dominant path to less dominant multipath ratio, which is denoted by signal to multipath ratio, SMR is less than 1, i.e., $SMR \ll 1$ the amplitude of the envelop of paths follows Rayleigh distribution (Geng & Zielinski, 1995). Case b) When the eigen path component dominates, as in the case of direct LOS, $SMR \gg 1$, and the amplitude of the envelop of the paths follows Gaussian distribution. Case c) When the dominant path is comparable to the less dominant paths, such that the dominant path exists as one single large path compared to the less dominant paths, i.e., $SMR \approx 1$ the amplitude of the envelop of the paths follows Rician distribution.

The symbol is sampled at each arrived multipath. Each path at each sample location is a combination of eigen and sub-eigen paths. At each sample location, these simultaneous paths can add constructively or destructively. The amplitude of the resultant path at each sample location can be subjected to one of the three conditions mentioned above resulting in Gaussian, Rayleigh or Rician fading distribution. Let each sample represent

FIGURE 4

Channel paths, symbol duration, and sample time: The bold lines represent dominant eigen and dashed lines represent sub-eigen paths. Each arrived path within symbol duration and outside of symbol duration may consist of one dominant and/or one/multiple sub-eigen paths.



a variable, G , RL , or RC identifying an amplitude with either Gaussian, Rayleigh, or Rician distribution, respectively.

These variables are an indication of the channel environment and are directly related to the environment parameters. For example, the value of the range parameter (short/medium/long) and/or depth parameter (close to surface/close to bottom, etc.) may determine the variable at each sample location to be G , RL , or RC .

If the channel delay spread is long and some paths arrive outside of the symbol duration, those outside paths will also contain combination of dominant and sub-eigen paths resulting in an amplitude variation, the distribution of which can be presented by a Gaussian, Rayleigh, or Rician variable according to the channel environment. Figure 4 illustrates the relationship between the paths, the symbol duration, and the sample time. The received signal representation in terms of Gaussian, Rayleigh, or Rician fading for the UAC channels described in the last subsection are given below. The SMR for *each path* can be expressed as

$$SMR_{path} = \frac{|Eigen_{path}|}{|\sum SubEigen_{path}|}. \quad (20)$$

Depending on the value of SMR_{path} of each path, the combination of eigen and sub-eigen components will follow Rayleigh, Gaussian, or Rician distribution. If the symbol duration encapsulate all paths, then

$$SMR_{Symbol} = \frac{|LOS|}{|\sum Other_{path}|}. \quad (21)$$

Depending on the value of SMR_{Symbol} , the combination of all paths (each path a combination of eigen and sub-eigen components) within the symbol duration will follow Rayleigh, Gaussian, or Rician distribution.

Fading characteristics of the shallow channel will be addressed first below, followed by the fading characteristics of the deep channel.

(i) Fading characteristics of shallow channel:

1) **Shallow Channel Close to Rough Surface:** The received signal in a close to a rough surface for long-, short-, and medium-range transmission can be expressed as $r_{S_{RS/L}}(t)$, $r_{S_{RS/S}}(t)$, and $r_{S_{RS/M}}(t)$, respectively. Using (12), in long-range transmission,

$$r_{S_{RS/L}}(t) = G_0 + \left[\underbrace{RC_1''(t)}_{Rician(GROUP1)} \right] + \left[\underbrace{RC_{J+1}(t) + RC_{J+2}(t) + \dots + RC_{L-1}(t)}_{Rician(GROUP5)} \right] n_1(t) + n_2(t), \quad (22)$$

where $RC_1''(t)$ represents the Rician envelop corresponding to surface reflected dominant path and sub-eigen paths. Each of RC_j s represent a Rician envelop corresponding to scatter/dominant paths due to refraction from sound speed variation and/or reflection/refraction/scatter on objects in the medium. The surface reflected path will produce Rician fading if the scatters are not negligible otherwise it will produce Gaussian fading.

In a short-range transmission, using (11), the received signal can be expressed as

$$\begin{aligned}
 r_{S_{RS}/S}(t) = & G_0 + \left[\underbrace{RL_1(t)}_{\text{Rayleigh}(GROUP1)} \right] \\
 & + \left[\underbrace{RL'_{II+1}(t) + RL'_{II+2}(t) + \dots + \dots + RL'_I(t)}_{\text{Rayleigh}(GROUP2)} \right] \\
 & + \left[\underbrace{RL'_{JJ+1}(t) + RL'_{JJ+2}(t) + \dots + RL'_J(t)}_{\text{Rayleigh}(GROUP4)} \right] \\
 & + \left[\underbrace{RL_{J+1}(t) + RL_{J+2}(t) + \dots RL_{L-1}(t)}_{\text{Rayleigh}(GROUP5)} \right] \\
 & + n_1(t) + n_2(t), \tag{23}
 \end{aligned}$$

where $RL_1(t)$ represents the Rayleigh envelop corresponding to surface reflected path and dominant scattered sub-eigen paths. The RL'_{II} s and RL'_{JJ} s represent Rayleigh envelop of combination of surface scattered sub-eigen paths corresponding to each negligible surface/bottom reflected (first reflection on surface for GROUP2 and first reflection on bottom for GROUP4) dominant path. Each of RL_{JS} represent a Rayleigh envelop corresponding to scatter/dominant paths due to refraction from sound speed variation and/or reflection/refraction/scatter on objects in the medium. In a medium range, paths in GROUP5 will result in some Rician variables and some Rayleigh variables. Therefore, using (11),

$$\begin{aligned}
 r_{S_{RS}/M}(t) = & G_0 + \left[\underbrace{RC_1(t)}_{\text{Rician}(GROUP1)} \right] \\
 & + \left[\underbrace{RL'_{II+1}(t) + RL'_{II+2}(t) + \dots + RL'_I(t)}_{\text{Rayleigh}(GROUP2)} \right] \\
 & + \left[\underbrace{RL'_{JJ+1}(t) + RL'_{JJ+2}(t) + \dots + RL'_J(t)}_{\text{Rayleigh}(GROUP4)} \right] \\
 & + \left[\underbrace{RC_{J+1}(t) + RC_{J+2}(t) + \dots RC_{J+J'}(t)}_{\text{Rician}(GROUP5)} \right] \\
 & + \left[\underbrace{RL_{J'+1}(t) + RL_{J'+2}(t) + \dots RL_{L-1}(t)}_{\text{Rayleigh}(GROUP5)} \right] \\
 & + n_1(t) + n_2(t), \tag{24}
 \end{aligned}$$

where $RC_1(t)$ represents the Rician envelop of dominant surface reflected path and sub-eigen scatters.

2) **Shallow Channel Close to Smooth Surface:** In case of smooth surface, the received signal in long, short, and medium range can be denoted as $r_{S_{SS}/L}(t)$, $r_{S_{SS}/S}(t)$, and $r_{S_{SS}/M}(t)$, respectively. The equations for long, short, and medium range will be same and using (13) can be expressed as

$$\begin{aligned}
 r_{S_{SS}/L,M,S}(t) = & G_0 + \left[\underbrace{G''_1(t)}_{\text{Gaussian}(GROUP1)} \right] \\
 & + \left[\underbrace{G_{J+1}(t) + G_{J+2}(t) + \dots G_{L-1}(t)}_{\text{Gaussian}(GROUP5)} \right] + n_1(t) + n_2(t), \tag{25}
 \end{aligned}$$

where G''' denotes the Gaussian variable corresponding to surface only reflected dominant path without any sub-eigen paths. The variable G_J s denote Gaussian variables representing dominant paths due to refraction from sound speed variation and/or reflection/refraction on objects in the medium.

3) **Shallow Channel Close to Rough Bottom:** The received signal in a close to a rough bottom for long-, short-, and medium-range transmission can be expressed as $r_{S_{RB/L}}$, $r_{S_{RB/S}}$, and $r_{S_{RB/M}}$, respectively. In a long-range transmission, the bottom reflected/refracted paths will produce Rician fading, if the scatters are not negligible otherwise it will produce Gaussian fading. Therefore, using (15),

$$r_{S_{RB/L}}(t) = G_0 + \left[\underbrace{RC_{JJ}''(t)}_{\text{Rician(GROUP3)}} \right] + \left[\underbrace{RC_{J+1}(t) + RC_{J+2}(t) + \dots + RC_{L-1}(t)}_{\text{Rician(GROUP5)}} \right] + n_1(t) + n_2(t), \quad (26)$$

where RC_{JJ}'' represents the Rician envelop corresponding to bottom reflected dominant path and negligible sub-eigen scatters. Using (14),

$$\begin{aligned} r_{S_{RB/S}}(t) = G_0 + & \left[\underbrace{RL'_{BII+1}(t) + RL'_{BII+2}(t) + \dots + RL'_{BI}(t)}_{\text{Rayleigh(GROUP2)}} \right] + \left[\underbrace{RL_{JJ}(t)}_{\text{Rayleigh(GROUP3)}} \right] \\ & + \left[\underbrace{RL'_{BJJ+1}(t) + RL'_{BJJ+2}(t) + \dots + RL'_{BJ}(t)}_{\text{Rayleigh(GROUP4)}} \right] \\ & + \left[\underbrace{RL_{J+1}(t) + RL_{J+2}(t) + \dots + RL_{L-1}(t)}_{\text{Rayleigh(GROUP5)}} \right] \\ & + n_1(t) + n_2(t), \end{aligned} \quad (27)$$

where RL'_{BII} s and RL'_{BJJ} s represent Rayleigh envelops of combination of bottom scattered sub-eigen paths corresponding to each negligible surface/bottom reflected path (first reflection on surface for GROUP2 and first reflection on bottom for GROUP4). In a medium range, paths in GROUP5 will result in some Rician variables and some Rayleigh variables. Therefore, using (14)

$$\begin{aligned} r_{S_{RB/M}}(t) = G_0 + & \left[\underbrace{RL'_{BII+1}(t) + RL'_{BII+2}(t) + \dots + RL'_{BI}(t)}_{\text{Rayleigh(GROUP2)}} \right] \\ & + \underbrace{RC_{JJ}(t)}_{\text{Rician(GROUP3)}} + \left[\underbrace{RL'_{BJJ+1}(t) + \dots + RL'_{BJ}(t)}_{\text{Rayleigh(GROUP4)}} \right] \\ & + \left[\underbrace{RC_{J+1}(t) + RC_{J+2}(t) + \dots + RC_{J+J'}(t)}_{\text{Rician(GROUP5)}} \right] + \left[\underbrace{RL_{J'+1}(t) + RL_{J'+2}(t) + \dots + RL_{L-1}(t)}_{\text{Rayleigh(GROUP5)}} \right] \\ & + n_1(t) + n_2(t), \end{aligned} \quad (28)$$

where $RC_{JJ}(t)$ represents the Rician variable corresponding to the bottom reflected dominant path and sub-eigen scatters.

4) **Shallow Channel Close to Smooth Bottom:** In case of smooth bottom, the equations can be expressed as $r_{S_{SB/L}}$, $r_{S_{SB/S}}$, and $r_{S_{SB/M}}$. Expressions for short, medium, and long range will be same and using (16) can be expressed as

$$\begin{aligned} r_{S_{SB/S}}(t) = G_0 + & \left[\underbrace{G_{JJ}''(t)}_{\text{Gaussian(GROUP3)}} \right] \\ & + \left[\underbrace{G_{J+1}(t) + G_{J+2}(t) + \dots + G_{L-1}(t)}_{\text{Gaussian(GROUP5)}} \right] + n_1(t) + n_2(t), \end{aligned} \quad (29)$$

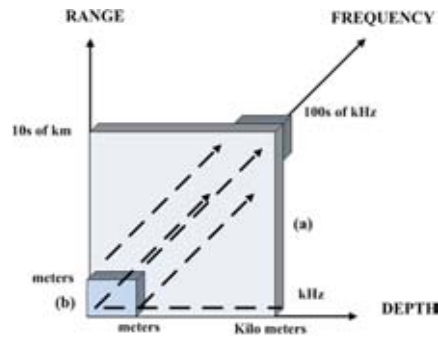
where G_{JJ}'' represents the Gaussian variable corresponding to bottom reflected dominant path.

5) **Shallow Channel in Between Surface and Bottom:** The received signal in an environment between surface and bottom will be affected by both surface and the bottom. The type of channel for long, short, and medium range transmission can be expressed as $r_{S_{BET/L}}$, $r_{S_{BET/S}}$, and $r_{S_{BET/M}}$ respectively. The equation for $r_{S_{BET/L}}$ can be expressed as a combination of $r_{S_{SS/L}}$ and $r_{S_{SB/L}}$, when both surface and the bottom are smooth. If either or both are rough, the equations can be modified to include more scatters. Similarly, $r_{S_{BET/S}}$ will be a combination of $r_{S_{SS/S}}$ and $r_{S_{SB/S}}$, and $r_{S_{BET/M}}$ will be a combination of $r_{S_{SS/M}}$ and $r_{S_{SB/M}}$. Rough surface/bottom will add scatters and equations will change accordingly. In a clear, unobstructed channel, the increase of transmission range and water column depth will produce dominant components. If the transmission is close to surface/bottom or there are smaller objects in the water, the resulting scatters combined with the dominant component may produce Rician fading. With farther increase of range and depth, scattering effect may be minimal and the Rician may become Gaussian only fading. In a clear, unobstructed short range and low water column depth channels, there will be dominant components. But due to the closeness of the two boundaries and the shorter range to travel, the scattering components will be significant and the scatters will be comparable to the dominant components, resulting in Rayleigh fading. Figure 5 illustrates this characteristics.

(ii) Fading characteristics in deep channel: Deep channel transmission will result in Gaussian fading due to the presence of noise, if the transmission happens far from surface/bottom boundaries, and the objects in the transmission path are scarce. If however

FIGURE 5

Shallow channel: (a) Long-range, high-depth, and low-frequency Rician fading zone. (b) Short-range, low-depth, and high-frequency Rayleigh fading zone.



the deep channel is close to surface/bottom, the fading characteristics of close to surface, close to bottom or in between channels may apply.

Frequency Dependent and Independent Noise

Table 2 presents the possible noise in UAC channel. Some of these noise is frequency independent and can be considered under, $n_1(t)$ as Additive White Gaussian Noise (AWGN) with zero mean and normal distribution. However, some of the noise in Table 2 can be frequency dependent, and if the operating transmission frequency is as same as the frequencies of any of these noise sources, the transmitted signal

TABLE 2

Self and ambient noise in UAC.

Self-Noise	Machinery Noise	Flow Noise	Cavitation	
	Pumps, reduction gears, power plant, etc.	Relative motion between object and the water	Bubble collapse	
Ambient Noise	Hydrodynamic	Seismic	Biological	Ocean traffic
	Movement of water	Movement of earth	Marine life	Other boats

will be affected. Frequency-dependent noise is included under $n_2(t)$.

Fading Characteristics, Distribution, Relationship Between Fading and Channel Parameters for Quasi-stationary Channels

In UAC channel, wide sense stationary (WSS) assumption is not always true (Bjerrum-Niese & Lutzen, 2000; Socheleau et al., 2011; Walree et al., 2008). When the transmitter and the receiver or their platforms are moving, the various taps can be correlated at different delays. There are different approaches to address non-WSS channels. One method is to consider the channel as quasi-WSS, i.e., the channel is WSS within a certain time and band of frequency. Another way of dealing with non-WSS is to define time and frequency dependent scattering functions (Walree et al., 2008). In this paper, the channels considered are WSS.

SNR Analysis Signal-to-Noise Ratio for WSS Uncorrelated Tap Channel

From the equations (22) through (29), it can be concluded that the received signal in any underwater environment of Figure 1 is a summation/combination of Gaussian random variables (RV),

Rician RVs, and Rayleigh RVs. Let the summation of Gaussian RVs, Rician RVs, and Rayleigh RVs be denoted as G_{SUM} , R_{SUM} , and RL_{SUM} , respectively. Therefore, the pdf of the received signal will be equal to the pdf of an RV that is a summation of G_{SUM} , R_{SUM} , and RL_{SUM} or any combination of them. If the RV representing the received signal is denoted by RV_{REC} , then

$$RV_{REC} = G_{SUM} + R_{SUM} + RL_{SUM} \quad (30)$$

Although RV_{REC} is expressed in (30) as summation of Gaussian, Rayleigh, or Rician variables, RV_{REC} represents the resultant after the vectorial addition of all paths within symbol duration. Since every path is an i.i.d. Gaussian, the resultant amplitude, i.e., $|RV_{REC}|$ will follow any one of Gaussian, Rayleigh, or Rician distributions. Rician fading is governed by two parameters, K , and Ω , which can be expressed as,

$$K = \frac{P_d}{\sum_{pi=1}^{LL-1} P_{pi}}, \quad (31)$$

$$\Omega = P_d + \sum_{pi=1}^{LL-1} P_{pi}, \quad (32)$$

where P_d represents the power of the dominant path, and P_{pi} , the power of each less dominant path. Clearly, when the power of any path is determined by the transmission loss in (6) and by the equation for α , the path powers will depend on R , H , and f . According to the UAC environment, R , H , f will vary resulting in different values of K and Ω . When $K \approx 0$ or $K \ll 1$, the denominator or the sum of powers of less dominant paths will be greater than the power of the dominant path, the received signal will follow Rayleigh fading. For $K \geq 1$, the received signal will follow Rician statis-

tics. For $K \gg 1$, the signal will follow Gaussian statistics.

The signal to noise ratio (SNR) can be expressed as,

$$SNR = \frac{\text{SignalPower}}{\text{NoisePower}} \quad (33)$$

$$= \frac{|\sum \text{Path}|^2}{\text{NoisePower}}.$$

Let the AWGN noise variance and the frequency dependent noise variance be denoted as σ^2 and N_{otr} , respectively. Therefore, (33) can be expressed as

$$SNR = \frac{(|RV_{REC}|)^2}{\sigma^2 + N_{otr}} \quad (34)$$

or using (19)

$$SNR = \frac{(|\sum_{l=0}^{L-1} \alpha_l(t)s(t - \tau_l)|)^2}{\sigma^2 + N_{otr}}. \quad (35)$$

The eigen and sub-eigen paths will vary in different environments. Hence, the SNR will vary according to each environment. The numerator of (35) will be the square of Rayleigh or Rice or Gaussian variable and the denominator will be the summation of Gaussian variance and variance of noise component, N_{otr} . The square of Rayleigh variable gives exponential distribution and the square of Rician variable gives non-chi-square distribution and hence can be expressed as RV_{EXP} and RV_{CHI} , respectively. Therefore, when RV_{REC} is a Rayleigh or Rician variable, SNR can be expressed as SNR_{EXP} and SNR_{CHI} respectively as shown below.

$$SNR_{EXP} = \frac{RV_{EXP}}{(\sigma^2 + N_{otr})} \quad (36)$$

$$SNR_{CHI} = \frac{RV_{CHI}}{(\sigma^2 + N_{otr})} \quad (37)$$

where the mean and the variance of the above SNR will be as follows,

$$\mu_{EXP} = \frac{\overline{RV_{EXP}}}{(\sigma^2 + N_{otr})},$$

$$\sigma_{EXP}^2 = \frac{\text{VAR}(RV_{EXP})}{(\sigma^2 + N_{otr})^2} \quad (38)$$

$$\mu_{CHI} = \frac{\overline{RV_{CHI}}}{(\sigma^2 + N_{otr})},$$

$$\sigma_{CHI}^2 = \frac{\text{VAR}(RV_{CHI})}{(\sigma^2 + N_{otr})^2} \quad (39)$$

Using the values of exponential mean and variance and non-central chi-square mean and variance, equations (38) and (39) become

$$\mu_{EXP} = \frac{\lambda^{-1}}{(\sigma^2 + N_{otr})},$$

$$\sigma_{EXP}^2 = \frac{\lambda^{-2}}{(\sigma^2 + N_{otr})^2}, \quad (40)$$

$$\mu_{CHI} = \frac{(K' + \lambda)}{(\sigma^2 + N_{otr})},$$

$$\sigma_{CHI}^2 = \frac{2(K' + 2\lambda)}{(\sigma^2 + N_{otr})^2}, \quad (41)$$

where $K' > 0$ represents the degrees of freedom and $\lambda > 0$ represents the rate in the first equation and noncentrality parameter in the second equation.

Benefits of Channel Classification and Selection of Channels

In this section, first, the benefits of channel classification will be provided briefly and, second, selection of channels will be discussed.

Benefits of Channel Classification

It is beneficial to classify the UAC channels according to their environments. Once the UAC environments

are determined, the appropriate channel representation can be used.

In shallow channel environments, close to surface channel may have LOS path (if both the transmitter and receiver are in sight of each other) arriving first, followed by one time surface reflected path, then one time bottom reflected path, followed by bottom-surface one time reflected path, surface-bottom one time reflected paths, followed by other multiple reflected paths. In close to bottom channel, the paths will be in the order of LOS, bottom reflected, surface reflected, bottom-surface one time reflected path, surface-bottom reflected path followed by other multiple reflected paths. In in-between channels, if the difference $|z_s - z_r|$ is small the order of the paths will be LOS, surface, bottom, surface-bottom one time reflected, bottom-surface one time reflected path followed by multiple reflected paths. If the difference $|z_s - z_r|$ is large, the paths will be LOS, surface, bottom, bottom-surface, surface-bottom followed by rest of the multiple reflected paths. Once the channel environment and hence the path origins are identified, it may be easier to retrieve the signal information. For example, a surface only reflected path will be affected by surface wave and other surface agitations. Knowledge of path origin will allow applying noise cancellation and small-scale fading compensation techniques suited for surface boundary agitation.

The UAC channels can be affected by geographical location of communication (longitude/latitude), transmitter and receiver distances from the surface and the bottom boundaries, water column height, transmission range, frequency, sound velocity, the water environment, etc. Channel parameters unique to each UAC environment

is used to differentiate each environment and its corresponding channel equations. For example, the longitude/latitude of location, time of year or season, wind velocity will determine the roughness of the sea surface. Knowing these parameters in addition to the transceiver depth from surface will determine if the channel is close to rough or smooth surface. Once rough surface is identified, scatters due to rough surface may be taken into account, and the channel equations corresponding to close to rough surface environment may be utilized.

Selection of Channel Models

The CI can sense channel environment parameters and map them to accurate UAC channel environment according to parameter values (Ahmed & Arslan, 2009a). Once the UAC channel environment is determined, the UAC channel environment can be mapped (Ahmed & Arslan, 2009b) onto any one of the appropriate channel representations that were presented in the previous sections.

Channel Representation of Closest Fit: In an event, when the channel database does not contain an exact match of a UAC environment, CI can choose a channel representation that fits closest to the UAC environment. This may happen when a significant number of channel parameters and/or parameter values defining the specific UAC environment differ from a known UAC environment in the database. For example, the depth value in a new UAC environment may be larger than the depth threshold for close to surface environment in the database, the temperature, and the location in the world may indicate the new environment to be in between the surface and the bottom. But the type of ocean traffic and the type of marine

life concentration may indicate the new UAC environment to be a close to surface channel environment. In such a case, depending on the deviation of parameter values of the new UAC environment from the thresholds of parameter values of a known UAC environment in the channel database, the in between surface and bottom environment may be selected. Correspondingly, the channel representation for in between surface and bottom can be chosen for communication.

Simulation Results

The simulation is carried out using the parameters in Table 3, MATLAB, and the Bellhop model (Porter, 2011) used and provided by the AcTUP software module (Maggi & Duncan, 2005).

The range to depth ratio can define an underwater channel to be shallow or deep. A range to depth ratio of 10:1 may define a channel as shallow (Bessios & Caimi, 1994) and the transmission can be considered horizontal. The range of transmission can define a channel to be short, medium, or long. A long-range channel over several tens of kilometers is limited to a few kilohertz; a medium-range channel over several kilometers has a bandwidth in the order of tens of kilohertz, while a short range channel over several tens of meters may have hundreds of kilohertz (Stojanovic, 1996) available.

First, the simulation results of the channel impulse response are presented. Second, the results of the fading characteristics of various channels are presented.

A) Channel Impulse Response in Different UAC Environments

- Shallow Channel (Constant Sound Velocity), Smooth Surface and Bottom:

TABLE 3

Values of depth, transmission distance, transmitter and receiver depth for shallow channel scenario: Long-, medium-, and short-range channels.

Depth (m)	Distance (m)	Transmitter Depth (m)	Receiver Depth (m)	Channel Type	Frequency (kHz)
1,000	10,000	995	995	Long, Close to bottom	1
		5	5	Long, Close to surface	1
		5	995	Long, In between	1
100	1,000	95	95	Medium, Close to bottom	10
		5	4	Medium, Close to surface	10
		5	95	Medium, In between	10
9	90	8.5	8.5	Short, Close to bottom	100
		1	1	Short, Close to surface	100
		1	8.5	Short, In between	100

In a shallow **in between surface and bottom** channel environment, when the boundaries are smooth, the CIR will contain paths from surface only reflection, multiple surface bottom reflections, bottom only reflection, multiple bottom surface reflections, and paths due to other reflections/refractions/scatters from in between objects as in (10). The CIR of in between channels in Figures 8, 11, and 14 contain all these groups of paths.

Figures 6, 9, and 12 illustrate close to smooth surface channels. If the paths reflected from the bottom are weak, they can be neglected. Figures 7, 10, and 13 illustrate close to smooth bottom channels. If the paths reflected on the surface are weak, they can be neglected.

In close to surface smooth channels, the values of source depth z_s and receiver depth z_r will be smaller compared to water column height H or transmission range D . When both H and D are small, in case of short range, the paths LOS, surface only, bottom-only, bottom-surface, surface-bottom, paths will be more distinctly apart from each other. If D is high as in long-range channels, the above paths will arrive

close to each other and will be less distinct.

For short and medium range, if H is higher, multiple boundary reflected paths will be grouped together and will almost overlap. For example, paths resulting from $2H$ will be grouped

together, $3H$ will be grouped together (using (4)).

Equations (4) and (6) are used to generate delay and transmission loss amplitudes of Figure 15. In this figure, only the LOS, surface-only, bottom-only, bottom-surface, and surface-bottom

FIGURE 6

Short range, close to surface, shallow channel (smooth surface and bottom): transmission loss/amplitude at various delays and at various ranges, depth = 9 m, transmission distance = 90 m, frequency = 100 kHz.

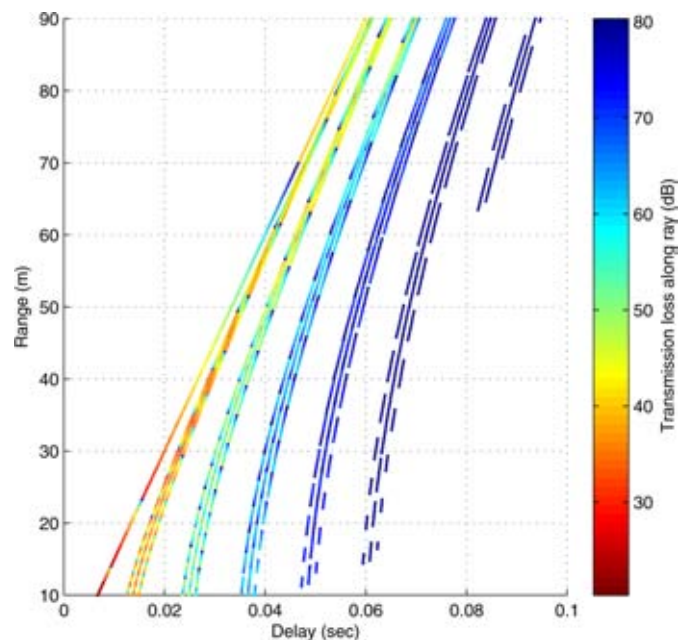


FIGURE 7

Short range, close to bottom, shallow channel (smooth surface and bottom): transmission loss/amplitude at various delays and at various ranges, depth = 9 m, transmission distance = 90 m, frequency = 100 kHz.

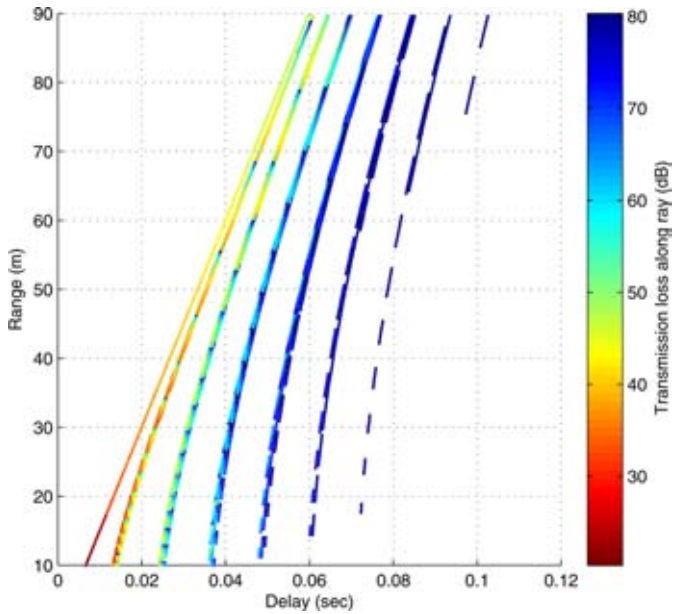


FIGURE 9

Medium range, close to smooth surface, shallow channel (smooth surface and bottom): transmission loss/amplitude at various delays and at various ranges, depth = 100 m, transmission distance = 1,000 m, frequency = 10 kHz.

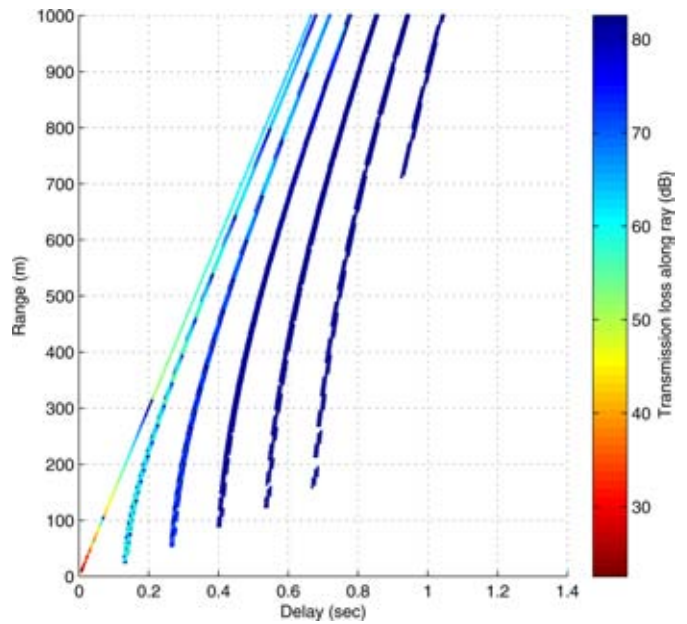


FIGURE 8

Short range, in between smooth surface and smooth bottom, shallow channel (smooth surface and bottom): transmission loss/amplitude at various delays and at various ranges, depth = 9 m, transmission distance = 90 m, frequency = 100 kHz.

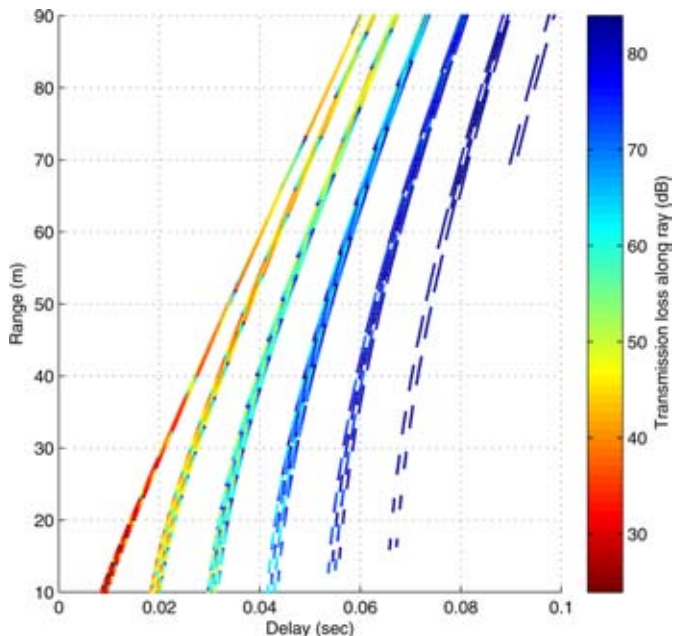


FIGURE 10

Medium range, close to smooth bottom, shallow channel (smooth surface and bottom): transmission loss/amplitude at various delays and at various ranges, depth = 100 m, transmission distance = 1,000 m, frequency = 10 kHz.

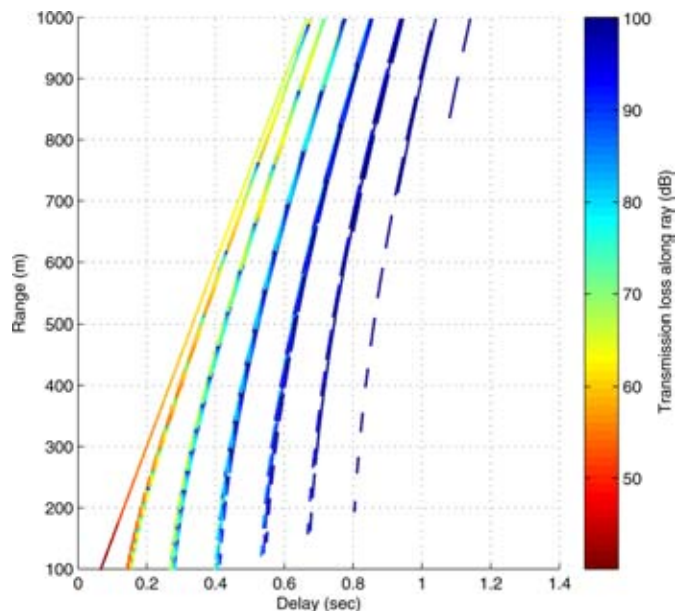


FIGURE 11

Medium range, in between smooth surface and smooth bottom, shallow channel (smooth surface and bottom): transmission loss/amplitude at various delays and at various ranges, depth = 100 m, transmission distance = 1,000 m, frequency = 10 kHz.

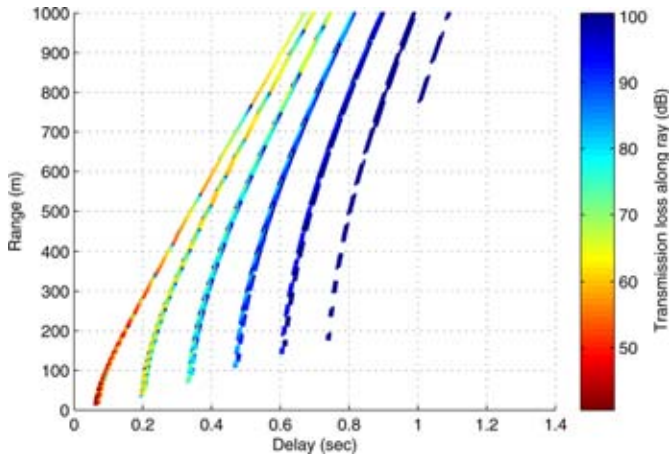


FIGURE 13

Long range, close to smooth bottom, shallow channel (smooth surface and bottom): transmission loss/amplitude at various delays and at various ranges, depth = 1,000 m, transmission distance = 10,000 m, frequency = 1 kHz.

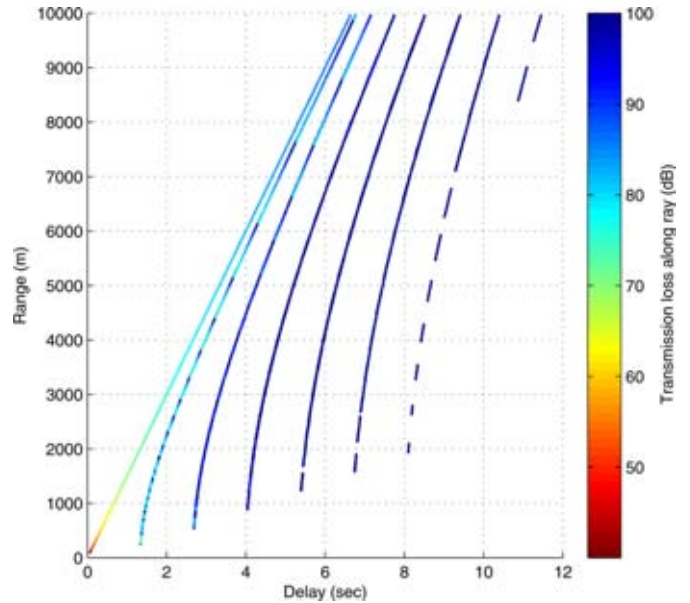


FIGURE 12

Long range, close to smooth surface, shallow channel (smooth surface and bottom): transmission loss/amplitude at various delays and at various ranges, depth = 1,000 m, transmission distance = 10,000 m, frequency = 1 kHz.

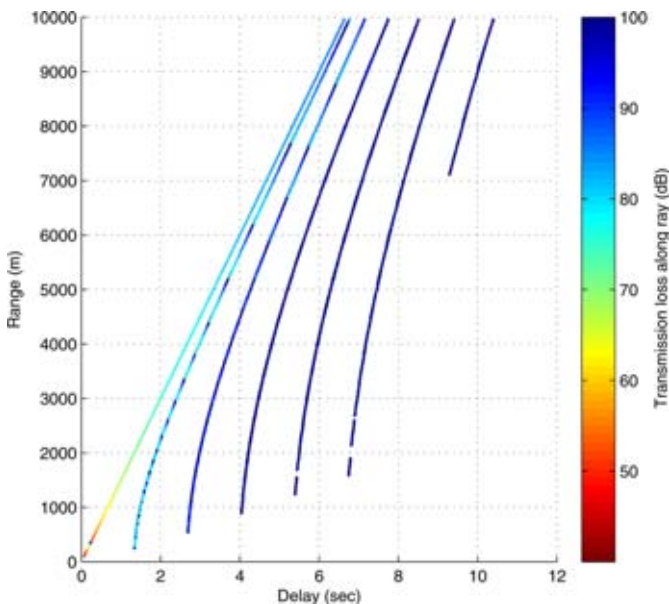
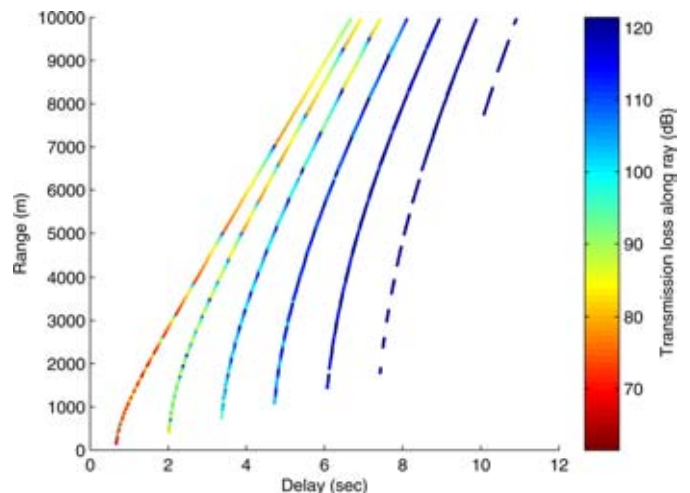


FIGURE 14

Long range, in between smooth surface and smooth bottom, shallow channel (smooth surface and bottom): transmission loss/amplitude at various delays and at various ranges, depth = 1,000 m, transmission distance = 10,000 m, frequency = 1 kHz.



paths are displayed. For short range channel (a), D is small and H is small, hence the LOS and surface only paths are distinct. For medium-range (b) and long-range (c) channels, both D and H are high and these two paths almost overlap each other. Paths interacting with the bottom boundary arrive later but these paths are close to the LOS and surface only reflected paths in terms of loss and delay and hence cannot be neglected. If z_s and z_r are small enough and H and D are large enough, the paths interacting with the bottom will have larger delay and loss and hence can be neglected as seen in equation (13).

In a **short range, shallow, close to smooth surface channels**, as in Figure 6, the paths are more spread out at each delay, i.e., at each delay, neighboring paths arrive without overlapping. In Figure 8, short range, in between surface and bottom channel, the paths are less spread out compared to closed to surface case. In a close to bottom channel, as in Figure 7, the paths are least spread out among the three short range channels.

Compared to the short range channels, the medium range channel paths are much less spread out and are almost overlapping, and are arriving as an overlapped bundle at each delay. This can be observed in Figures 9, 10, and 11. In long-range channels, the neighboring paths completely overlap each other. As a result, at each delay, there is only one path instead of spreading of paths. Figures 12, 13, and 14 illustrate this.

In the shallow channel environments presented above, the paths in different groups arrive very close to each other. Because of this reason, the paths in different groups are not separately shown in the figures.

■ Shallow Channel (Constant Sound Velocity), Rough Surface and Bottom:

If the bottom or the surface varies in shallow channels, the power delay profile varies drastically, where only a few paths arrive at the receiver at different delays and at different power levels.

For a varying surface, the number of paths, their amplitudes, and de-

lays in Figures 6, 9, and 12 will vary. This variation will be more prominent in short and medium range channels.

For a varying bottom, the number of paths, their amplitudes, and delays in Figures 7, 10, and 13 will vary. This variation will be more prominent in short- and medium-range channels.

■ Deep Channel Simulation (Varying Sound Velocity Profile):

Sound velocity will vary in a deep channel. Considering a variable sound velocity profile simulation can be carried out in SOFAR and other deep channels. Simulation results will be similar to that of the shallow channel figures as presented above. Because of high depth and long range that characterize the deep channels, there will be high loss associated with each path arriving at very long delays.

B) Fading Characteristics of WSS Uncorrelated Tap Channel

In Figure 16, the power (power calculated in terms of path loss) ratios of direct path to other paths, in various ranges, in shallow water close to bottom channels are illustrated. The power

FIGURE 15

Shallow channel, close to surface (smooth surface and bottom): transmission loss at various delay. (a) Depth = 9 m, distance = 90 m, transmitter depth = 1 m, receiver depth = 1 m, frequency = 100 kHz. (b) Depth = 100 m, distance = 1,000 m, transmitter depth = 5 m, receiver depth = 4 m, frequency = 10 kHz. (c) Depth = 1,000 m, distance = 10,000 m, transmitter depth = 5 m, receiver depth = 5 m, frequency = 1 kHz.

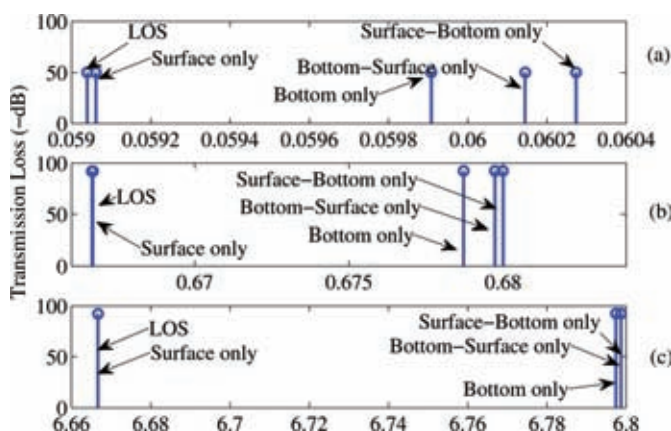
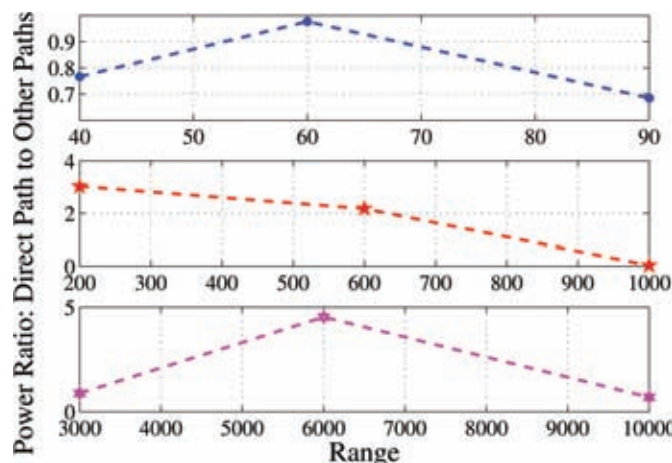


FIGURE 16

Top: Short range, close to bottom, shallow channel; Middle: Medium range, close to bottom, shallow channel; Bottom: Long range, close to bottom, shallow channel.



values are taken from Figures 7, 10, and 13. All the arrived paths are considered. In medium- and long-range channels, the ratio is greater than 1 at all three distances, indicating Rician or Gaussian fading. At 6,000 m in long range and at 600 m in medium range, it is Gaussian fading. At 3,000 m in long range and at 200 m in medium range, it is also Gaussian fading. At longer distances, the direct path loses power significantly and becomes comparable to the less dominant paths. Hence at 1,000 m in medium and at 10,000 m in long range channels, it becomes Rician fading. In short range channels, the indirect paths have significant power and hence results in mostly Rayleigh fading at all three distances.

Conclusion

Once the UAC environments are determined from the channel parameters, the channel representations can be derived according to the environments. In this paper, a high level classification of the UAC channel environments are presented and channel representations are proposed, which are derived according to the classified UAC environments. The channel analysis is shown in terms of channel impulse response equations and fading characteristics of the received signals. As part of future research, correlated taps and non-WSS channels can be considered.

Authors:

Sadia Ahmed
Huseyin Arslan
Department of Electrical Engineering,
University of South Florida,
4202 East Fowler Avenue,
ENB 118, Tampa, FL 33620
Email: ahmed3@mail.usf.edu;
arslan@eng.usf.edu

References

- Ahmed, S., & Arslan, H.** 2009a. Cognitive intelligence in UAC channel parameter identification, measurement, estimation, and environment mapping. In: Proc. MTS/IEEE Oceans. Bremen, Germany. doi: 10.1109/OCEANSE.2009.5278161.
- Ahmed, S., & Arslan, H.** 2009b. Cognitive intelligence in the mapping of underwater acoustic communication environments to channel models. In: Proc. MTS/IEEE Oceans. Biloxi, Mississippi, USA.
- Appleby, S., & Davies, J.** 1998. Time, frequency and angular dispersion modeling in the underwater communications channel. In: Proc. MTS/IEEE Oceans. Nice, France. doi: 10.1109/OCEANS.1998.724318.
- Bessios, A., & Caimi, F.** 1994. Multipath compensation for underwater acoustic communication. In: Proc. MTS/IEEE Oceans. Brest, France. doi: 10.1109/OCEANS.1994.363905.
- Bjerrum-Niese, C., & Lutzen, R.** 2000. Stochastic simulation of acoustic communication in turbulent shallow water. *IEEE J Ocean Eng.* 25(4):523-32. doi: 10.1109/48.895360.
- Byun, S., Kim, S., Lim, Y., & Seong, W.** 2007. Time-varying underwater acoustic channel modeling for moving platform. In: Proc. MTS/IEEE Oceans. Vancouver, BC. doi: 10.1109/OCEANS.2007.4449361.
- Galvin, R., & Coats, R.** 1996. A stochastic underwater acoustic channel model. In: Proc. MTS/IEEE Oceans. Fort Lauderdale, FL. doi: 10.1109/OCEANS.1996.572599.
- Geng, X., & Zielinski, A.** 1995. An eigenpath underwater acoustic communication channel model. In: Proc. MTS/IEEE Oceans. San Diego, CA. doi: 10.1109/OCEANS.1995.528591.
- Gutierrez, M.A.M., Sanchez, P.L.P., & Neto, J.V.V.** 2005. An eigenpath underwater acoustic communication channel simulation. In: Proc. MTS/IEEE Oceans. Washington, DC, USA. doi: 10.1109/OCEANS.2005.1639788.
- Lurton, X.** 1996. *An Introduction to Underwater Acoustics: Principles and Applications.* UK: Springer.
- Maggi, A., & Duncan, A.** 2005. Underwater acoustic propagation modeling software-actup v2.2l. Center for Marine Science and Technology (CMST). January 25, 2012.
- Morozov, A.K.** 1995. The sequential analysis application in the problem of estimation of stochastic channel impulse response. In: Proc. MTS/IEEE Oceans. San Diego, CA. doi: 10.1109/OCEANS.1995.528570.
- Porter, M.B.** 2011. *The bellhop manual and user's guide: Preliminary draft.* Heat, Light, and Sound Research, Inc. May 30, 2012.
- Socheleau, F., Laot, C., & Passerieux, J.** 2011. Stochastic replay of non-WSSUS underwater acoustic communication channels recorded at sea. *IEEE Trans Signal Process.* 59(10):4838-49. <http://dx.doi.org/10.1109/TSP.2011.2160057>.
- Stojanovic, M.** 1996. Recent advances in high-speed underwater acoustic communications. *IEEE J Ocean Eng.* 21(2):125-36. <http://dx.doi.org/10.1109/48.486787>.
- Walree, P., Jenserud, T., & Smedsrud, M.** 2008. A discrete-time channel simulator driven by measured scattering functions. *IEEE J Selected Areas Commun.* 26(9):1628-37.

Wrecks on the Bottom: Useful, Ecological Sentinels?

AUTHOR

Andrea Peirano
 ENEA-Marine Environment
 Research Centre, La Spezia, Italy

Introduction

Wrecks are artificial habitats that may enhance marine biodiversity (Baine, 2001; Svane & Petersen, 2001; Massin et al., 2002; Mallefet et al., 2008). Their geometrical complexities, structures, and textures provide suitable substrates for settlements of several benthic species (Svane & Petersen, 2001). On soft bottoms, wrecks especially play an important role by offering suitable surfaces for the larvae of benthic organisms, which otherwise would not be able to settle.

Given their importance as promoters of marine biodiversity, old ships and sunken oil and gas platforms, both of which have become popular as dive attractions, have been included within Marine-protected areas (MPA) of the world (Bonshack & Sutherland, 1985; Baine, 2001; Walker et al., 2007; Kaiser & Kasprzak, 2008). World War II ships are the most common and best preserved wrecks because of the thickness of their hulls and the armoring of their superstructures. Moreover, some of them have been included on lists of archaeological importance to ensure that their historical importance is passed on to future generations (UNESCO, 2001; Church et al., 2007; Wessex Archaeology Limited, 2008; Underwood, 2009).

ABSTRACT

Wrecks play an important role in enhancing marine biodiversity. SCUBA diving video-samplings were performed on eight wrecks, including seven shipwrecks and a sunken airplane, scattered over 180 km along the Ligurian coastline in the north-western Mediterranean Sea, in water depths of 30–65 m. Differences in composition of macrobenthic communities were found to be related to the bottom sedimentology and the composition and geometry of the investigated structures. The iron, flat, and even substrata of shipwrecks were dominated by *Bivalvia* (*Ostrea edulis*) and Anthozoa (*Corynactis viridis*), whereas the aluminum, cage-like structure of the airplane was dominated by massive sponges and bryozoans. Furthermore, abundances of some macrobenthic invertebrates were greater on the wrecks than those observed on natural, rocky substrates. Because of the increasing popularity of use of video and photo digital apparatuses among recreational divers, combined with wreck resistance to corrosion, artificial geometries and available surfaces that facilitate species' settlement and growth, data from wrecks consisting of images and related metadata (depth, date, water temperature, etc.) could provide a new opportunity for monitoring Mediterranean marine biodiversity.

Keywords: wrecks, macrobenthos, video-sampling, CCR scientific diving

Because of the function and use of these artificial structures, however, the presence of pollutants, such as heavy metals in cables and paints and oil and explosive residuals (Church et al., 2007) may be found within their compartments. Thus, before being eligible to be positioned intentionally on the seabed, these structures should be cleaned and treated to remove any pollutant representing serious threat to marine life. Furthermore, their scuttling should be limited by appropriate regulations (Bell et al., 1997; Helton, 2003).

On the Ligurian Sea seabed in the northwest Mediterranean Sea, more than 50 wrecks were found along the coastline in water depths of 20–100 m (Carta, 2000; Carta et al., 2008; Mirto et al., 2009). The major-

ity are ships that were sunk during World War II. Airplanes that were lost in the war often have been destroyed and dispersed by trawlers. The interest in Italian wrecks has generally come from archeologists because of their importance as sites of national heritage (<http://www.archeomar.it>). However, except for a few general observations, the importance of the Ligurian wrecks as a possible promoter of Mediterranean marine biodiversity has not been taken into account.

The aim of the present work is to analyze and compare the characteristics and composition of macrobenthic communities colonizing eight wrecks, taking into account the structural geometry, composition, and texture of the materials composing the wrecks. Comparisons between macrobenthic

taxa on wrecks with those living on neighboring natural substrates also were made to elucidate factors influencing colonization and the wrecks' role in contributing to coastal community richness and conservation. The wrecks as tools for monitoring marine biodiversity are discussed.

Material and Methods

Study Site

SCUBA video surveys were performed in 2008–2009 on eight “wrecks” lying on the Ligurian seabed (Figure 1), scattered over 180 km along the coastline. The Liguria region is dominated by a large and well-defined anticlockwise circulation and by biodiversity hot spots promoted by the presence of a coralligenous community, usually growing below 25 m in depth (Cattaneo-Vietti et al., 2010). With the purpose of analyzing only mature communities, wrecks that sank 30 or more years ago (Perkon-Finkel et al., 2006; Relini et al., 2007) were selected for this study. Among these

artificial structures, only those lying between 30 and 65 m in depth were taken into account to reduce the impact caused by wave action and the seasonal thermocline. Seven of the eight wrecks investigated were ships; six were iron ships that sank between 1917 and 1967 (*Mohawk Deer*, *Genova*, *Marcella*, *Vittoria*, *Equa*, *Concordia*) and one was a wooden ship (the *Cycnus*) sunk in 1981. The other wreck, the BR.20, was an Italian bomber shot down near Imperia in 1941. The *Cycnus* and the bomber were situated on sandy bottoms close to *Posidonia oceanica* seagrass beds (Bianchi & Peirano, 1995). One of the iron ships, the *Mohawk Deer*, lay on a detritic seabed with the bow against a rocky wall dominated by a rich coralligenous assemblage. The other shipwrecks were positioned on muddy bottoms.

Video-Sampling

The videos were taped by means of SCUBA diving performed using a mixed-gas, closed-circuit rebreather (CCR) apparatus APD “Inspiration”®

FIGURE 2

Exploring the wreck of the *Equa* using the mixed-gas closed-circuit rebreather (CCR) apparatus APD Inspiration®.



(Figure 2). Compared to an open-circuit (OC) apparatus, CCR allowed dives at greater depths with longer stays and a reduced number and duration of decompression stops (Parrish & Pyle, 2002). A Sony full-HD (1,920 × 1,080 pixels) video camera was enclosed in an underwater housing with a wide-angle lens and two lamps (50 W each). A frame (25 × 25 cm) was fixed on the camera at distance of 30 cm (Figure 3). Short videos (video clips) were shot at random in different parts of each wreck, as hull, cranes, and propeller, etc. In the laboratory, videos

FIGURE 1

Wrecks' distribution along the Liguria region. 1 = *Cycnus*, 2 = BR.20 Bomber, 3 = *Mohawk Deer*, 4 = *Genova*, 5 = *Marcella*, 6 = *Vittoria*, 7 = *Equa*, 8 = *Concordia*.

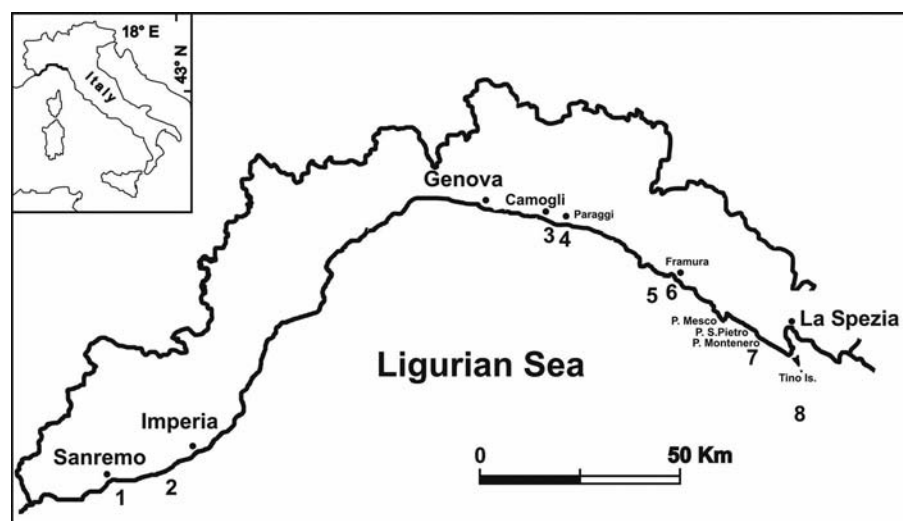


FIGURE 3

One video image from the *Concordia* starboard side of the ship, colonized by *Ostrea edulis* and *Corynactis viridis* (dark points). During the video shootings, the frame allowed the diver to maintain the video camera perpendicular to and at a fixed distance from the surface.



were analyzed, and for each wreck, several variables, divided in different categories, were evaluated. Data on depth range (30–40 m, 40–50 m, 50–60 m), bottom/seabed (sediment) type (1 = sand, 2 = mud, 3 = detritic, 4 = rock), wreck zone (1 = internal, 2 = external), wreck material (1 = wood, 2 = iron, 3 = aluminum), surface texture (1 = even, 2 = rough, 3 = grid-like, 4 = with cracks), geometrical shape of the structure (1 = round, 2 = flat, 3 = angular, 4 = complex), and structure slope (1 = horizontal, 2 = subhorizontal, 3 = vertical, 4 = overhanging) were extracted from each video clip.

Among benthic organisms found on the wrecks, only the long-living macrobenthic taxa were considered in the present study because of their multiannual lifespan of colonization. Taxonomical identification of the macrobenthic species was facilitated by using HD digital video softwares (Picture Motion Brower[®] by Sony and Media Player Classic[®] by Gabest). Macrobenthic species abundance was evaluated in terms of cover on still-frames selected randomly from each video clip. The minimum surface analyzed in each video clip was 1 m². The total abundance of a species was estimated following semiquantitative scale adopted in cover visual estimation (Boudouresque, 1971; Kenchington, 1978; Bianchi et al., 2004; Work et al., 2008): <1% = rare, 1–10% = present, 10–50% = abundant, > 50% = very abundant. The resulting matrix (wrecks × variables) was analyzed by using the principal component analysis (PCA).

Data on species abundance recorded on wrecks were compared with those collected with video and/or photo sampling on natural substrata nearby. Differences between wrecks and natural substrata were examined.

Results

A minimum dive-time of 20 min allowed a careful exploration of each wreck. The resulting high-definition (HD) videos extracting single frames (maximum resolution of about 5 megapixels each) guaranteed suitable images for identifying macrobenthic species more than 1 cm in size. Macrobenthic species were classified at species or family level. A total of 35 macrobenthic organisms (7 Algae, 11 Porifera, 9 Anthozoa, 1 Bivalvia, 2 Anellida, 4 Bryozoa) were identified (Table 1).

Principal component analysis (PCA) revealed that the first two components were both significant: the first (PC1) explained 10.5 % of the variance, the second (PC2) explained 7.9 %. (Figures 4a and 4b). The analysis of the variable importance, represented in Figure 5, showed that species ordination was mainly related to the type of the bottom (muddy bottoms vs. detritic/sandy bottoms) and to the type of material composing the wreck (aluminum vs. iron). Hence, variables were divided into two main groups, represented on the right and on the left sides of the PCA diagram respectively (Figure 4a). Flat and vertical surfaces of the iron shipwrecks, lying on muddy bottoms, were characterized by the highest cover of the bivalve *Ostrea edulis* and the anthozoan *Corynactis viridis*, reaching the 90% of cover (Figure 4a). Subhorizontal, overhanging rough structures favored settlement and growth of low-light tolerant species such as the anthozoans *Paramuricea clavata*, *Leptopsamia pruvoti*, *Eunicella cavolinii*, bryozoans (*Aedonidae* spp.), serpulids, and red encrusting algae (*Corallinales* spp.), as shown in the upper right side of the diagram (Figure 4a). In contrast, other species such as *Caulerpa racemosa* v. *cylindracea*, *Chartella* sp., *Codium*

vermilara, *Flabellia petiolata* and *Goio-cladia* sp. clustered around the center of the PCA diagram were only found occasionally. The aluminum hull of the BR.20 bomber was dominated by sponges (*Dictyoceratida* sp. 2, *Aplysina aerophoba*), and one bryozoan (*Celleporidae* sp.) was found (Figure 4a); see the lower left quadrant of the PCA diagram. The scatterplot of row scores (wrecks) confirmed the ordination of variable; almost all taxa growing on the BR.20 bomber were grouped in the lower left quadrant (Figure 4b).

The three types of seabed identified during the present study were mud with >88 % of fines and sand and detritic seabed each with <10 % of fines. Fines included clay + silt following Bertolotto et al. (2005). Neither the amount of fines ($R = -0.14$; $p > 0.05$) nor the distance of the wrecks from the coast ($R = 0.23$, $p > 0.05$) were correlated with the number of species found.

Data collected on “wrecks” were compared with those extracted from the literature and referring to natural substrata (Figure 6). An increase in the number of different benthic species on natural substrata was found from the Western to Eastern side of the Ligurian coast. In contrast, the number of species colonizing wrecks showed a weak negative trend from west to east. In the cases of the *Mohawk Deer* (114 %) and *Genova* (111%), species abundances were higher than those recorded on the nearby natural substrates (Table 2).

Discussion

The combination of close-circuit rebreather (CCR) diving with high-definition (HD) video shooting was useful in the deep-diving surveys. As

TABLE 1

List of species found on wrecks. Wreck numbers are referred to Figure 1. Numbers for bottom type, material structure, surface typology and slope are reported in material and methods.

Wreck number	1	2	3	4	5	6	7	8
Distance from the coast (nm)	0.5	1.5	0	1	0.9	8.6	2.5	14
Video samples (<i>n</i>)	5	12	16	9	12	10	8	7
Depth range (m)	35–38	46	30–46	52–55	42–60	35–38	38–40	40–42
Bottom type	1	4	4	2	2	2	2	2
Wreck zone	1	1	1–2	1	1	1	1	1
Material	1–2	2–3	2	2	2	2	2	2
Surface texture	1–2–4	1–2–3–4	1–2	1–2–3–4	1–2	1–3–4	1–2–3	1–3
Structure shape	1–2–3	1–2–3–4	1–2–3	1–2–3–4	1–2–3–4	1–2–3	1–2–3–4	1–2–3
Structure slope	1–2–3	1–2–3	1–2–3–4	1–2–3	2–3–4	1–3–4	1–2–3	1–3
Algae								
1 <i>Corallinales</i> sp.1	+	+	+		+			
2 <i>Corallinales</i> sp.2			+					
3 <i>Gloiocladia</i> sp.							+	
4 <i>Peyssonellia</i> sp.							+	
5 <i>Caulerpa racemosa</i>			+					
7 <i>Codium vermilara</i>								+
8 <i>Flabellia petiolata</i>			+					
Porifera								
9 <i>Haliclona</i> sp.					+			
10 Dictyoceratida sp.1		+		+				
11 Dictyoceratida sp.2					+			
12 <i>Dysidea</i> sp.				+	+		+	+
13 <i>Aplysina aerophoba</i>		+		+	+			
14 Porifera indet. sp.1				+				+
15 Porifera indet. sp.2	+		+	+	+		+	+
16 Porifera indet sp.3	+				+			
17 Porifera indet sp.4					+			
18 Porifera indet sp.5		+	+	+	+		+	+
19 Porifera indet sp.6					+			
Anthozoa								
20 <i>Eunicella cavolinii</i>			+					
21 <i>Eunicella singularis</i>			+					
22 <i>Eunicella verrucosa</i>			+		+			+
23 <i>Leptogorgia sarmentosa</i>			+		+			+
24 <i>Paramuricea clavata</i>			+					

continued

TABLE 1

Continued

Wreck number	1	2	3	4	5	6	7	8
25 <i>Corynactis viridis</i>					+	+	+	+
26 <i>Balanophyllia europaea</i>		+		+				+
27 <i>Leptpsammia pruvoti</i>			+					
28 <i>Phyllangia</i> sp.					+			
Bivalvia								
29 <i>Ostrea edulis</i>	+		+	+	+	+	+	+
Anellida								
30 <i>Sabella spallanzanii</i>			+		+			
31 <i>Serpulidae</i> spp.	+			+	+			
Bryozoa								
32 <i>Aedonidae</i> sp.			+	+				
33 <i>Watersiporidae</i> sp.						+		
34 <i>Celleporidae</i> sp.		+	+					
35 <i>Chartella</i> sp.	+							

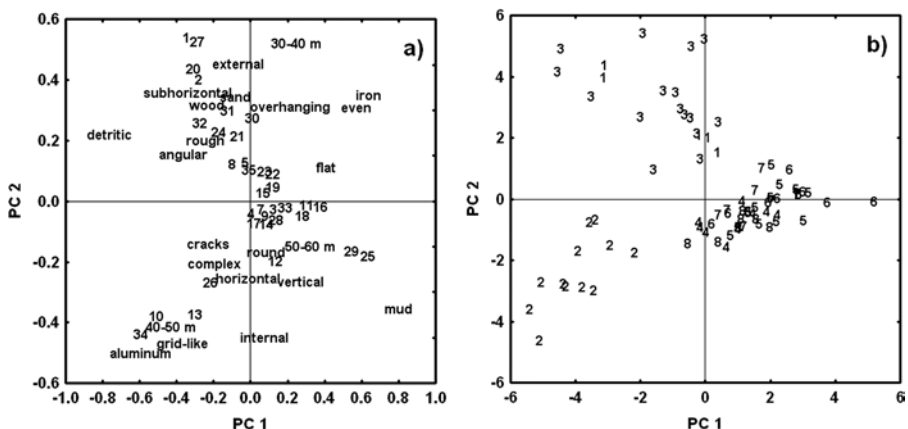
a noninvasive sampling method, video-sampling had no impact on the investigated organisms. The only possible disturbance from sampling was the bioturbation effect that was prevented by using CCR. Bubble emission during the diver's exhalation, normally occurring with the open

circuit (OC) diving apparatus that enhances turbidity during video shooting on vertical and below overhanging structures, was drastically reduced by the use of CCR. By comparing visual and photo-sampling on macrobenthic organisms of Mediterranean hard substrates, Parravicini et al. (2009) did not

find any differences between the two methods when photographs had a significant area coverage and adequate resolution. The video procedure used in the present work assured the analysis of a minimum area larger than 0.25 m², in accordance with methods suggested for the sampling of Mediterranean hard bottoms and artificial substrata such as artificial reefs (Weinberg 1978; Bianchi et al., 2004, Relini 2004; Parravicini et al., 2009), while HD resolution proved its potential in species identification.

FIGURE 4

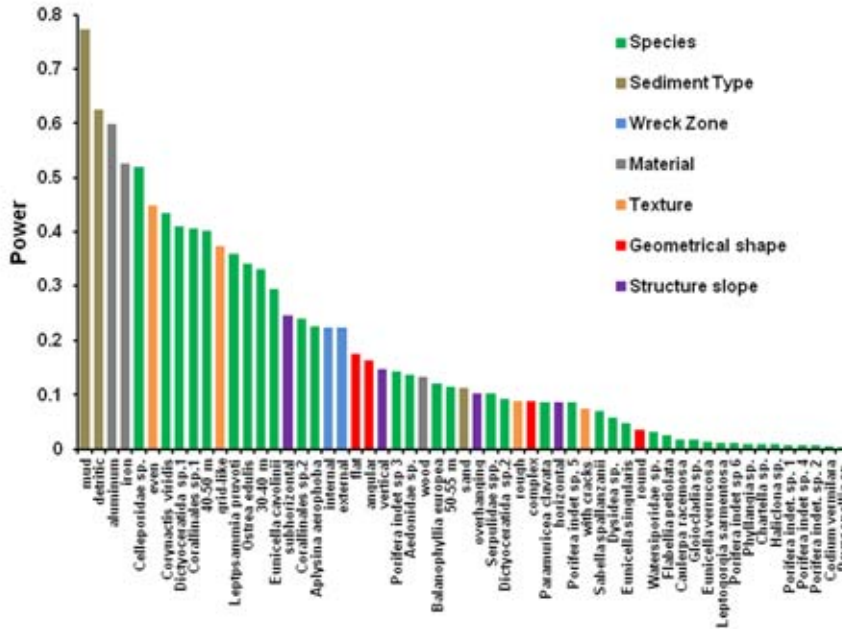
PCA of the loading factors between principal components axis (PC1 and PC2): a) scatterplots of categorical variable categories (depth, bottom type, wreck material, and structure characteristics) and continuous variables (species); b) scatterplots of wrecks' scores. Wrecks and species numbers are reported in Table 1.



In the present study, PCA analysis revealed that bottom type is fundamental in epibenthic colonization of wrecks and it has a key role in determining marine community structures. A connection between species occurrence and sediment typology is in agreement with findings of Zintzen et al. (2008) and Guerin (2009), who showed a relationship among epifaunal communities on wrecks and oil platforms, and the bottom sediment of

FIGURE 5

Plot of variable importance in scatterplot of Figure 4. Variable importance varies from a maximum (1) on the left to a minimum (0) on the right.



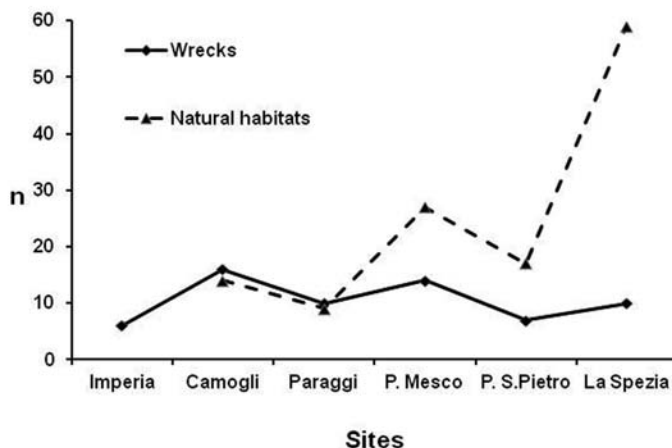
the Baltic Sea. In Liguria this is also true for natural, rocky bottoms where littoral photophilic communities are influenced by substratum mineralogy (Cattaneo-Vietti et al., 2002).

Also, wreck material is fundamental in macrobenthos colonization. Experiments comparing natural habitats

and artificial substrata such as concrete, rocks, ceramic, and earthenware material demonstrated that species recruitment and survival were strictly dependent on the substrate-type (Burt et al., 2009; Perkol-Finkel & Benayahu, 2006; Antoniadou et al., 2010). Relini et al. (2007) showed

FIGURE 6

Number of species found on wrecks (present work) versus nearby natural substrata (from Peirano & Sassarini, 1991; Cocito et al., 2002; Cattaneo-Vietti, 2004).



in Liguria that wooden barges and shipwrecks were less appropriate for colonization, in agreement with video shot on the *Cycnus*. Iron structures of wrecks are usually damaged by corrosion, which first attacks the thinnest parts (Relini et al., 2007) and at the end, may contribute to the collapse of the whole structure (Bell et al., 1997). This damage is enhanced by bubbles emitted by SCUBA open-circuit apparatus and by chains used to anchor diving buoys. The illegal predation of wrecks further contributed to their destruction (UNESCO, 2001; Tilburg, 2006). Videos of this study showed that the aluminum on the aircraft BR-20 and the massive structures such as the propellers, cranes and portholes of the iron ships were to be the most resistant materials to the effects of corrosion.

Studying wrecks in the North Sea, Australia and Red Sea, Guerin (2009), Walker et al. (2007) and Perkol-Finkel et al. (2005, 2006) also agreed that the geometrical complexity of wreck structures plays a key role in determining species colonization. On muddy bottoms of the Ligurian Sea, vertical surfaces of studied shipwrecks were dominated by *Ostrea edulis* and *Corynactis viridis*. The cage-like structure of the bomber BR-20 probably limited sediment accumulation by allowing enough water circulation to remove sediments. These environmental conditions determined the settlement and colonization of Porifera and Bryozoa, and the two taxa became the dominant filter-feeders colonizing the airplane remnants.

Wrecks are not only devices for attracting divers but play an important role in increasing production normally associated with bare bottoms (mud and sandy) (Svane & Petersen, 2001; Massin et al., 2002; Church et al.,

TABLE 2

Comparison among taxa composition of macrobenthic assemblages found on wrecks studied in the present work (pw) and those reported on natural substrata in nearby sites in previous papers (1 = Cattaneo-Vietti, 2004; 2 = Peirano & Sassarini, 1991; 3 = Cocito et al., 2002).

Reference number	pw	pw	pw	pw	(1)	pw	(1)	pw	(1)	pw	(2)	pw	(2)	pw	(3)
area	Imperia	Imperia	Camogli	Paraggi	Paraggi	Paraggi	Paraggi	Framura	Framura	P. Mesco	P. Montenero	P. Montenero	P. Montenero	La Spezia	La Spezia
Wreck/sample number	1	2	3	POC	4	C4	5	6	7	-	-	8	-	-	-
Method	Video	Video	Video	Photo	Video	Photo	Video	Video	Video	Photo	Video	Video	Photo	Video	Photo
Depth range (m)	30	46	30-46	24-33	30-52	12-16	42-60	38	38	18-27	38	18-27	42	15-24	15-24
Bottom (sediment) type	1	3	3	4	2	4	2	2	2	4	2	4	2	4	4
Samples (n)	5	12	16	10	9	10	12	10	8	7	8	4	7	30	30
Taxa															
Algae	1	1	4	4		6	1	1	2	3	2	4	1	10	10
Spongiae	2	3	2	2	6	1	9	7	3	12	3	7	4	23	23
Anthozoa		1	6	5	1	2	4	1	1	7	1	4	4	13	13
Bivalvia	1		1		1		1	1	1		1		1		
Anellida	1		1		1		2			1				3	3
Bryozoa	1	1	2	3	1			1		2				9	9
Ascidiacea										2				1	1
Species (n)	6	6	16	14	10	9	17	11	7	27	7	17	10	59	59
Wrecks vs. natural habitat (%)	-	-	114		111		63	41	41		41		17		

2007; Mallefet et al., 2008). Their importance in the Ligurian Sea was previously highlighted by Relini et al. (2007). The author analyzed 15 years of benthos colonization on artificial reefs along the Ligurian coast concluding that the concrete blocks acted in the same way as natural, rocky bottoms. Data from the present work showed that the abundance of macrobenthos on shipwrecks may be similar and, in some cases, greater than that found on natural substrates. These findings are in agreement with the observations of Perkol-Finker et al. (2006), which reported values for epifaunal colonization on a shipwreck similar to those found on neighboring natural bottoms in the Red Sea. Moreover, Church et al. (2007), studying an historical shipwreck in the Gulf of Mexico, showed not only that the epibenthos of the artificial structure was richer than that of the surrounding natural areas, but also that it could be the source for the colonization of the neighboring substrata.

Because of their role as historical attractions for recreational divers, shipwrecks could become good “sentinels” of biological changes affecting marine environments. Large surfaces of shipwrecks may favor, for example, invasive species colonization, as observed by Work et al. (2008) in the Central Pacific and by Perkon-Finkel et al. (2006) in the Red Sea. In this study, the presence of the green alga *Caulerpa racemosa* var. *cylindracea*, one invasive species that colonized almost all the Mediterranean coasts in one decade (Piazzi et al., 2005), was recorded on the *Mohawk Deer* shipwreck.

Massive wreck structures such as propellers or cranes, which are more resistant to deterioration, are easily recognizable in monitoring studies. By comparing video of the *Mohawk Deer*

with previous ones taped 13 years before by recreational divers, in the same areas of the wreck a reduction in the number of the gorgonians *Eunicella cavolinii* and *Paramuricea clavata* was evidenced. These observations could be related with the mortality event that affected the gorgonian species living on natural rocky walls in the late summer 1999 (Cerrano et al., 2000). In order to heighten the general awareness of the ecological and historical importance of wrecks and to obtain low-cost data on their associated biodiversity, ‘wreck monitoring programs’ involving recreational divers should be promoted (UNESCO, 2001; Wessex Archaeology Limited, 2008; Underwood, 2009). The increasing interest in wrecks, mainly due to the spread of high technology diving equipment and low-cost HD photographic and video apparatuses, combined with the use of the Internet as a source of information exchange, delivers possibilities to easily gain ecological data that will considerably help scientists in monitoring marine biodiversity.

Acknowledgments

The author is grateful to his friend and rebreather instructor G. Paparo for his assistance during the dives on wrecks, to his colleagues C. Lombardi and S. Cocito for their help with bryozoan taxonomy and the critical comments on the manuscript, and to E. Taylor, A. Jochens, and N. Lucey for their suggestions and language revision.

Author:

Andrea Peirano
 ENEA-Marine Environment Research Centre, C.P. 224, La Spezia (Italy)
 Email: andrea.peirano@enea.it

References

- Antoniadou, C.,** Voultsiadou, E., & Chintiroglou, C. 2010. Benthic colonization and succession on temperate sublittoral rocky cliffs. *Est Coast Shelf Sci.* 82:426-32.
- Baine, M.** 2001. Artificial reefs: a review of their design, application, management and performance. *Ocean Coast Manage.* 44:241-59. [http://dx.doi.org/10.1016/S0964-5691\(01\)00048-5](http://dx.doi.org/10.1016/S0964-5691(01)00048-5).
- Bell, M.,** Buchanan, M., Culbertson, J., Dodrill, J., Kasprzak, R., Lukens, R., & Tatum, W. 1997. Guidelines for marine artificial reef materials. Artificial Reef Subcommittee of the Technical Coordinating Committee, Gulf States Marine Fisheries Commission. Ocean Springs: Gulf States Marine Fisheries Commission office. 118 pp.
- Bertolotto, R.M.,** Tortarolo, B., Frignani, M., Bellucci, L.G., Albanese, S., Cuneo, C., ... Gollo, E. 2005. Heavy metals in surficial coastal sediments of the Ligurian Sea. *Mar Pollut Bull.* 50:344-59. <http://dx.doi.org/10.1016/j.marpolbul.2004.12.002>.
- Bianchi, C.N.,** & Peirano, A. 1995. Atlante delle Fanerogame marine della Liguria: *Posidonia oceanica* e *Cymodocea nodosa*. La Spezia: Enea-Centro Ricerche Ambiente Marino. 146 pp.
- Bianchi, C.N.,** Pronzato, R., Cattaneo-Vietti, R., Benedetti-Cecchi, L., Morri, C., Pansini, M., ... Bavestrello, G. 2004. Mediterranean marine benthos: a manual of methods for its study and sampling. *Biol Mar Medit.* 10(1):185-215.
- Bohnsack, J.A.,** & Sutherland, D.L. 1985. Artificial reef research: a review with recommendations for future priorities. *Bull Mar Sci.* 37(1):11-39.
- Boudouresque, C.F.** 1971. Méthodes d'étude qualitative e quantitative du benthos (en particulier du Phytobenthos). *Tethys.* 3(1):79-104.
- Burt, J.,** Bartholomew, A., Bauman, A., Saif, A., & Sale, P.F. 2009. Coral recruitment and early benthic community development on several materials used in the construction of artificial reefs and breakwaters. *J Exp Mar Biol Ecol.* 373:72-8. <http://dx.doi.org/10.1016/j.jembe.2009.03.009>.

- Carta**, E. 2000. Navi e relitti tra Montecarlo e il promontorio di Portofino. Rapallo: Azienda grafica Busco editrice. 143 pp.
- Carta**, E., Maggiori, A., & Penco, A. 2008. Navi e relitti tra Sestri Levante e la Spezia. Rapallo: Azienda grafica Busco editrice. 143 pp.
- Cattaneo-Vietti**, R., Albertelli, G., Bavestrello, G., Bianchi, C.N., Cerrano, C., Chiantore, M., ... Schiaparelli, S. 2002. Can rock composition affect sublittoral epibenthic communities? *PSZNI: Mar Ecol.* 23(1):65-77. <http://dx.doi.org/10.1111/j.1439-0485.2002.tb00008.x>.
- Cattaneo-Vietti**, R. 2004. Progetto di studio per la valutazione e valorizzazione delle emergenze naturalistiche dell'Area Naturale Marina Protetta del Promontorio di Portofino. Parte I: Valutazione della struttura delle principali cenosi presentinell'area anche allo scopo di definirne la ricchezza specifica (biodiversità). Relazione finale. Genova: URL-CoNISMa-Università degli Studi di Genova - Dipteris. 36 pp. (<http://www.portofinoamp.it/it/prodotti-editoriali/relazioni-tecniche/699-2004-qvalutazione-e-valorizzazione-delle-emergenze-naturalistiche-dellamp-portofinoq.html>).
- Cattaneo-Vietti**, R., Albertelli, G., Aliani, S., Bava, S., Bavestrello, G., Benedetti-Cecchi, L., ... Wurtz, M. 2010. The Ligurian Sea: Present status, problems and perspective. *Chem Ecol.* 26:319-40. <http://dx.doi.org/10.1080/02757541003689845>.
- Cerrano**, C., Bavestrello, G., Bianchi, C.N., Cattaneo-Vietti, R., Bava, S., Morganti, C., ... Sponga, F. 2000. A catastrophic mass-mortality episode of gorgonians and other organisms in the Ligurian Sea. *Ecol Lett.* 3:284-93. <http://dx.doi.org/10.1046/j.1461-0248.2000.00152.x>.
- Church**, R., Warren, D., Cullimore, R., Johnston, L., Schroeder, W., Patterson, W., ... Moore, J. 2007. Archaeological and Biological Analysis of World War II Shipwrecks in the Gulf of Mexico: Artificial Reef Effect in Deep Water. U.S. Dept. of the Interior, Minerals Management Service, Gulf of Mexico OCS Region, New Orleans: LA. OCS Study MMS 2007-015. 387 pp.
- Cocito**, S., Bedulli, D., & Sgorbini, S. 2002. Distribution patterns of the sublittoral epibenthic assemblages on a rocky shoal in the Ligurian Sea (NW Mediterranean). *Sci Mar.* 66(2):175-81.
- Guerin**, A.J. 2009. Marine Communities of North Sea Offshore Platforms, and the Use of Stable Isotopes to Explore Artificial Reef Food Webs. Thesis for the degree of Doctor of Philosophy University of Southampton, Faculty of Engineering, Science and Mathematics. Southampton: School of Ocean and Earth Sciences. 226 pp.
- Helton**, D. 2003. Intentional scuttling of vessels as a response alternative. *IOSC papers*, 420:1-15. <http://www.iosc.org/papers/IOSC%202003%20a272.pdf>.
- Kaiser**, M.J., & Kasprzak, R.A. 2008. The impact of the 2005 hurricane season on the Louisiana Artificial Reef Program. *Mar Policy.* 32:956-67. <http://dx.doi.org/10.1016/j.marpol.2008.02.006>.
- Kenchington**, R.A. 1978. Visual surveys of large areas of coral reefs. In: *Coral reefs: research methods*. UNESCO - Monographs on oceanographic methodology, eds. Stoddart, D.R., & Johannes, R.E., 149-62. Paris: UNESCO.
- Mallefet**, J., Zintzen, V., Massin, C., Norro, A., Vincx, M., DeMaerschalck, V., ... Cattrijsse, A. 2008. Belgian shipwreck: hotspots for marine biodiversity (BEWREMABI). Final Scientific Report. Brussels: Belgian Science Policy. 153 pp.
- Massin**, C.L., Norro, A., & Mallefet, J. 2002. Biodiversity of a wreck from the Belgian continental shelf: monitoring using scientific diving. Preliminary results. *Biologie.* 72:67-72.
- Mirto**, G., Pivetta, S., & Spazzapari, G. 2009. Relitti e navi sommerse. Liguria e Toscana. Milano: Magenes Editoriale srl. 510 pp.
- Parravicini**, V., Morri, C., Ciribilli, G., Montefalcone, M., Albertelli, G., & Bianchi, C.N. 2009. Size matters more than method: Visual quadrats vs photography in measuring human impact on Mediterranean rocky reef communities. *Est Coast Shelf Sci.* 81:359-67. <http://dx.doi.org/10.1007/s10750-006-0450-3>.
- Parrish**, F.A., & Pyle, R.L. 2002. Field comparison of open-circuit SCUBA to closed-circuit rebreather for deep mixed-gas diving operations. *Mar Technol Soc J.* 30(2):13-22. <http://dx.doi.org/10.4031/002533202787914052>.
- Peirano**, A., & Sassarini, M. 1991. Analisi delle caratteristiche distributive di alcune *facies* di substrato duro dei fondali delle Cinque Terre (Mar Ligure). *Oebalia.* 17(2):523-8.
- Perkol-Finkel**, S., & Benayahu, Y. 2006. The role of differential survival patterns in shaping coral communities on neighboring artificial and natural reefs. *J Exp Mar Biol Ecol.* 369:1-7. <http://dx.doi.org/10.1016/j.jembe.2008.09.016>.
- Perkol-Finkel**, S., Shashar, N., Barnea, O., Ben-Daviv-Zaslav, R., Oren, U., Reichart, T., ... Benayahu, Y. 2005. Fouling reefal communities on artificial reefs: does age matter? *Biofouling.* 21:127-40. <http://dx.doi.org/10.1080/08927010500133451>.
- Perkol-Finkel**, S., Shashar, N., & Benayahu, Y. 2006. Can artificial reefs mimic natural reef communities? The roles of structural features and age. *Mar Environ Res.* 61:121-35. <http://dx.doi.org/10.1016/j.marenvres.2005.08.001>.
- Piazza**, L., Meinesz, A., Verlaque, M., Akçali, B., Antolić, B., Argyrou, M., ... Ceccherelli, G. 2005. Invasion of *Caulerpa racemosa* var. *cylindracea* (Caulerpaes, Chlorophyta) in the Mediterranean Sea: An assessment of the spread. *Cryptogam Algol.* 26(2):189-202.
- Relini**, G. 2004. Mediterranean marine benthos: a manual of methods for its study and sampling. *Biol Mar Medit.* 10(1):267-307.
- Relini**, G., Relini, M., Palandri, G., Merello, S., & Beccornia, E. 2007. History, ecology and trends for artificial reefs of the Ligurian sea, Italy. *Hydrobiologia.* 580:193-217. <http://dx.doi.org/10.1007/s10750-006-0453-0>.
- Svane**, I., & Petersen, J.K. 2001. On the problems of epibioses, fouling and artificial reefs, a review. *PSZN I: Mar Ecol.* 22(3):169-88.
- Tilburg**, H.V. 2006. Japanese Midget Sub at Pearl Harbor: Collaborative Maritime Heritage Preservation. In: *Heritage at risk. Special*

edition. Underwater cultural heritage at risk: Managing natural and human impacts, eds. Grenier, R., Nutley, D., & Cochran, I., 67-9. Munchen: ICOMOS - International Council on Monuments and Sites.

Underwood, C. 2009. Public archaeology. In: Shared heritage: Joint responsibilities in the management of British warships wrecks overseas, ed. Gallagher, S., 93-109. Worverhampton: University of Worverhampton International seminar.

UNESCO. 2001. Underwater cultural heritage. Text of the 2001 Convention. Paris: UNESCO. <http://ww.unesco.org/new/en/unesco/themes/underwater-cultural-heritage/the-2001-convention/official-text/>.

Walker, S.J., Schlacher, T.A., & Schlacher-Hoenlinger, M.A. 2007. Spatial heterogeneity of epibenthos on artificial reefs: fouling communities in the early stages of colonization on an East Australian shipwreck. *Mar Ecol.* 28:435-45.

Weinberg, S. 1978. The minimal area problem in invertebrate communities and the abiotic environment. *Mar Biol.* 49:41-57. <http://dx.doi.org/10.1007/BF00390728>.

Wessex Archaeology Limited. 2008. Aggregate levy sustainability fund marine aggregates and the historic environment. Wrecks ecology 2007-08. Report Ref: 57456.02. Salisbury: Wessex Archaeology. 117 pp.

Work, T.M., Aeby, G.S., & Maragos, J.E. 2008. Phase shift from a coral to a corallimorph-dominated reef associated with a shipwreck on Palmyra Atoll. *PLoS ONE.* 3(8):e2989. <http://dx.doi.org/10.1371/journal.pone.0002989>.

Zintzen, V., Norro, A., Massinand, C., & Mallefet, J. 2008. Spatial variability of epifaunal communities from artificial habitat: Shipwrecks in the Southern Bight of the North Sea. *Est Coast Shelf.* 76:327-44. <http://dx.doi.org/10.1016/j.ecss.2007.07.012>.

UPCOMING MTS JOURNAL ISSUES

July/August 2013

Marine Renewable Energy Technologies: Outstanding Papers from the 4th Annual Marine Renewable Energy Technical Conference

Guest editors: Kenneth Baldwin, Stephan Grilli, Brian Howes, Daniel MacDonald, and Maggie L. Merrill

September/October 2013

The State of Technology in 2013

Guest editor: Donna Kocak

November/December 2013

Technologies and Techniques for 21st Century Wet Diving

Guest editor: Michael Lombardi

January/February 2014

Marine Technology Developments in Asia

Guest editors: Dhugal Lindsay and Hiroyuki Nakahara.
Manuscripts due end of August 2013.



marine technology
SOCIETY

Opportunity runs deep™

Check the Society website for future *Journal* topics.
www.mtsociety.org

CALL FOR PAPERS

The *MTS Journal* includes technical papers, notes and commentaries of general interest in most issues.

Contact Managing Editor
Amy Morgante

(morganteeditorial@verizon.net)

if you have material you would like considered.

Specifications for submitting a manuscript are on the MTS website under the Publications menu.

www.mtsociety.org

E-mail:

morganteeditorial@verizon.net

Or visit our homepage at

www.mtsociety.org

Marine Technology Society Member Organizations

CORPORATE MEMBERS

ABCO Subsea
Houston, Texas

AMETEK Sea Connect Products, Inc.
Westerly, Rhode Island

Bluefin Robotics
Quincy, MA

C & C Technologies, Inc.
Lafayette, Louisiana

CDL, Inc.
Houston, Texas

C-MAR Group
Houston, Texas

Compass Publications, Inc.
Arlington, Virginia

DOF Subsea USA
Houston, Texas

Dynacon, Inc.
Bryan, Texas

EMAS AMC
Houston, Texas

Fluor Offshore Solutions
Sugar Land, Texas

Forum Energy Technologies
Houston, Texas

Fugro Atlantic
Norfolk, Virginia

Fugro Chance, Inc.
Lafayette, Louisiana

Fugro Geoservices, Inc.
Houston, Texas

Fugro-McClelland Marine Geosciences
Houston, Texas

Fugro Pelagos, Inc.
San Diego, California

Geospace Offshore Cables
Houston, Texas

GE Energy Power Conversion
Houston, Texas

GL Noble Denton
Houston, Texas

HARRIS CapRock Communications
Melbourne, Florida

Hydroid, LLC
Pocasset, Massachusetts

Innerspace Corporation
Covina, California

INTECSEA
Houston, Texas

InterMoor, Inc.
Houston, Texas

J P Kenny, Inc.
Houston, Texas

Kongsberg Maritime, Inc.
Houston, Texas

L-3 Communications
Houston, Texas

L-3 MariPro
Goleta, California

Lockheed Martin Sippican
Marion, Massachusetts

MacArtney, Inc.
Houston, Texas

Marine Cybernetics AS
Trondheim, Norway

Mitsui Engineering and Shipbuilding Co. Ltd.
Tokyo, Japan

Oceaneering Advanced Technologies
Hanover, Maryland

Oceaneering International, Inc.
Houston, Texas

OceanWorks International
Houston, Texas

Odyssey Marine Exploration
Tampa, Florida

Oil States Industries, Inc.
Arlington, Texas

OceanWorks International
Houston, Texas

Petrustech Oil & Gas
Houston, Texas

Phoenix International Holdings, Inc.
Largo, Maryland

Pratt & Whitney Rocketdyne Inc.
Beverly, MA

QinetiQ North America – Technology Solutions Group
Slidell, Louisiana

Raytheon Technical Service Company, LLC

Saipem America, Inc.
Houston, Texas

SBM Atlantia
Houston, Texas

Schilling Robotics, LLC
Davis, California

SEA CON Brantner and Associates, Inc.
El Cajon, California

Seanic Ocean Systems
Houston, Texas

Siemens Energy, Inc.
Houston, Texas

SonTek/YSI, Inc.
San Diego, California

South Bay Cable Corp.
Idyllwild, California

Stress Engineering Services, Inc.
Houston, Texas

Subsea 7 (US), LLC
Houston, Texas

Technip
Houston, Texas

Teledyne Benthos
North Falmouth, Massachusetts

Teledyne Oil & Gas
Daytona Beach, Florida

Teledyne RD Instruments, Inc.
Poway, California

UniversalPegasus International, Inc.
Houston, Texas

Wachs Subsea LLC
Houston, Texas

BUSINESS MEMBERS

Aanderaa Data Instruments, Inc.
Attleboro, Massachusetts

Ashtead Technology, Inc.
Houston, Texas

Baker Marine Solutions
Mandeville, Louisiana

Bastion Technologies, Inc.
Houston, Texas

BioSonics, Inc.
Seattle, Washington

Braemar Technical Services, Inc. (Engineering)
Houston, Texas

C.A. Richards and Associates, Inc.
Houston, Texas

Cochrane Technologies, Inc.
Lafayette, Louisiana

Contros Systems & Solutions GmbH
Kiel, Germany

DeepSea Power and Light
San Diego, California

Deepwater Rental and Supply
New Iberia, Louisiana

DPS Offshore Inc.
Houston, Texas

Embient GmbH
Halstenbek, Germany

Energy Sales, Inc.
Redmond, Washington

Falmat, Inc.
San Marcos, California

FASTORQ
New Caney, Texas

Fugro Atlantic
Norfolk, Virginia

Fugro GeoSurveys, Inc., a division of Fugro
Canada Corp.
St. John's, Newfoundland and Labrador, Canada

GAC Shipping (USA) Inc.
Houston, TX

Horizon Marine, Inc.
Marion, Massachusetts

HortonGMC
Houston, Texas

Huisman North America Services
Rosenberg, Texas

ISR Group
Savannah, Tennessee

iXBlue, Inc.
Cambridge, Massachusetts

Knight, LLC
Lake Forest, California

International Submarine Engineering, Ltd
Port Coquitlam, British Columbia, Canada

Liquid Robotics, Inc.
Palo Alto, California

London Offshore Consultants, Inc.
Houston, Texas

Makai Ocean Engineering, Inc.
Kailua, Hawaii

Maritime Assurance & Consulting Ltd.
Aberdeen, United Kingdom

Matthews-Daniel Company
Houston, Texas

Oceanic Imaging Consultants, Inc.
Honolulu, Hawaii

Offshore Inspection Group, Inc.
Houston, TX

Poseidon Offshore Mining
Oslo, Norway

QPS
Portsmouth, New Hampshire

Quest Offshore Resources
Sugar Land, Texas

Remote Ocean Systems, Inc.
San Diego, California

RRC Robotica Submarina
Macacá, Brazil

SeaBotix
San Diego, California

SeaLandAire Technologies, Inc.
Jackson, Mississippi

SEATECHRIM
Moscow, Russia

SeaView Systems, Inc.
Dexter, Michigan

Sonardyne, Inc.
Houston, Texas

SIMCorp Marine Environmental, Inc.
St. Stephens, Canada

Sound Ocean Systems, Inc.
Redmond, Washington

Stress Subsea, Inc.
Houston, Texas

SURF Subsea, Inc.
Magnolia, Texas

Technip – Global Industries
Houston, Texas

Technology Systems Corporation
Palm City, Florida

Teledyne Impulse
San Diego, California

Tension Member Technology
Huntington Beach, California

VideoRay, LLC
Phoenixville, Pennsylvania

W2S2, LLC
Houston, Texas

WET Labs, Inc.
Philomath, Oregon

WFS Technologies Ltd
Livingston, United Kingdom

Xodus Group
Houston, Texas

INSTITUTIONAL MEMBERS

Associacio Institut Ictineu Centre, Catala De Recerca Submarina
Barcelona, Spain

Canadian Coast Guard
St. John's, Newfoundland and Labrador, Canada

City of St. John's
Newfoundland and Labrador, Canada

CLS America, Inc.
Largo, Maryland

Consortium for Ocean Leadership
Washington, DC

Department of Innovation, Trade and Rural Development
St. John's, Newfoundland and Labrador, Canada

Fundação Homem do Mar
Rio de Janeiro, Brazil

Harbor Branch Oceanographic Institute
Fort Pierce, Florida

International Seabed Authority
Kingston, Jamaica

Jeju Sea Grant Center
Jeju-City, South Korea

Marine Institute
Newfoundland and Labrador, Canada

Monterey Bay Aquarium Research Institute
Moss Landing, California

National Research Council Institute for Ocean Technology
St. John's, Newfoundland and Labrador, Canada

Naval Facilities Engineering Service Center
Port Hueneme, California

NAVFAC Atlantic
Norfolk, VA

NewcastleGateshead Initiative
Gateshead, United Kingdom

Noblis
Falls Church, Virginia

OceanGate, LLC
Miami, Florida

Oregon State University College of Oceanic and Atmospheric Sciences
Corvallis, Oregon

Richard Stockton College of New Jersey
Port Republic, New Jersey

Schmidt Ocean Institute
Lake Forest Park, Washington

U.S. Naval Academy Library
Annapolis, Maryland

University of Massachusetts–Dartmouth
New Bedford, Massachusetts

marine technology SOCIETY
 1100 H Street NW, Suite LL-100
 Washington, DC 20005



Postage for periodicals is paid at Washington, DC and additional mailing offices.

